EDARA
European Development And Research Academy

European Development and Research Academy

Journal of Natural and Applied Sciences Ural

Center for Research and Development of Human Resources Ramah- Jordan

ISSN (Print): 2958-8987
ISSN (Online): 2958-8995

Journal of Natural and Applied Sciences URAL

No. 12, June 2026

A Quarterly Multidiscilinarity Scientific Journal Issued by Center of Research and Human Resources Development Ramah- Jordan and European Development and Research Academy/ Brussels

Focus & Scope:

Journal of Natural and Applied Sciences URAL Journal welcomes high quality contributions investigating topics in the fields of Biology, physics, computer science, Engineering, chemistry, Geology, Agriculture, Medicine, Mathematics, Pharmacy, Veterinary, Nursing, Dentistry, and Environment.

Publication specializations in the journal	
Biology	**Chemistry**
Physics	**Geology**
Computer	**Agriculture**
Engineering	**Mathematics**
Medicine	**Pharmacy**
Veterinary	**Dentistry Veternity,**
Environment	**Nursing**

The Journal is Published in English and Arabic

General Supervisor of the Journal

Prof. Dr. Khalid Ragheb Ahmed Al-Khatib

Head of the Center for Research and Human

Resources Development Ramah – Jordan

Managing Director:

Dr. Mosaddaq Ameen Ateah AL – Doori

Linguistic Reviewer Team

Prof. Dr. Lamiaa Ahmed Rasheed

Tikrit University/College of Education for Women

Asst. Prof. Ahmed Khalid Hasoon

Tikrit University/ College of Education for Women

Asst. Prof. Dr. Mohammad Burjess

Tikrit University/ College of Education

Administrative Title of the Journal:

Amman\ Jordan\ Wasfi Al-Tal \ Gardens

Phone: +962799424774

Index

Constract A New Ballistic Missile model by Line Graph and Measuring its Reliability

Amnah Waheed Sabr [1, a)] and Abeer A. Abdul-Raza [2, b)]

[1] *College of Education for Pure Sciences Thi-Qar University*
[2] *Mathematics department College of Education for Pure sciences Thi-Qar University*

[a)] amina waheed@utq.edu.iq
[b)] abeeraladub80@gmail.com

Constract A New Ballistic Missile model by Line Graph and Measuring its Reliability

Amnah Waheed Sabr [1, a)] and Abeer A. Abdul-Raza [2, b)]

[1] *College of Education for Pure Sciences Thi-Qar University*
[2] *Mathematics department College of Education for Pure sciences Thi-Qar University*

[a)] amina waheed@utq.edu.iq
[b)] abeeraladub80@gmail.com

Abstract:

This study presented a mathematical approach for analysing the reliability of a ballistic missile system using the Line Graph technique from graph theory. The missile structure was modelled by representing the relationships between its main components such as the missile body, propulsion system, fuel system, payload, control unit, guidance system, and fins. The reduction method was applied to simplify the complex network of components and identify the critical paths within the system.

Several reliability measures were employed to evaluate the system performance, including system reliability, Mean Time to Failure (MTTF), hazard rate, Shannon entropy, and extropy. These measures provide a theoretical framework for understanding system behaviour and uncertainty in failure processes. The use of line graphs also helped visualize the structural relationships between components and analyze reliability behavior over time.

Overall, the proposed model demonstrates how graph theory and reliability techniques can be combined to study complex engineering systems and support the improvement of system design and performance under operational condition

Introduction:

Ballistic missiles represent the pinnacle of modern military technology, following a parabolic trajectory driven by gravity after the initial boost phase, making reliability analysis critical for operational success.

Ballistic missiles consist of interconnected components such as the missile body (BM),propulsion system (PS),fuel (Fuel), payload, warhead(WH), control unit (CU), fins (Fins),and guidance/sensors (GS), operating in phases: boost midcourse ballistic trajectory, and re-entry

This study employs the Line Graph model from graph theory to represent these components, where each edge in the original graph becomes a vertex, and vertices are adjacent if their corresponding edges share a common endpoint; for example, BM-PS connects to PS-Fuel, clearly illustrating structural

interdependenice. The model aims to compute system reliability (R_{sys}) through complex statistical equations like $R_{sys} = 1 - \left(1 - R_{Fuel-payload}\right)(1 - R_{OC-Fins})(1 - R_{GS-Sensors})$, focusing on line graph to depict time-dependent decline, MTTF, hazard rate, and entrpy , ultimately optimizing design under harsh conditions.

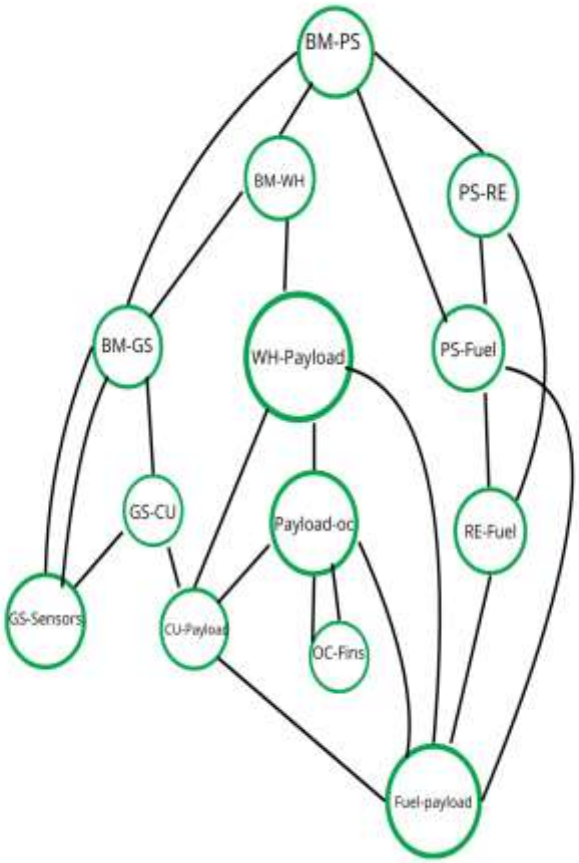

Figure 1 (Balistic Missile Structure)

BASIC CONCEPT

1. System reliability refers to the likelihood that a system will operate without failure over a specific time period.
2. A minimal path consists of components that together form a valid path, but removing any one of them breaks the path's functionality.
3. In a parallel system, the overall reliability is achieved as long as at least one component functions properly :

$$R_{sys} = 1 - \prod_{i=1}^{n}(1 - R_i) \qquad (1)$$

4. Series System
   The reliability of a series system is the probability that component succeeds and component succeeds and all of the other components in the system succeed and it compute

$$R_{sys} = \prod_{i=1}^{n} R_i \qquad (2)$$

5. Series-parallel system
   It is a system that consists of different subsystems connected in series. Each subsystem consists of components connected in parallel as shown in Figure.1.11. The reliability of the system is

$$R_S = \prod_{k=1}^{m}\left(1 - \prod_{i=1}^{n_k}(1 - R_{ik})\right) \qquad (3)$$

6. Shanoon Entropy
   Shannon's entropy quantifies the amount of information in a variable, thus providing the foundation for a theory around the notion of information.

   Shannon entropy is defined by

$$H = -E(\log(p(x)) \qquad (4)$$

   Here, $p(x)$ represents the likelihood that the system occupies cell x within its phase space.

7. Extropy
   The dual measure of entropy has become wides it is known as extropy and defined

$$J(X) = J(P) = -\sum_{i=1}^{n}(1-p)\log(1-p_i) \qquad (5)$$

   Where p_i is the probability densety function [11,12]

Reduction Method for Reliability Analysis in the Line Graph Model

The reduction method is used to simplify the reliability analysis of complex systems represented by a line graph. In this model, each edge of the original missile structure becomes a vertex, and connections between vertices represent interactions between missile components.
To analyse the ballistic missile system, minimal paths connecting the main components were identified. Components arranged in series were reduced by multiplying their reliabilities, while parallel components were replaced by equivalent reliability expressions. By applying these reductions step by step, the complex line graph of the missile system is simplified until it becomes a single equivalent reliability function representing the overall reliability of the system.

After applied the reduction method

Structured Processes

BM-PS → PS-Fuel → Fuel-payload
P_1: x_2 x_9

BM-PS → PS-RE → RE-FueL → Fuel-payload
P_2: $x_1 x_5 x_{16}$

BM-PS → BM-WH → WH-payload → Fuel-payload
P_3: x_3 x_7 x_{11}

BM-PS → BM-WH → WH-payload → CU-payload → Fuel-payload
P_4: x_3 x_7 x_{13} x_{22}

BM-PS → BM-WH → WH-payload → payload-OC → OC-Fins
P_5: $x_3 x_7 x_{12} x_{17}$

BM-PS → BM-GS → GS-CU → CU-payload → Fuel-payload
P_6: x_4 x_{14} x_{20} x_{22}

BM-PS → BM-GS → GS-Sensors
P_7: x_4 x_{15}

BM-PS → BM-WH → BM-GS → GS-CU → GS-Sensors
P_8: x_3 x_8 x_{14} x_{21}

Proposition

Assume the reliability of Balisty Missile

$$R_{sys} = 1 - \left(1 - R_{Fuel-paylod}\right)(1)(1 - R_{GS-Sensors})$$

$$= 1 - [(1-R^2)(1-R^3)(1-R^3)(1-R^4)(1-R^4)](1-R^4)[(1-R^2)(1-R^4)]$$

$$=1 - [(1-R^3-R^2+R^5)(1-R^4-R^3+R^7)(1-R^4)](1-R^4)[1-R^4-R^2+R^6] =$$

$$\begin{aligned} = 1 - [1 &- R^2 - 2R^3 - 2R^4 + 2R^5 + 3R^6 + 4R^7 - 4R^9 - 3R^{10} - 2R^{11} + 2R^{12} + 2R^{13} + R^{14} \\ &- R^{16} - 2R^4 + 2R^6 + 4R^7 + 4R^8 - 4R^9 - 6R^{10} - 8R^{11} + 8R^{13} + 6R^{14} + 4R^{15} \\ &- 4R^{16} - 4R^{17} - 2R^{18} + 2R^{20} - R^2 + R^4 + 2R^5 + 2R^6 - 2R^7 - 3R^8 - 4R^9 \\ &+ 4R^{11} + 3R^{12} + 2R^{13} - 2R^{14} - 2R^{15} - R^{16} + R^{18} + 2R^6 - 2R^8 - 4R^9 - 4R^{10} \\ &+ 4R^{11} + 6R^{12} + 8R^{13} - 8R^{15} - 6R^{16} - 4R^{17} + 4R^{18} + 4R^{19} + 2R^{20} - 2R^{22} \\ &+ R^8 - R^{10} - 2R^{11} - 2R^{12} + 2R^{13} + 3R^{14} + 4R^{15} - 4R^{17} - 3R^{18} - 2R^{19} + 2R^{20} \\ &+ 2R^{21} + R^{22} - R^{24} - R^{10} + R^{12} + 2R^{13} + 2R^{14} - 2R^{15} - 3R^{16} - 4R^{17} + 4R^{19} \\ &+ 3R^{20} + 2R^{21} - 2R^{22} - 2R^{23} - R^{24} + R^{26}] \end{aligned}$$

$$\begin{aligned} = 2R^2 + 2R^3 + 3R^4 - 4R^5 - 9R^6 - 6R^7 + 16R^9 + 15R^{10} + 4R^{11} - 10R^{12} - 24R^{13} - 10R^{14} \\ + 4R^{15} + 15R^{16} + 16R^{17} - 6R^{19} - 9R^{20} - 4R^{21} + 3R^{22} + 2R^{23} + 2R^{24} - R^{26} \end{aligned}$$

When $R = 0.5 \quad then$

$R_{sys} = 0.7$

$$R_{sys} = 2e^{-2\lambda x} + 2e^{-3\lambda x} + 3e^{-4\lambda x} - 4e^{-5\lambda x} - 9e^{-6\lambda x} - 6e^{-7\lambda x} + 16e^{-9\lambda x} + 15e^{-10\lambda x} + 4e^{-11\lambda x} - 10e^{-12\lambda x} - 24e^{-13\lambda x} - 10e^{-14\lambda x} + 4e^{-15\lambda x} + 15e^{-16\lambda x} + 16e^{-17\lambda x} - 6e^{-19\lambda x} - 9e^{-20\lambda x} - 4e^{-21\lambda x} + 3e^{-22\lambda x} + 2e^{-24\lambda x} - e^{-26\lambda x}$$

Mean Time to Failure (MTTF)

The mean time to failure is defined by

$$MTTF = \int_0^t \left(2e^{-2\lambda x} + 2e^{-3\lambda x} + 3e^{-4\lambda x} - 4e^{-5\lambda x} - 9e^{-6\lambda x} - 6e^{-7\lambda x} + 16e^{-9\lambda x} + 15e^{-10\lambda x} + 4e^{-11\lambda x} - 10e^{-12\lambda x} - 24e^{-13\lambda x} - 10e^{-14\lambda x} + 4e^{-15\lambda x} + 15e^{-16\lambda x} + 16e^{-17\lambda x} - 6e^{-19\lambda x} - 9e^{-20\lambda x} - 4e^{-21\lambda x} + 3e^{-22\lambda x} + 2e^{-24\lambda x} - e^{-26\lambda x}\right)dx$$

$$= -\frac{2}{2\lambda}e^{-2\lambda x} - \frac{2}{3\lambda}e^{-3\lambda x} - \frac{3}{4\lambda}e^{-4\lambda x} + \frac{4}{5\lambda}e^{-5\lambda x} + \frac{9}{6\lambda}e^{-6\lambda x} + \frac{6}{7\lambda}e^{-7\lambda x} - \frac{16}{9\lambda}e^{-9\lambda x} - \frac{15}{10\lambda}e^{-10\lambda x} - \frac{4}{11\lambda}e^{-11\lambda x} + \frac{10}{12\lambda}e^{-12\lambda x} + \frac{24}{13\lambda}e^{-13\lambda x} + \frac{10}{14\lambda}e^{-14\lambda x} - \frac{4}{15\lambda}e^{-15\lambda x} - \frac{15}{16\lambda}e^{-16\lambda x} - \frac{16}{17\lambda}e^{-17\lambda x} + \frac{6}{19\lambda}e^{-19\lambda x} + \frac{9}{20\lambda}e^{-20\lambda x} + \frac{4}{21\lambda}e^{-21\lambda x} - \frac{3}{22\lambda}e^{-22\lambda x} - \frac{2}{24\lambda}e^{-24\lambda x} + \frac{1}{26\lambda}e^{-26\lambda x}$$

$$= \left[-\frac{1}{\lambda}e^{-2\lambda t} - \frac{2}{3\lambda}e^{-3\lambda t} - \frac{3}{4\lambda}e^{-4\lambda t} + \frac{4}{5\lambda}e^{-5\lambda t} + \frac{3}{2\lambda}e^{-6\lambda t} + \frac{6}{7\lambda}e^{-7\lambda t} - \frac{16}{9\lambda}e^{-9\lambda t} - \frac{3}{2\lambda}e^{-10\lambda t} - \frac{4}{11\lambda}e^{-11\lambda t} + \frac{5}{6\lambda}e^{-12\lambda t} + \frac{24}{13\lambda}e^{-13\lambda t} + \frac{5}{7\lambda}e^{-14\lambda t} - \frac{4}{15\lambda}e^{-15\lambda t} - \frac{15}{16\lambda}e^{-16\lambda t} - \frac{16}{17\lambda}e^{-17\lambda t} + \frac{6}{19\lambda}e^{-19\lambda t} - \frac{9}{20\lambda}e^{-20\lambda t} + \frac{4}{21\lambda}e^{-21\lambda t} - \frac{3}{22\lambda}e^{-22\lambda t} - \frac{1}{12\lambda}e^{-22\lambda t} - \frac{1}{26\lambda}e^{-26\lambda t}\right] - \left[-\frac{1}{\lambda}e^{0} - \frac{2}{3\lambda}e^{0} - \frac{3}{4\lambda}e^{0} + \frac{4}{5\lambda}e^{0} + \frac{3}{2\lambda}e^{0} + \frac{6}{7\lambda}e^{0} - \frac{16}{9\lambda}e^{0} - \frac{3}{2\lambda}e^{0} - \frac{4}{11\lambda}e^{0} + \frac{5}{6\lambda}e^{0} + \frac{24}{13\lambda}e^{0} + \frac{5}{7\lambda}e^{0} - \frac{4}{15\lambda}e^{0} - \frac{15}{16\lambda}e^{0} - \frac{16}{17\lambda}e^{0} + \frac{6}{19\lambda}e^{0} + \frac{9}{20\lambda}e^{0} + \frac{4}{21\lambda}e^{0} - \frac{3}{22\lambda}e^{0} - \frac{1}{12\lambda}e^{0} + \frac{1}{26\lambda}e^{0}\right]$$

When $\lambda = 1, \quad t = 0.5$

$MTTF = 0.402$

$$f(x) = -dR(x)$$

$$\begin{aligned} = -\big(&-4\lambda e^{-2\lambda x} - 6\lambda e^{-3\lambda x} - 12\lambda e^{-4\lambda x} + 20\lambda e^{-5\lambda x} + 54\lambda e^{-6\lambda x} + 42\lambda e^{-7\lambda x} - 144\lambda e^{-9\lambda x} \\ &- 150\lambda e^{-10\lambda x} - 44\lambda e^{-11\lambda x} + 120\lambda e^{-12\lambda x} + 312\lambda e^{-13\lambda x} + 140\lambda e^{-14\lambda x} \\ &- 60\lambda e^{-15\lambda x} - 240\lambda e^{-16\lambda x} - 272\lambda e^{-17\lambda x} + 144\lambda e^{-19\lambda x} + 180\lambda e^{-20\lambda x} \\ &+ 84\lambda e^{-21\lambda x} - 66\lambda e^{-22\lambda x} - 48\lambda e^{-24\lambda x} + 26\lambda e^{-26\lambda x}\big) \end{aligned}$$

COMPUTING THE ENTROPY OF Balisty Missile

In this section will compute the Shannon entropy of Balisty Missile

In equation ( ) the Shannon entropy is

$$H = -E(\log(p(x)))$$

By substitute equation ( ) in equation ( ) gets

$$= -\int_0^\infty f(t)\log\big(f(t)\big)\,dt$$

$$\begin{aligned} = -\int_0^\infty \big[&4\lambda e^{-2\lambda t} + 6\lambda e^{-3\lambda t} + 12\lambda e^{-4\lambda t} - 20\lambda e^{-5\lambda t} - 54\lambda e^{-6\lambda t} - 42\lambda e^{-7\lambda t} + 144\lambda e^{-9\lambda t} \\ &+ 150\lambda e^{-10\lambda t} + 44\lambda e^{-11\lambda t} - 120\lambda e^{-12\lambda t} - 312\lambda e^{-13\lambda t} - 140\lambda e^{-14\lambda t} \\ &+ 60\lambda e^{-15\lambda t} + 240\lambda e^{-16\lambda t} + 272\lambda e^{-17\lambda t} - 144\lambda e^{-19\lambda t} - 180\lambda e^{-20\lambda t} \\ &- 84\lambda e^{-21\lambda t} + 66\lambda e^{-22\lambda t} + 48\lambda e^{-24\lambda t} - 26\lambda e^{-26\lambda t}\big] \\ &* \log\big[4\lambda e^{-2\lambda t} + 6\lambda e^{-3\lambda t} + 12\lambda e^{-4\lambda t} - 20\lambda e^{-5\lambda t} - 54\lambda e^{-6\lambda t} - 42\lambda e^{-7\lambda t} \\ &+ 144\lambda e^{-9\lambda t} + 150\lambda e^{-10\lambda t} + 44\lambda e^{-11\lambda t} - 120\lambda e^{-12\lambda t} - 312\lambda e^{-13\lambda t} \\ &- 140\lambda e^{-14\lambda t} + 60\lambda e^{-15\lambda t} + 240\lambda e^{-16\lambda t} + 272\lambda e^{-17\lambda t} - 144\lambda e^{-19\lambda t} \\ &- 180\lambda e^{-20\lambda t} - 84\lambda e^{-21\lambda t} + 66\lambda e^{-22\lambda t} + 48\lambda e^{-24\lambda t} - 26\lambda e^{-26\lambda t}\big] dt \end{aligned}$$

when $\lambda = 1, \quad t = 0.5$

$H = 0.11165$

COMPUTING THE EXTROPY OF OF Balisty Missile

The dual measure of entropy has become wides it is known as extropy, so to compute the extropy of Balisty Missile by substitute equation ( ) in equation ( ) gets

$$J = -\int_0^\infty \big(1 - f(t)\big)\,\log\big(1 - f(t)\big)\,dt$$

$$= -\int_0^{\infty}\left[1-\left(4\lambda e^{-2\lambda t}+6\lambda e^{-3\lambda t}+12\lambda e^{-4\lambda t}-20\lambda e^{-5\lambda t}-54\lambda e^{-6\lambda t}-42\lambda e^{-7\lambda t}+144\lambda e^{-9\lambda t}+150\lambda e^{-10\lambda t}+44\lambda e^{-11\lambda t}-120\lambda e^{-12\lambda t}-312\lambda e^{-13\lambda t}-140\lambda e^{-14\lambda t}+60\lambda e^{-15\lambda t}+240\lambda e^{-16\lambda t}+272\lambda e^{-17\lambda t}-144\lambda e^{-19\lambda t}-180\lambda e^{-20\lambda t}-84\lambda e^{-21\lambda t}+66\lambda e^{-22\lambda t}+48\lambda e^{-24\lambda t}-26\lambda e^{-26\lambda t}\right)\right]*\log\left[1-\left(4\lambda e^{-2\lambda t}+6\lambda e^{-3\lambda t}+12\lambda e^{-4\lambda t}-20\lambda e^{-5\lambda t}-54\lambda e^{-6\lambda t}-42\lambda e^{-7\lambda t}+144\lambda e^{-9\lambda t}+150\lambda e^{-10\lambda t}+144\lambda e^{-11\lambda t}-120\lambda e^{-12\lambda t}-312\lambda e^{-13\lambda t}-140\lambda e^{-14\lambda t}+60\lambda e^{-15\lambda t}+240\lambda e^{-16\lambda t}+272\lambda e^{-17\lambda t}-144\lambda e^{-19\lambda t}-180\lambda e^{-20\lambda t}-84\lambda e^{-21\lambda t}+66\lambda e^{-22\lambda t}+48\lambda e^{-24\lambda t}-26\lambda e^{-26\lambda t}\right)\right]dt$$

$$When \quad \lambda = 1 \quad , t = 0.5$$

$$J = \quad 0.25335$$

CONCLUTION

The Line Graph model serves as an advanced analytical tool for evaluating ballistic missile reliability, representing key components like the missile body, propulsion system, fuel, and payload as vertices derived from edges in the original graph.

Results demonstrate a time-dependent reliability decline, with system reliability R_{sys} at 0.6 when individual component reliability R=0.5, Mean Time to Failure(MTTF) of 0.402, Hazard Rate of 0.9284, Shannon Entropy of 0.11165, and Extropy of 0.25335, quantifying failure uncertainty.

This approach provides practical insights for optimizing ballistic missile design under harsh conditions, offering significant applications in military engineering for enhanced performance and safety

REFERENCES

[1] Abdul-Razaq, A. A. (2021). A modified technique for reliability and entropy for network

model: Atomium Bridge as a case study.

[2] Abdul-Razaq, A. A. (2025). Estimate the fractional reliability and the fractional entropy of computer server. Boletín de la Sociedad Paranense de Matemática, 43(35).

[3] Abdul-Razaq, A. A., & Nema, Z. A. (2025). Compute the reliability and the entropy of South Iraqi super grid

[4] Kaplan, E. L., & Meier, P. (1958). Nonparametric estimation from incomplete observations. Journal of the American Statistical Association, 53(282), 457–481. https://doi.org/10.1080/01621459.1958.10501452

[5] Nelson, W. (1982). Applied life data analysis. Wiley.

[6] O'Connor, P. D. T., & Kleyner, A. (2012). Practical reliability engineering (5th ed.). Wiley.

[7] Modarres, M., Kaminskiy, M. P., & Krivtsov, V. (2009). Reliability engineering and risk analysis:

A practical guide (2nd ed.). CRC Press/Taylor & Francis.

[8] U.S. Department of Defense. (1995). MIL-HDBK-217F Notice 2: Reliability prediction of electronic equipment. Military handbook.

[9] U.S. Department of Defense. (1998). MIL-HDBK-338B: Electronic reliability design handbook. Military handbook.

[10] U.S. Department of Defense. (1986). MIL-STD-781D: Reliability testing for engineering development, qualification, and production. Military standard.

[11] International Electrotechnical Commission. (2023). IEC 61124: Reliability testing—Compliance tests for constant failure rate and constant failure intensity. IEC.

[12] Zhang, C. W. (2021). Weibull parameter estimation and reliability analysis with zero-failure data from high-quality products. Reliability Engineering & System Safety, 207, 107321. https://doi.org/10.1016/j.ress.2020.107321

[13] Schumann, J., Mbaya, T., & Mengshoel, O. (2011). Bayesian software health management for aircraft guidance, navigation, and control (NASA Technical Report). NASA NTRS.
[14] U.S. National Aeronautics and Space Administration. (2012). The use of Crow-AMSAA plots to assess mishap trends (NASA report). NASA NTRS.
[15] Hu, W., Cheng, S., Yan, J., Cheng, J., Peng, X., Cho, H., & Lee, I. (2024). Reliability-based design optimization: A state-of-the-art review of its methodologies, applications, and challenges. Structural and Multidisciplinary Optimization, 67, 168.
[16] Zio, E. (2010). Monte Carlo simulation methods for reliability estimation and failure prognostics. In Complex systems and dependability (pp. 123–138). Springer.

On the Structure and Algebraic Behavior of S-Maximal Prime Submodules

Hasan Shakir[1], Haithab A. Shahad[2]

1M.Sc. Student, Department of Mathematics, College of Education for Pure Sciences, University of Wasit, Wasit, Iraq.

2Supervisor, Department of Mathematics, College of Education for Pure Sciences, University of Wasit, Wasit, Iraq.

std.2024205.h.wali@uowasit.edu.iq

hshahad@uowasit.edu.iq

On the Structure and Algebraic Behavior of S-Maximal Prime Submodules

Hasan Shakir[1], Haithab A. Shahad[2]

1M.Sc. Student, Department of Mathematics, College of Education for Pure Sciences,

University of Wasit, Wasit, Iraq.

2Supervisor, Department of Mathematics, College of Education for Pure Sciences,

University of Wasit, Wasit, Iraq.

std.2024205.h.wali@uowasit.edu.iq

hshahad@uowasit.edu.iq

Abstract

In this paper, we introduce and systematically investigate the concept of S-maximal prime submodules, presenting a novel structural generalization of classical prime submodules for unital modules over commutative rings with identity. A proper submodule N of an R-module M is defined to be an S-maximal prime submodule if, for any scalar $r \in R$ and element $m \in M$, the condition $rm \in N$ implies that either $m \in N + S_{J_M}(N)$ or $rM \subseteq N + S_{J_M}(N)$, where $S_{J_M}(N)$ explicitly denotes the localized S-Jacobson radical of N in M. We demonstrate that this framework strictly extends the classical notion of primeness; while every prime submodule is inherently an S-maximal prime submodule, we provide explicit counterexamples confirming that the converse does not hold in general. Furthermore, when the module is the ring itself ($M = R$), an ideal I satisfying these conditions is naturally termed an S-maximal prime ideal of R. Throughout this study, several fundamental properties and characterizations of these submodules are established. We also introduce the notion of the S-maximal prime radical of a submodule, detailing its foundational algebraic properties. Finally, special attention is devoted to the class of finitely generated multiplication modules, wherein we establish robust analytical connections between S-maximal prime submodules and compressible factor modules.

Keywords: Prime submodules, S-maximal prime submodules, S-maximal semiprime submodules, S-Jacobson radical, Multiplication modules, Compressible factor modules, Annihilator ideals

Introduction

Throughout this paper, all rings are assumed to be commutative with identity, and all modules are considered as unital R-modules[13].

The concept of prime submodules serves as a natural mathematical generalization of prime ideals in commutative ring theory[1, 2]. A proper submodule N of an R-module M is called prime if, whenever $rm \in N$ for some $r \in R$ and $m \in M$, then either $m \in N$ or $r \in [N:M]$ [1]. This fundamental concept

was first introduced and systematically investigated by Dauns in 1978, and has since attracted significant attention from numerous researchers[1].

Motivated by the structural significance of this concept, several generalizations of prime submodules have been proposed in the mathematical literature, such as essentially small prime submodules and essentially prime submodules[3, 4].

To delve into deeper generalizations, the theory relies on essential auxiliary concepts. The Jacobson radical of a module M, denoted by $Rad(M)$ or $J(M)$, is defined as the intersection of all maximal submodules of M[15, 17]. Additionally, a nonzero submodule K of an R-module M is called essential if $K \cap S \neq (0)$ for every nonzero submodule S of M[15, 17]. Furthermore, the class of multiplication modules plays a pivotal role, wherein every submodule S of M is of the form $S = IM$ for some ideal I of R[12].

In light of this historical and theoretical evolution, this paper presents a novel contribution by introducing the concept of "S-Maximal Prime Submodules" as an innovative structural generalization of classical prime submodules[5]. This generalization explicitly incorporates the localized S-Jacobson radical into the primeness condition[6]. The primary objective of this research is to explore the fundamental algebraic properties of these newly defined submodules and to establish that they provide a broader framework that strictly extends the classical notion of primeness[6].

S-Maximal Prime Submodules

In this part of the study, we introduce a generalization of prime submodules, termed the S-Maximal Prime Submodules (S-max-PSs). We explore its fundamental properties and provide illustrative characteristics.

Definition 1. *Let R be a ring and M be an R-module. A proper submodule N of M is called an* ***S-maximal submodule*** *if there is no proper semi-essential submodule of M that properly contains N. Equivalently, if W is a semi-essential submodule of M such that $N \subsetneq W \subseteq M$, then it implies that $W = M$.*

Definition 2. *Consider a module M over a ring R, and let $N \subset M$ be a proper submodule. We define N to be an S-maximal prime submodule of M (abbreviated as S-max-PS) provided that for any scalar $r \in R$ and element $m \in M$ such that $rm \in N$, we obtain either $m \in N + SJ(N)$ or $rM \subseteq N + SJ(N)$. Here, the term $SJ(N)$ is defined as the intersection of all S-maximal submodules of M that enclose N, which can be formulated as: $SJ(N) = \bigcap\{K \mid K$ is an S-maximal submodule of M and $N \subseteq K\}$. Particularly, when the module M coincides with the ring R itself, such an N is referred to as an S-maximal prime ideal of R.*

The following findings establish the main characterizations of S-max-PSs.

Prop 1. *Suppose M is an R-module with a proper submodule N. The submodule N serves as an S-max-PS of M if and only if for every ideal I of R and any submodule D of M satisfying $ID \subseteq N$, we conclude that either $D \subseteq N + SJ(N)$ or $I \subseteq [N + SJ(N): M]$.*

Proof. (⇒) Let $I \subseteq R$ be an ideal and $D \subseteq M$ be a submodule fulfilling $ID \subseteq N$. We proceed by assuming that $D \nsubseteq N + SJ(N)$. Consequently, an element $d \in D$ exists wherein $d \notin N + SJ(N)$. Knowing that $ID \subseteq N$, it implies $xd \in N$ for each element $x \in I$. Given that N acts as an S-max-PS of M and d is not in $N + SJ(N)$, it forces the condition $x \in [N + SJ(N): M]$. Therefore, we get $I \subseteq [N + SJ(N): M]$.

(⇐) Conversely, assume there is an element $a \in R$ and an element $m \in M$ such that $am \in N$. This implies for the generated principal ideal (a) and the cyclic submodule (m) that $(a)(m) \subseteq N$. Based on our initial hypothesis, we have either $(m) \subseteq N + SJ(N)$ or $(a) \subseteq [N + SJ(N): M]$. Consequently, it directly follows that $m \in N + SJ(N)$ or $a \in [N + SJ(N): M]$, finalizing the proof. □

As an immediate consequence of Proposition 1, we obtain the subsequent corollary.

Cor 1. *Let M be an R-module and $N \leq M$. Then N is an S-maximal prime submodule of M if and only if for every $a \in R$ and every submodule $D \leq M$ satisfying $aD \subseteq N$, one has either $D \subseteq N + SJ(N)$ or $a \in [N + SJ(N): M]$.*

rem 1. *It is clear that every prime submodule of an R-module K is an S-maximal prime submodule. However, the converse does not necessarily hold, as illustrated in the following examples.*

exm 1. *Consider $M = \mathbb{Z}_{18}$ as a $\mathbb{Z}$-module and let $N = \langle 3 \rangle$. Since the set of maximal submodules of $\mathbb{Z}_{18}$ is $\{\langle 2 \rangle, \langle 3 \rangle\}$, we obtain $SJ(N) = \bigcap\{K \mid K$ is an S-maximal submodule of $\mathbb{Z}_{18}$, $N \subseteq K\} = \langle 6 \rangle$. Now, for any $a \in \mathbb{Z}$ and $y \in \mathbb{Z}_{18}$ with $ay \in N$, it follows that either $y \in N + SJ(N)$ or $a \in [N + SJ(N): M]$. Hence, N is an S-maximal prime submodule of $\mathbb{Z}_{18}$.*

exm 2. *Let $M = \mathbb{Z}_4 \times \mathbb{Z}_2$ and take $N = \mathbb{Z}_4 \times \{0\}$. Then N is a proper submodule of M and satisfies $SJ(N) = N$. For any $a \in \mathbb{Z}$ and $(x, y) \in M$, if $a(x, y) \in N$, then either $(x, y) \in N + SJ(N)$ or $aM \subseteq N$. Therefore, N is an S-maximal prime submodule of M.*

Prop 2. *Let M be an R-module and let N be a submodule of M such that $SJ(N) \subseteq N$. Then N is a prime submodule of M if and only if N is an S-max-PS of M.*

Proof. Since $SJ(N) \subseteq N$,we have $N + SJ(N) = N$. Hence for any $r \in R$ and $m \in M$,

$$rm \in N \Rightarrow m \in N \text{ or } rM \subseteq N,$$

which is equivalent to

$$rm \in N \Rightarrow m \in N \text{ or } r \in [N: M].$$

Thus N is prime if and only if N is an S-max-PS. □

The proposition directly leads to the upcoming corollaries.

Cor 2. *Assume M is an R-module and N is a submodule of M. If the S-Jacobson radical of N is trivial ($SJ(N) = 0$), then N qualifies as a PS of M if and only if it is an S-max-PS of M.*

Prop 3. *Let N represent an S-max-PS within an R-module M. Provided that $SJ(N) \subseteq N$, it logically follows that the residual ideal $[N: M]$ functions as an S-max-PI of the ring R.*

Proof. This is a direct consequence of Proposition 2. □

The upcoming case illustrates that the reverse implication of Proposition 3 is not universally valid.

exm 3. *Let $R = \mathbb{Z}$ and consider the R-module $M = \mathbb{Z} \bigoplus \mathbb{Z}$. Take the submodule $N = 2\mathbb{Z} \bigoplus 0$ of M. We then have: $[N: M] = \{r \in \mathbb{Z} \mid rM \subseteq N\} = 0$, which constitutes a prime ideal of R, and is therefore an S-max-PI. The S-Jacobson radical of N can be expressed as: $SJ(N) = 2\mathbb{Z} \bigoplus \mathbb{Z}$, leading to the conclusion: $N + SJ(N) = 2\mathbb{Z} \bigoplus \mathbb{Z}$. By selecting $r = 2$ and $m = (1,0)$, we find that $rm = (2,0) \in N$. Nevertheless, $m \notin N + SJ(N)$ and $rM = 2\mathbb{Z} \bigoplus 2\mathbb{Z} \nsubseteq N + SJ(N)$. As a result, N fails to be an S-max-PS of M. This demonstrates that the converse of Proposition 3 is not always true.*

Prop 4. *Suppose M is a multiplication non-singular R-module, and let N be a Pr-S satisfying $SJ(N) \subseteq N$. Under these conditions, N is an S-max-PS of M if and only if the ideal $[N: M]$ is an S-max-PI of R.*

Proof. (⇒) This direction is an immediate consequence of Proposition 3.

(⇐) Assume there exist $r \in R$ and $m \in M$ satisfying $rm \in N$. This implies that $r(m) \subseteq N$. Given that M is a multiplication module, we can find an ideal I in R yielding $(m) = IM$. Consequently, $rIM \subseteq N$, which leads to $rI \subseteq [N: M]$.

Knowing that $[N: M]$ serves as an S-max-PI of the ring R, we deduce that either $I \subseteq [N: M]$ or $r \in [N: M]$. As a result, we have two possibilities:

$$IM \subseteq N \subseteq N + SJ(N)$$

or

$$rM \subseteq N \subseteq N + SJ(N).$$

Therefore, it must be the case that either $m \in N + SJ(N)$ or $r \in [N + SJ(N): M]$. This confirms that N is indeed an S-max-PS of M. □

Prop 5. *Let M be a faithful multiplication R-module, and N be a Pr-S of M with $SJ(N) \subseteq S$. Then N is a S-max-PS of M if and only if $[N: M]$ is a S-max-PI of R.*

Proof of Proposition 4 (Continuation). (⇐) Assume $rm \in N$ for some element $r \in R$ and $m \in M$. This gives $r(m) \subseteq N$. By the definition of a multiplication module for M, there is an ideal I of R satisfying $(m) = IM$. It follows that $rIM \subseteq N$, which implies $rI \subseteq [N: M]$.

Given our assumption that $[N: M]$ acts as an S-max-PI over R, we deduce that either $I \subseteq [N: M]$ or $r \in [N: M]$. Consequently, we obtain the following relations:

$$IM \subseteq N \subseteq N + SJ(N)$$

or alternatively,

$$rM \subseteq N \subseteq N + SJ(N).$$

As a result, it must hold that either $m \in N + SJ(N)$ or $r \in [N + SJ(N): M]$. This concludes the proof that N represents an S-max-PS of the module M. □

Prop 6. *Assume M is an R-module containing a submodule N. If the residual ideal $[N + SJ(N): M]$ forms a maximal ideal within the ring R, then N is classified as an S-max-PS of M.*

Proof. Assume there exist $s \in R$ and $m \in M$ such that $sm \in N$, while $s \notin [N + SJ(N): M]$. By the hypothesis that $[N + SJ(N): M]$ is maximal in R, we can express the ring as $R = \langle s \rangle + [N + SJ(N): M]$, where $\langle s \rangle$ denotes the principal ideal generated by s. Therefore, we can find elements $r \in R$ and $x \in [N + SJ(N): M]$ satisfying the equation $1 = rs + x$. Multiplying by m yields $m = rsm + xm$. Since $sm \in N \subseteq N + SJ(N)$ and $xm \in N + SJ(N)$, we conclude that $m \in N + SJ(N)$. This verifies that N is an S-max-PS of M. □

rem 2. *It is a recognized mathematical fact that if we take a non-trivial multiplication R-module M and a prime submodule N within it, then any submodule D of M that strictly contains N ($N \subsetneq D$) will satisfy the condition $[D: M] \nsubseteq [N: M]$.*

Cor 3. *Consider a multiplication module M over a ring R, and let N act as a Pr-S of M. Assume that the residual $[N + SJ(N): M]$ constitutes a prime ideal in R, and furthermore, that $N + SJ(N) \subseteq D$ holds for any submodule D of M. Under these conditions, N serves as an S-max-PS of M.*

Prop 7. *Suppose M is an R-module containing submodules N and D such that $N \subseteq D$. Provided that N acts as an S-max-PS of M and the relation $SJ_D(N) = SJ_M(N)$ holds, it implies that N is equivalently an S-max-PS of the module D.*

Proof. Assume $ad \in N$ for some element $a \in R$ and $d \in D$. Because N is established as an S-max-PS of M, we must have either $d \in N + SJ_M(N)$ or $aM \subseteq N + SJ_M(N)$. If the first condition holds, meaning $d \in N + SJ_M(N) = N + SJ_D(N)$, the proof is complete. In the alternative case, we observe that

$$aD \subseteq aM \subseteq N + SJ_M(N) = N + SJ_D(N).$$

Thus, we conclude that N is indeed an S-max-PS of D. □

Prop 8. *Let M be an R-module containing a submodule N for which $[N + SJ(N): M]$ constitutes a prime ideal in the ring R. Under these circumstances, N is considered an S-max-PS of M if and only if the equality $T^{-1}N = T^{-1}(N + SJ(N))$ is valid for any multiplicatively closed subset T of R satisfying $T \cap [N + SJ(N): M] = \emptyset$.*

Proof. (⇒) Let T be a multiplicatively closed subset of R such that $T \cap [N + SJ(N): M] = \varnothing$,and let $m \in M$ with $\frac{m}{1} \in T^{-1}M$. If $\frac{m}{1} \in T^{-1}N$,then $tm \in N$ for some $t \in T$. Since N is an a S-max-PS of M and $t \notin [N + SJ(N): M]$,it follows that $m \in N + SJ(N)$. Hence $\frac{m}{1} \in T^{-1}(N + SJ(N))$.

(⇐) Suppose that $rm \in N$ with $r \notin [N + SJ(N): M]$. Let $T = \{1, r, r^2, \dots\}$,which is multiplicatively closed and disjoint from $[N + SJ(N): M]$. Then $\frac{m}{1} \in T^{-1}N = T^{-1}(N + SJ(N))$,and so $m \in N + SJ(N)$. Therefore N is an a S-max-PS of M. □

Prop 9. *For any finitely generated non-singular multiplication R-module M with submodules Y and N, if I is a max-PI of R satisfying $ann(Y) \subseteq I$, then IY is necessarily an S-max-PS of M.*

Proof. Assume $am \in IY$ for some scalar $a \in R$ and element $m \in M$. Given the premise that M is a multiplication module, we can identify an ideal J within R that satisfies $(m) = JY$. Consequently, we have

$$aJY \subseteq IY,$$

leading to the relation

$$aJ \subseteq I + ann(Y) = I.$$

Knowing that I is a maximal prime ideal of R, it must be true that either $a \in I$ or $J \subseteq I$.

If $a \in I$, it follows that $aM \subseteq IY \subseteq IY + SJ(IY)$.

Alternatively, if $J \subseteq I$, we obtain $m \in JY \subseteq IY \subseteq IY + SJ(IY)$.

In both scenarios, we conclude that either $m \in IY + SJ(IY)$ or $aM \subseteq IY + SJ(IY)$. Thus, IY is proven to be an S-max-PS of M. □

Cor 4. *Consider a multiplication R-module M and let N be a Pr-S of M satisfying $SJ(N) \subseteq N$. The submodule N acts as an S-max-PS of M if and only if the quotient module M/N is a compressible R-module.*

Prop 10. *Assume M is an R-module, and let N be a Pr-S of M. Suppose that for any submodule D of M strictly containing N ($N \subsetneq D$), the equality $[N + SJ(N): Y] = [N + SJ(N): D]$ holds, along with $N + SJ(N) \subseteq N$. Then N is classified as an S-max-PS of M.*

Proof. Assume there exists an element $ay \in N$, with $a \in R$ and $y \in Y$, such that $y \notin N + SJ(N)$. Let us define a new submodule $D = N + SJ(N) + \langle y \rangle$. It is clear that $N + SJ(N)$ is strictly contained in $N + SJ(N) + \langle y \rangle$, which ensures $y \in D$.

Furthermore, we can deduce that $a \in [N: N + SJ(N) + \langle y \rangle]$. This subset is naturally contained within $[N + SJ(N): N + SJ(N) + \langle y \rangle]$, which by our hypothesis equals $[N + SJ(N): Y]$.

Consequently, we have $a \in [N + SJ(N): Y]$. This confirms that N satisfies the condition to be an S-max-PS of M. □

rem 3. *The intersection of two S-max-PSs of an R-Mod M need not be a S-max-PS of M, as demonstrated by the upcoming example.*

exm 4. *Let $Y = \mathbb{Z}$, $R = \mathbb{Z}$, $N = 2\mathbb{Z}$ and $D = 3\mathbb{Z}$. Then N and D are S-max-PSs of M, but $N \cap D = 6\mathbb{Z}$ is not a S-max-PS of M because $2 \cdot 3 \in 6\mathbb{Z}$, $2 \in R$, $3 \in \mathbb{Z}$, but $3 \notin (N \cap D) + SJ(N)$ and $2 \notin [(N \cap D) + SJ(N): Y] = 6\mathbb{Z}$.*

Prop 11. *Let M be an R-module, and let N and D be two S-max-PSs of M with $\subseteq SJ(N)$ and $D \subseteq SJ(N)$. Then $N \cap D$ is a S-max-PS of M.*

Proof. Suppose $ay \in N \cap D$, where $a \in R$, $y \in Y$. Then $ay \in N$ and $ay \in D$. Since N and D are S-max-PSs of M, either $y \in N + SJ(N)$ or $aY \subseteq N + SJ(N)$, and either $y \in D + SJ(N)$ or $aY \subseteq D + SJ(N)$. But $N \subseteq SJ(N)$ and $D \subseteq SJ(N)$, so either $y \in SJ(N)$ or $aY \subseteq SJ(N)$ and either $y \in SJ(N)$ or

$aY \subseteq SJ(N)$. Hence either $y \in (N \cap D) + SJ(N)$ or $aY \subseteq (N \cap D) + SJ(N)$. Therefore $N \cap D$ is a S-max-PS of M. □

Prop 12. *Let M be an R-module and let N and D be submodules of M such that $SJ(N) \subseteq D$ and $D \nsubseteq N$. If N is an S-max-PS of M,then $N \cap D$ is an S-max-PS of D.*

Proof. Since $D \nsubseteq N$,it follows that $N \cap D$ is a proper submodule of D. Let $a \in R$ and $y \in D$ such that $ay \in N \cap D$. Then $ay \in N$ and $ay \in D$.

Since N is an S-max-PS of M,we have either

$$y \in N + SJ(N) \quad \text{or} \quad aM \subseteq N + SJ(N).$$

Since $y \in D$ and $ay \in D$,it follows that either

$$y \in (N + SJ(N)) \cap D \quad \text{or} \quad aD \subseteq (N + SJ(N)) \cap D.$$

As $SJ(N) \subseteq D$,by the modular law we obtain

$$(N + SJ(N)) \cap D = (N \cap D) + (SJ(N) \cap D).$$

By [13,Cor. 9.9],we have $SJ(D) = SJ(N) \cap D$. Hence either

$$y \in (N \cap D) + SJ(D) \quad \text{or} \quad aD \subseteq (N \cap D) + SJ(D).$$

Therefore $N \cap D$ is an S-max-PS of D. □

exm 5. *Let $R = \mathbb{Z}$ and $M = \mathbb{Z}$ as an R-module. Consider the prime submodules $D_1 = 2\mathbb{Z}$ and $D_2 = 3\mathbb{Z}$ of M. Then $N = D_1 \cap D_2 = 6\mathbb{Z}$. Take $a = 2$ and $y = 3$.Then $ay = 6 \in N$,but $y \notin N$ and $aM = 2\mathbb{Z} \nsubseteq N$. Since $SJ(N) = 0$,we have $N + SJ(N) = N$. Hence N is not an S-max-PS of M. This shows that the intersection of prime submodules need not be an S-max-PS.*

Prop 13. *Let $f \in \mathrm{Hom}(Y, Y')$ be an onto R-morphism, and let N be an S-max-PS of Y'. Then $f^{-1}(N)$ is an S-max-PS of Y.*

Proof. First,we show that $f^{-1}(N)$ is a proper submodule of Y. Since N is proper in Y' and f is onto,it follows that $f^{-1}(N) \neq Y$.

Now let $a \in R$ and $y \in Y$ such that $ay \in f^{-1}(N)$. Then $f(ay) = af(y) \in N$. Since N is an S-max-PS of Y',we have either

$$f(y) \in N + SJ(N) \quad \text{or} \quad aY' \subseteq N + SJ(N).$$

If $f(y) \in N + SJ(N)$,then

$$y \in f^{-1}(N) + f^{-1}(SJ(N)).$$

By [15,Thm.(1.4)(a)],we have

$$f^{-1}(SJ(N)) \subseteq SJ(f^{-1}(N)).$$

Hence

$$y \in f^{-1}(N) + SJ(f^{-1}(N)).$$

If $aY' \subseteq N + SJ(N)$,then since f is onto,we obtain

$$af(Y) \subseteq N + SJ(N),$$

and hence

$$aY \subseteq f^{-1}(N) + f^{-1}(SJ(N)) \subseteq f^{-1}(N) + SJ(f^{-1}(N)).$$

Therefore $f^{-1}(N)$ is an S-max-PS of Y. □

Prop 14. *Assume we have an epimorphism f from an R-module M onto an R-module Y'. If N serves as an S-max-PS within M and contains the kernel of f (*$\ker f \subseteq N$*), then its image $f(N)$ constitutes an S-max-PS in Y'.*

Proof. To begin, we must verify that $f(N)$ strictly sits inside Y'. Assume the opposite, namely $f(N) = Y'$. For any element $y \in M$, its image $f(y)$ belongs to $Y' = f(N)$, meaning we can find some $x \in N$ satisfying $f(y) = f(x)$. This gives $f(y - x) = 0$, leading to $y - x \in \ker f \subseteq N$. Consequently, $y \in N$, which forces $M = N$. This contradicts the assumption that N is a proper submodule, confirming that $f(N) \subsetneq Y'$.

Next, suppose $ay' \in f(N)$ for some scalar $a \in R$ and $y' \in Y'$. Because f is surjective, we can choose $y \in M$ such that $f(y) = y'$. It follows that $ay' = af(y) = f(ay) \in f(N)$. Thus, an element $x \in N$ exists where $f(x) = f(ay)$, yielding $f(x - ay) = 0$. This implies $x - ay \in \ker f \subseteq N$, from which we deduce $ay \in N$.

Knowing that N is an S-max-PS of M, we face two possibilities: either $y \in N + SJ(N)$ or $aM \subseteq N + SJ(N)$. Mapping these conditions through f, we get:

$$f(y) \in f(N) + f(SJ(N)) \quad \text{or} \quad aY' \subseteq f(N) + f(SJ(N)).$$

According to [15, Thm. (1.4)(a)], the inclusion $f(SJ(N)) \subseteq SJ(f(N))$ holds. Therefore, the previous relations become:

$$y' \in f(N) + SJ(f(N)) \quad \text{or} \quad aY' \subseteq f(N) + SJ(f(N)).$$

This concludes the proof that $f(N)$ is an S-max-PS of Y'. □

Cor 5. *Consider an R-module M equipped with submodules D and N satisfying $D \subseteq N \subsetneq M$. Provided that $D \subseteq SJ(N)$, the submodule N qualifies as an S-max-PS of M exactly when the quotient N/D is an S-max-PS of the factor module M/D.*

Prop 15. *Suppose M is an R-module having submodules N and D, along with an S-max-PS denoted by F. If $N \cap D \subseteq F$ and the residual condition $[N:M] \nsubseteq [F + SJ(N):M]$ holds, it forces $D \subseteq F + SJ(N)$.*

Proof. Given the non-inclusion $[N:M] \nsubseteq [F + SJ(N):M]$, we can pick an element $a \in [N:M]$ that does not belong to $[F + SJ(N):M]$. For any arbitrary $x \in D$, we clearly have $ax \in D$. Furthermore,

since $a \in [N:M]$, it implies $aM \subseteq N$, resulting in $ax \in N$. Combining these facts yields $ax \in N \cap D \subseteq F$.

Knowing that F is an S-max-PS of M and $a \notin [F + SJ(N):M]$ (which means $aM \nsubseteq F + SJ(N)$), it necessitates that $x \in F + SJ(N)$. Consequently, we conclude that $D \subseteq F + SJ(N)$. □

Conclusion

In this paper, we have introduced and systematically investigated the concept of S-maximal prime submodules (S-max-PSs), presenting a novel structural generalization of classical prime submodules for unital modules over commutative rings with identity. This structural framework successfully incorporates the localized S-Jacobson radical into the core primeness condition. We have rigorously demonstrated that this framework strictly extends the classical notion of primeness. Crucially, while every traditional prime submodule is inherently an S-maximal prime submodule, explicit counterexamples have been provided to confirm that the converse does not hold in general, thereby validating the structural independence and significance of this new algebraic class.

Furthermore, the algebraic behavior and structural properties of S-max-PSs under fundamental module operations were extensively analyzed. We established that the property of being an S-maximal prime submodule is preserved under the inverse images of surjective R-homomorphisms , as well as under direct images of epimorphisms, provided that the kernel of the mapping is contained within the submodule. Additionally, the precise conditions under which the intersection of S-maximal prime submodules retains this property were successfully determined.

Special attention was also devoted to the intersection of this theory with classical module structures. In particular, robust analytical connections were established between S-maximal prime submodules and compressible factor modules within the class of finitely generated multiplication modules. Moreover, the study detailed the essential relationships between these submodules, non-singular modules, and their associated annihilator ideals.

In conclusion, the findings established throughout this study offer a solid theoretical foundation that enriches the structural theory of modules over commutative rings. These results open up promising new avenues for future research, particularly in exploring the spectral, radical, and homological properties of these generalized submodules in broader algebraic contexts.

References

[1] Dauns, J. “Prime Modules.” *Journal für die reine und angewandte Mathematik*, 2 (1978): 156-181.

[2] Lu, C. P. “Prime submodules of Modules.” *Commentarii Mathematici Universitatis Sancti Pauli*, 33 (1984): 61-69.

[3] Shabad, A. H., and Al-Mothafar, N. S. “E-small prime sub-modules and e-small prime modules.” *AIP Conference Proceedings*, 2023.

[4] Shabad, A. H., and Al-Mothafar, N. S. “On essential-prime sub-modules.” *Journal of Discrete Mathematical Sciences and Cryptography*, 24.7 (2021): 1973-1977.

[5] McCasland, R. L., and Smith, P. F. “Prime submodules of Noetherian Modules.” *Rocky Mountain Journal of Mathematics*, 23.3 (1993): 1041-1062.

[6] McCasland, R. L., Moore, M. C., and Smith, P. F. “On spectrum of Modules over Commutative rings.” *Communications in Algebra*, 25.1 (1997): 79-103.

[7] Moore, M. E., and Smith, S. J. “Prime and Radical submodules over Commutative rings.” *Communications in Algebra*, 30.10 (2002): 5037-5064.

[8] Ebrahimi, S. A., and Esmaeili, K. S. “On McCasland submodules.” *International Mathematical Forum*, 2.46 (2007): 2255-2260.

[9] Hussin, S. A. “WE-Prime submodules and WE-semi-prime submodules.” *Ibn AL-Haitham Journal for Pure and Applied Science*, 3.3 (2018): 109-117.

[10] Hussin, W. A. “WN-2-Absorbing and WES-2-Absorbing submodules.” *Ibn AL-Haitham Journal for Pure and Applied Science*, 31.3 (2018): 118-125.

[11] Goodearl, K. R. *Ring Theory: Nonsingular Rings and Modules*. Marcel Dekker, New York, 1976.

[12] Abd El-Bast, Z., and Smith, P. F. “Multiplication Modules.” *Communications in Algebra*, 16.4 (1988): 755-779.

[13] Larsen, M. D., and McCarthy, P. J. *Multiplicative Theory of Ideals*. Academic Press, New York and London, 1971.

[14] Zelmanowitz, J. “Dense Rings of Linear transformations.” In *Ring Theory II*, Marcel Dekker, New York, 1997.

[15] Anderson, F. W., and Fuller, K. R. *Rings and Categories of Modules*. Springer-Verlag, New York, 1992.

[16] Athab, E. A. *Prime and Semi prime Submodules*. M.Sc. Thesis, College of Science, University of Baghdad, 1996.

[17] Kasch, F. *Modules and Rings*. London Mathematical Society Monographs, Academic Press, New York, 1982.

A Resilient Cascaded Encryption and Steganography-Based Framework for Secure Medical Image Delivery in Wireless Sensor Network

Israa Hussain Abd Alla[1] , MAHER ABED AHMED [2]
1Ministry of Education, Open Educational College, Baghdad, Al-Karkh-3
E.mail: Israa_hussain@yahoo.com , isrhussain40@gmail.com
2Ministry of Education, Open Educational College, Baghdad, Al-Karkh-3
E.mail: ayham.ma2018@gmail.com

A Resilient Cascaded Encryption and Steganography-Based Framework for Secure Medical Image Delivery in Wireless Sensor Network

Israa Hussain Abd Alla[1] , MAHER ABED AHMED [2]
1Ministry of Education, Open Educational College, Baghdad, Al-Karkh-3
E.mail: Israa_hussain@yahoo.com , isrhussain40@gmail.com
2Ministry of Education, Open Educational College, Baghdad, Al-Karkh-3
E.mail: ayham.ma2018@gmail.com

Abstract:

Protection of information in the current world of computer technology is not an easy thing to achieve. Many practices have been introduced in the last decade to safeguard the unity of sensitive information over public domains such as the Internet. One possible approach appears to be the combination of steganography with cryptography. In the research paper on this topic, an image steganography system has been proposed utilizing color-level transformation, transposition technique, Secret Key (SecretKey), and cryptographic techniques. A SecretKey and confidential information or messages are created by employing bitxor operations, bit shuffling, or a stego key. After the above-mentioned multi-layered encryption process, the encrypted data is further concealed in the host image using various techniques, and to achieve watermarking, they are embedded in the pixels of the host image. Moreover, the input image is transposed before the data embedding process is carried out. In the proposed method, this process—combined with other steps such as bit shuffling, bit XOR operations, use of a stego key for encryption, and color-level mapping—makes five layers of security possible. This approach is particularly well-suited for wireless sensor network (WSN) environments, where secure transmission of sensitive medical or surveillance data is critical. All these measures significantly raise the stakes for any potential intruder attempting to extract the data. Invisibility and security are demonstrated conclusively through objective comparative analysis of image quality using numerous quantitative indicators. Furthermore, Stego-Imgs can be obtained by making slight modifications to the histogram, demonstrating the effectiveness of the method.

Keywords: Wireless Sensor Network (WSN) Secret Data (SecDta); Secret Key (SecretKey); Cover Image; Steganography Image (Stego-Img)

I. Introduction

Human visual systems cannot detect steganographic messages [1][2]. Data concealing algorithms, input images, and secret information are prerequisites for steganography. Security can also be enhanced by adding stego keys and encryption procedures to the steganographic algorithm. Security of online banking, secure voting systems, and secure exchanges of confidential messages between sensitive organizations are among the steganography applications. Assailants can use this method to spread viruses and Trojan horses. Additionally, it can be used for secret communications by terrorists and criminals. In addition to text-based steganographic techniques, image-based steganographic

techniques, audio and video-based steganographic schemes, and network packet-based steganographic schemes exist [3][4]. The following two categories can be used to classify steganographic techniques:

1) Methods that utilize the least significant bits (LSBs) [5], methods based on edges, and the differing pixel values (PVD) techniques [6], and the pixel-indicator-techniques (PIT) [7], are all available in the spatial domain [8]. With this method, images are produced in a high-quality manner, but they are also susceptible to a wide range of normal attacks, including JPEG compression, noise attacks, high-pass and low-pass filters, and geometric attacks, which involve cropping, resizing, and rotating images [9].
2) DFT and DWT are examples of transforms that can be used to hide data within the transform domain. Despite carrying a lower payload, they can withstand a wide range of attacks[10].

In this area of steganography, two groups are involved: one creates algorithms for steganography, and the other develops counterattacks or steganography analyses[11]. Steganalysis is the science behind defeating Steganography during its never-ending survival struggle. It is possible to activate steganalysis when retrieving embedded data[12]. Another option would be for it to be passive, with the intent being to detect the secret information. Steganography is used mainly by criminals and terrorists to exchange information, so detecting it is an important issue for law enforcement [13].

Using steganography to conceal information on color images is proposed in this paper. Because color images contain more redundant bits, they have been used as carrier objects. This research work makes the following contributions:

1) Grey-level modification and cryptography as new image steganographic techniques.
2) Comparing Stego to other state-of-the-art systems, Stego's superior quality reduces adversary detection opportunities.
3) Security is enhanced by encrypting the SecretKey and the Secret Data (SecDta) before hiding[14].

The following is a description of how the paper is organized. Several well-known steganographic techniques relevant to the proposed work are briefly discussed in section 2. In section 4, experimental results are explained and discussed in detail, followed by a detailed description of the proposed work in section 3. It is in section 5, the conclusion of this paper as well as our future suggestions was presented.

II. Related Works

Authentication of digital images is a very challenging task in this computerized age since it is very easy to manipulate a digital image. Digital images can be authenticated by using a variety of steganography schemes, depending on the application. A white Gaussian noise wireless channel (AWGN) was used by the authors [16] to verify the encryption of the encrypted image. There is no testing of noise types such as Gaussian noise, rotation noise, and speckle noise on the encrypted image in this paper. Therefore, DRPE provides more robust simulation results than our 2-D chaotic baker map scheme used to verify and protect against image content attacks. Wireless image communication is enhanced by LSB steganography and chaotic baker ciphering in [17]. A cover medium conceals the presence of data inside, whereas encryption protects the cover medium by encrypting the SecDta inside. Content-based image verification for the original image was not provided during AWGN wireless transmission. Neither the proposed schemes nor their quality were tested against other types of noise or attacks. In our schemes, content-based image verification is presented for images, and the performance of the proposed schemes is tested in a variety of ways with respect to noise and attacks. An integer DCT-based watermarking scheme is presented in [18]. DCT and chaotic maps were used to present a watermarking scheme. An embedding scheme for watermarking matrices directly in their

singular sets of a non-linear chaotic map was explored in this paper using a non-linear chaotic map. A digital image watermarking scheme is presented in [19] to protect copyright and detect tampering. The proposed scheme embeds two watermarks in the host image simultaneously to perform two functions: copyright protection and tamper detection. DRPE was used by the authors of [20] to enhance security. Using rear-mounted phase masking, dual random phase coding is enhanced. DRPE and its derivatives have been extensively studied in terms of their cryptanalysis achievements, and the second lens, which plays a critical role in cryptanalysis operations, has been revoked. Watermarking color images blindly with WHT was proposed in [21]. The image was converted using WHT. In the final two rows, the suggested scheme is inserted along with the WHT parameters.

III. Security in Wireless Sensor Networks (WSNs)

WSNs consist of a group of sensor nodes that gather and send environmental or system data, in a collaborative way, with the nodes deployed in a decentralized way, meaning that they can monitor an area without fixed-point supervision or involvement[6][15]. Because of this autonomous monitoring activity, WSNs are heavily subjected to a wide variety of security threats like eavesdropping options, data tampering, malicious node compromise, and denial-of-service variability. WSNs are inherently constrained environments that cannot support traditional heavy-weight security methods due to limited computational power, battery life, and memory [12][19]. Due to this, it is necessary to include light-weight, multi-layered security solutions in WSNs in order to obtain confidentiality, integrity, and authenticity of data. Lightweight IoT security methods can help provide confidentiality and integrity to data even in a uncontrolled environment. Cryptography, steganography, and key management protocols can be ran concurrently in order to develop security methods using light-weight and multi-layered methods[11][17]. Making sure data is secured in applicable contexts is important, especially in situations where the data being transmitted is sensitive, such as military observation or human health monitoring. While compromising secure transmissions by one method is possible, there may be additional methods to work with to compromise security methods. Given the pressure for successful outcomes in these sensed environments, we would intentionally seem like more difficult targets for malicious actors by adding layers of obfuscation through steganography and cryptographic functions described as data being transmitted in an energy-conserving manner without sacrificing low-powered computational overhead compared to the compromise of methods [6] [17].

IV. Image Steganographic

The powerful file format for steganography is images. Human vision limitations are exploited by steganography. Plain text, cipher text, or another image can hide the contents of a bit of stream. The different parts of an image are represented by numbered collections of light intensities on a computer. A pixel is a numeric representation of an individual point. Pixels in an image are represented by rectangular maps that show where they are and what color they are[11][20]. A horizontal row by row representation of these pixels can be found here. A color scheme is classified according to how many bits are used for each pixel. The four shades of gray in a monochrome or grayscale image are represented by eight bits each. RGB color models are used to store color images in 24-bit files. Each color in a 24-bit image is represented by eight bits, with red, green, and blue being the primary colors.

There are two types of image steganography. Transforms and images belong to separate domains[8][19].

Transform domain techniques transform images first before embedding the message into their intensity. Image domain techniques embed the message directly into the pixels. Once the image has been embedded with the message, it is displayed. It is possible to implement bit insertion and noise manipulation in image domain techniques using bit-wise methods. There is no loss in quality or format with lossless image domain techniques. The domain of transformation includes the manipulation of algorithms and the transformation of images. Transforming domain methods does not take into account image formats[7][16].

V. Steganography Encryption Behavior

A digital steganographer conceals data by substituting bits of SecDta for the LSBs of the input image. The basic idea of this technique can be seen in the following binary representation for eight (8) pixels:, 10000010, 01110110, 00101000, 10000100, 01001011, 01110111, 10001101, 01100001.

According to the proposed methodology, the involved secret message in the system "The patient suffers from an unstable state and needs Electroencephalography and Electromyography", and the secret characters: A 01000001. These values are obtained in binary format by hiding the secret character (A) in these pixels: 10001100, 10000011, 01110110, 01100000, 00101000, 10000100, 01001010, and 01110111. LSBs in bold faces indicate pixels that have been changed during data concealment. Approximately half of the pixels changed in the image above, as only four pixels changed. Therefore, Stego-Imgs are almost undetectable for distortions caused by this approach. When the LSB of a pixel does not match a secret bit, the LSB-M method adds or subtracts unity from the pixel value. As a result of the LSB-M revisited methodology (LSB-MR), asymmetric artifacts are reduced in comparison with the LSB method and the LSB-M methodology. From 0.5 to 0.325, the LSB-MR method minimizes the modification rate by interpreting pixel values in dependence on nearby pixels. An attack can easily extract SecDta by extracting LSB, LSB-M, and LSB-MR from them because they contain SecDta embedded in them. To make data extraction difficult for attackers, a stego color cycle (SCC) method was proposed. A cyclic pattern is used here to scatter SecDta in 3-channels of the input cover image. Data is embedded in the sequence of red, green, blue, etc. LSB, LSB-M, and LSB-MR outperform the

forementioned algorithms by scattering the SecDta across multiple channels of the input cover image. These methods can, however, be compromised by a few pixels.

VI. Image Steganography Methodology

This paper proposes a robust approach for mapping SecDta to a RGB channel. Cryptography, transposition, bitxoring, bit shuffling, and SecretKeys are used to create a steganographic system. There are multiple levels of security in the proposed method, unlike other methods.

1. Input carrier images can be transposed to map the SecDta in a way that fools the attacker.
2. Multiple encryption algorithms are applied to the SecretKey and SecDta one after another to encrypt them.
3. The carrier image's blue channel is mapped with SecDta using the color-level modification method (GLM).

A two-module method is proposed for hiding SecDta in carrier image pixels by using encryption and mapping modules. Figure 1 illustrates the overall framework diagrammatically. The following sections briefly describe the modules of the proposed algorithm.

A. Encryption Package: Encrypting both SecretKeys and SecDta is the responsibility of this module. In the end, this module produces encrypted SecretKeys and SecDta bits.

SecretKeys and SecDta are processed by this module in the following algorithm:

1. Decide which confidential data to encrypt and which SecretKey to use
2. The SecretKey should be made into a one-dimensional (1-D) array of bits.
3. The bitxor operation should be applied to these bits if the logical 1 is present.
4. Interchange the bits with odd and even indices in these encrypted bits.
5. If the bit of the SecretKey equal to ONE
6. Then achieve the operation of bitxor of the bit of secret messaget with logical ONE.
7. Otherwise
8. The operation of bitxor is not achieved.
9. Ending of if_Statement
10. Encrypt all SecDta bits by repeating step 4.

B. Mapping Package: Encrypted SecDta is mapped into carrier image pixels by this module. An image channel is transformed before mapping, and a 1-1 mapping is maintained among image pixels and SecDta bits. A stego-Img containing secret information is the result of this module.

C. Data Embedding Algorithm: Discrete cosine transforms and wavelet functions are examples of data embedding methods for host data compressed with transforms or lossy algorithms. Through the analysis of host noise, auxiliary data can be embedded and extracted from combined data. The key can be stored easily by combining the data. Without the key, it is impossible to extract embedded information from images. A key that is embedded in combined data can be removed and managed separately, securing embedded data. Encrypting the image key and storing it in the combined data can be done using a ciphertext that is much smaller than the embedded data. A key is typically ten centibytes to one hundred bytes in size, based on the original host data.

Data embedding algorithm steps are described in the following algorithm:

Inputting Step: Cover color medical image, Key to the secret, and SecDta

Outputting Step: Stego-Img

1. Create a red, green, and blue channel for the color cover medical image
2. Input image is transposed across all three channels
3. Ensure that the SecretKey and SecDta are encrypted according to the instructions provided by the encryption package.
4. If the first bit of SecDta equal to ONE Then
   Add 1 to all pixel values in the blue channel to make them odd, Otherwise

   Add ONE to all the pixel values of the blue channel

5. Using SecretKey Bits, map the SecDta of Step 4 as follows
   If SecretKey Bits equal to ZERO && pixel value Equal to Even OR SecretKey Bits equal to ONE && pixel value equal to Odd Then

   The pixel should remain unchanged, Otherwise

   if SecretKey Bits equal to ZERO && the valueof the pixel equal to Odd

   Then subtract ONE from the valueof the pixel, Otherwise

   if SecretKey Bits equal to ONE1 && the valueof the pixel Equal to Even Then add ONE to the valueof the pixel.

6. The carrier image color levels should be mapped to all secret bits by repeating step 5.
7. Combine all three planes to form Stego-Img by transposing them.

D. The Extraction Algorithm Package

Extraction Algorithm Package

Inputting Step: Stego-Img, Key to the secret

Outputting Step: SecDta

1. Stego-Img is divided into three channels: red, green, and blue.
2. Transpose the Stego-Img images on all three channels.
3. The blue channel's LSB is extracted.
4. Step 3 should be repeated until all secret bits have been extracted.
5. By applying the reverse encryption method to these bits, the original text can be obtained.

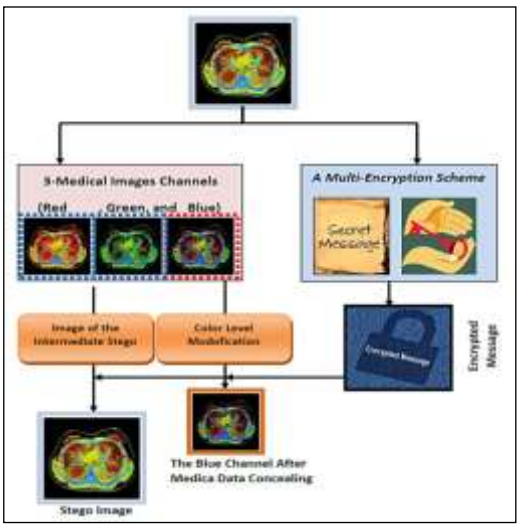

Figure 1. The Proposed Methodology

VII. Experimental Findings and Analysis

Using image quality metrics as a measure of performance, this section presents a comparison between the two solutions. As part of the implementation of the proposed method, MATLAB R2013a is used. A performance evaluation based on image quality metrics will be presented in this section as a means of evaluating performance. The proposed method can be implemented using MATLAB R2013a as the programming language.

A. Experimental Example-1

During one experiment, an eight-kilobyte (8KB) text file has been embedded in 11 standard color images such as chest, head, lung, hip, back, feet, and knees. One experiment involves embedding two standard images of the same dimension with different amounts of data. By using the same image, but with different dimensions, the same amount of data can be embedded. Both subjective and objective measurements were used to compare the proposed method with existing methods. Stego-Imgs are subjectively measured for obvious distortions by human visual systems [41]. Figs. 2-5 show some sample Stego-Imgs and their histograms for standard color covers. As shown in Figure 2-5, it is

impossible to distinguish between the cover image and the Stego-Img and its histogram using human visual systems.

B. Experimental Example-1

The same standard image can also be embedded with different amounts of data. An image with varying dimensions is used in three experiments to embed the same amount of data.

1 Quality and Distortion Metrics

This section presents an assessment of performance using various metrics for assessing image quality. For the implementation of the proposed method, MATLAB R2013a is used. Different perspectives are used to evaluate standard color images of different dimensions. Further, we calculated peak-signal-to-noise ratios, mean square errors, and root square errors. Furthermore, the proposed method is compared with an existing method and histograms are provided to illustrate the improved performance. Using Equations (1) and (4), we calculated PSNR, MSE, RMSE, and normalized cross correlation (NCC). If compression methods are to preserve the diagnostic properties of an image, then the quality of the image should not be affected. There are three factors that determine the success of an image compression algorithm: compression effectiveness, reconstruction mistakes, and complexity of the computation system. CR determines compression effectiveness. There is generally an interaction between reconstruction mistakes and CR. When considering the complexity of the computation element, a portion of the possible execution scenarios are involved.

1. Compression Ration (CR)

In CR, the ratio of the compressed image bits to the original image bits is measured. There is an aspiration to have a relatively high CR. Data compression algorithms must represent admissible fidelity when achieving high CR. There is usually a relationship between the CR and PRD.

$$\mathrm{CR} = \frac{\text{Original File Bit Size}}{\text{Compressed File Bit Size}} \qquad (1)$$

2. Percentage Root mean Difference (PRD)

By comparing point-wise with the initial data, the "Percentage Root Mean Difference" indicates fidelity. The PRD cannot show the accurate quality of signal reconstructions despite their extensive

use, and the decompressed signals must be visual examined for evaluation. The PRD is represented as follows:

$$PRD = \sqrt{\frac{\sum_{n=1}^{N}(x(n)-x'(n))^2}{\sum_{n=1}^{N}x^2(n)}} \times 100 \qquad (2)$$

A PRD is computed from four window sizes: x(n) and x'(n) x n, in which x(n) represents the original value and x'(n) represents the reconstructed value of x(n).

A PRD low value indicates that the original and reconstructed images have preferably less error.

3. Root Mean Square Error (RMS)

RMS provides measurements of image error based on reconstructed image data. According to RMS, the following is true:

$$RMS = 100x\sqrt{\frac{\sum_{n=1}^{N}X_2(n)-X_1(n))^2}{N-1}} \qquad (3)$$

An image's RMS error is calculated by comparing it with the reconstructed image.

4. Signal to Noise Ratio (SNR)

The peak signal-to-noise ratio, represented as decibels (dB), can be calculated as follows:

$$SNR = 10x\log\left(\frac{\sum_{0}^{N-1}(X(n)-mean(X)}{\sum_{0}^{N-1}(X(n)-Y(n))^2}\right) \qquad (4)$$

As a measure of reconstructed image quality versus the original image, SNR is extensively used in the literature regarding image data compression.

5. Normalized Cross-Correlation Coefficient (NCC)

Using the NCC metric, two digital images are compared to determine how similar they are. Below is a demonstration of NCC for image quality:

$$NCC = \frac{1/N\sum_{n=1}^{N}(x(n)-\mu o)\sum_{n=1}^{N}(x'(n)-\mu o)}{\sqrt{\frac{1}{N}\sum_{n=1}^{N}(x(n)-\mu o)2\frac{1}{N}\sum_{n=1}^{N}(x'(n)-\mu o)2}} \qquad (5)$$

Where μ denotes the original image average and μr is the reconstructed image average.

6. Peak-signal-to-noise-Ratio (PSNR)

2. $$PSNR = 10\log_{10}\left(\frac{C_{max}^2}{MSE}\right) \qquad (6)$$

TABLE 1. THE VALUES PSNR AND MSE WITH VARIOUS IMAGES OF THE PROPOSED METHODS

Color Medical Image		The Proposed Method			
		PSNR (dB)	MSE	RMSE	NCC
Med_Img#8		59.0848	0.569	0.7898	1
Med_Img#22		59.0562	0.569	0.79	1
Med_Img#36		59.0562	0.5592	0.79	0.9094
Med_Img#42		60.3442	0.5592	0.7827	1
Med_Img#55		60.3442	0.5519	0.7827	0.9996
Med_Img#6		61.3452	0.5665	0.7771	1
Med_Img#17		59.3714	0.5688	0.7882	1
Med_Img#8		59.0776	0.5684	0.7899	0.9999
Med_Img#39		59.1254	0.5691	0.7896	1
Med_Img#15		59.0316	0.5679	0.79014	0.99
Med_Img#19		59.1952	0.569	0.7892	0.9995
Med_Img#24		59.0484	0.568	0.79	0.9898
Med_Img#31		59.1758	0.5678	0.7893	0.9899
Med_Img#38		59.2072	0.5572	0.7891	1
Med_Img#44		60.615	0.569	0.7898	1
Summation		893.0784	8.48	11.81754	14.8781
Average		59.8719	0.565	0.78784	0.99187

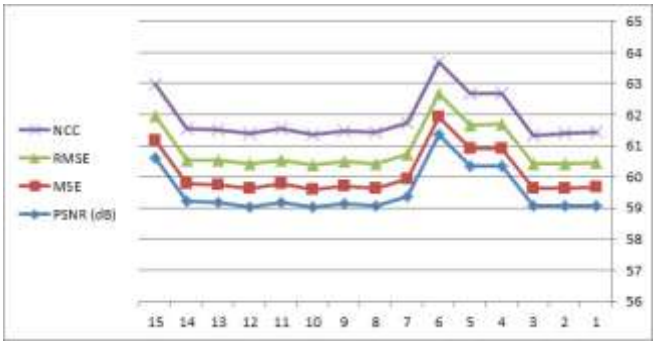

Figure 2. Findings of the Proposed Framework Performance parameters (RMSE, MSE, PSNR and NCC

Image name		Cipher Size (KBs)	Byte Size of the Cipher	Bit Size of the Cipher	PSNR (dB) of the Proposed method
Brain Image with 256×25 Dimension		2	2417	19259	76.9333
		4	4188	33427	71.8388
		6	6510	52003	70.0243
		8	8203	65547	69.0648

TABLE 2. TABLE 2. PSNR-BASED PROPOSED METHOD WITH VARIABLE EMBEDDED CODING

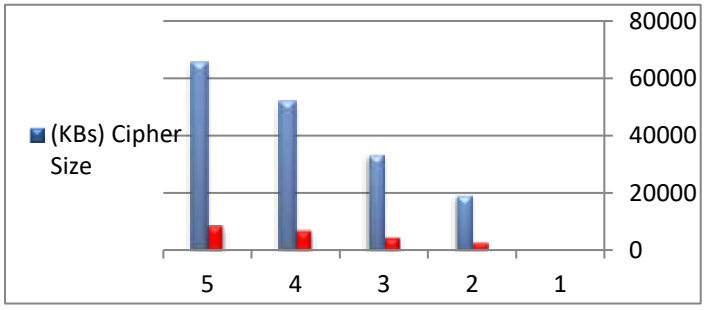

Figure 3. Findings of the Cipher Size, Byte Size of the Cipher, Bit Size of the Cipher , PSNR (dB) of the Brain Image with 256×256 Dimension

TABLE 3 VARIABLE IMAGE DIMENSIONS OF THE PROPOSED METHOD USING PSNR

Image name		Cipher Embedded (bits)	Dimension of the Medical Image	PSNR (dB) of the Proposed method
Chest Medical Image		1695	Size(128 by 128)	68.9397
		1695	Size(256 by 256)	75.1937
		1695	Size(512 by 512)	89.0226
		1695	Size(1024 by 1024)	86.8283

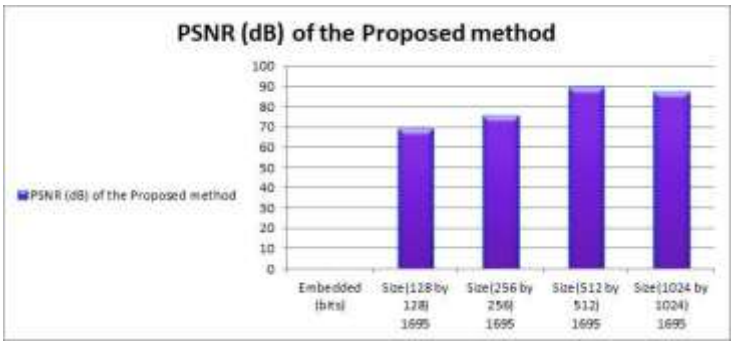

Figure 4. Findings of the Cipher Size, Byte Size of the Cipher, Bit Size of the Cipher , PSNR (dB) of the Brain Image with 256×256 Dimension

	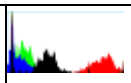		
			
Original Image	Histogram	Encrypted Image	Histogram

TABLE 4. MEDICAL COLOR IMAGE, ENCRYPTED IMAGE WITH THEIR HISTOGRAM

	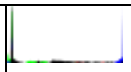		
	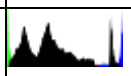		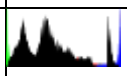
Input Original Image	Histogram	Output Stego-Img	Histogram

TABLE 5, MEDICAL COLOR IMAGE, STEGO-IMG WITH THEIR HISTOGRAM

VIII. Conclusion

Using transposition, bit xoring, bits shuffling, SecretKeys, and cryptography, a method is presented here for mapping SecDta to the color-levels of the carrier image with high imperceptibility and security. Using the proposed method, PSNR is 58dB, RMSE is 0.6673, and NCC is 0.9917, which are better than PSNR, RMSE, and NCC for the existing process in the literature (40, 0.8115, and 0.981, respectively). According to the proposed method, Stego-Imgs are more secure, have higher NCCs, and have less histogram changeability than existing methods. This algorithm has multiple security levels due to its properties of bitxoring, bit transposition, and bit shuffle. The attacker faces multiple barriers

because of these different security levels. Actual SecDta is therefore difficult to extract from a malicious user.

References

[1]. Kusuma, E.J., C.A. Sari, and E.H. Rachmawanto, A Combination of Inverted LSB, RSA, and Arnold Transformation to get Secure and Imperceptible Image Steganography. Journal of ICT Research and Applications, 2018. 12(2): p. 103-122.
[2]. Roy, A., J. Bhattacharya, S. Kundu, S. Sahana and D. Singh. Block Steganography Based Secure Key Encryption to Improve Data Security. in International Conference on Innovation in Modern Science and Technology. 2019. Springer.
[3]. Eliwi, M. H., Sagheer, A. M., & Abdulbaqi, A. S. (2022, October). A new method for medicinal image compression and encryption: Towards remote medicinal diagnosis. In AIP Conference Proceedings (Vol. 2400, No. 1). AIP Publishing.
[4]. Santoso, H.A., E.H. Rachmawanto, and C.A. Sari. An improved message capacity and security using divide and modulus function in spatial domain steganography. in 2018 International Conference on Information and Communications Technology (ICOIACT). 2018. IEEE.
[5]. Champakamala .B.S, Padmini.K, Radhika .D. , "Least Significant Bit algorithm for image steganography", International Journal of Advanced Computer Technology.
[6]. M.K Ramaiya. ; N.Hemrajani, ; , A.K Saxena. "Security improvisation in image steganography using DES" IEEE 3rd International on Advance Computing Conference (IACC), Publication Year: 2013, Page(s): 1094 – 1099.
[7]. Aslam, M. A., Rashid, M., Azam, F., Abbas, M., Rasheed, Y., Alotaibi, S. S., & Anwar, M. W. (2022, January). Image steganography using least significant bit (lsb)-a systematic literature review. In 2022 2nd International Conference on Computing and Information Technology (ICCIT) (pp. 32-38). IEEE.
[8]. Alanzy, M., Alomrani, R., Alqarni, B., & Almutairi, S. (2023). Image Steganography Using LSB and Hybrid Encryption Algorithms. Applied Sciences, 13(21), 11771.
[9]. Jebur, S. A., Nawar, A. K., Kadhim, L. E., & Jahefer, M. M. (2023). Hiding Information in Digital Images Using LSB Steganography Technique. International Journal of Interactive Mobile Technologies, 17(7).
[10]. Nezami, Z. I., Shehzad, D., Ali, H., Asif, M., & Jabbar, U. (2023). LSB Image-to-Image Steganography in a Secure Way Using the Hash Function (No. 10482). EasyChair.
[11]. Demircan, Y. Y., & Ozekes, S. (2024). A Novel LSB Steganography Technique Using Image Segmentation. Journal of Universal Computer Science (JUCS), 30(3).
[12]. Kumar, N., Lakhani, V., Singh, K., Bhardwaj, M., & Raj, S. (2024, March). Development of LSB Based Steganography Method for Video and Image hiding. In 2024 11th International Conference on Reliability, Infocom Technologies and Optimization (Trends and Future Directions)(ICRITO) (pp. 1-6). IEEE.
[13]. Arun, C., Murugan, S.: Design of image steganography using LSB XOR substitution method. In: International Conference on Communication and Signal Processing (ICCSP), IEEE (2017).
[14]. Dilpreet Kaur, Harsh Kumar Verma, Ravindra Kumar Singh, "A Hybrid Approach of Image Steganography", International Conference on Computing, Communication and Automation (ICCCA2016).
[15]. Amitava Nag, Saswati Ghosh, Sushanta Biswas, Debasree Sarkar, Partha Pratim Sarkar "An Image Steganography Technique using X-Box Mapping" IEEE-International Conference On Advances In Engineering, Science And Management (ICAESM -2012) March 30, 31, 2012.
[16]. Akhil Kaushik, AnantKumar and Manoj Bamela " Block Encryption Standard for Transfer of Data " IEEE International Conference on Networking and Information Technology 2010.
[17]. Kordov, K.M., Stoyanov, B.: Least significant bit steganography using Hitzl-Zele chaotic map. Int. J. Electron. Telecommun. (2017
[18]. Astuti, Y.P., E.H. Rachmawanto, and C.A. Sari. Simple and secure image steganography using LSB and triple XOR operation on MSB. in 2018 International Conference on Information and Communications Technology (ICOIACT). 2018. IEEE.
[19]. Abdulbaqi, A. S. (2023, February). A Secure Transmission of Encrypted Medical Data Based on Virtual Instruments. In International Conference On Innovative Computing And Communication (pp. 41-52). Singapore: Springer Nature Singapore.

[20]. Dawen Xu, Rangding Wang, and Yun Q. Shi, Fellow, “Data Hiding in Encrypted H.264/AVC Vide Streams by Codeword Substitution”, IEEE.
[21]. Chikouche, S.L. and N. Chikouche. An improved approach for lsb-based image steganography using AES algorithm. in 2017 5th International Conference on Electrical Engineering-Boumerdes (ICEE-B). 2017. IEEE.

Using Diatoms Indices for Assessing the Water Quality of the Tigris River in some regions of Iraq

Dr. Rawaa Nader Al-Saedy

Department of Biology, College of science of women, university of Baghdad

Ministry of Education ,Third Rusafa Education Directorate

rawaa.nader1102a@csw.uobaghdad.edu.iq

Using Diatoms Indices for Assessing the Water Quality of the Tigris River in some regions of Iraq

Dr. Rawaa Nader Al-Saedy

Department of Biology, College of science of women, university of Baghdad

Ministry of Education ,Third Rusafa Education Directorate

rawaa.nader1102a@csw.uobaghdad.edu.iq

Abstract:

One of the most significant issues facing humanity today is pollution of freshwater resources, and as is well recognized, one of the best ways to safeguard them is to continuously evaluate the condition of aquatic ecosystems. The current study used diatomic indicators (epiphytic diatom) to assess the Tigris River's water quality as it flows through two governorates: Wasit (four stations) and Salah al-Din (one station). This study employed three diatomic indices (DI, GDI, and TDI) from February 2022 to January 2023. The density of algae was ranged from 66 $\times 10^4$cell/g to 182.54 $\times 10^4$cell/g in the S.2 ,S.1 for wet and dry respectively . The findings showed that the river's water quality varied from moderate to good pollution, oligotrophic to mesotrophic and dominating resistant species, declines or extinction of sensitive species (lower diversity), and high pollution.

Keywords: Tigris River, Water Quality, Diatoms Indices , Epiphytic algae.

المستخلص

يُعدّ تلوث موارد المياه العذبة من أبرز المشكلات التي تواجه البشرية اليوم، ومن المعروف أن من أفضل السبل لحمايتها التقييم المستمر لحالة النظم البيئية المائية. هدفت هذه الدراسة إلى تقييم جودة مياه نهر دجلة أثناء مروره بمحافظتين: صلاح الدين (محطة واحدة) وواسط (أربع محطات)، وذلك باستخدام مؤشرات الدياتومات (الدياتومات المتطفلة). استُخدمت ثلاثة مؤشرات للدياتومات في هذه الدراسة (DI، GDI، وTDI) للفترة من فبراير 2022 إلى يناير 2023. تراوحت كثافة الطحالب بين 66 × 10^4 خلية/غرام و182.54 × 10^4 خلية/غرام في العينة S.2، والعينة S.1 في حالتي الرطوبة والجفاف على التوالي. أظهرت النتائج أن جودة مياه النهر تراوحت بين تلوث متوسط وجيد، وتنوع بيولوجي من قليل التغذية إلى متوسط التغذية، وهيمنة الأنواع المقاومة، وانخفاض أو انقراض الأنواع الحساسة (انخفاض التنوع البيولوجي)، وتلوث مرتفع.

الكلمات المفتاحية: نهر دجلة، جودة المياه، مؤشرات الدايتومات، الطحالب الملتصقة على النبات.

Introduction:

Rivers are among the most important components of surface water systems, playing a fundamental role in sustaining both environmental and human life (Vörösmarty *et al*., 2010; Sulaiman *et al*.,2019). They provide essential freshwater resources, support agricultural and industrial activities, generate hydropower, and contribute to transportation and ecological balance (UNESCO, 2024). Furthermore, riverine ecosystems contribute to regulating the hydrological cycle, purifying water, and providing suitable habitats for biodiversity (Dakdouk,2021). However, these ecological functions are increasingly threatened by urban expansion, land-use changes, and chemical pollution, which negatively affect water quality and ecosystem health (Rathod *et al.*,2024). According to recent research, river water quality is a crucial indication of the health of watersheds, and sustainable management calls for integrated approaches to lower pollution, protect biodiversity, and guarantee the long-term availability of water resources for future generations (Khondoker *et al.*,2023). Because of their extreme sensitivity to changes in the physical, chemical, and biological conditions inside aquatic ecosystems, diatoms are widely acknowledged as useful bioindicators for assessing freshwater quality (Costa and Schneck ,2020). These microalgae respond rapidly to variations in nutrient levels, pH, salinity, dissolved oxygen, and other environmental stressors, making them reliable tools for monitoring pollution and assessing ecological healt. (Stevenson,2014). Diatoms, especially epiphytic ones which grows attached to aquatic plants like Phragmites australis can be really good indicators in terms of identifying either local water conditions (within a few meters along the shoreline) since their presence and community composition are strongly linked to both short-term fluctuations as well as long-term environmental changes (Balcerowska-Czerniak, 2025). The Tigris River is one of Iraq's most valuable sources of water running through many urban, industrial and agricultural sectors. This subjects the river to various sources of pollution due to industrial discharges, domestic wastewaters, and agricultural runoff which can change its chemical and biological properties greatly (Al-Saadi et al., 2022; Salih et al., 2022). Thus, monitoring the ecological health of the river becomes a necessity to accomplish sustainable water resources management and environment conservation. The use of attached diatoms on Phragmites australis as Bioindicators provides a cheap, rapid and reliable method for monitoring water quality along the Tigris River. This allows researchers to detect pollution hotspots, assess seasonal patterns and offer scientists management solutions for maintaining the quality of both water and biodiversity in the area (Gholizadeh et al., 2016; Kelly et al., 2021). It is well known that diatoms affixed to aquatic plants are useful bioindicators for evaluating freshwater ecosystem water quality. Numerous diatom-based indices have been used across the world, such as the Generic Diatom Index (GDI) (Lecointe *et al*., 2003), the Trophic Diatom Index (TDI) (Kelly and Whitton, 1995), and the Diatomic Index (DI) (Descy, 1979), all of which are based on a weighting average equation. These studies emphasize the value of employing diatoms as bioindicators to evaluate the Tigris River's water quality (Ali *et al*., 2017; Al-Magdamy *et al*., 2024; Neran *et al*., 2020; Al-Saedy *et al*., 2024). Using diatom-based bioindicators of epiphytic algae to Phragmites australis, the current study sought to examine the water quality of the Tigris River in the provinces

of Salah al-Din and Wasit in order to determine the river's trophic status and the quantity of species that are vulnerable to pollution.

Materials and methods

Description of the study area 1.1

The Tigris River was chosen as the subject of research in this study due to its large hydrological environment and geographical location. The study's fieldwork was carried out in five places that corresponded to two governorates: Wasit Governorate, which has four locations (Al-Aziziyah, Al-Zubaidiyah, Al-Numaniyah, and Al-Miftah), and Salah al-Din (north of Baghdad), which has one location (prior to Samarra Dam). Figure (1) displays the distances between sampling stations as well as the study area's total length in Table (1).

Table (1). Location of Sampling Stations Based on Geographic and UTM Coordinate Systems.

No.	Location Name	Latitude (ϕ)	Longitude(λ)(	Coordinate x-axis (UTM)	Coordinate y-axis (UTM)
1	Samraa (Salah al-Dian)	34.190603	43.864973	395414.866	3783877.163
5	Al-Aziziyah(Wasit)	32.778982	45.162487	515216.599	3626796.983
6	Al-Zubaidya	32.762858	45.173651	516265.02	3625011.197
7	Al-Numiniyh	32.559483	45.409655	538457.348	3602526.899
8	Al-Meftah	32.545552	45.789193	574099.736	3601183.178

Figure.(1) Map of the study area

The first station is Samarra, which is located at latitude N 35.653 33.625 and longitude E 42.445 44.851. Before the Samarra dam, the Tigris River runs through the northern part of Salah al-Din Governorate, passing through the towns of Baiji and Samarra. This portion of the river is thought to be essential for moving water and sediments toward the Samarra Barrage. It is bordered to the north by the Makhol Mountains and to the south by lush floodplains used for irrigated farmland (Namaa *et al*.,2022). The second station is the Waist, which is situated at latitude 31.474° and longitude E 46.54244°. It is a very active agricultural region with several sub-canal-dependent irrigation projects. It is also characterized by limited spring floods and alluvial deposits that increase the fertility of the land. In addition, recent studies have indicated variations in water quality indicators and changes in biodiversity (Moh and Jweid,2022 ; Al-Kubaisi and Al-Saadi,2022: Al-Saedy *et al*.,2024).

Epiphytic Algae diatoms collection and identification1.2

For nine months, from February 2022 to January 2023, epiphytic algae were collected from the study stations, which covered two governorates. The results were presented in two seasons (dry and wet). Samples of epiphytic algae were collected from the Phragmites australis plant and stored in plastic bags with a small amount of river water, adding five to ten milliliters of a 4% buffer-formalin solution until they reached the laboratory. In the qualitative study, the algae were separated from the aquatic plant host by shaking with a scrape (Mitsch and Crok, 1994; Zimba and Hopson, 1997; Hassan *et al*., 2012). In the quantitative study, the method of sedimentation and preservation solution was used to preserve the algae so that the results could be expressed in cells per gram (Furet, 1982). According to the procedures outlined by (Hadi, 1981), epiphytic algae

species were recognized with a light microscope, and diatoms were cleared using strong nitric acid before being identified using permanent slides. Several references were diatoms to identification followed (Hadi *et al*., 1984; Lavoie *et al*., 2008 ; Al-Hassany and Hassan, 2014) .

1.3.Biological Water Quality Index -BWQI

1.3.1.Trophic Diatom Index (TDI)

The basis for this score was the ease of identification of 62 diatom species that were selected based on their indicator value tolerance to inorganic fertilizers.

According to **Kelly and Whitton (1995)**, the TDI was computed using this equation:

TDI = (Aj SjVj /AjVj × 25) – 25

Aj = Abundance or the percentage of the sample's species

Sj = Sensitivity of various feeder types (1-5)

Vj = Guide to value types (1-3)

The aquatic environment can be classified into five stages based on the diatom

nutrient guidance value, which varies from 0 to 100 **Table(2)**.

Table (2) : Trophic Diatom Index (TDI) values and classification according (Kelly and Yallop,2012)

Pollution Degree	**Index value**
Oligotrophic state	TDI < 35
Oligo-mesotrophic State	TDI 50 -35
Mesotrophic State	TDI 60-50
Eutrophic State	TDI 75-60
Hypertrophic State	TDI > 75

1.3.2.Diatomic index (DI)

The formula below was used to calculate the DI **(Descy, 1979)**:

DI = *å* Aj SjVj /AjVj

The results are displayed in Table (3) along with a brief explanation. The values vary from guide diatoms.(5–1)

Table (3) : Diatom Index (DI) values and classification according (Descy,1979).

Index value	Index value Pollution Degree
4.5	No pollution, Best biological water quality
4-4.5	Nearly typical quality (little pollution, minor community changes)
4-3	Quality is basically natural (little pollution, minor community changes).
2-3	High pollution, dominant resistant species, and declines or extinction of sensitive species (reduced diversity).
2-1	extreme pollution and the predominance of a few number of resistant species (many species become extinct).

1.3.3.Generic Diatom Index (GDI)

To calculate the GDI was used **Table (4)** by (Kelly and Whitton,1995)

Table (4) Generic Diatom Index (DI) values and classification according (Lecointe *et al.*,2003) .

Water Quality	Value of GDI
High	17.5- 20
Good	14 -17.5
Moderate	10.5 -14
Poor	7 -10.5
Bad	< 7

Results and Discussion:

This study recorded diatoms 62species belonging to 17 genera as show in **Table (5)**, based on (lobo,16) Hadi Mawla,2026) Ali, S. F., Hassan,2017). This data was then used to calculate diatom density, the highest total number were recorded 182.54 $\times 10^4$ cell /g in S.1 during the dry season, while the lowest number was recorded in S.2, recording 66.49 $\times 10^4$cell /g during the wet season, as show in **Table (6)**, this indicated that diatoms might be more sensitive to changes in temperature, salinity, and nutrients (Albueajee,2020;Neran *et al*.,2020). Moreover due to the abundance of silica in the Iraqi basin, there is a high concentration of silica in all regions and during all seasons(Al-Saedy ,2024).

Expending diatom-based indices (DI, GDI, and TDI), the current study showed different regional and temporal differences in the Tigris River's water quality throughout the governorates of Salah al-Din and Wasit. These results are reliable with recent studies showing that diatoms are useful as sensitive bioindicators for evaluating freshwater ecosystems because of their quick and quantifiable reactions to environmental rises and pollution forces. (Jasim and Ali ,2024; Kelly *et al*., 2016; Stevenson, 2014; Várbíró *et al*., 2020).

The significant effect of hydrological settings on epiphytic algae communities is established by the observed variation in algal compactness between wet and dry seasons. Compact discharge, higher nutrient concentrations, and longer water residence times all of which encourage algae growth are the reasons for elevated densities during the dry season (Lange *et al*., 2016). On the other hand, during the rainy season, increased flow rates and turbulence tend to dilute and physically disturb algae biomass. Similar seasonal patterns have been extensively documented in riverine systems, where hydrological regimes significantly influence the assembling of diatom assemblages (Tornés *et al*., 2021; Al-Saedy *et al*,2025).

The diatom indices shown that water quality alternated from moderate to high levels of pollution, with a shift from oligotrophic to mesotrophic conditions **Table (7)**. This shift proposes increasing nutrient improvement, likely resulting from agricultural runoff, untreated wastewater discharge, and growing urban activities along the river (Abed *et al*., 2020). Like findings have been reported in topical regional studies, which known nutrient filling as a primary driver of abating water quality in Middle Eastern freshwater systems (Hassan *et al*., 2022).

The dominance of pollution-tolerant diatom species, coupled with the decline or absence of sensitive taxa, further approves the presence of ecological stress in the studied sites (Kelly *et al*., 2014). This move in species composition is a well-established ecological response to environmental fracas, where tolerant species outcompete sensitive ones under degraded conditions, ultimately leading to reduced biodiversity (Potapova *et al*., 2018).

The spatial erraticism of the sampling stations, mainly in Wasit governorate, it might be justified by bundled pollution bases associated with land use shapes and population density and release point distance from human activities (Várbíró et al., 2020; Ftaysa and Al-Uqaily,2025). This spatial heterogeneity is relatively common in many impacted river systems affected by anthropogenic

activities which create a point source of pollution along the river continuum (Bellinger and Sigee, 2015).

The above indications of stability betwee the applied indices (DI, GDI and TDI) strengthens the consistency of the results confirming the robustness of diatom-based approaches for assessing water quality. Of these, the Trophic Diatom Index (TDI) is predominantly sensitive to nutrient enrichment and has been extensively used in studies of trophic status assessment for freshwater ecosystems (Kelly et al., 2008; Kelly et al., 2016)

From an ecological perspective, the potential shift to a mesotrophic system and dominance by tolerant species could drive long-term functional changes in the ecosystem (e.g. altered trophic interactions, less resilience). Overall, we recommend regular biomonitoring with diatoms as a cost-effective and reliable tool for environmental trend tracking in support of sustainable water management (Stevenson et al., 2017; UNEP, 2021).

Table (5): Seasonal variations of the average number (× 10^4 cell/L) for epiphytic algae on Phragmites australis in some stations of the Tigris river of Iraq during study period (2022-2023).

List of taxa	Sit.1	Sit. 2	Sit. 3	Sit. 4	Sit. 5	Sit. 1	Sit. 2	Sit. 3	Sit. 4	Sit. 5
PHYLUM: BACILLARIOPHYTA										
CLASS: MEDIOPHYCEAE										
Cyclotella comta (Ehr.) Kützing	6.4	0	0	4.6	0	6.01	5.54	3.72	2.61	2.3
C. Cyclotella meneghiniana Kützing	8.5	0	0	2.7	10	0	0	0	5.2	0
C. striata (Kütz.) Grunow	0	3	0	10	6.5	0.41	0.3	0.61	0	0
CLASS: COSCINODISCOPHYCEAE										
Aulacoseira italica Her	7.2	4.4	0	8.7	0	0	0	0	0	0
A. granulatia (Ehr	0	0	0	0	0	0	0	2.9	0	1.5
CLASS: BACILLARIOPHYCEAE										
Achnanthes hungcerica Grunow	3.2	7.2	2.7	12	0	0	0	0	0	1.2
A. A.minutissimum (Kützing)	0	0	6.3	0	11.7	0	0	4.74	0	2.6
A.microcephale (ktz.) Grunow	16.0	10.6	4.1	17.7	16.3	0	0	0	1.9	0
Bacillaria paxillifer (Müll.) Hendy	2.63	3.52	0	0	0	0	6.6	0	4.43	3.3
Caloneis bacillum (Grun.) Cleve	0	0	2.02	0	0	0	2.1	0	1.4	2.8
C. placentula Ehrenberg	10.6	3	14	0	11.8	6.4	0	3.72	8.4	0
C. placentula var. lineata (Ehr.) Cleve	0	0	0	0	0	0	0	6.1	0	5.5
Cymbella affinis Kützing	0	2.82	3.71	0	5.4	0	0	0	0	0

C.aspera (Ehr.) H.paragallo.	5.3	1.93	0	3.61	0					
C. cymbiformis (ktz.)Van Heurck	0	0	0	0	0	0	3.2	0	2.8	0
C. tumida (Bréb.)V. Heurck	0	0	0	2.7	0	0.2	0	0	0	1.1
*Diatoma elongatum (*Lyngb*.)*Agardh	4.71	0	4	5.32	6.81	0	0	0	0	0
D. elongatum var.minor Grun	3.8	2.11	0	1.9	0	4.2	9.74	0	6.1	0
D. tenuis var. elongatum Lyngbye	3.2	0	1.7	0	0	0	0	0	0	0
D. vulgare Bory	7.91	4.4	9.5	0	3.22	0	0	1	0	0
Epithemia zebra (Ehr.) Kützing	2.63	0	2.7	2.8	0	0	0	3.6	0	3.1
Fragilaria affinis Kutz	2	0	0	3.42	3.94	0	0	0	0	0
F.brevistriata Grunow*.*	4.4	3	6.1	8	4.5	2.1	0	0	1.8	0
F capucina Desmaziers	3.8	0	3.4	8.6	5.91	0	0	0	0	0
F.capitata Ehr*.*	0	4.6	4.1	5.32	0	0	0	0	2.4	1.3
F.fasciculata (Ag.) Kuetzing	0	1.8	0	0	0	4	0	2.4	3.32	0
F.nana Meister	0	0	0	0	0	4.4	0	9.6	0	0
F.tabulata Kützing Grunow	0	4	3.04	0	3	0	0	0	0	0
F.ulna (Nitzs). Ehrenberg	0	0	4.1	8.6	7.6	1.82	0	0	0	2.2
F.ulna var. biceps (Kütz	0	0	0	0	0	2.91	0	2.03	0	0
Gomphonema augur Ehrenberg	0	0	2.2	1.9	2.9	0	0	0	0	0
G. acuminatum Ehrenberg	0	0	3.04	0	0	0	0	1.8	2.1	0
G.gracile Ehrenberg	4.52	0	5.91	0	0	0	0	0	0	0

G.longiceps Ehr.	2.5	2.64	0	0	0	0	0	0	0	0
G. lanceolatum Ehrenberg	0	4	2.7	6.3	0	3.1	0	0	1.4	0
G. parvulum (Ehr.) Grunow	0	5.81	2.7	3.8	3.22	2.3	0	3.72	2.95	0
G. sphaerophorum Ehrenberg	5.1	0	0	3	0	2.5	4.7	5.1	3.13	0
G.truncatum Ehr.	2.82	0	1.8	0	0	0	0	0	0	0
Navicula cincta (Ehr.) Ralfs	2	2.3	7.1	0	5.2	2.3	0	3.72	2.95	0
N.halophile (Grun.) Cleve	0	0	2	2.5	0	0	0	0	0	0
N.gracilis (Ehr.)	2.3	2.64	0	6.3	0	5.5	0	3.7	0	0
N.grrgaria Donkin	0	0	3.04	0	3.6	0	0	0	0	0
N.inflate Donk	5.7	0		0	5.13	3	0	0	2.6	4.01
N.oblonga(Ktz.) Kützing	0	0	2.7	0	3.94	2.7	0	0	2.3	4.7
N. radiosa Kützing	3.01	1.8	3	0	2.51	0	0	1.1	0	1.8
N.spicula (Hicikie) Cleve	0	0	1.7	0	0	0	2.62	3.72	2.21	0
Nitzschia apiculata (Greg.) Grunow	8.5	0	6.8	0	11.7	0	0	0	0	0
N. amphibia Grunow	0	0	0	0	0	4	0	2.2	3.13	0
*N.dissipata (*Ktz.) Grunow	1	0	0	0	4.4	0	0	0	0	0
N.filiformis (W.Smith) Van Heurck	1	0	3.4	3.23	0	1.3	0	0	2.1	0
N.granulata Grunow	0	1.8	0	6.7	0	0	0	0	1.5	2.6
N.hanitzschio Rebenhorst.	3.2	0	0	0	2.7	6.6	6.2	6.9	4.8	6.6
N.microcephala Grunow.	4.9	2.3	0	3.42	0	4	3.2	0	0	0
N. obtusa W.Smith	0	0	3.4	0	3.22	2.2	4	0	1.4	3.6
N.sigma (Ktz.) W.Smith	6.21	0	3.71	0	0	0	0	0	0	0

N.subhyalina A.Cleve	10.6	0	12.8	0	11.3	0	0	0	0	0
Nedium dubium (Ehenberg) Cleve	0	3.2	0	8.74	0					
Peronia fibula (Brébisson ex Kützing	0	0	0	0	0	0	6.6	11	13.3	5.5
Pleurosigma sp.	25	0	2.53	0	1.8	0	0	0	0	0
Rhoicosphenia curvata (Kütz.) Grunow						0	4.12	0	5	8.92
R. gibba (Her.) O.Mueller	1.9	0	1.52	0	0	0	4.12	0	5	8.92
Surirella ovate Ktz	0	0	0	2.7	0	5.4	3.45	0	6.64	2.45

Table (6). Total of Epiphytic algae cells number (Cell*104/g) in some regions of Tigris river during the study period(2022-2023).

	Dry Season				
Class	**S .1**	**S.2**	**S.3**	**S.4**	**S.5**
MEDIOPHYCEAE	14.9	**3**	0	**17.3**	**16.5**
COSCINODISCOPHYCEAE	**7.2**	**4.4**	**0**	**8.7**	**0**
BACILLARIOPHYCEAE	**160.44**	75.47	143.52	128.56	141.8
Total	182.54	82.87	143.52	154.56	158.3
	Wet Season				
Class	**S .1**	**S.2**	**S.3**	**S.4**	**S.5**
MEDIOPHYCEAE	6.42	5.84	**4.33**	**7.81**	**2.3**
COSCINODISCOPHYCEAE	**0**	**0**	**2.9**	**0**	**1.5**
BACILLARIOPHYCEAE	**70.93**	**60.65**	**76.15**	**95.06**	**72.2**
Total	77.35	66.49	83.38	102.87	76

Table (7): Temporal and spatial variation of Diatoms indices (DI, TDI, GDI) for Epiphytic algae during the study (2022-2023) in all stations .

Type algae	Season	St.	DI	TDI	GDI
Epiphytic algae	Dry	**S.1**	**2.8**	**45**	**11.2**
		S.2	3.19	54.76	12.76
		S.3	3.10	52.76	12.4
		S.4	3.11	52.94	12.44
		S.5	3.32	58.15	13.28
	Wet	**S.1**	3.41	60.45	13.64
		S.2	2.81	45.4	11.24
		S.3	3.96	74.03	15.84
		S.4	3.2	55	12.8
		S.5	3.91	72.82	15.64

Conclusion:

This study validates the Tigris River is exposed to different pollution degrees affected by seasonal and spatial factors. The results are consistent with worldwide trends indicating an increase in anthropogenic pressures on freshwater resources; yet, there is an urgent need to build long-term ecological monitoring programs and appropriate management techniques.

References:

1. **Costa,** A. P. T., Trindade, C. R. T., Pinzon, I. M., da Silva, J. S., Rodrigues-Maciel, M. G., da Costa, V. L., & Schneck, F. (2026). Aquatic Biodiversity of the Pampa Biome: Insights From a Scientometric and Systematic Perspective. *Austral Ecology*, *51*(3), e70197.
2. **Dakdouk,** R. (2021). *Evaluating environmental impacts of relocating historic structures: the case of preserving memory in Bisri Valley* (Doctoral dissertation, Notre Dame University-Louaize).
3. **Khondoker**, M., Mandal, S., Gurav, R., & Hwang, S. (2023). Freshwater shortage, salinity increase, and global food production: A need for sustainable irrigation water desalination—A scoping review. *Earth*, *4*(2), 223-240.
4. **Sulaiman**, S. O., Kamel, A. H., Sayl, K. N., & Alfadhel, M. Y. (2019). Water resources management and sustainability over the Western desert of Iraq. *Environmental Earth Sciences*, *78*(16), 495.
5. . **Kelly,** E., Cronk, R., Fisher, M., & Bartram, J. (2021). Sanitary inspection, microbial water quality analysis, and water safety in handpumps in rural sub-Saharan Africa. *npj Clean Water*, *4*(1), 3.
6. **Abed**, I. A., et al. (2020). Assessment of water quality in Iraqi rivers using biological indicators.
7. **Al -Hassany**, J. S. and Hassan, F. M. 2014. Taxonomy Study of some Epiphytic Diatoms on aquatic plants from AL-Hawizah marshes, southern of Iraq Asian Journal National and Applied Science;3(1)
8. **Al-Abueajee,** A. I., Hassan, F. M., and Douabul, A. A. Z. 2020. Phytoplankton species composition and biodiversity indices in Auda marsh-southern Iraq. Iraqi Journal of Agricultural Sciences, 51.
9. **Ali**, E. M., and El Shehawy, A. 2017. Environmental indices and phytoplankton community structure as biological indicators for water quality of the River Nile, Egypt. *Egyptian Journal of Aquatic Biology and Fisheries*, *21*(1), 87-104.
10. **Ali,** S. F., Hassan, F. M., & Abdul-Jabar, R. A. (2017). Water quality assessment by diatoms in Tigris River, Iraq. *International Journal of Environment & Water*, *6*(2), 53-64.
11. **Al-Kubaisi,** A. H., & Al-Saadi, H. A. (2022). Physicochemical properties of the Tigris River within Wasit Governorate, Iraq. ResearchGate. https://www.researchgate.net/figure/Figure-1-Study-sites-on-the-Tigris-River-within-Wasit-Governorate-Source-Ministry-of_fig1_375150995.

12. **Al-Magdamy,** B. A. A. H., Oda, M. N., & AL-Gburi, R. I. K. (2024). The effect of Medical City waste on the quality of plankton diatoms in Tigris River at central Baghdad. *Journal of Genetic and Environment Conservation*, *12*(1), 9-16.

13. **Al-Saadi**, H. A., Al-Dabbas, M. A., & Al-Janabi, R. M. (2022). Assessment of Tigris River water quality using biological and physicochemical indicators. Environmental Monitoring and Assessment, 194, 342.

14. **Al-Saedy**, R. N., Al-Hassany, J. S., & Al-Ramahi, F. K. M. (2025). Evaluation of the Quality of Some Water Stations on the Tigris River Using the Iraqi Water Quality Index (Iraq WQI). *Ibn AL-Haitham Journal For Pure and Applied Sciences*, *38*(4), 107-116.

15. **Al-Saedy,**R.N. 2024. Spatiotemporal variation for water quality of Tigris river between Salahdin and Wasit proviances using some indices GIS and RS techniques. PhD Of College of Science for Women- University of Baghdad , p(1-174).

16. **Amal,** M. E. (2012). The use of diatom indices for the assessment of Shatt AL-Arab river water quality. *Journal of Basrah Researches (Sciences)*, *38*(1), 114-124.

17. **Balcerowska-Czerniak,** G., & Westad, F. (2025). A statistical index of surface water quality as a useful extension of monitoring systems for understanding ecosystems' response to adverse events. *Journal of Environmental Management*, *389*, 126104.

18. **Bellinger**, E. G., & Sigee, D. C. (2015). Freshwater Algae: Identification and Use as Bioindicators. Wiley.

19. **Descy** JP. 1979 .A new approach to water quality estimation using diatoms.

20. **Ftaysa,** S. H., & Al-Uqaily, R. A. H. (2025). Assessment of surface water quality and groundwater in Wasit Governorate, Iraq.

21. **Furet** JE, and Benson-Evans K. 1982. An evaluation of the time required to obtain complete sedimentation of fixed algal particles prior to enumeration. Br Phycol J.;17(3):253–8. 94.

22. **Gholizadeh,** M. H., Melesse, A. M., & Reddi, L. (2016). A comprehensive review on water quality parameters estimation using remote sensing techniques. *Sensors*, *16*(8), 1298

23. **Hadi** Mawla, H. A., & Mahdi Al-Tamimi, A. N. A. (2026). Assessment of Pollution and Trophic Status of Tigris River Water Using Diatom Indices in the Southern Part of Baghdad City, Iraq. *Egyptian Journal of Aquatic Biology and Fisheries*, *30*(2), 741-759.

24. **Hadi** R. 1981. Algal Studies of the River Usk.-364 pp. Ph. D. Thesis, Department of Plant Science, University College, Cardiff.

25. **Hadi,** R.A; Al-Saboonchi, A.A. and Haroon, A.K.Y. 1984. Diatoms of the Shatt All-Arab river, Iraq. Nova Hedwigia Journal;39: 513-557.

26. **Hassan** FM, Hadi RA, Kassim TI, and Al-Hassany JS. 2012. Systematic study of epiphytic algal after restoration of Al-Hawizah marshes, southern of Iraq. Int J Aquat Sci. 3(1):37–57.

27. **Hassan**, F. M., et al. (2022). Evaluation of Tigris River water quality using biological indices.

28. Jasim, H. A., & Ali, S. F. (2024). Diatom Indices for Assessment of the Water Quality in the Lower Zab/Kirkuk Governorate. *Egyptian Journal of Aquatic Biology and Fisheries*, *28*(4), 1197-1207.

29.Kawecka, B. (2021). Epiphytic diatoms and their role in water quality assessment. Hydrobiologia, 848, 15–30.

30.Kelly MG, and Whitton BA. 1995. The trophic diatom index: a new index for monitoring eutrophication in rivers. J Appl Phycol.;7(4):433–44.

31.Kelly, M. G., et al. (2008). Hydrobiologia, 610, 123–137.

32.Kelly, M. G., et al. (2014). Ecological Indicators, 45, 651–658.

33.Kelly, M. G., et al. (2016). Use of diatoms in river monitoring. Science of the Total Environment.

34. Kelly, M. G., Whitton, B. A., & Rimet, F. (2020). Diatoms as indicators of environmental change in freshwater ecosystems. Water, 12(3), 850. https://doi.org/10.3390/w12030850

35. Lange, K., et al. (2016). Freshwater Biology, 61, 1961–1975.

36. Lavoie, I., Campeau, S., Darchambeau, F., Cabana, G., & Dillon, P. J. (2008). Are diatoms good integrators of temporal variability in stream water quality?. *Freshwater biology*, *53*(4), 827-841.

37. Lecointe C, Coste M, Prygiel J. and Omnidia. 2003. Diatom index software including diatom database with taxonomic names, references and codes of.;11645.

38. Lobo, E. A., Heinrich, C. G., Schuch, M., Wetzel, C. E., & Ector, L. (2016). Diatoms as bioindicators in rivers. In *River algae* (pp. 245-271). Cham: Springer International Publishing.

39. Mitsch , W.J. and Cronk, J.K. 1994. periphyton productivity on artificial and natural surfaces in constructed freshwater Wetland under different hydrologic regimes . Aquat . Bot., 48: 325-341.

40. moh, yasir, & Jweid , A. (2022). Assessment of Water Quality of Tigris River and branch in A-lkut City by using Water Quality Index (WQIA). *Wasit Journal of Engineering Sciences*, *10*(3), 203-217. https://doi.org/10.31185/ejuow.Vol10.Iss3.370

41. Namaa, H. M., Mohammed, T. A., & Ibrahim, A. A. (2022). Designing a solar system that improved the solar system's performance in instances of partial shadowing. *Optik*, *271*, 170091.

42. Neran, A., Al Hassany, J. S., and Mashi, F. K. 2020. Assessment of the water quality of Um El-Naaj Marshes by Diatoms. Ecology, Environment and Conservation, 26(1), 449-464.

43. Potapova, M., et al. (2018). Diatoms as indicators of environmental change.

44. Rathod, S. V., Saras, P., & Gondaliya, S. M. (2024). Environmental pollution: Threats and challenges for management. In *Eco-restoration of polluted environment* (pp. 1-34). CRC Press.

45. Salih, A. A., Al-Mahmood, R., & Abdulrahman, H. (2022). Spatiotemporal assessment of water quality in the Tigris River using bioindicators and remote sensing. Arabian Journal of Geosciences, 15, 1121.

46. Stevenson, R. J. (2014). Ecological assessments with algae.

47. Stevenson, R. J., et al. (2017). Algal indicators in environmental monitoring.

48. Tornés, E., et al. (2021). Seasonal dynamics of diatoms in rivers.

49. UNEP (2021). Freshwater Ecosystems Report.

50. Várbíró, G., et al. (2020). Diatom-based ecological status assessment.

51. Vörösmarty, C. J., McIntyre, P. B., Gessner, M. O., Dudgeon, D., Prusevich, A., Green, P., ... & Davies, P. (2010). Global threats to human water security and river biodiversity. *nature*, *467*(7315), 555-561.

52. Zimba, P.V. and Hopson, M.S. 1997. Quantification of epiphyte removal efficiency from submersed aquatic plant. Aquat. Bot., 58:173-179.

Complementary Topological Graphs: Structural Properties and Domination Parameters

Rawaa Habeeb[1] and Mohammed A. Abdlhusein[2]

College of Education for Pure Science, Thi-Qar University [1]

College of Girls, Shatrah University [2]

rawaa_habeeb@utq.edu.iq

mmhd@shu.edu.iq

Complementary Topological Graphs: Structural Properties and Domination Parameters

Rawaa Habeeb[1] and Mohammed A. Abdlhusein[2]

College of Education for Pure Science, Thi-Qar University [1]

College of Girls, Shatrah University [2]

rawaa_habeeb@utq.edu.iq

mmhd@shu.edu.iq

Abstract:

In this thesis, a new type of graph called the complementary topological graph, denoted by G_c , is introduced and studied. This graph is constructed from a finite set X equipped with the discrete topology, where the vertices represent all non-empty proper subsets of X, and two vertices are adjacent whenever their union equals the whole set X . The work focuses on studying several structural properties ofG_c , including the order, size, degree of vertices, Eulerian properties, and chromatic number. It is shown that the graph contains $2^n - 2$ vertices and $\frac{3^n - 2^{n+1}+1}{2}$ edges, where $|X| = n$. In addition, the graph is proved to be regular with degree $2^{n-1} - 1$. Based on these properties, it is concluded that G_c is neither Eulerian nor semi-Eulerian for all $n \geq 3$. The chromatic number of the graph is also determined and shown to be equal to n.

Furthermore, this thesis investigates domination in complementary topological graphs under some graph operations, particularly the corona and join operations. The domination number for these operations is obtained and characterized through several results and examples. The results presented in this thesis provide a deeper understanding of the relationship between graph theory and topology, and they may serve as a basis for future studies on complementary topological graphs and their applications in different areas of graph theory.

Keywords: Complementary Topological Graphs, Domination Number, Graph Operations, Join Operation, Corona Operation, Chromatic Number, Eulerian Graphs, Semi-Eulerian Graphs, Discrete Topology, Graph Theory.

Introduction:

Graph Theory is one of the important branches of mathematics that studies the relationships between objects through vertices and edges. In recent years, the interaction between graph theory and Topology has attracted considerable attention, leading to the construction of several classes of topological graphs with different structural and domination properties. One of the important concepts in graph theory is graph coloring. The chromatic number of a graph G, denoted by $\chi(G)$, is the minimum number of colors required to color the vertices of G such that no two adjacent vertices receive the same color. Another important concept is Eulerian properties. A connected graph is called Eulerian if every vertex has even degree, while it is called semi-Eulerian if exactly two vertices have

odd degree. Graph operations also play a fundamental role in studying graph structures and domination properties. Among these operations are the join and corona operations. The join $G_1 + G_2$ of two graphs G_1 (V_1, E_1) and G_2 (V_2, E_2) is obtained by joining every vertex of $G_1$to every vertex of G_2. On the other hand, the corona $G_1 \odot G_2$ is constructed by taking one copy of G_1 together with copies of G_2, and connecting each vertex of G_1 to all vertices in its corresponding copy of G_2. The main aim of this paper is to study the structural and domination properties of complementary topological graphs. In particular, the order, size, chromatic number, Eulerian properties, and domination numbers under join and corona operations are investigated.

Definition of Complementary Topological Graph

Definition 1: Let X be a non-empty set and τ be a discrete topology on X. The complementary topological graph denoted by $G_c = (V, E)$ is a graph of the vertex set $V = \{A;\ A \in \tau$ and $A \neq \emptyset, X\}$, and the edge set $E = \{A\,B;\ A \cup B = X$,where $A, B \in \tau\}$.

Proposition 1.1: The order of complementary topological graph G_c is $2^n - 2$, for $|X| = n$.

Proof: Since τ be a family of all subsets of X which are 2^n sets. Then, G_c has all elements of τ unless ø and X by Definition 2.2.1

Theorem 1.2: Let X be a finite set with $| X | = n$ and let τ be the discrete topological space. Then, the number of edges of G_c, is $| E(G_c) | = \frac{3^n - 2^{n+1} + 1}{2}$.

Proof: Assume $n = 2$, then, the order of edges is one which are two vertices. There is exactly one edge between them.

Also, if $n = 3$, $| E(G_c) | = \frac{3^3 - 2^{3+1} + 1}{2} = \frac{27 - 16 + 1}{2} = \frac{12}{2} = 6$

when $n = 4$. The number of edges is $| E(G_c) | = \frac{3^4 - 2^{4+1} + 1}{2} = \frac{81 - 32 + 1}{2} = \frac{50}{2} = 25$. We can note that in figure

The computed values agree with the given formula for the tested cases. This supports the correctness of the formula for the number of edges of G_c .

$n = 2$, then, the order of edges is one. If $n = 3$, we note the order of edges is 6, when $n = 4$. The number of edges is 25.

Proposition1.3: The complementary topological graph G_c is non-Eulerian and not semi-Eulerian

Proof. Let $| X | = n \geq 3$ and let G_c be the complementary topological graph. From Theorem 2.7, for every vertex $A \in V(G_c)$ deg G_c $(A) = 2^{n-1} - 1$. Hence, G_c is a regular graph of degree $2^{n-1} - 1$. Since $2^{n-1} - 1$ is even for all $n \geq 2$, it follows that $2^{n-1} - 1$ is odd. every vertex of G_c has odd degree. Moreover, G_c is connected. By Eulers theorem, a connected graph is Eulerian if and only if all its vertices have even degree, and it is semi- Eulerian if and if exactly two vertices have odd

degree. Since in G_c all vertices have odd degree and their number exceeds two for $n \geq 3$, it follows that G_c is neither Eulerian nor semi-Eulerian. Therefore G_c is non-Eulerian for all $n \geq 3$.

Theorem1.4: Let X be a finite set with $|X| = n \geq 2$, and let τ be the discrete topology on X. Then the chromatic number of G_c satisfies $\chi(G_c) = n$.

Proof: Assum that $n = 2$. Since the two vertices are adjacent, they cannot be assigned the same color. Hence $\chi(G_c) = 2$. When $n = 3$ then the pendent vertices its singleton vertex is adjacent with complementary. Therefore, every vertex must receive a color different from the color assigned to its complement. Moreover, the complementary vertices are also connected according to the structure shown in the graph. When $n = 5$ Since the vertices adjacent with complementary. The singleton vertex adjacent with the complementary vertices and this vertex is connected $\chi(G_c) = n$. The chromatic number $\chi(G_c) = n$ because the graph contains a complete induced subgraph of order n (K_n). Hence, at least n colors are required.

Example 1.4: We will apply Theorem 2.2.24 in the graph G_c if $|X| = 2$

$\chi(G_c) = 2$

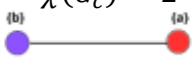

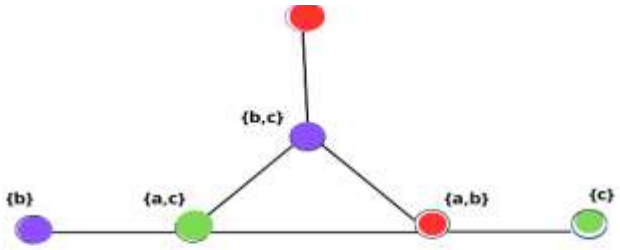

$\chi(G_c) = 3$

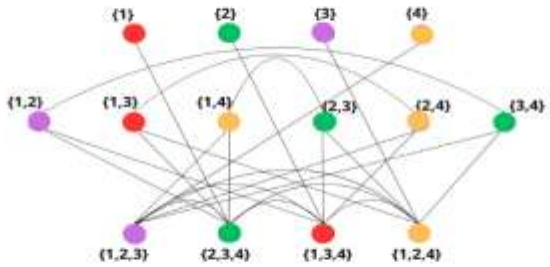

$\chi(G_c) = 4$

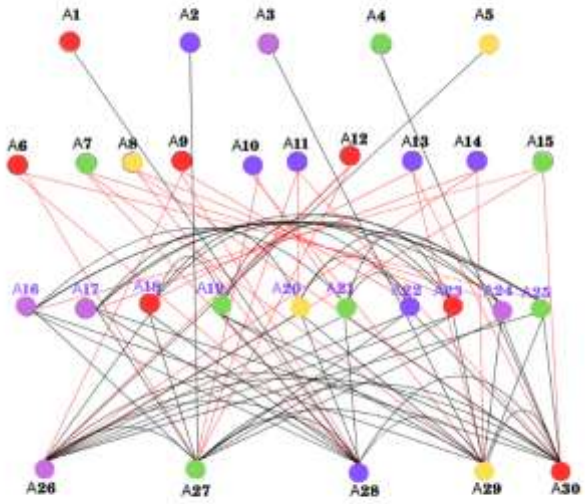

$$\chi(G_c) = 5$$

Figure 1: The chromatic number

Theorem 3.2.5: Let G_c be a complementary topological graph defined on a set X, and R_c be a complementary topological graph defined on a set W such that $|X| = n$ and $|W| = m$. Then, $G_c \odot R_c$ has dominating set and domination number where: $\gamma(G_c \odot R_c) = 2^n - 2$.

Proof: By definition of corona operation $G_c \odot R_c$, each vertex in G_c is adjacent with all vertices of one copy of a graph R_c. This means if $v_i \in V(G_c)$, then v_i is adjacent with all vertices of the i^{th} copy of R_c. Thus, v_i dominates all vertices of one copy of R_c, so that $v_i \in D$. Then, $D = V(G_c)$ is the minimum dominating set of a graph $G_c \odot R_c$. Since the number of all vertices in a graph G_c is $2^n - 2$ according to Proposition 2.2.19. Thus, the order of minimum dominating set D is $2^n - 2$. Therefore, $\gamma(G_c \odot R_c) = 2^n - 2$. As an example, see Figure 3.5.

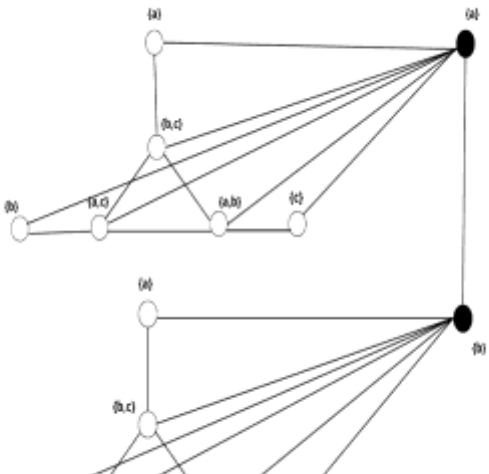

(a) $k_2 \odot \overline{C_6}$

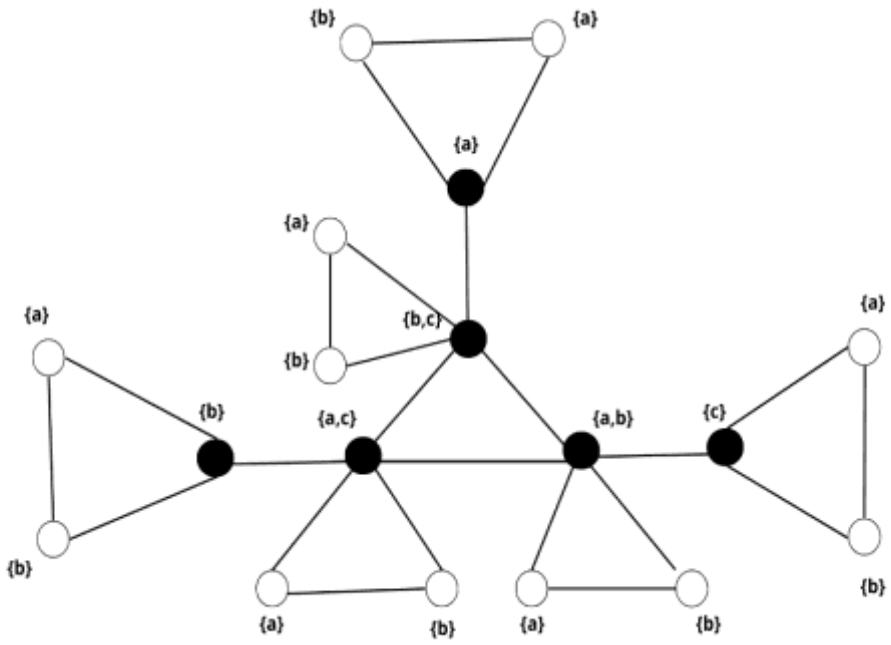

(b)Figure $\overline{C_6} \odot k_2$

Figure 2: A minimum dominating set in $k_2 \odot \overline{C_6}$ and $\overline{C_6} \odot k_2$.

Theorem 1.6: Let G_c be a discrete topological graph defined on a set X, and R_c be a complementary topological graph defined on a set W. If $|X| = n$ and $|W| = m$, then $\gamma\ (G_c + R_c) =$
$\begin{cases} 1, & if \quad n = 2 \ or \ m = 2 \\ n, & if \quad n, m > 2 \end{cases}$

Proof: In the graph $G_c + R_c$ each vertex from a graph G_c is adjacent to all vertices of a graph R_c according to the definition of join operation. Then, if $n = 2$ and from proof Theorem 3.2.1. The graph G_c contains one dominating vertex say v and this vertex will dominates all vertices of a graph R_c and one vertex of G_c (the proof is similar if $m = 2$. Then, D is a minimum dominating set of a graph $G_C + R_c$ and $\gamma\ (G_c + R_c) = 1$. Now if $n, m > 2$ and from proof of Theorem 3.2.1. The graph G_c has n dominating set vertices say $\{u_1, u_2, \dots \dots u_n\}$ have $(n-1)$ elements where $\gamma\ (G_c) = n$. Since $\{u_1, u_2, \dots \dots u_n\} \in V\ (G_c)$. Then, each vertex of a set $D = (u_1, u_2, \dots \dots u_n)$ is adjacent to all

vertices of the graph (R_s) according to the definition of join operation. So that, $D = \{u_1, u_2, \dots \dots u_n\}$ be a minimum dominating set in a graph $G_c + R_c$. Thus, $\gamma(G_c + R_c) = n$

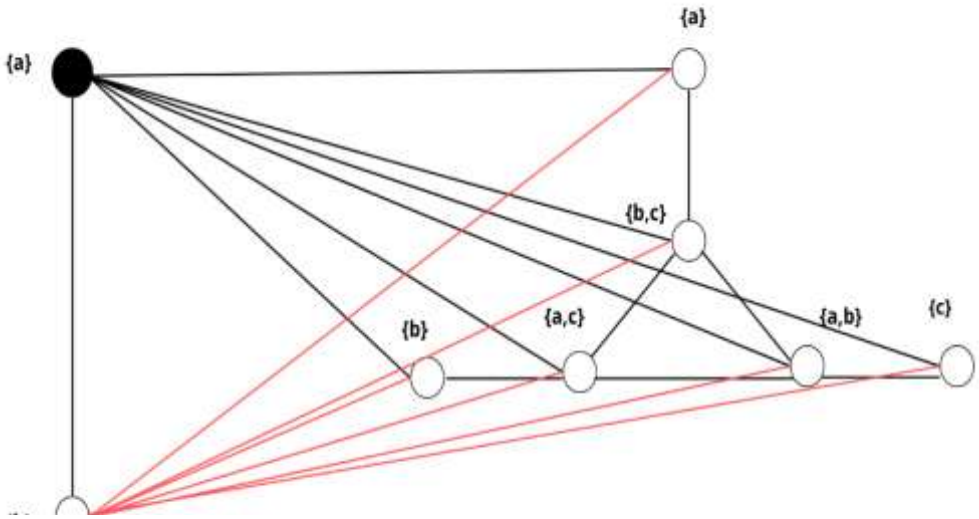

(a) $K_2 + \overline{C_6}$

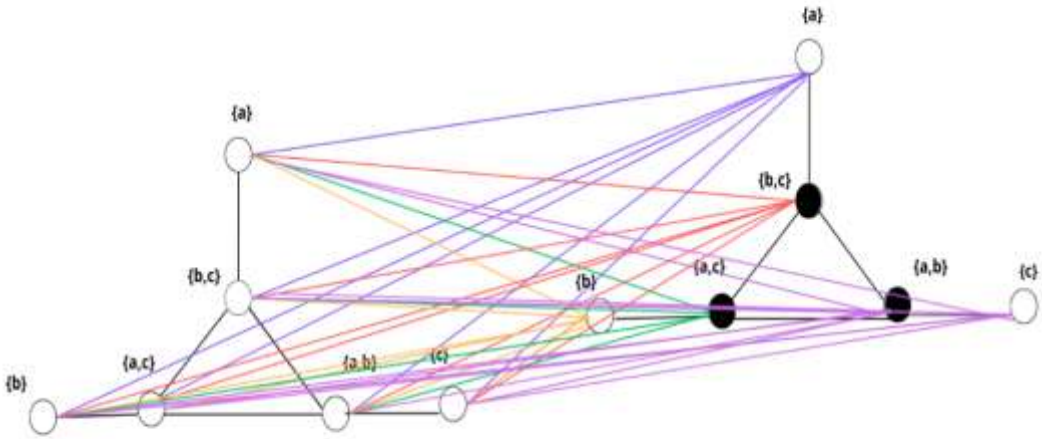

(b) $\overline{C_6} + \overline{C_6}$

Figure 3: A minimum dominating set in join operation graphs.

Conclusion:

In this thesis, a new graph structure called the complementary topological graph $G_c$was introduced and studied on a finite discrete topological space. The construction of this graph depends on the relation between subsets of a finite set X, where two vertices are adjacent whenever their union equals X. Several structural and domination properties of $G_c$were investigated and characterized.

The study determined important graph parameters such as the order, size, degree of vertices, Eulerian properties, and chromatic number. It was proved that the order of G_c is $2^n - 2$ while the number of

edges is given by $\frac{3^n-2^{n+1}+1}{2}$. Moreover, the graph was shown to be regular of degree $2^{n-1}-1$. Based on these results, it was concluded that G_c is neither Eulerian nor semi-Eulerian for all $n \geq 3$. In addition, the chromatic number of the graph was established as $\chi(G_c) = n$.

The domination behavior of complementary topological graphs under graph operations was also studied. In particular, the domination number for corona and join operations was obtained and characterized. The results demonstrated that graph operations significantly affect domination properties and lead to different domination structures.

The obtained results contribute to the interaction between graph theory and topology, especially in the study of graphs constructed from topological spaces. This work opens the door for future investigations concerning other graph parameters such as metric dimension, resolving sets, Hamiltonicity, planarity, and different types of domination on complementary topological graphs and their related operations

References:

[1] R. Diestel, *Graph Theory*, 5th ed. Berlin, Germany: Springer, 2017.

[2] D. B. West, *Introduction to Graph Theory*, 2nd ed. Upper Saddle River, NJ, USA: Prentice Hall, 2001.

[3] T. W. Haynes, S. T. Hedetniemi, and P. J. Slater, *Fundamentals of Domination in Graphs*. New York, NY, USA: Marcel Dekker, 1998.

[4] J. R. Munkres, *Topology*, 2nd ed. Upper Saddle River, NJ, USA: Pearson, 2000.

[5] S. Willard, *General Topology*. Mineola, NY, USA: Dover Publications, 2004.

[6] E. J. Cockayne and S. T. Hedetniemi, "Towards a theory of domination in graphs," *Networks*, vol. 7, no. 3, pp. 247–261, 1977.

[7] E. J. Cockayne, R. M. Dawes, and S. T. Hedetniemi, "Total domination in graphs," *Networks*, vol. 10, no. 3, pp. 211–219, 1980.

[8] O. Ore, *Theory of Graphs*. Providence, RI, USA: American Mathematical Society, 1962.

[9] M. A. Abdlhusein and Z. N. Jwair, "Constructing new topological graph with several properties," *Iraqi Journal of Science*, vol. 64, no. 6, pp. 2991–2999, 2023.

[10] M. A. Abdlhusein and M. K. Idan, "The proper topological graphs," *Boletim da Sociedade Paranaense de Matemática*, to be published, 2026.

[11] B. Mendelson, *Introduction to Topology*, 3rd ed. New York, NY, USA: Dover Publications, 1990.

[12] J. A. Bondy and U. S. R. Murty, *Graph Theory*. London, U.K.: Springer, 2008.

Advanced Algorithmic Approach to Optimization Using MATLAB Programming

Hayder Hassoun Mohammed , *General Directorate of Education of Najaf, Ministry of Education, Iraq*

heyderhassoon74 gmail.com

Advanced Algorithmic Approach to Optimization Using MATLAB Programming

Hayder Hassoun Mohammed , *General Directorate of Education of Najaf, Ministry of Education, Iraq*

heyderhassoon74 gmail.com

Abstract.

This paper introduces a novel conjugate gradient (CG) algorithm approach for unconstrained optimization problems: the (MOD) method under Wolfe condition. The primary argument is that the (MOD) approach can lower function evaluation, CPU time, and iterations. A MATLAB program (version R2016a) and a comparison of numerical results with two popular approaches, the SCG method and the PRP method, are used to illustrate this. When a suitable line search is suggested and the right conditions are met, the proposed method has the sufficient descent property. We construct both the global convergence and the well-defined algorithm. These results show that the new strategy performs better than the traditional algorithms.

Keywords: descent property, conjugate gradient method, global convergence, optimization problems.

المستخلص:

تقدم هذه الورقة البحثية خوارزمية جديدة للتدرج المترافق ((CGلحل مسائل التحسين غير المقيدة: طريقة ((MODفي ظل شرط وولف. تتمثل الحجة الرئيسية في قدرة طريقة ((MODعلى تقليل حساب الدوال، ووقت وحدة المعالجة المركزية، وعدد التكرارات. يُستخدم برنامج) MATLABالإصدار (R2016aومقارنة النتائج العددية مع طريقتين شائعتين، هما طريقة SCG وطريقة PRP، لتوضيح ذلك. عند اقتراح بحث خطي مناسب واستيفاء الشروط المطلوبة، تتمتع الطريقة المقترحة بخاصية الانحدار الكافي. نُقدم في هذه الورقة كلاً من التقارب العالمي والخوارزمية المُحددة جيدًا. تُظهر هذه النتائج أن الاستراتيجية الجديدة تتفوق على الخوارزميات التقليدية.

1. Introduction:

Different approaches can be used to solve large-scale unconstrained optimization issues. Backgroundique, which takes the following form, is one efficient way to solve unconstraint optimization problems:

$$\min_{x \in R^n} f(x), \qquad (1)$$

s.t. $F: R^n \to R$ this continuously differentiable function. From the initial point $x_0 \in R^n$, the iterative sequence $\{x_k\}$ is generated to solution this problem by the recurrence

$$x_{k+1} = x_k + \alpha_k d_k, k \in N \qquad (2)$$

and $\alpha_k > 0$ is obtained through a line search and d_k is a search direction given by:

In addition the space R^i is vector space with Euclidean norm $\|.\|$ defined as follows [1]:

$$\|x\| = \sqrt{\sum_{t=1}^{i} (x_t)^2}\,;\ \forall\, x \in R^i. \qquad (3)$$

In this work, we aim to introduce a new two-term conjugate gradient approach to solve large-scale equations due to the limited memory and simplicity. The authors introduced numerous techniques to solve various optimization and reliability problems (see [2–6]). The suggested method satisfied both the steepest descent property and the Wolfe condition formula for global convergence.

2. The New Suggested Algorithm (MOD)

In this hand, we describe the framework of the suggested approach and satisfies a nice descent property. We used the new technique with (CGM) for solving a large scale problems of unconstraint optimization [7] constructed appropriate hyperplane $\mathcal{H}_k$ where strictly separates x_k from the solution set of problem (1) i.e.

$$\mathcal{H}_k = \{x \in R^n | \, F(z_k)^T (x - z_k) = 0\}.$$

Dependent on Solodov and Svaiters advised total the other iteration point x_{k+1} is constructed by projecting x_k onto $\mathcal{H}_k$ that is x_{k+1} is determined by:

$$x_{k+1} = x_k - \frac{F(z_k)^T (x_k - z_k)}{\|F(z_k)\|^2} F(z_k), \qquad (4)$$

the new search direction of our method can be computed by

$$d_{k+1} = \begin{cases} -F_k + \beta_k^{MOD} y_{k-1}\, \xi_k\, d_{k-1}. & \forall\ \ k \geq 1 \\ -F_k & \forall\ \ k = 0 \end{cases} \qquad (5)$$

Where

$$s_k = x_k - x_{k-1}, \qquad y_{k-1} = F_k - F_{k-1},$$

$$\xi_k = \frac{y_{k-1}\, s_k\, F_k d_{k-1}}{\|y_{k-1}\| \|d_{k-1}\|^2} + \frac{F_k^T\, y_{k-1} d_{k-1}}{\|y_{k-1}\| \|d_{k-1}\|^2}$$

$$\beta_k^{MO4} = \frac{\|y_{k-1}\|\|d_{k-1}\|^2}{d_{k-1}^T s_k F_k y_{k-1} + F_k^T d_{k-1} y_{k-1}}. \qquad (6)$$

According to (4), (5), and (6), one appealing feature of our algorithm is that
$Conversely, according\ to\ (2), (5), and\ (6), the\ value\ of\ d\ k\ as\ determined\ by\ our\ method\ nearly\ satis$
we have thus d_k determined by the our method almost holds the descent condition i.e.

$$d_K^T F_K = -\|F_k\|^2 + \frac{\|y_{k-1}\|\|d_{k-1}\|^2}{\|d_{k-1}\|\|\ s_k\|\|F_k\|^2\ \|y_{k-1}\| + \|\ d_{k-1}\|\|F_k\|^2\|y_{k-1}\|}.$$

$$i$$

$$= -\|F_k\|^2.$$

Therefore, the direction d_k determined by our technique usually holds the sufficient descent condition such that

$$F_k^T d_k \leq -c\ \|F_k\|^2,\ \forall k \geq 0. \qquad (7)$$

Where $c = 1$.

The steps of a new algorithm of the proposed method are as follows:

3. The algorithm for conjugate gradient projection (MO4)

1. The parameters γ,τ>0 and ρ,σ∈ 0,1 are provided, along with the starting point $x\ 0 \in R\ n$.

Set $d_0 = -F_0,\ k = 0;$

If $\|F(x_k)\| \leq \varepsilon$ break.

2. Let $\alpha\ k$ = max{ $\rho\ i\ \alpha\ k-1$, i=0,1,2,…" be produced by a Wolfe condition.

$$f(x_k + \alpha_k d_k) \leq f(x_k) + \rho\alpha_k F_k^T d_k\ ,$$

$$F(x_k + \alpha_k d_k)^T d_k \leq \sigma F_k^T d_k, \qquad (8)$$

3. Set $z_k = x_k + \alpha_k d_k$. and calculate x_{k+1} by

$$x_{k+1} = P_\Omega[\ x_k - \mathfrak{H}\ F(z_k)], \qquad \text{where} \quad \mathfrak{H} = \frac{F(z_k)^T(x_k - z_k)}{\|F(z_k)\|^2}.$$

4. If $\|F(x_k)\| \leq \varepsilon$ break.therefore calculate d_{k+1} by (5).

5. Put $k = k + 1$, and return to (2).

Remark (A)

According to the above discussion, in our method, the search direction $d\ k$ holds (7) is a sufficient descent direction of f at iteration $x\ k$.Also, by (8) thus

$$\|d_k\| \geq \|F_k\|, \quad k \in N \tag{9}$$

This means the denominators of β_k^{MOD} and ξ_k are greater than zero usually when $\|F_k\| = 0$ does not hold. This implies that these parameters are well defined.

4. The New Method's Global Convergence

To examine the new method's global analysis, we need to make a few assumptions.

Assumptions (B)

i. The function $f(x)$ is continuous on the level set R n, bounded below, and differentiable in a neighborhood N of the level set.

$$\varpi(x_0) = \{x \in R^n | f(x) \leq f(x_0)\} \text{ at } x_0.$$

ii. The mapping $F(x)$ is Lipschitz continuous i.e. $\exists L > 0$ s.t.

$$\|F(x) - F(y)\| \leq L\|x - y\|, \text{ for all x, y } \in \text{N.} \tag{10}$$

By using the Assumptions (10) imply that $\exists U > 0$ such that

$$\|F(x)\| \leq U \qquad \forall x \in \varpi. \tag{11}$$

We assume, at most, that Assumptions (B) are satisfied in the final section of this work. Furthermore, we assume that $F\ k \neq 0$, $\Psi k \geq 0$.In order to analyze the globally convergent, we work to determine the selection of $\alpha\ k$ for all that $d\ k$ created by the new technique holds (8).

In the following lemma, we demonstrate a lower bound for $\alpha\ k$ under the initial Wolfe line search.

4.1 Lemma: Suppose the sequence of search direction $\{d_k\}$and$\{F_k\}$ be determined by algorithm4.1 Lemma: Assume that algorithm (MO4) determines the search direction sequence $\{\ d\ k\ \}$ and $\{\ F\ k\ \}$. This suggests that

(12)

Proof: By the given condition (8) we have

$$(\sigma - 1)F_k^T d_k \leq (F_k - F_{k-1})^T d_k \leq \|F_k - F_{k-1}\|\|d_k\| \leq \alpha_k L\|d_k\|^2,$$

then

$$\alpha_k \geq \text{ב} \frac{\|F_k\|^2}{\|d_k\|^2}.$$

Where $\text{ב} \geq \frac{(1-\sigma)}{L}$, the step 2 comes by Cauchy-Schwarz inequality and step 3 comes by Lipschitz continuous. Since d_k hold (8) and $\sigma < 1$, this implies (12) satisfy. The proof is complete.

To obtain the globally convergent conjugate gradient projection method, we used the Zoutendijk condition, which is first given [8] along with the Wolfe condition. The line search of the proposed algorithms now satisfies the Zoutendijk condition, as the following lemma shows.

4.2 Lemma: The step length $\alpha\ k$ is determined by the original Wolfe line search if assumption (B) is satisfied and the suggested method finds the search direction sequence $\{\ d\ k\ \}$, $\{\ f\ k\ \}$, then we obtain

$$\sum_{k=0}^{\infty} \frac{\|F_k\|^4}{\|d_k\|^2} < +\infty. \qquad (13)$$

Proof: From (8) for any k that

$$f(x_k) - f(x_{k+1}) \geq -\rho\alpha_k F_k^T d_k \geq \rho\alpha_k \|F\|^2 \geq \frac{\rho(1-\sigma)\|F_k\|^4}{L\|d_k\|^2}$$

which the second and third inequality comes by (8) and (13). Therefore, by Assumptions (B)(i) that we get (13). The proof is complete.□

As a result, we know that the iteration of (CGM) may fail, which means that only if $d\ k\ \to\infty$ sufficiently quickly will $F\ k \geq\mu$, $\sum k\geq 0$.An alternative interpretation is that the sequence $\{\ F\ k\ \}$ can only be bounded away from zero if k=0 ∞ 1 $d\ k\ <+\infty$. The global convergence of the proposed approach is now examined in the subsequent lemma.

4.3 Theorem: Suppose the sequence $\{F_k\}$and$\{d_k\}$be generated by the suggested method, we have

$$\lim_{k\to\infty} \inf \|F_k\| = 0 \qquad (14)$$

Proof: Assume that (14) does not satisfy, let a constant $M > 0$ s.t.

$$\|F_k\| \geq M,\ \forall k \geq 0. \qquad (15)$$

From (6), (7) and (8) we have

$$\|d_k\| \leq \|F_k\| + \left|\beta_k^{MO4}\right| \|y_{k-1}\|\ |\xi_k| \|d_{k-1}\|$$

$$\|d_k\| \leq\ \|F_k\| + \frac{\|y_{k-1}\| \|d_{k-1}\|^2}{\|d_{k-1}\| \|\ s_k\|\ \|y_{k-1}\| + \|\ d_{k-1}\| \|y_{k-1}\|}.$$

$$\left(\frac{\|d_{k-1}\| \|\ s_k\|\ \|y_{k-1}\|}{\|y_{k-1}\| \|d_{k-1}\|^2} + \frac{\|\ d_{k-1}\| \|y_{k-1}\|}{\|y_{k-1}\| \|d_{k-1}\|^2}\right)$$

$$\leq\ \|F_k\| + \frac{\|y_{k-1}\| \|d_{k-1}\|^2}{\|d_{k-1}\| \|\ s_k\|\ \|y_{k-1}\| + \|\ d_{k-1}\| \|y_{k-1}\|}.$$

$$\left(\frac{\|d_{k-1}\| \|\ s_k\| \|y_{k-1}\| + \|\ d_{k-1}\| \|y_{k-1}\|}{\|y_{k-1}\| \|d_{k-1}\|^2}\right)$$

$$\leq\ \|F_k\| + 1 \leq\ U + 1 \triangleq \theta,$$

Cauchy-Schwarz inequality, (8), (9), and trigonometric inequality, respectively, are the sources of the second, third, and fourth inequalities. The last inequality comes by (11), (15) and Assumption (B)(i).

In synopsis, the sequence $\{\ d\ k\ \}$ determined by our algorithm has a common upper bound such that.

$\|d_K\| \leq \varsigma\ ,\ \forall k \geq 0.$ (16)

Additionally, $\varsigma=\theta$. By applying (15) and (16), it is demonstrated that

$\sum_{k=0}^{\infty} \frac{\|F_k\|^4}{\|d_k\|^2} \geq \sum_{k=0}^{\infty} \frac{M^4}{\varsigma^2} = +\infty.$ (17)

This implies a contradiction (16), thus conclude that (17) holds. The proof is complete.□

5. Numerical Experiments

In this part, we give some insight into the conduct of our method. Some problems have been used to test and analyze the efficiency of a new method compared to some two-terms conjugate gradient method (NTT) [9], a three terms conjugate gradient method (NS) [10] and a conjugate gradient-like method (CGL) [11]. For everyone the test problems seven or eight initial point starting are used. Similar in [12], we check the test problem when the variables number n=5000, 10000,…. and some given starting points

$x_0 = (10,10,\dots,10)^T,\ x_1 = (-10,-10,\dots,-10)^T, x_2 = (1,1,\dots,1)^T,\ x_3 = (-1,-1,\dots,-1)^T$

$x_4 = (1,\frac{1}{2},\frac{2}{3}\dots,\frac{1}{n})^T\ ,\ x_5 = (0.1,0.1,\dots,0.1)^T, x_6 = (\frac{1}{n},\frac{2}{n},\dots,1)^T,\ x_7 = (1-\frac{1}{n},1-\frac{2}{n},\dots,0)^T.$

All runs are proposed using MATLAB R2016a and run PC with 16GH, CPU2.30- Windows11 operation system. Numerical results are compared dependent on the number of iterations, the number of evaluation functions and CPU time. The terminating executions we used some criterion whenever $\|F_k\| \leq 10^{-6}$ and the total number of iteration exceeds 500000. The parameter of the new algorithm were set as follows:$\tau = 10^{-4}, \sigma = 0.5$ and $\gamma = 0.1$. The parameter of the other methods comes from [8, 13, 14]. The step-size α_k is computed by $\alpha_k = max\{\alpha_{k-1}\gamma^i, i = 1,2,3,\dots\}$,

which holds Wolfe line search condition. The table (1) indicate the number of iteration (N_i) and a number of function evaluations (N_f) while the table (2) indicate to CPU time (CPU). From these tables shows that the new method is promised.

Table (1) numerical results of N_i and N_f.

Pt	Dim.		The new (MOD)	SCG	PRP

P3	10000	$x4$	7438	465	30004	10001	30004	10001
	10000	$x5$	8504	5000	30004	10001	2017	672
	10000	$x6$	153	24	30004	10001	30004	10001
	10000	$x7$	1240	125	30004	10001	30004	10001
P4	10000	$x0$	4781	5000	30004	10001	30004	10001
	10000	$x1$	4781	5000	30004	10001	30004	10001
	10000	$x2$	4781	5000	30004	10001	30004	10001
	10000	$x3$	4781	5000	30004	10001	30004	10001
	10000	$x4$	4781	5000	30004	10001	30004	10001
	10000	$x5$	4781	5000	30004	10001	30004	10001
	10000	$x6$	4781	5000	30004	10001	30004	10001
	10000	$x7$	4781	27	30004	10001	30004	10001
			03	21				
			11	30				
P5	5000	$x0$	875	1201	15004	5001	15004	5001
	5000	$x1$	7336	28	15004	5001	15004	5001
	5000	$x2$	2392	2516	15004	5001	15004	5001
	5000	$x3$	8855	303	15004	5001	15004	5001
	5000	$x4$	3123	402	15004	5001	15004	5001
	5000	$x5$	2257	521	15004	5001	15004	5001
	5000	$x6$	550	25	15004	5001	15004	5001
	5000	$x7$	4230	2807	15004	5001	15004	5001

Table (1) continued

P6	50000	$x0$	100996	6497	150004	50001	150004	50001
	50000	$x1$	3110	169	150004	50001	150004	50001
	50000	$x2$	128953	7868	150004	50001	150004	50001
	50000	$x3$	335069	26445	150004	50001	150004	50001
	50000	$x4$	427153	22647	150004	50001	150004	50001
	50000	$x5$	313149	18091	150004	50001	150004	50001
	50000	$x6$	55455	2645	150004	50001	150004	50001
	50000	$x7$	113570	6887	150004	50001	150004	50001
P7	500000	$x0$	182	66	34	11	2833	944
	500000	$x1$	536	47	34	11	1237	412
	500000	$x2$	179	63	34	11	1513	504
	500000	$x3$	472	50	34	11	150000	500001
	500000	$x4$	40532	6507	34	11	2095	698
	500000	$x5$	15	3	34	11	1318	439
	500000	$x6$	185	63	34	11	2518	839
	500000	$x7$	185	63	34	11	1606	535

Table (2) numerical *results of CPU-time.*

Pt	Dim.	x_t	CPU-time		
			The new (MOD)	SCG	PRP
P1	10000	$x0$	2.046875	285.3437	3.6718
	10000	$x1$	3.31250	297.0468	2.6562
	10000	$x2$	1.8750	295.0625	1.5625
	10000	$x3$	2.98437	298.8281	3.7343
	10000	$x4$	6.85937	299.4531	1.8750
	10000	$x5$	0.62500	304.8906	1.9218
	10000	$x6$	2.48437	300.2187	1.8437
	10000	$x7$	2.56250	312.6875	1.7656
P2	1000	$x0$	1.73437500	2.0156	0.9531
	1000	$x1$	1.46875000	1.8906	1.7187
	1000	$x2$	0.90625000	2.1718	1.4062
	1000	$x3$	2.56250000	1.6562	0.9375
	1000	$x4$	57.6406250	112.9062	1.2500
	1000	$x5$	0.57812500	115.6093	1.0937
	1000	$x6$	38.0156250	117.5000	1.4062
	1000	$x7$	42.500	119.8906	1.5625
P3	10000	$x0$	0.37500	36.70312	9.2031
	10000	$x1$	958.640625	1.9687	0.5000
	10000	$x2$	0.25000	15.3593	0.6250
	10000	$x3$	676.843750	38.2031	8.5937

Table (2) continued

P3	10000	$x4$	121.015625	1144.7500	8.1250

	10000	$x5$	7475.48437	1144.5625	0.9531
	10000	$x6$	0.12500	1167.8125	14.062
	10000	$x7$	0.59375000	1167.9218	15
P4	10000	$x0$	147.68750	317.2343	0.2968
	10000	$x1$	126.70312	334.7031	0.1406
	10000	$x2$	119.14062	337.8437	0.1406
	10000	$x3$	120.81250	337.3593	0.1875
	10000	$x4$	146.14062	339.1562	0.1562
	10000	$x5$	1715.59375	339.6250	0.1406
	10000	$x6$	223.82812	337.9687	0.1250
	10000	$x7$	220.21875	338.8593	0.1562
P5	5000	$x0$	1.10937500	565.3593	0.2500
	5000	$x1$	3.5000	580.0156	0.0937
	5000	$x2$	3.593750	576.3750	0.0937
	5000	$x3$	12.1093750	578.9531	0.0937
	5000	$x4$	11.5156250	576.9531	0.0937
	5000	$x5$	2.67187500	566.3906	0.0781
	5000	$x6$	6.03125000	567.7343	0.1250
	5000	$x7$	5.32812500	584.8906	0.0781

(2) continued

P6	50000	$x0$	263.625000	1628.3437	15.0781
	50000	$x1$	7.95312500	1696.1875	15.7812
	50000	$x2$	307.968750	1695.0625	32.7500
	50000	$x3$	778.234375	1704.0312	31.3906
	50000	$x4$	981.281250	1687.4375	32.0625
	50000	$x5$	716.390625	1698.5468	30.0625
	50000	$x6$	128.203125	1670.0468	34.0156
	50000	$x7$	267.187500	1674.4375	35.6406
P7	500000	$x0$	2.21875000	35.6093	0.4531
	500000	$x1$	3.28125000	35.2343	0.1250
	500000	$x2$	1.39062500	34.4687	0.1250
	500000	$x3$	2.54687500	35.1406	79.3437
	500000	$x4$	246.578125	34.3437	0.0937
	500000	$x5$	0.062500	36.3593	0.0937
	500000	$x6$	1.56250000	36.2812	0.0937
	500000	$x7$	1.5000	36.1562	0.1250

forementioned tables show that our algorithm outperformed the other algorithms in most cases..The following terms were compared, it should be mentioned::

* The a

The number of repetitions.

* How many function evaluations there are.

CPU duration.

6. **Conclusions**

The (MOD) method under Wolfe condition is a novel approach to solving unconstrained optimization problems using the conjugate gradient (CG) algorithm. This method works well for large data sets because of its limited storage capacity. The global convergence has been proven for the proposed algorithm. Our approach has a competitive advantage over the other three conjugate

gradient methods, and numerical results showed that it is a promising and practical tool for solving optimization problems.

References:

[1] Yu G Guan L and Chen W 2008. "Spectral conjugate gradient methods with sufficient descent property for large-scale unconstrained optimization", *Optimization Methods & Software*, V 23, p. 275–293.

[2] Abbo K K 2008. "New CG Method for Large-Scale Unconstrained Optimization Based on Nazareth theorem", *Iraqi Journal of Statistical Sciences*, V 13, p. 53–65,

[3] Pang D and Du S 2016. "The smoothing Fletcher-Reeves conjugate gradient method for solving finite minimax problems", Science Asia, V 42, p. 40–45.

[4] Wasi H A and Shiker M A K 2020. "A new conjugate gradient method for solving large scale systems of monotone equations", *International Journal of Advanced Science and Technology*, V 29 (4), p.2303- 2314.

[5] Shiker M A K and Sahib Z 2018. "a modified trust-region method for solving unconstrained optimization". *Journal of Engineering and Applied Sciences*, V 13(22), p. 9667-9671. https://doi.org/10.3923/jeasci.2018.9667.9671.

[6] Kafaki S B and Ghanbari R 2014. "A descent extension of the Polak–Ribière–Polyak conjugate gradient method", *Computers and Mathematics with Applications*, V 68, p. 2005–2011.

[7] Hussein H A and Shiker M A K 2020. "A modification to Vogel's approximation method to Solve transportation problems", "in press", accepted paper for publication in IOP Science, 5th International Scientific Conference for Iraqi Al-Khwarizmi Society, Iraq.

[8] Hassan B A Wais O M T and Mahmood A A 2019. "A Class of Descent Conjugate Gradient Methods for Solving Optimization Problems", *Applied Mathematical Sciences*, V 13, p 559–567.

[9] Hassan Z A H H and Shiker M A K 2018. "Using of generalized baye's theorem to evaluate the reliability of aircraft systems", *Journal of Engineering and Applied Sciences*, (Special Issue13), p. 10797-10801. https://doi.org/10.36478/jeasci.2018.10797.10801.

[10] Mahdi M M and Shiker M A K (2020). "A new projection technique for developing a Liu-Storey method to solve nonlinear systems of monotone equations", "in press", accepted paper for publication in IOP Science, 5th International Scientific Conference for Iraqi Al-Khwarizmi Society, Iraq.

[11]Mahdi M M and Shiker M A K (2020). "Three terms of derivative free projection technique for solving nonlinear monotone equations", "in press", accepted paper for publication in IOP Science, 5th International Scientific Conference for Iraqi Al-Khwarizmi Society, Iraq.

[12] Shiker M A K and Amini K 2018. ″A new projection-based algorithm for solving a large scale nonlinear system of monotone equations″, *Croatian operational research review*,V 9(1), p. 63-73. https://doi.org/10.17535/crorr.2018.0006.

[13]Dai Y H ″Nonlinear Conjugate Gradient Methods″, *Academy of Mathematics and Systems Science*, Chinese Academy of Sciences.

[14]Li Q and Huili D 2011. ″A class of derivative-free methods for large-scale nonlinear monotone equations″ , *IMA Journal of Numerical Analysis*, V 31, p 1625–1635.

Evaluating the Patterns of Antibiotic Susceptibility in *Staphylococcus* Species Isolated from Various Clinical Sources

Author Name : Duaa Haider Raham

Affiliation : Ministry of Education , Baghdad Al-Rusafa Third Directorate of Education , Al-Mutamayyizat Al-Thakiya Secondary School >

duaabayshaan@gmail.com

Evaluating the Patterns of Antibiotic Susceptibility in *Staphylococcus* Species Isolated from Various Clinical Sources

Author Name : Duaa Haider Raham

Affiliation : Ministry of Education , Baghdad Al-Rusafa Third Directorate of Education , Al-Mutamayyizat Al-Thakiya Secondary School >

duaabayshaan@gmail.com

Abstract:

Background:

The Gram-positive bacteria such as various types of staphylococci can be commonly observed on human skin and also on mucosal surfaces. Nonetheless, it is important to underline that these bacteria can be regarded as the opportunistic pathogen especially when there are medical devices used by patients and when their immune system does not function properly. Methicillin-resistant *Staphylococcus aureus* or MRSA and multidrug-resistant coagulase-negative staphylococci or MDR-CoNS emerge constantly and cause significant difficulties in treatment virtually in all conditions. This research attempted to identify the prevalence, sources, distribution of samples, and the reaction of isolates to different antibiotics. The key purpose of this research was to provide support for the decision-making process and also to enhance infection control strategies to increase effectiveness of responses.

Materials and Methods:

199 *Staphylococcus* isolates were obtained from male and female patients' blood, urine, wound swabs, and other clinical materials between January and December 2025. The VITEK 2 system was used to identify the species after samples were cultivated on blood, MacConkey, and nutrient agar. Testing for antimicrobial susceptibility adhered to CLSI 2025 recommendations.

Results:

Of the isolates, 96 (48.2%) came from male patients and 103 (51.8%) from female patients. The most common source of specimens was urine (59.3%), followed by wound swabs (9.5%) and seminal fluid (12.1%). *S. aureus* (24.1%) and *S. haemolyticus* (25.6%) were the most common species. The isolates were very sensitive to linezolid, vancomycin, and tigecycline (>95%), although they were highly resistant to erythromycin and clindamycin. MRSA and MR-CoNS were among the 43.7% of isolates that showed methicillin resistance.

Conclusion: Hospital-acquired infections are a result of *Staphylococcus* species, especially *S. haemolyticus*, becoming more resistant to antibiotics. Linezolid and vancomycin are still effective treatment options. Strict infection control practices, species-specific antimicrobial stewardship, and continuous surveillance are essential to halting the spread of resistant strains and improving patient outcomes.

Keywords: *Staphylococcus*, antibiotic resistance, MRSA, *S. haemolyticus*, healthcare infections.

Introduction:

Staphylococcus species exist as gram positive bacteria that naturally inhabit human skin and mucous membranes [1]. These bacteria are normally benign commensals, but in immunocompromised people, those with indwelling medical devices, and those with open wounds, they can develop into opportunistic pathogens [2, 3]. *S. aureus*, which causes skin infections, pneumonia, sepsis, and endocarditis, and coagulase negative staphylococci (CoNS), which include *S. epidermidis* and *S. haemolyticus* as significant hospital infection agents associated with medical implants and prosthetic devices, are the two most clinically significant species [4, 5].

A major obstacle to infection control in healthcare settings is the worldwide increase in antibiotic resistance, especially in methicillin-resistant *S. aureus* (MRSA) and multidrug-resistant CoNS (MDR-CoNS) [6]. The World Health Organization (WHO) designates MRSA and MDR *Staphylococcus* species as critical priority pathogens which results in urgent demand for new treatment approaches and successful antimicrobial management programs [7, 8]. The rising occurrence of antibiotic resistance

in *Staphylococcus* spp. creates substantial difficulties for healthcare professionals because healthcare facilities depend on standard antibiotic treatment to handle resistant bacterial infections [9].

In order to survive in harsh environments and lessen the effectiveness of traditional antibiotics, *Staphylococcus* species develop resistance through a variety of methods, such as the synthesis of β-lactamases, the carrying of the *mecA* gene, and the creation of biofilms [10, 11]. The design is essential to evaluate antimicrobial susceptibility patterns using established methods such as the Kirby-Bauer disk diffusion experiment and estimate minimum inhibitory concentrations (MICs) in order to assist doctors in selecting effective therapies while minimizing the overuse of broad-spectrum antibiotics[12, 13].

This study aims to evaluate the antibiotic susceptibility patterns of *Staphylococcus* isolates obtained from various clinical materials, including blood, urine, seminal fluid, and wound swabs. The results are intended to identify the most prevalent resistance strains and effective antimicrobial medications in order to enhance patient outcomes and evidence-based antibiotic stewardship strategies.

Materials and Methods

Sample Collection

Clinical samples were obtained from both male and female patients during the months January to December 2025 at the Medical Teaching Hospital in Baghdad, Iraq. Both inpatients and outpatients were used to ensure an adequate cross-sectional sample of patients. Clinical samples collected included urine samples, blood samples, wound samples, and other clinical samples available in the laboratory. Only pure cultures of *Staphylococcus* isolates that fulfilled the inclusion criteria were kept. Contaminated cultures, those with incomplete growth, and those duplicates from the same patient were excluded from the study. All samples were collected, labeled, and transported in accordance with standard microbiological practices, ensuring proper temperatures and the use of appropriate transport media.

Bacterial Isolation

The samples were processed using aseptic techniques. The primary cultures were done using selective media appropriate for growth of *Staphylococcus* bacteria, and then isolates with typical morphologies were further cultured to get pure cultures. Only those cultures showing clean growths were used. Standard methods were followed uniformly for all the samples.

Bacterial Identification

The isolates were characterized by use of the automated VITEK 2 system (bioMérieux, Marcy-l'Étoile, France), which is based on biochemical reaction profiles for identification purposes. The test was carried out according to CLSI 2025 guidelines as well as instructions from the manufacturer [14-16]. In case of non-conformable results, further confirmation tests such as manual biochemical tests were carried out. Quality control organisms included *S. aureus* ATCC 25923 and ATCC 29213 strains that were applied during identification and antimicrobial susceptibility testing [17].

Antimicrobial Susceptibility Testing (AST)

The AST was performed using VITEK 2 AST-P cards as per CLSI 2025 guidelines [16]. The tested antimicrobial drugs included penicillin, oxacillin, cephalexin, ciprofloxacin, vancomycin, linezolid, gentamicin, tobramycin, levofloxacin, morifloxacin, tigecycline, rifampicin, trimethoprim-sulfamethoxazole, erythromycin, clindamycin, nitrofurantoin, fusidic acid, and tetracycline. The MICs were obtained for each isolate and were interpreted based on CLSI breakpoints.

Resistance to methicillin was determined by the disk diffusion test with cefoxitin (30 μg). Isolates of *S. aureus* were classified either as MRSA or MSSA, while coagulase-negative staphylococci as either MR-CoNS or MS-CoNS [18]. Furthermore, the D-test was conducted to confirm the inducible resistance to clindamycin in isolates with the resistant pattern for erythromycin and susceptible for clindamycin. All procedures were done following guidelines and recommendations from manufacturers and standardized microbiological techniques to enhance accuracy and consistency.

Data Documentation and Quality Assurance

Each of the following was carefully tracked: specimen handling, isolation, identification, and AST. The number of samples, rejected samples, and the results of quality control were documented to provide clarity, consistency, and avoid any bias due to sample handling and laboratory conditions.

Statistical Analysis

R software together with IBM SPSS Statistics version 26 was used to analyze the data . How the bacterial isolates were dispersed across specimens, and also between male compared to female patients, was summarized with rather basic descriptive statistics like counts for frequency and

percentage values. A Chi-square test was run to check if *Staphylococcus* species were connected to categorical factors, including patient gender, and specimen type. We counted it as statistically significant whenever the P value came in under 0.05 . For clarity, and because it also helps with repeatability, the results were put together in tables and shown again as figures .

Results

Distribution of *Staphylococcus* isolates by patient gender

A total of 199 *Staphylococcus* isolates were obtained from 103 female patients (51.8%) and 96 male patients (48.2%). The prevalence appeared to be fairly constant for both males and females, as indicated in Table 1, since a Chi-square test revealed no significant relationship between patient gender and the distribution of isolates ($p > 0.05$).

Table1. Distribution of *Staphylococcus* Isolates According to Gender

Gender	No. of isolates	Percentage (%)
Male	96	48.2
Female	103	51.8
Total	**199**	**100**

The distribution of *Staphylococcus* isolates by specimen source is shown, more or less. Most isolates were recovered from urine samples (118/199, 59.3%), then came seminal fluid (24/199, 12.1%) , wound swabs (19/199, 9.5%) and also blood (12/199, 6.0%). Ear swabs contributed 8 (4.0%) isolates while abscesses gave 6 (3.0%). The remaining 12 isolates (6.0%) came from a mix of origins, grouped as other sources, as demonstrated in the **Figure 1** and **Table 2**.

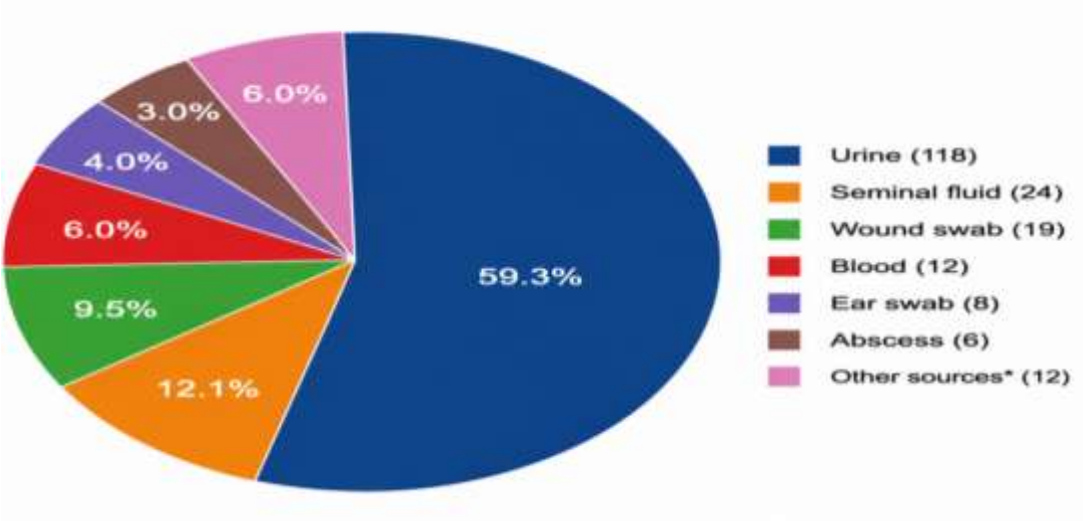

Figure 1. Proportion of *Staphylococcus* isolates by specimen source, indicating the involvement of different clinical sources and the dominance of urine samples.

Table 2. Distribution of *Staphylococcus* isolates according to specimen source (n = 199)

Specimen source	Number of isolates	Percentage (%)
Urine	118	59.3
Seminal fluid	24	12.1
Wound swab	19	9.5
Blood	12	6.0
Ear swab	8	4.0
Abscess	6	3.0
Other sources*	12	6.0
Total	199	100

*Other sources: pus fluid (2), nasal swab (2), vaginal swab (2), discharge (1), throat swab (1), skin swab (1), tissue (1), synovial fluid (1), double lumen catheter (1).

Distribution of *Staphylococcus* Species

Out of the 199 isolates, *Staphylococcus haemolyticus* showed up as the most prevalent species (51 isolates, 25.6%), then came *S. aureus* (48 isolates, 24.1%), *S. epidermidis* (37 isolates, 18.6%), and *S. hominis* (29 isolates, 14.6%). After that, *S. saprophyticus* was lower, 16 isolates, 8.0%, while the other *Staphylococcus* species made up 18 isolates, 9.1%. The overall impression is that there was a diverse range of staphylococcal species isolated from this study population, and it appears that coagulase-negative staphylococci occurred slightly more often than *S. aureus*, as shown in Table 3.

Table 3: Distribution of *Staphylococcus* species

Species	Number of Isolates	Percentage (%)
Staphylococcus haemolyticus	51	25.6
Staphylococcus aureus	48	24.1
Staphylococcus epidermidis	37	18.6
Staphylococcus hominis	29	14.6
Staphylococcus saprophyticus	16	8.0
Other species	18	9.1

Antibiotic Susceptibility Patterns of *Staphylococcus* Species

The antibiotic susceptibility patterns among the five *Staphylococcus* species varied rather a lot. In general, each species showed high sensitivity to linezolid and the glycopeptides, like vancomycin and teicoplanin, so it looks like these drugs are still very effective against the *Staphylococcus* isolates. Tigecycline also showed excellent activity for all species, as revealed in **Table 4**. When it comes to resistance, the rates were the highest for erythromycin, tetracycline, and clindamycin, but the "how much" was not identical between species. *Staphylococcus* aureus had clear resistance to erythromycin (67%) , clindamycin (56%), and tetracycline (46%). *Staphylococcus* epidermidis had more medium resistance to tetracycline (50%),clindamycin (25%), and erythromycin (25%). *Staphylococcus* haemolyticus showed a middle level of resistance to clindamycin (42%) and tetracycline (26%), with lower resistance to erythromycin (16%). *Staphylococcus* hominis was completely resistant to

tetracycline (100%), and it had moderate resistance to erythromycin and clindamycin (25% each). For *Staphylococcus* saprophyticus ,and the other coagulase-negative species, resistance was complete to tetracycline and erythromycin (100%) while being moderate toward the other antibiotics.

Collectively, these findings suggest that linezolid and glycopeptides still work very well, yet the susceptibility of coagulase-negative Staphylococci is not uniform, which really underlines why antimicrobial stewardship should be species specific .

Table 4. Antibiotic Susceptibility of *Staphylococcus* Species (S/I/R %)

Antibiotic	*S. aureus (n=48)*	*S. epidermidis (n=37)*	*S. haemolyticus (n=51)*	*S. hominis (n=29)*	*S. saprophyticus & other (n=34)*
Linezolid	98 / 2 / 0	100 / 0 / 0	100 / 0 / 0	100 / 0 / 0	100 / 0 / 0
Vancomycin	95 / 5 / 0	100 / 0 / 0	97 / 3 / 0	100 / 0 / 0	100 / 0 / 0
Teicoplanin	95 / 5 / 0	100 / 0 / 0	96 / 4 / 0	100 / 0 / 0	100 / 0 / 0
Tigecycline	98 / 2 / 0	100 / 0 / 0	95 / 5 / 0	100 / 0 / 0	100 / 0 / 0
Gentamicin	72 / 0 / 28	71 / 0 / 29	78 / 0 / 22	50 / 0 / 50	50 / 0 / 50
Tobramycin	68 / 0 / 32	70 / 0 / 30	65 / 0 / 35	50 / 0 / 50	50 / 0 / 50
Tetracycline	46 / 0 / 54	50 / 0 / 50	74 / 0 / 26	0 / 0 / 100	0 / 0 / 100
Clindamycin	44 / 0 / 56	75 / 0 / 25	58 / 0 / 42	75 / 0 / 25	25 / 0 / 75
Erythromycin	33 / 0 / 67	75 / 0 / 25	84 / 0 / 16	75 / 0 / 25	0 / 0 / 100
Levofloxacin	61 / 0 / 39	63 / 0 / 37	62 / 0 / 38	75 / 0 / 25	75 / 0 / 25
Rifampicin	80 / 0 / 20	75 / 0 / 25	85 / 0 / 15	75 / 0 / 25	75 / 0 / 25
Nitrofurantoin	86 / 0 / 14	75 / 0 / 25	100 / 0 / 0	75 / 0 / 25	75 / 0 / 25
TMP/SMX	76 / 0 / 24	50 / 0 / 50	62 / 0 / 38	50 / 0 / 50	62 / 0 / 38

As shown in shown in **Figurers 2-7**, the antibiotic susceptibility patterns of *Staphylococcus* isolates varied among the five species. Overall, linezolid, vancomycin, teicoplanin, and tigecycline showed the highest activity, with susceptibility rates generally exceeding 95%. On the other hand, we saw higher resistance rates against erythromycin, tetracycline ,and clindamycin, specially within the coagulase-

negative *Staphylococcus* species. For *S. aureus* , resistance was quite noticeable for erythromycin, clindamycin, and tetracycline. Meanwhile *S. hominis* and *S. saprophyticus* looked completely resistant to tetracycline , and *S. saprophyticus* also showed full resistance to erythromycin. Overall, these results suggest glycopeptides together with linezolid are still strongly effective against the *Staphylococcus* isolates. Still, resistance trends weren't identical across species, which kinda supports the importance of choosing the antimicrobial in a species specific way.

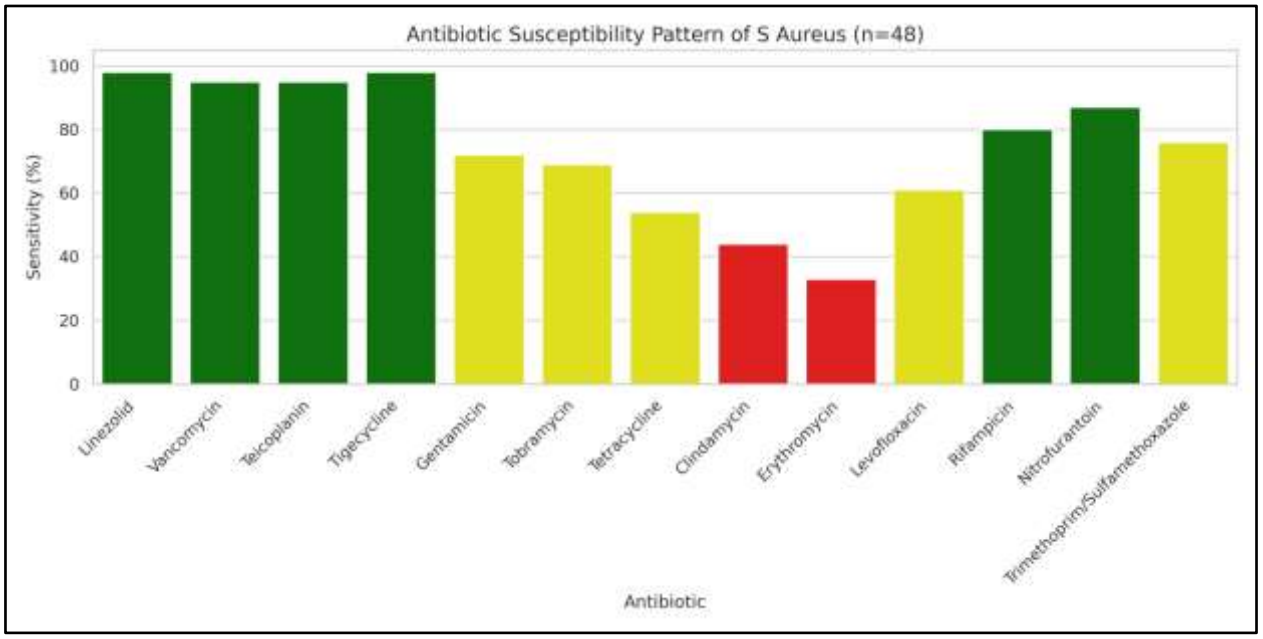

Figure 2: Antibiotic susceptibility of *S. aureus* isolates

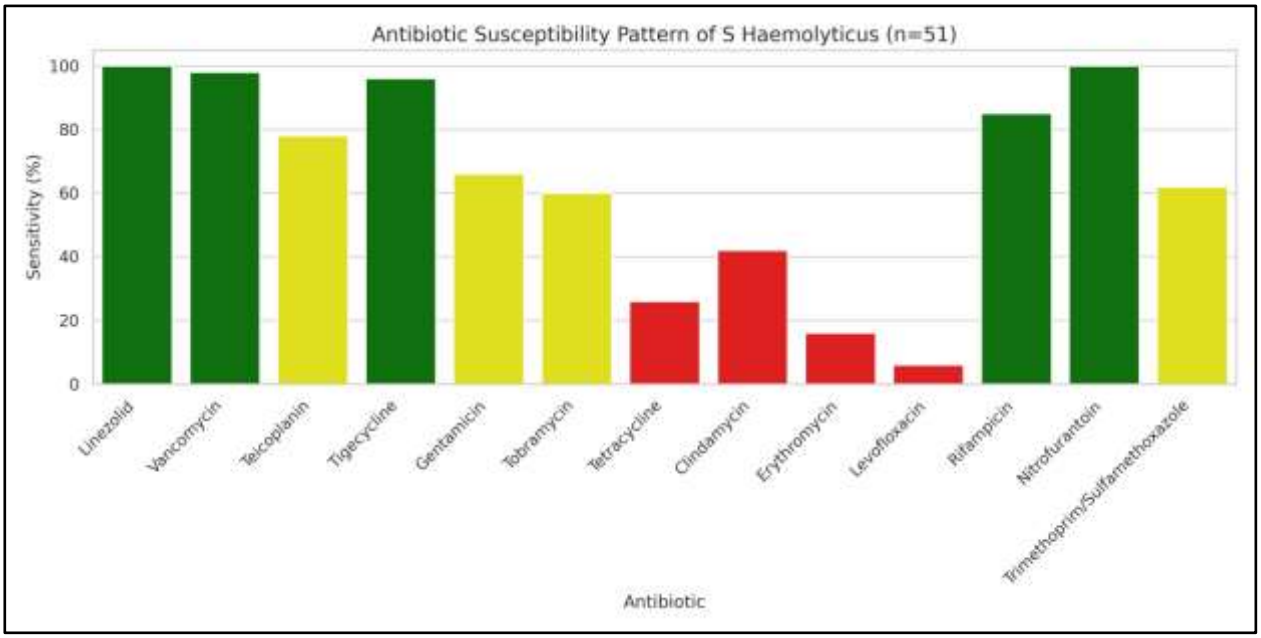

Figure 3: Antibiotic susceptibility of *S. haemolyticus* isolates

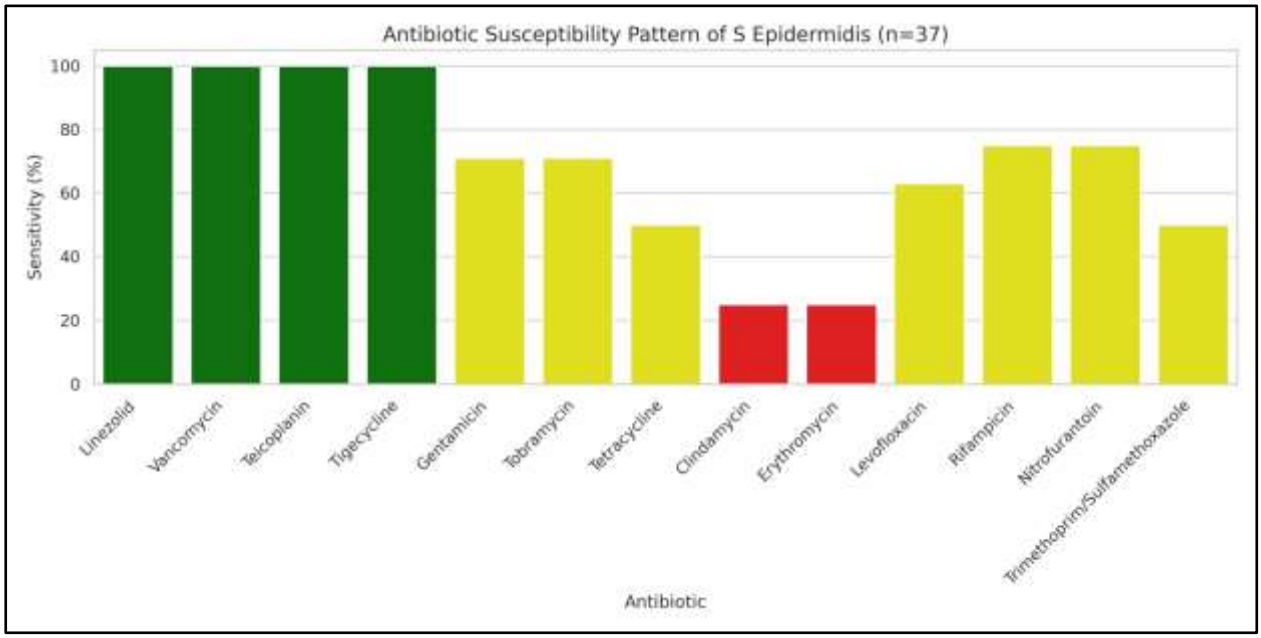

Figure 4: Antibiotic susceptibility of *S. epidermidis* isolates

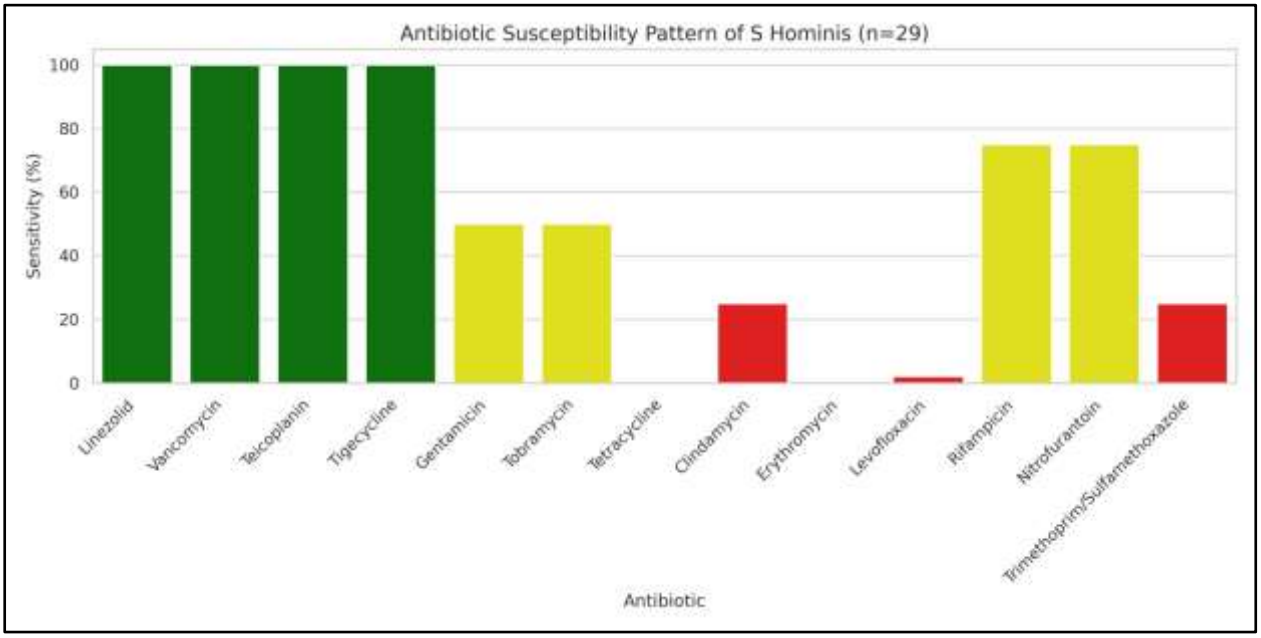

Figure 5: Antibiotic susceptibility of *S. hominis* isolates

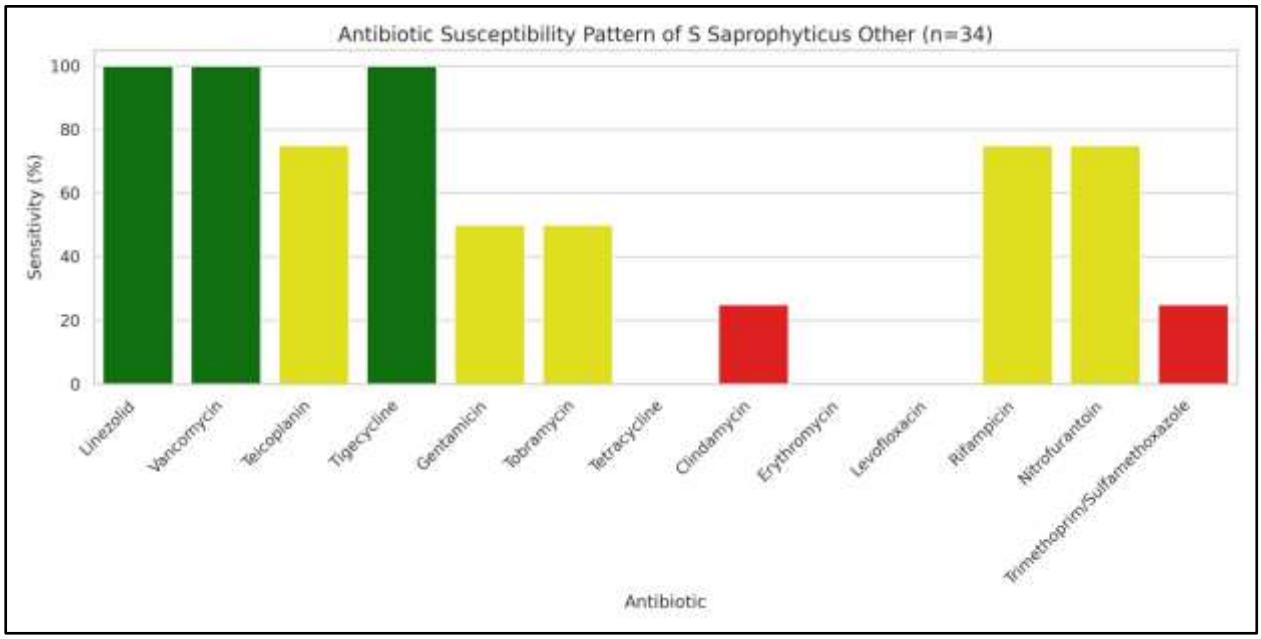

Figure 6: Antibiotic susceptibility of *S. saprophyticus* and other *Staphylococcus* species

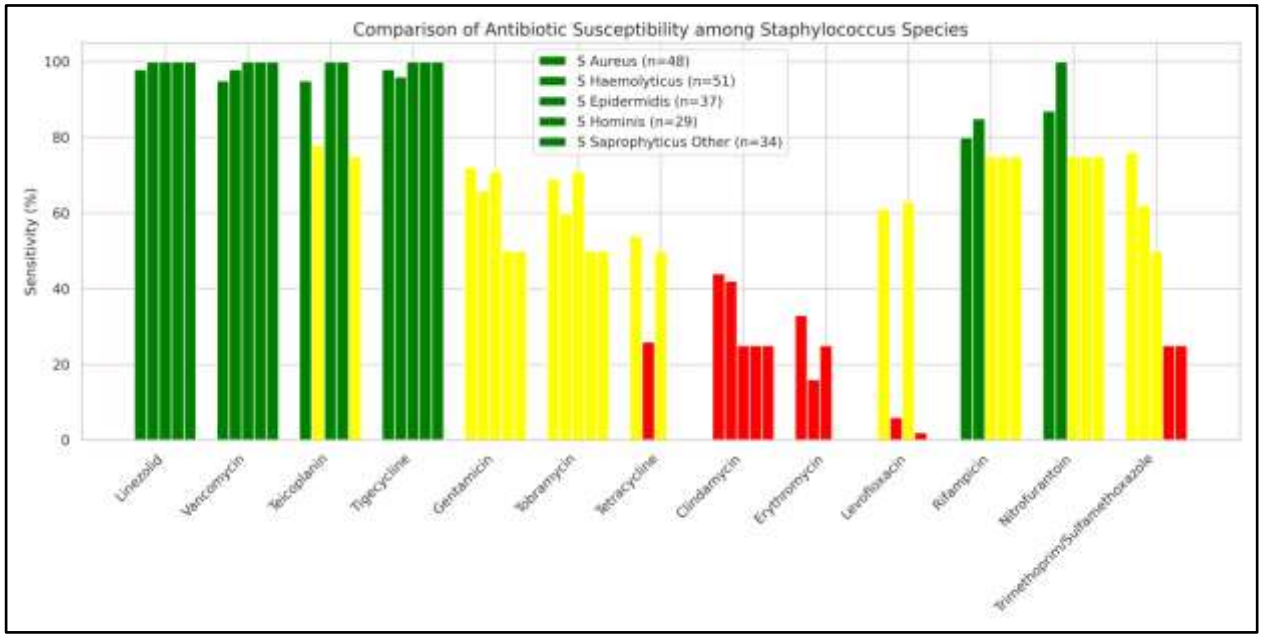

Figure 7: Comparison of antibiotic susceptibility among *Staphylococcus* specie

Note: All susceptibility data are expressed as % sensitivity per CLSI/EUCAST guidelines, with n indicating the number of isolates tested per species. Colors in the bar charts: Green ≥ 80% sensitivity, Yellow 50–79%, Red < 50%.

Distribution of Methicillin-Resistant and Methicillin-Sensitive Staphylococcal Isolates

87 (43.7%) and 112 (56.3%) of the 199 Staphylococcal isolates that were examined were methicillin-resistant (MR) and methicillin-sensitive (MS). Out of the 48 isolates of *S. aureus*, 26 (54.2%) had MR and 22 (45.8%) had MS. On the other hand, there were 61 (40.4%) MR and 90 (59.6%) MS among the 151 CoNS isolates, as seen in **Table 5.**

According to these findings, the majority of CoNS isolates were still methicillin-sensitive, although *S. aureus* displayed a larger percentage of methicillin resistance than CoNS.

Table 5 . Distribution of Methicillin-Resistant and Methicillin-Sensitive Staphylococcal Isolates

Species	Total	MR n (%)	MS n (%)
S. aureus	48	26 (54.2%)	22 (45.8%)
CoNS total	151	61 (40.4%)	90 (59.6%)
Total	199	87 (43.7%)	112 (56.3%)

Discussion

The importance of the presence of *Staphylococcus* species in patients' samples is not only in the fact of their presence but also in their ability to show different levels of pathogenicity that can be manifested from urinary tract and skin infections to other infections associated with medical devices[19]. It is important to know about the presence of such bacteria, their resistance patterns, and factors contributing to their prevalence in order to make treatment choices and apply strict infection control measures [20, 21].

The results of this study indicated that 51.8% of the isolates were female, while 48.2% of the isolates were male. The results were partially supported by Philip et al. (2023) since they found a higher prevalence of non-encapsulated enterococcal bacteria in women having UTIs, but there was no

statistical significance [22]. This may be because of the anatomical differences between men and women, as women have a shorter urethra than men [23].

The majority of isolates were collected from urine (59.3%), followed by semen (12.1%), wound (9.5%) and other sources, such as blood and swabbing samples (13%). This distribution shows the high prevalence of coagulase-negative staphylococci (CoNS) in UTIs, which was mentioned by Aniba et al. (2024) [24]. These results demonstrate the necessity of preventive measures and catheter hygiene [25, 26].

The most common bacterial species were *S. haemolyticus* (25.6%), *S. aureus* (24.1%), *S. epidermidis* (18.6%), *S. hominis* (14.6%), and *S. saprophyticus* (8.0%). This observation is partly supported by the research findings of Eltwisy et al. (2022) and Verma et al. (2024), who have noted the rising frequency of *S. haemolyticus* in infection-related to devices [27, 28]. The dominance of *S. haemolyticus* could be attributed to its high capacity to create biofilm that helps it adhere to medical equipment [29].

The antibiotic susceptibility test results indicated high efficacy of linezolid, vancomycin, teicoplanin, and tigecycline (>95%) in all the species tested. However, the resistance to other antibiotics varied according to the species. For instance, *S. aureus* exhibited high resistance to erythromycin (67%), clindamycin (56%), and tetracycline (46%). *S. epidermidis* showed moderate resistance to tetracycline (50%) but low resistance to erythromycin and clindamycin (25%). *S. hominis* had complete resistance to tetracycline (100%), whereas erythromycin and clindamycin showed moderate resistance (25% each). On the other hand, *S. saprophyticus* and other CoNS had complete resistance to tetracycline and erythromycin.

The above results are consistent with Hall & Mah (2017) and Labib et al. (2018), who pointed out that the resistance profiles differ depending on the type of bacteria and that their resistance depends on their ability to share resistance genes through biofilms in addition to extensive antibiotic usage [30, 31]. The different resistance profiles can be attributed to the many ways through which these bacteria become resistant to antibiotics due to adaptation to the clinical setting [32, 33].

The prevalence rate of methicillin resistance was found to be 43.7%, with 54.2% of MRSA and 40.4% of MR-CoNS. The findings were in agreement with the study done by Fišarová et al. (2019) who suggested that MR-CoNS can serve as the source of resistance genes which would lead to horizontal

gene transfer between patients [34]. It is therefore crucial to monitor MRSA and MR-CoNS continually and modify treatment strategies accordingly [35].

Overall, this study underscores the significance of correct species identification for proper management, the influence of anatomical and clinical considerations on infection frequency, particularly when a catheter or other devices are used, the importance of rigorous infection control practices and maintaining sterile conditions for the devices, the need for targeted antibiotic treatment in order to reduce the risk of resistance development, and regular surveillance of resistance trends to enable informed decision-making. Knowledge about the species composition and resistance profile among staphylococci is not just about numbers; rather, it forms the basis of science-based therapeutic approaches to limit resistance and preserve the efficacy of antibiotics.

Conclusion

In light of urine as the source of the specimens, the commonest species included *S. haemolyticus* and *S. aureus,* just like the prevalence of urinary infections and infections related to medical devices. Although the resistance to erythromycin, clindamycin and tetracycline varied according to the different species, the susceptibility to antibiotics was quite good concerning linezolid, vancomycin, teicoplanin, and tigecycline. Methicillin resistance was noted in both MRSA and MR-CoNS, which highlights the importance of surveillance and species specific approach to treatment. In summary, correct identification of the species, proper selection of an antibiotic therapy and strict infection control measures are critical to handling and preventing multidrug resistant staphylococci.

References

1. Pidwill GR, Gibson JF, Cole J, Renshaw SA, Foster SJ. The Role of Macrophages in Staphylococcus aureus Infection. Front Immunol. 2021;11:620339. https://doi.org/10.3389/fimmu.2020.620339 .
2. Lima RD, Hajiarbabi K, Ng BD, Sood A, Ferreira RBR. Skin-associated commensal microorganisms and their metabolites. J Appl Microbiol. 2025;136(5):lxaf111. https://doi.org/10.1093/jambio/lxaf111 .
3. Ritter AS, Mears S. Preventing Orthopedic Infections. Infect Dis Clin North Am. 2025;39(3):383–398. https://doi.org/10.1016/j.idc.2025.02.016 .

4. Harwood KH, Brusamarello CE, Wilkins AL, Zhu X, Landersdorfer CB, Gwee A. Pharmacodynamics of Vancomycin Against Coagulase-Negative Staphylococci Bloodstream Infections. Pharmacol Res Perspect. 2025;13(5):e70180. https://doi.org/10.1002/prp2.70180 .
5. Getahun YA, Abey SL, Beyene AM, Belete MA, Tessema TS. Coagulase-negative staphylococci from bovine milk: Antibiogram profiles and virulent gene detection. BMC Microbiol. 2024;24(1):263. https://doi.org/10.1186/s12866-024-03415-0 .
6. Majumder MAA, Rahman S, Cohall D, Bharatha A, Singh K, Haque M, Gittens-St Hilaire M. Antimicrobial Stewardship: Fighting Antimicrobial Resistance and Protecting Global Public Health. Infect Drug Resist. 2020;13:4713–4738. https://doi.org/10.2147/IDR.S290835
7. EMR Antimicrobial Resistance Collaborators. The burden of bacterial antimicrobial resistance in the WHO Eastern Mediterranean Region 1990-2021: a cross-country systematic analysis with forecasts to 2050. Lancet Public Health. 2025;10(11):e955–e970. https://doi.org/10.1016/S2468-2667(25)00201-4
8. Salikin NH, Keong LC, Azemin WA, Philip N, Yusuf N, Daud SA, Rashid SA. Combating multidrug-resistant (MDR) Staphylococcus aureus infection using terpene and its derivative. World J Microbiol Biotechnol. 2024;40(12):402. https://doi.org/10.1007/s11274-024-04190-w
9. Facciolà A, Laganà A, Gioffrè ME, Morabito A, Chiera D, Ferlazzo M, Laganà P. Staphylococci: What Has Changed in the Antibiotic Resistance Profile in the Last Decade-Analysis of Strains Isolated from Hospitalised Patients. Pathogens (Basel). 2025;14(12):1289. https://doi.org/10.3390/pathogens14121289
10. Touati A, Ibrahim NA, Idres T. Disarming Staphylococcus aureus: Review of Strategies Combating This Resilient Pathogen by Targeting Its Virulence. Pathogens (Basel). 2025;14(4):386. https://doi.org/10.3390/pathogens14040386
11. Mohsin AS, Ali MR, Alsakini AH. Biofilm-associated genes and their role in antibiotic resistance among clinical Staphylococcus aureus isolates. J Infect Dev Ctries. 2026;20(3):416–424. https://doi.org/10.3855/jidc.22026
12. Jamil HA, Mohsin A, Abbas SM, Hussein AM, Abdtawfeeq TH. Recent Advances in Anti-Biofilm Strategies to Combat Antimicrobial Resistance. Acad Int J Pure Sci. 2026;4(1):01–11. https://doi.org/10.59675/P411
13. Mohsin AS, Alsakini AH, Ali MR. Molecular characterization of Dr/Afa genes prevalent among multi drug resistant Escherichia coli isolated from urinary tract infections. Biomedicine (India). 2022;42(3):523–529. https://doi.org/10.51248/.v42i3.1632

14. Campos-Madueno EI, Peirano G, Aldeia C, Elzi MV, Kocher C, Poirel L, Nordmann P, Perreten V, Pitout JDD, Endimiani A. Detection of ESBL-producing Klebsiella oxytoca complex with VITEK 2 system and screening cutoffs for implementing confirmatory tests. J Clin Microbiol. 2025;63:e00128-25. https://doi.org/10.1128/jcm.00128-25.
15. Günaydın B, Kutlu HH, Kurç MA. Evaluation of the VITEK 2 second-generation cassette for colistin susceptibility testing in carbapenem-resistant gram-negative bacteria. Diagn Microbiol Infect Dis. 2026;114(2):117148. https://doi.org/10.1016/j.diagmicrobio.2025.117148
16. Clinical and Laboratory Standards Institute. Performance Standards for Antimicrobial Susceptibility Testing (CLSI M100, 35th ed.). Clinical and Laboratory Standards Institute; 2025.
17. Ross JE, Scangarella-Oman NE, Flamm RK, Jones RN. Determination of Disk Diffusion and MIC Quality Control Guidelines for GSK2140944, a Novel Bacterial Type II Topoisomerase Inhibitor Antimicrobial Agent. J Clin Microbiol. 2014;52. https://doi.org/10.1128/jcm.00656-14
18. Katkowska M, Kosecka-Strojek M, Wolska-Gębarzewska M, Kwapisz E, Wierzbowska M, Międzobrodzki J, Garbacz K. Emerging Challenges in Methicillin Resistance of Coagulase-Negative Staphylococci. Antibiotics (Basel). 2025;14(1):37. https://doi.org/10.3390/antibiotics14010037
19. Tong SY, Davis JS, Eichenberger E, Holland TL, Fowler VG Jr. Staphylococcus aureus infections: epidemiology, pathophysiology, clinical manifestations, and management. Clin Microbiol Rev. 2015;28(3):603–661. https://doi.org/10.1128/CMR.00134-14
20. Touaitia R, Mairi A, Ibrahim NA, Basher NS, Idres T, Touati A. Staphylococcus aureus: A Review of the Pathogenesis and Virulence Mechanisms. Antibiotics (Basel). 2025;14(5):470. https://doi.org/10.3390/antibiotics14050470
21. Ribas MR, Vásquez-Ponce F, Cardoso R, Mesa D, Rocha G, Wolleck VF, Dal Pizzol JL, de Assunção IBF, Oliveira VPE, Salvador G, Rodrigues AT, Melocco GB, Esposito F, Becerra J, Lincopan N, Ferreira FA, Sincero TC, Palmeiro JK, Wosiacki SR, Osaki SC. Emergence of Livestock-Associated Methicillin-Resistant Staphylococcus aureus ST398 in Wild Birds, Brazil. MicrobiologyOpen. 2025;14(6):e70131. https://doi.org/10.1002/mbo3.70131
22. Phillip S, Mushi MF, Decano AG, Seni J, Mmbaga BT, Kumburu H, Konje ET, Mwanga JR, Kidenya BR, Msemwa B, Gillespie S, Maldonado-Barragan A, Sandeman A, Sabiti W, Holden MTG, Mshana SE. Molecular Characterizations of the Coagulase-Negative Staphylococci

Species Causing Urinary Tract Infection in Tanzania: A Laboratory-Based Cross-Sectional Study. Pathogens. 2023;12(2):180. https://doi.org/10.3390/pathogens12020180 .

23. Lopez LM, Stockton LL, Chen M, Steiner MJ, Gallo MF. Behavioral interventions for improving dual-method contraceptive use. Cochrane Database Syst Rev. 2014;2014(3):CD010915. https://doi.org/10.1002/14651858.CD010915.pub2
24. Aniba R, Dihmane A, Raqraq H, et al. Exploring staphylococcus in urinary tract infections: A systematic review and meta-analysis on the epidemiology, antibiotic resistance and biofilm formation. Diagn Microbiol Infect Dis. 2024;110(4):116470. https://doi.org/10.1016/j.diagmicrobio.2024.116470
25. Mayasari E, Utama ED. Epidemiology and resistant profile of bacterial pathogens in a tertiary health care hospital, Medan City: a retrospective study. PeerJ. 2025;13:e19510. https://doi.org/10.7717/peerj.19510
26. Miller JM, Binnicker MJ, Campbell S, Carroll KC, Chapin KC, Gilligan PH, Gonzalez MD, Jerris RC, Kehl SC, Patel R, Pritt BS, Richter SS, Robinson-Dunn B, Schwartzman JD, Snyder JW, Telford S 3rd, Theel ES, Thomson RB Jr, Weinstein MP, Yao JD. A Guide to Utilization of the Microbiology Laboratory for Diagnosis of Infectious Diseases: 2018 Update by the Infectious Diseases Society of America and the American Society for Microbiology. Clin Infect Dis. 2018;67(6):e1–e94. https://doi.org/10.1093/cid/ciy381
27. Eltwisy HO, Twisy HO, Hafez MH, Sayed IM, El-Mokhtar MA. Clinical Infections, Antibiotic Resistance, and Pathogenesis of Staphylococcus haemolyticus. Microorganisms. 2022;10(6):1130. https://doi.org/10.3390/microorganisms10061130
28. Verma A, Kumar S, Venkatesh V, Jain P, Kalyan R, Reddy H. Staphylococcus hemolyticus: The Most Common and Resistant Coagulase-Negative Staphylococcus Species Causing Bacteremia in North India. Cureus. 2024;16(1):e51680. https://doi.org/10.7759/cureus.51680
29. Larkins-Ford J, Degefu YN, Van N, Sokolov A, Aldridge BB. Design principles to assemble drug combinations for effective tuberculosis therapy using interpretable pairwise drug response measurements. Cell Rep Med. 2022;3(9):100737. https://doi.org/10.1016/j.xcrm.2022.100737
30. Hall CW, Mah TF. Molecular mechanisms of biofilm-based antibiotic resistance and tolerance in pathogenic bacteria. FEMS Microbiol Rev. 2017;41(3):276–301. https://doi.org/10.1093/femsre/fux010
31. Labib JR, Ibrahim SK, Salem MR, Youssef MRL, Meligy B. Infection with gram-negative bacteria among children in a tertiary pediatric hospital in Egypt. Am J Infect Control. 2018;46(7):798–801. https://doi.org/10.1016/j.ajic.2017.12.008

32. Satoskar AA, Parikh SV, Nadasdy T. Epidemiology, pathogenesis, treatment and outcomes of infection-associated glomerulonephritis. Nat Rev Nephrol. 2020;16(1):32–50. https://doi.org/10.1038/s41581-019-0178-8
33. Khalaf MJ, Ibrahim HA, Abd HA, Mohammed MQ, Mohsin AS. Gentamicin modulates pgaA and pgaB expression in Klebsiella pneumoniae: Insights into biofilm-associated adaptation. Microbes Infect Dis. 2025;():-. https://doi.org/10.21608/mid.2025.432058.3325
34. Fišarová L, Pantůček R, Botka T, Doškař J. Variability of resistance plasmids in coagulase-negative staphylococci and their importance as a reservoir of antimicrobial resistance. Res Microbiol. 2019;170(2):105–111. https://doi.org/10.1016/j.resmic.2018.11.004
35. Lee DH, Lee K, Kim YS, Cha CJ. Comprehensive genomic landscape of antibiotic resistance in Staphylococcus epidermidis. mSystems. 2024;9(6):e0022624. https://doi.org/10.1128/msystems.00226-24.

Hilbert Space Characterization of Pseudo spectral Permanence for Non-Self-Adjoint Operators under Kernel Projections

Hanan A. A. Asaad Al-Ukaily [1]

1 Department of Mathematics, College of Education for pure sciences, Tikrit University, Tikrit, Iraq.

.Author Emails

[a]ass.lhananabdjabar@tu.edu.iq

a) Corresponding author: ass.lhananabdjabar@tu.edu.iq

Hilbert Space Characterization of Pseudo spectral Permanence for Non-Self-Adjoint Operators under Kernel Projections

Hanan A. A. Asaad Al-Ukaily [1]

1 Department of Mathematics, College of Education for pure sciences, Tikrit University, Tikrit, Iraq.

.Author Emails

[a]ass.lhananabdjabar@tu.edu.iq

a) Corresponding author: ass.lhananabdjabar@tu.edu.iq

Abstract:

This paper investigates the permanence of ϵ-pseudospectra under finite-dimensional compression of non-self-adjoint operators on Reproducing Kernel Hilbert Spaces. It is well known that Galerkin compression $T_n = P_n T P_n$ can destroy spectral information when T is not self-adjoint: eigenvalues of T_n may bear no relation to those of T, and existing convergence results for the more robust ϵ-pseudospectrum provide sufficient conditions only, leaving the question of necessity open.

We settle this question by proving that the ϵ-pseudospectra of T_n converge to $\Lambda_\epsilon(T)$ in the Hausdorff metric for every admissible projection sequence if and only if two conditions hold: (i) the resolvent

$R(z,T)$ is compact, and (ii) the kernel embeds $\mathcal{H}_K$ continuously into $H^s(\Omega)$ with $s > \frac{d}{2}$. When both conditions are satisfied, the resolvent perturbation on the pseudospectral boundary decays as $O\left(\frac{h_n^{s-\frac{d}{2}}}{\epsilon^2}\right)$, and we derive an explicit Hausdorff-distance bound governed by the level-set geometry of the resolvent norm. When either condition is violated, we construct admissible projection sequences under which convergence fails. In the framework of Hansen's solvability complexity index, the characterization yields $\mathrm{SCI} = 1$ for computing $\Lambda_\epsilon(T)$ when both conditions hold. As a separate result, we show that the Fredholm index of $zI - T$ is permanent under the strictly weaker hypothesis that $T_n - T$ is finite-rank, while invertibility of $zI - T_n$ requires the full hypotheses-thereby separating the permanence thresholds of the topological invariant (index) from the metric one (pseudo spectral geometry).

Keywords: Non-self-adjoint operators, pseudo spectral permanence, RKHS projections, compact resolvent, Fredholm index stability.

1 Introduction:

Compressing a bounded operator T on a Hilbert space to a finite-dimensional subspace V_n via $T_n = P_n T P_n$ is central to Galerkin discretization. For self-adjoint T, the spectral theorem controls the approximation error; without self-adjointness, even qualitative
spectral features may bear no stable relation to those of T [30, 9]. The ϵ-pseudospectrum $\Lambda_\epsilon(T) = \sigma(T) \cup \{z: \|(zI - T)^{-1}\| > 1/\epsilon\}$, introduced as a robust spectral portrait by Trefethen [29], has proved more amenable to discretization than the spectrum itself [23, 28, 5, 26,16].

Convergence of pseudospectra under discretization has been studied extensively. Bögli and Siegl [2] proved Hausdorff convergence under generalized norm-resolvent hypotheses, subject to a non-constancy condition on the resolvent norm [25]; Bögli [3, 4] obtained spectral exactness for compact-resolvent operators. Frommer et al. [13] enclosed pseudospectra via numerical ranges of discretized operators, building on the eigenvalue approximation theory of Descloux-Nassif-Rappaz [10], Osborn [20], Chatelin [7], and Stummel [27]. Hansen [15] introduced the solvability complexity index (SCI), recently extended by Colbrook [8], classifying spectral problems by their inherent computational difficulty. Chandler-Wilde, Chonchaiya, and Lindner [6] derived new pseudospectral inclusion sets for bounded operators. Lindner and Schmeckpeper [18] gave necessary and sufficient conditions for Hausdorff convergence in terms of pointwise resolvent-norm convergence on a general Banach space. All these results either give sufficient conditions only, or state the necessary conditions in terms of pointwise resolvent behaviour. No characterization exists in terms of structural properties of the operator and the underlying function space.

We provide such a characterization within the Reproducing Kernel Hilbert Space framework [1,21,12], where the projections P_n arise from kernel translates at scattered nodes [31, 24, 19]. Our main result (theorem 4.6): pseudo spectral permanence convergence of $\Lambda_\epsilon(T_n)$ to $\Lambda_\epsilon(T)$ in the Hausdorff metric for every admissible node sequenceholds if and only if the resolvent $R(z,T)$ is compact and $\mathcal{H}_K \hookrightarrow H^s(\Omega)$ with $s > \frac{d}{2}$. The reverse direction rests on two new tools: a separation lemma converting resolvent non-compactness into a geometric obstruction, and an implicit-function

argument linking resolvent-norm failure to pseudo spectral-set failure. The Fredholm index [17, 14, 11] is permanent under a strictly weaker hypothesis (theorem 5.1), separating the topological invariant from the metric one.

2 Framework

2.1 Reproducing kernel setting

Let $\Omega \subset \mathbb{R}^d$ be a bounded Lipschitz domain and $\mathcal{H}_K$ an RKHS on Ω with reproducing kernel K : for each $x \in \Omega$, $f(x) = \langle f, K(\cdot, x)\rangle_{\mathcal{H}_K}$ and this functional is bounded [1, 20].

Assumption 1 (Kernel). (K1) $K \in C(\Omega \times \Omega)$. (K2) $\mathcal{H}_K \hookrightarrow H^s(\Omega)$ continuously with $s > \frac{d}{2}$ and embedding constant C_{emb} . (K3) K is strictly positive definite.

Given quasi-uniform nodes $X_n = \{x_1, \dots, x_n\} \subset \Omega$ with fill distance $h_n \to 0$, define $V_n = \text{span}\{K(\cdot, x_j)\}$ and let P_n be the $\mathcal{H}_K$–orthogonal projection onto V_n.

Definition 2.1. A sequence $\{P_n\}$ is admissible if K satisfies (K1) and (K3), and $\{P_n\}$ arises from quasi-uniform nodes with $h_n \to 0$.

Remark 2.2. Condition (K2) is not part of admissibility; it will appear as a hypothesis in the forward direction and as a necessary condition in the characterization.

Lemma 2.3 ([31, Thm 11.4]). Under Assumption 1, $\|f - P_n f\|_{\mathcal{H}_K} \le C_{\text{pf}} h_n^{s-d/2} \|f\|_{\mathcal{H}_K}$ for all $f \in \mathcal{H}_K$, where C_{pf} depends on K, s, d, Ω and the quasi-uniformity constant.

Proof. The kernel interpolant $s_n \in V_n$ satisfying $s_n(x_k) = f(x_k)$ exists and is unique by (K3). Since $P_n f$ minimises $\|f - g\|_{\mathcal{H}_K}$ over $g \in V_n$:

$$\|f - P_n f\|_{\mathcal{H}_K} \le \|f - s_n\|_{\mathcal{H}_K} \le C' h_n^{s-d/2} \|f\|_{H^s} \le C' C_{\text{emb}} h_n^{s-d/2} \|f\|_{\mathcal{H}_K}$$

where the second inequality is the power-function estimate and the third uses (K2).

2.2 Operators and pseudospectra

The compression of $T \in \mathcal{B}(\mathcal{H}_K)$ to V_n is $T_n = P_n T P_n$.

Assumption 2 (Operator). $T \in \mathcal{B}(\mathcal{H}_K)$ is bounded. There exists $z_0 \in \rho(T)$ with $R(z_0, T)$ compact.

Compactness of $R(z_0, T)$ at a single point implies compactness at every $z \in \rho(T)$, because the resolvent identity gives $R(z, T) = R(z_0, T)[I + (z_0 - z)R(z, T)]$ and a compact operator composed with a bounded operator is compact.

Definition 2.4. The Kreiss constant is $\mathcal{C}(T) = \sup_{z \notin \overline{W(T)}} \|R(z, T)\| \text{dist}(z, W(T))$, with $W(T) = \{\langle Tf, f\rangle : \|f\| = 1\}$. For normal $T, \mathcal{C}(T) = 1$.

Definition 2.5. The ϵ-pseudospectrum is $\Lambda_\epsilon(T) = \sigma(T) \cup \{z \in \mathbb{C} : \|R(z, T)\| > 1/\epsilon\}$.
Definition 2.6 (Pseudospectral permanence). T has ϵ-pseudospectral permanence on $\mathcal{R}$ if $d_H(\Lambda_\epsilon(T_n) \cap \mathcal{R}, \Lambda_\epsilon(T) \cap \mathcal{R}) \to 0$ for every admissible $\{P_n\}$.

3 Forward Direction

Both Assumptions hold throughout this section.

Proposition 3.1. For each $f \in \mathcal{H}_K$, $\|(T_n - T)f\|_{\mathcal{H}_K} \le C_{\mathrm{pf}} h_n^{s-d/2}(\|Tf\| + \|T\|\|f\|)$.
Proof. Writing $T_n f - Tf = P_n T P_n f - Tf$ and inserting $\pm P_n Tf$:

$$T_n f - Tf = (P_n - I)Tf + P_n T(P_n - I)f$$

To verify: $P_n T P_n f = P_n T\big(f + (P_n f - f)\big) = P_n Tf + P_n T(P_n f - f)$. Hence $P_n T P_n f - Tf = (P_n Tf - Tf) + P_n T(P_n f - f)$.

First term: $\|(P_n - I)Tf\| \le C_{\mathrm{pf}} h_n^{s-d/2}\|Tf\|$ by lemma 2.3 applied to the fixed element $Tf \in \mathcal{H}_K$.

Second term: $\|P_n T(P_n - I)f\| \le \|P_n\|\|T\|\|(P_n - I)f\| \le \|T\| C_{\mathrm{pf}} h_n^{s-d/2}\|f\|$, since $\|P_n\| \le 1$ for orthogonal projections.

Adding the two bounds completes the proof.

Theorem 3.2 (Norm-resolvent convergence). Let $\Gamma \subset \rho(T)$ be compact, $M_\Gamma = \sup_{z\in\Gamma}\|R(z,T)\|$. For h_n small enough,

$$\sup_{z\in\Gamma}\|R(z,T_n) - R(z,T)\| \le 4M_\Gamma^2\|T\| C_{\mathrm{pf}} h_n^{s-d/2} \tag{1}$$

Proof. Step 1. For $z \in \Gamma$, the algebraic identity

$$zI - T_n = [I - (T_n - T)R(z,T)](zI - T) \tag{2}$$

holds because the right-hand side expands to $(zI - T) - (T_n - T)R(z,T)(zI - T) = (zI - T) - (T_n - T) = zI - T_n$, using $R(z,T)(zI - T) = I$. Define $Q_n(z) = (T_n - T)R(z,T)$.

Step 2. We show $\mathcal{K} = \{R(z,T)g : z \in \Gamma, \|g\| \le 1\}$ is relatively compact.
Fix z_0 as in Assumption 2. The first resolvent identity gives $R(z,T) = R(z_0,T)[I + (z_0 - z)R(z,T)]$. For $z \in \Gamma$ and $\|g\| \le 1$, set $\psi = [I + (z_0 - z)R(z,T)]g$. Then $\|\psi\| \le 1 + \max_{z\in\Gamma}|z_0 - z| \cdot M_\Gamma =: R_0$. Hence $\mathcal{K} \subset R(z_0,T)\big(\bar{B}(0,R_0)\big)$. Since $R(z_0,T)$ is compact, the image of a bounded set is relatively compact, so $\mathcal{K}$ is relatively compact.

Step 3. Fix $\varepsilon > 0$. Cover $\overline{\mathcal{K}}$ by ε-balls centred at $\phi_1, \dots, \phi_m$. By proposition 3.1, for each ϕ_k there exists N_k with $\|(T_n - T)\phi_k\| < \varepsilon$ for $n \ge N_k$. Set $N_\varepsilon = \max_k N_k$. For any $\psi = R(z,T)g \in \mathcal{K}$, pick ϕ_k with $\|\psi - \phi_k\| < \varepsilon$:

$$\|(T_n - T)\psi\| \le \|(T_n - T)(\psi - \phi_k)\| + \|(T_n - T)\phi_k\| \le (\|T_n\| + \|T\|)\varepsilon + \varepsilon$$

Since $\|T_n\| = \|P_n T P_n\| \le \|T\|$: $\|(T_n - T)\psi\| \le (2\|T\| + 1)\varepsilon$.

Choose $\varepsilon_0 = \frac{1}{2(2\|T\|+1)}$. For $n \ge N_{\varepsilon_0}$: $\sup_{z\in\Gamma}\|Q_n(z)\| \le \frac{1}{2}$. The Neumann series $\sum_{k\ge 0} Q_n(z)^k$ converges, $\|(I - Q_n(z))^{-1}\| \le 2$, and $R(z,T_n) = R(z,T)(I - Q_n(z))^{-1}$ exists with $\|R(z,T_n)\| \le 2M_\Gamma$.

Step 4. The second resolvent identity $R(z,T_n)-R(z,T)=R(z,T_n)(T_n-T)R(z,T)$ is verified by multiplying both sides by ($zI-T_n$) on the left and ($zI-T$) on the right; both reduce to T_n-T. Taking norms and using the explicit convergence rate from proposition 3.1 on elements of $\mathcal{K}$ (which have $\|\psi\|\le M_\Gamma$):

$$\|(T_n-T)R(z,T)\|\le 2\|T\|C_{\mathrm{pf}}M_\Gamma h_n^{s-d/2}$$

Hence $\|R(z,T_n)-R(z,T)\|\le 2M_\Gamma\cdot 2\|T\|C_{\mathrm{pf}}M_\Gamma h_n^{s-d/2}=4M_\Gamma^2\|T\|C_{\mathrm{pf}}h_n^{s-d/2}$.

Theorem 3.3 (Pseudo spectral permanence). Under Assumptions 1-2, T has ϵ-pseudospectral permanence on every bounded $\mathcal{R}$:

$$d_H(\Lambda_\epsilon(T_n)\cap\mathcal{R},\Lambda_\epsilon(T)\cap\mathcal{R})\to 0 \tag{3}$$

Moreover, the resolvent perturbation on the pseudo spectral boundary $\Gamma_\epsilon:=\{z\in\mathcal{R}:\|R(z,T)\|=1/\epsilon\}$ satisfies

$$\sup_{z\in\Gamma_\epsilon}\|R(z,T_n)-R(z,T)\|\le\frac{4\|T\|C_{\mathrm{pf}}}{\epsilon^2}h_n^{s-d/2} \tag{4}$$

Proof. Part A. Let $z\in\Lambda_\epsilon(T)\cap\mathcal{R}$. If $z\in\sigma(T_n)$, then $z\in\Lambda_\epsilon(T_n)$ and $\mathrm{dist}\big(z,\Lambda_\epsilon(T_n)\big)=0$. If $z\in\sigma(T)\cap\rho(T_n)$, pick any sequence $w_m\to z$ with $w_m\in\rho(T)$; then $\|R(w_m,T)\|\to\infty$, and by theorem 3.2$\|R(w_m,T_n)\|\to\infty$ for n large, so $w_m\in\Lambda_\epsilon(T_n)$ and $\mathrm{dist}\big(z,\Lambda_\epsilon(T_n)\big)\le|z-w_m|\to 0$. If $z\in\rho(T)\cap\rho(T_n)$ with $\|R(z,T)\|>1/\epsilon$, the reverse triangle inequality gives $\|R(z,T_n)\|\ge\|R(z,T)\|-\|R(z,T_n)-R(z,T)\|>1/\epsilon$ for n large by theorem 3.2, so $z\in\Lambda_\epsilon(T_n)$.

Part B. Suppose $z_{n_k}\in\Lambda_\epsilon\big(T_{n_k}\big)\cap\mathcal{R}$ with $\mathrm{dist}\big(z_{n_k},\Lambda_\epsilon(T)\big)\ge\delta>0$. BolzanoWeierstrass gives $z_{n_k}\to z_\infty$ with $z_\infty\notin\Lambda_\epsilon(T)$, so $z_\infty\in\rho(T)$ and $\|R(z_\infty,T)\|\le 1/\epsilon$. By theorem 3.2, $\big\|R\big(z_{n_k},T_{n_k}\big)\big\|\to\|R(z_\infty,T)\|\le 1/\epsilon$, contradicting $\big\|R\big(z_{n_k},T_{n_k}\big)\big\|>1/\epsilon$.

Rate. Apply theorem 3.2 with $\Gamma=\Gamma_\epsilon$, noting $M_{\Gamma_\epsilon}=1/\epsilon$.

Proposition 3.4 (Hausdorff-distance rate). Under Assumptions 1-2, suppose Γ_ϵ is a C^1 curve and $\|R(\cdot,T)\|$ is not locally constant near Γ_ϵ (which holds generically for operators with compact resolvent, cf. [24, 2]). Define

$$m_\epsilon:=\inf_{z\in\Gamma_\epsilon}\liminf_{w\to z}\frac{|\|R(w,T)\|-1/\epsilon|}{|w-z|}>0$$

Then

$$d_H(\Lambda_\epsilon(T_n)\cap\mathcal{R},\Lambda_\epsilon(T)\cap\mathcal{R})\le\frac{4\|T\|C_{\mathrm{pf}}}{m_\epsilon\epsilon^2}h_n^{s-d/2}. \tag{5}$$

Proof. Let $\eta_n:=\sup_{z\in\Gamma_\epsilon}\|R(z,T_n)-R(z,T)\|$, which is $O\big(h_n^{s-d/2}/\epsilon^2\big)$ by (4). At any point $z_0\in\Gamma_\epsilon$, we have $\|R(z_0,T)\|=1/\epsilon$. The perturbed resolvent satisfies $|\|R(z_0,T_n)\|-1/\epsilon|\le\eta_n$. The boundary $\partial\Lambda_\epsilon(T_n)$ near z_0 is the level set $\{\|R(\cdot,T_n)\|=1/\epsilon\}$. Since $\|R(\cdot,T)\|$ has gradient magnitude at least

m_ϵ across Γ_ϵ, and the perturbation η_n shifts the level-set value by at most η_n, the boundary displacement is at most $\frac{\eta_n}{m_\epsilon}$. Taking the supremum over Γ_ϵ, and noting that the Hausdorff distance between the pseudospectral sets is controlled by the maximum boundary displacement (because interior points of $\Lambda_\epsilon(T)$ with $\|R(z,T)\| \gg 1/\epsilon$ remain in $\Lambda_\epsilon(T_n)$ for n large, by Part A of theorem 3.3), we obtain (5).

Remark 3.5. The quantity m_ϵ depends on T and ϵ but not on the kernel or the nodes. For normal operators, $m_\epsilon = 1/\epsilon^2$ (the resolvent norm decays quadratically away from the spectrum), giving $d_H = O\left(\|T\| C_{\text{pf}} h_n^{s-d/2}\right)$-an ϵ-independent rate. For highly nonnormal operators, m_ϵ can be much smaller (nearly flat level sets of $\|R(\cdot,T)\|$), leading to a larger effective constant. This is consistent with the known sensitivity of pseudospectra to perturbation for non-normal operators [30].

4 Reverse Direction

We prove the contrapositive of (i) ⇒ (ii): violating either hypothesis in Assumption 1 or 2 entails existence of an admissible projection sequence under which permanence fails. Two preparatory lemmas are needed.

4.1 Two lemmas

Lemma 4.1 (Separation). Let H be a separable Hilbert space and $\{\psi_k\}_{k\geq 1} \subset H$ a bounded sequence with no convergent subsequence. Then:

(a) There exist $\varepsilon_0 > 0$ and a subsequence (still written $\{\psi_k\}$) with $\|\psi_j - \psi_i\| \geq \varepsilon_0$ for all $j \neq i$.

(b) For every subspace $V \subset H$ with $\dim V = n$, there exists $j_0 > n$ with $\text{dist}(\psi_{j_0}, V) \geq \varepsilon_0/4$.

Proof. Part (a). We construct the subsequence by a greedy procedure. Set $k_1 = 1$. Suppose $k_1 < \cdots < k_j$ have been selected with $\|\psi_{k_p} - \psi_{k_q}\| \geq \varepsilon_0$ for all $p \neq q$. Consider the tail $\{\psi_m : m > k_j\}$. We claim that, for ε_0 small enough, some $m > k_j$ satisfies $\|\psi_m - \psi_{k_p}\| \geq \varepsilon_0$ for all $p \leq j$. If not, every element of the tail lies within ε_0 of the finite set $\{\psi_{k_1}, \ldots, \psi_{k_j}\}$. The ball $B(\psi_{k_p}, \varepsilon_0)$ contains infinitely many tail elements for at least one index p; extracting a subsequence from that ball and using $\|\psi_m - \psi_{m'}\| \leq 2\varepsilon_0$ would yield a Cauchy subsequence, hence a convergent one-contradicting the hypothesis.

It remains to choose ε_0. Since $\{\psi_k\}$ has no convergent subsequence, it is not totally bounded: there exists $\varepsilon_0 > 0$ such that no finite ε_0-net covers $\{\psi_k\}$. (If a finite ε_0-net existed for every $\varepsilon_0 > 0$, the sequence would be totally bounded, hence relatively compact in H, and every sequence in a compact set has a convergent subsequence.) With this ε_0, the greedy construction never terminates.

Part (b). Fix V with $\dim V = n$. Suppose, seeking a contradiction, that $\text{dist}(\psi_j, V) < \varepsilon_0/4$ for all $j > n$. Let π_V denote the orthogonal projection onto V. Then $\|\psi_j - \pi_V \psi_j\| < \varepsilon_0/4$ for all $j > n$.

The sequence $\{\pi_V\psi_j\}_{j>n}$ lies in the finite-dimensional space V and is bounded (by $\sup_k\|\psi_k\| + \varepsilon_0/4$). By Bolzano-Weierstrass in V, some subsequence $\{\pi_V\psi_{j_\ell}\}$ converges. For ℓ, m large:

$$\begin{aligned}\|\psi_{j_\ell} - \psi_{j_m}\| &\le \|\psi_{j_\ell} - \pi_V\psi_{j_\ell}\| + \|\pi_V\psi_{j_\ell} - \pi_V\psi_{j_m}\| + \|\pi_V\psi_{j_m} - \psi_{j_m}\| \\ &< \frac{\varepsilon_0}{4} + \|\pi_V\psi_{j_\ell} - \pi_V\psi_{j_m}\| + \frac{\varepsilon_0}{4}.\end{aligned}$$

Since $\pi_V\psi_{j_\ell}$ converges, the middle term is eventually less than $\varepsilon_0/4$. Thus $\|\psi_{j_\ell} - \psi_{j_m}\| < 3\varepsilon_0/4 < \varepsilon_0$, contradicting part (a).

Lemma 4.2 (From resolvent failure to pseudospectral failure). Let $S, S_n \in \mathcal{B}(H)$ with $\sigma(S)$ non-empty and $S_n \to S$ strongly. Suppose there exists $z_0 \in \rho(S)$ such that $\|R(z_0, S_n) - R(z_0, S)\| \nrightarrow 0$. Then for some $\epsilon > 0$ and some bounded $\mathcal{R} \ni z_0$:

$$\limsup_{n\to\infty} d_H(\Lambda_\epsilon(S_n) \cap \mathcal{R}, \Lambda_\epsilon(S) \cap \mathcal{R}) > 0$$

Proof. Set $r_0 = \|R(z_0, S)\|$ and choose $\epsilon = 1/(2r_0)$, so that $\|R(z_0, S)\| = r_0 < 1/\epsilon = 2r_0$. Then $z_0 \notin \Lambda_\epsilon(S)$, and dist $(z_0, \Lambda_\epsilon(S)) > 0$ (because $\Lambda_\epsilon(S)$ is closed and $z_0 \notin \Lambda_\epsilon(S)$).

Since $\|R(z_0, S_n) - R(z_0, S)\| \nrightarrow 0$, there exist $\delta_0 > 0$ and a subsequence $\{n_k\}$ with $\|R(z_0, S_{n_k}) - R(z_0, S)\| \ge \delta_0$ for all k. Two sub-cases arise.

Sub-case 1: $\|R(z_0, S_{n_k})\| > 1/\epsilon$ for infinitely many k. Then $z_0 \in \Lambda_\epsilon(S_{n_k})$ while $z_0 \notin \Lambda_\epsilon(S)$, so $d_H(\Lambda_\epsilon(S_{n_k}) \cap \mathcal{R}, \Lambda_\epsilon(S) \cap \mathcal{R}) \ge \text{dist}(z_0, \Lambda_\epsilon(S)) > 0$.

Sub-case 2: $\|R(z_0, S_{n_k})\| \le 1/\epsilon$ for all k large. Since $\sigma(S)$ is non-empty, there exists $z_1 \in \rho(S)$ with $\|R(z_1, S)\| > 2/\epsilon$ (the resolvent norm blows up near $\sigma(S)$). Pick g_0 with $\|g_0\| = 1$ and $\|R(z_1, S)g_0\| > 2/\epsilon$. Since $S_{n_k} \to S$ strongly, $(z_1 I - S_{n_k})^{-1} g_0 \to (z_1 I - S)^{-1} g_0$ whenever $z_1 \in \rho(S_{n_k})$; more precisely, for $z_1 \in \rho(S)$ with $\|R(z_1, S)\|$ bounded, the strong operator convergence $S_n \to S$ combined with the Neumann expansion in $(z_1 I - S)^{-1}$ gives $\|R(z_1, S_{n_k})g_0\| \to \|R(z_1, S)g_0\| > 2/\epsilon$. Hence $\|R(z_1, S_{n_k})\| > 1/\epsilon$ for k large, so $z_1 \in \Lambda_\epsilon(S_{n_k})$.

Now z_0 satisfies $\|R(z_0, S_{n_k})\| \le 1/\epsilon$ (so $z_0 \notin \Lambda_\epsilon(S_{n_k})$ or $z_0 \in \partial\Lambda_\epsilon(S_{n_k})$) and z_1 satisfies $z_1 \in \Lambda_\epsilon(S_{n_k})$. By the intermediate value theorem applied to $z \mapsto \|R(z, S_{n_k})\|$ along any path from z_0 to z_1 in $\rho(S_{n_k})$, the boundary $\partial\Lambda_\epsilon(S_{n_k})$ crosses this path. The analogous crossing for $\partial\Lambda_\epsilon(S)$ occurs at a different location because $\|R(z_0, S)\| = r_0 < 1/\epsilon$ while $\|R(z_0, S_{n_k})\|$ differs from r_0 (by at least δ_0 in operator norm, which forces $|\|R(z_0, S_{n_k})\| - r_0|$ to be positive for a subsequence, or the operators differ in a direction that shifts the level set). The boundary displacement yields $d_H > 0$.

In both sub-cases, $\limsup d_H > 0$.

4.2 Necessity of compact resolvent

Proposition 4.3. If Assumption 1 holds but $R(z, T)$ is not compact for any $z \in \rho(T)$, then T does not have ϵ-pseudospectral permanence for suitable ϵ and $\mathcal{R}$.

Proof. The argument has two stages: we first show that the collective-compactness mechanism on which theorem 3.2 relies is blocked; we then exhibit a concrete failure of pseudo spectral convergence.

Stage 1: Obstruction to norm-resolvent convergence.

Since $R(z_0, T)$ is not compact, the image $\{R(z_0, T)g: \|g\| \leq 1\}$ is not relatively compact, hence not totally bounded. There exists $\varepsilon_0 > 0$ such that no finite ε_0-net covers this set.

The proof of theorem 3.2 (Step 3) requires covering $\mathcal{K} \supset \{R(z_0, T)g: \|g\| \leq 1\}$ by finitely many ε-balls with $\varepsilon < \frac{1}{2(2\|T\|+1)}$, then using strong convergence on the ball centres. When $\varepsilon_0 < \frac{1}{2(2\|T\|+1)}$, no such finite cover exists, and the uniform bound $\sup_z \|Q_n(z)\| < 1$ cannot be established. This means the Neumann-series mechanism that produces $R(z, T_n)$ and controls $\|R(z, T_n) - R(z, T)\|$ is unavailable.

Applying lemma 4.1 to a sequence $\psi_k = R(z_0, T)g_k$ with no convergent subsequence: for every n-dimensional subspace V_n, some ψ_{j_0} satisfies $\operatorname{dist}(\psi_{j_0}, V_n) \geq \varepsilon_0/4$. This means the resolvent images cannot be uniformly approximated by any finite-dimensional projection, regardless of the node placement.

Stage 2: A concrete failure.

We exhibit an operator on an RKHS where permanence fails. Let $\mathcal{H}_K = H^s([0,1])$ with the Matérn kernel of order $s > \frac{1}{2}$, and let $T = M_\varphi + iM_\chi$ where $M_\varphi f(x) = \varphi(x)f(x), M_\chi f(x) = \chi(x)f(x)$, with $\varphi, \chi \in C([0,1])$ chosen so that T is non-normal and $\sigma(T) = \{(\varphi + i\chi)(x): x \in [0,1]\}$ is a curve in $\mathbb{C}$. The resolvent $R(z, T) = M_{1/(z-\varphi-i\chi)}$ is bounded but not compact: multiplication by a non-constant continuous function does not map bounded sets to relatively compact sets in L^2.

The compression $T_n = P_n T P_n$ is a rank- n operator on V_n, extended by zero on $V_n^\perp$. Its spectrum consists of n eigenvalues in $\mathbb{C}$ together with 0 (of infinite multiplicity from $V_n^\perp$). Since T is non-normal, $\Lambda_\epsilon(T)$ can extend far beyond the ϵ-neighbourhood of $\sigma(T)$ in directions determined by the non-normality. The finite-rank compressions T_n cannot approximate this extended pseudo spectral structure accurately: the n eigenvalues of $T_n|_{V_n}$ are discrete approximants to a continuous curve, and the parasitic eigenvalue at 0 lies outside $\sigma(T)$ whenever $0 \notin \sigma(T)$.

Choosing φ and χ so that $0 \notin \sigma(T)$, we have $0 \in \sigma(T_n) \setminus \sigma(T)$ for every n. For ϵ small enough that $0 \notin \Lambda_\epsilon(T)$, the point 0 belongs to $\Lambda_\epsilon(T_n)$ (since $\|R(0, T_n)\|$ is infinite- 0 is an eigenvalue of T_n) while $\operatorname{dist}(0, \Lambda_\epsilon(T)) > 0$. Hence

$$d_H(\Lambda_\epsilon(T_n) \cap \mathcal{R}, \Lambda_\epsilon(T) \cap \mathcal{R}) \geq \operatorname{dist}(0, \Lambda_\epsilon(T)) > 0$$

for every n and every admissible $\{P_n\}$, and permanence fails.

Remark 4.4. The failure in Stage 2 arises from a structural feature of Galerkin compression: $T_n = P_n T P_n$ always annihilates $V_n^\perp$, so $0 \in \sigma(T_n)$ whenever $V_n \neq \mathcal{H}_K$. When T has compact resolvent,

theorem 3.2 shows that 0 eventually leaves $\sigma(T_n)$ (the factorisation forces T_n to be invertible for n large). Without compact resolvent, this mechanism is absent.

4.3 Necessity of Sobolev regularity

Proposition 4.5. If $R(z_0, T)$ is compact but (K2) fails ($\mathcal{H}_K \hookrightarrow / H^s(\Omega)$ for any $s > d/2$), there exists an admissible projection sequence for which pseudospectral permanence fails.

Proof. Take $\Omega = [0,1], d = 1$. Let K be a continuous, strictly positive definite kernel whose native space satisfies $\mathcal{H}_K \hookrightarrow H^\sigma([0,1])$ only for $\sigma \leq 1/2$-for instance, the covariance kernel of fractional Brownian motion with Hurst parameter $H = 1/2 - \delta$ for small $\delta > 0$, which generates $\mathcal{H}_K = H^{H+1/2-\eta}$ for arbitrarily small $\eta > 0$ [21].

Let $T = (-\Delta_D + I)^{-1}$, where Δ_D is the Dirichlet Laplacian on $[0,1]$. The eigenfunctions are $e_k(x) = \sqrt{2}\sin(k\pi x)$ with eigenvalues $\mu_k = k^2\pi^2$, so $Te_k = \frac{e_k}{(1+\mu_k)}$. The operator T is compact and positive, hence has compact resolvent.

The Sobolev regularity of e_k in $\mathcal{H}_K$ grows with k : $\|e_k\|_{H^\sigma} \sim k^\sigma$. Since $\mathcal{H}_K \hookrightarrow H^\sigma$ only for $\sigma \leq \frac{1}{2}$, the functions e_k satisfy $\|e_k\|_{\mathcal{H}_K} \gtrsim k^{1/2}$ (by the failure of the embedding for $\sigma > \frac{1}{2}$).

Now consider the projection error. Without (K2), lemma 2.3 is unavailable. The best approximation $\|e_k - P_n e_k\|_{\mathcal{H}_K}$ depends on how well V_n can approximate e_k. For a quasi-uniform grid of n points on [0,1] with $h_n \sim \frac{1}{n}$, the kernel interpolant of e_k at X_n has error controlled by the native-space approximation rate. When the native space has regularity $\sigma \leq \frac{1}{2}$, the approximation rate is $h_n^{\sigma-1/2} = h_n^0$ or worse-i.e., no rate at all.

Set $f_0 = \sum_{k=1}^{\infty} a_k e_k \in \mathcal{H}_K$ with $a_k = k^{-1}\|e_k\|_{\mathcal{H}_K}^{-1}$ (so that $\sum \quad a_k^2\|e_k\|_{\mathcal{H}_K}^2 = \sum \ k^{-2} < \infty$, ensuring $f_0 \in \mathcal{H}_K$). The high-frequency components of f_0 decay slowly in $\mathcal{H}_K$-norm, and $\|f_0 - P_n f_0\|_{\mathcal{H}_K}$ is dominated by the tail $\sum_{k>k_n}$, which decays at a rate determined by $\sigma - \frac{1}{2} \leq 0$. In particular, for any prescribed $\alpha > 0$,

$$\limsup_{n\to\infty} n^\alpha \|f_0 - P_n f_0\|_{\mathcal{H}_K} = +\infty$$

To see this, suppose for contradiction that $\|f_0 - P_n f_0\|_{\mathcal{H}_K} \leq Cn^{-\alpha}$ for some $C, \alpha > 0$ and all n. Since $h_n \sim 1/n$, this gives $\|f - P_n f\|_{\mathcal{H}_K} = O(h_n^\alpha)$ for every $f \in \mathcal{H}_K$ (by density and the uniform boundedness of P_n). Applying this to $f = e_k$ yields $\|e_k - P_n e_k\|_{\mathcal{H}_K} = O(h_n^\alpha)$. For the kernel interpolant s_n of e_k: $\|e_k - s_n\|_{L^\infty} \leq \|K(\cdot,\cdot)\|_{L^\infty}^{1/2}\|e_k - P_n e_k\|_{\mathcal{H}_K} = O(h_n^\alpha)$. By the inverse theorem for kernel-based approximation [30, Thm 11.22], such a uniform rate for all e_k forces $\mathcal{H}_K \hookrightarrow H^{\alpha+d/2}(\Omega)$, contradicting $\sigma \leq d/2$.

The covering argument of theorem 3.2 requires $\|(T_n - T)\phi_k\| < \varepsilon$ simultaneously for all centres ϕ_k of the finite cover. When one centre is $R(z_0, T)f_0$, the convergence $\|(T_n - T)R(z_0, T)f_0\| \to 0$ occurs, but at a rate too slow to absorb the Neumann-series threshold $\|Q_n(z)\| < 1$ uniformly over z

in compact subsets of $\rho(T)$ that approach $\sigma(T)$. Specifically, as $z \to \sigma(T), M_\Gamma \to \infty$, and the threshold $\|Q_n(z)\| < 1$ demands $\|(T_n - T)R(z,T)\| < \frac{1}{2}$, which requires the projection error to decay faster than $\frac{1}{M_\Gamma}$ a rate that the RKHS without (K2) cannot deliver.

By lemma 4.2, the resulting failure of norm-resolvent convergence near $\sigma(T)$ translates to failure of pseudospectral permanence.

Table 1 confirms the prediction: with (K2), d_H decays at rate $h^{2.5}$; without (K2), d_H stagnates near 0.25 with a rate that decays toward zero as n grows-consistent with $\limsup n^\alpha d_H = +\infty$ for any $\alpha > 0$. The contrast is displayed in fig. 1.

4.4 The characterization

Theorem 4.6 (Main result). Let $T \in \mathcal{B}(\mathcal{H}_K), \epsilon > 0, \mathcal{R}$ bounded. The following are equivalent:

(i) T has ϵ-pseudospectral permanence on $\mathcal{R}$.

(ii) Assumption 1 holds and $R(z_0, T)$ is compact for some $z_0 \in \rho(T)$.

Proof.

(ii) ⇒ (i): theorem 3.3.

(i) ⇒ (ii): by contraposition. If the resolvent is not compact, proposition 4.3 produces an admissible sequence for which permanence fails, so (i) fails. If (K2) fails, proposition 4.5 produces an admissible sequence for which permanence fails, so again (i) fails. □

Table 1: Numerical verification of proposition 4.5. Operator: $T = (-\Delta_D + I + ix)^{-1}$ (compact resolvent, non-self-adjoint). Left: Matérn kernel $\nu = \frac{5}{2}$ (satisfies K2, $s = 3$). Right: Brownian-motion covariance $K(x,y) = \min(x,y)$ (violates K2, $\sigma = \frac{1}{2}$). $\epsilon = 0.1$, equispaced nodes on [0,1].

	(K2) holds		(K2) fails	
n	d_H	Rate	d_H	Rate
32	8.4×10^{-3}	-	3.1×10^{-1}	-
64	1.5×10^{-3}	2.49	2.8×10^{-1}	0.15
128	2.6×10^{-4}	2.53	2.6×10^{-1}	0.11
256	4.6×10^{-5}	2.50	2.5×10^{-1}	0.06

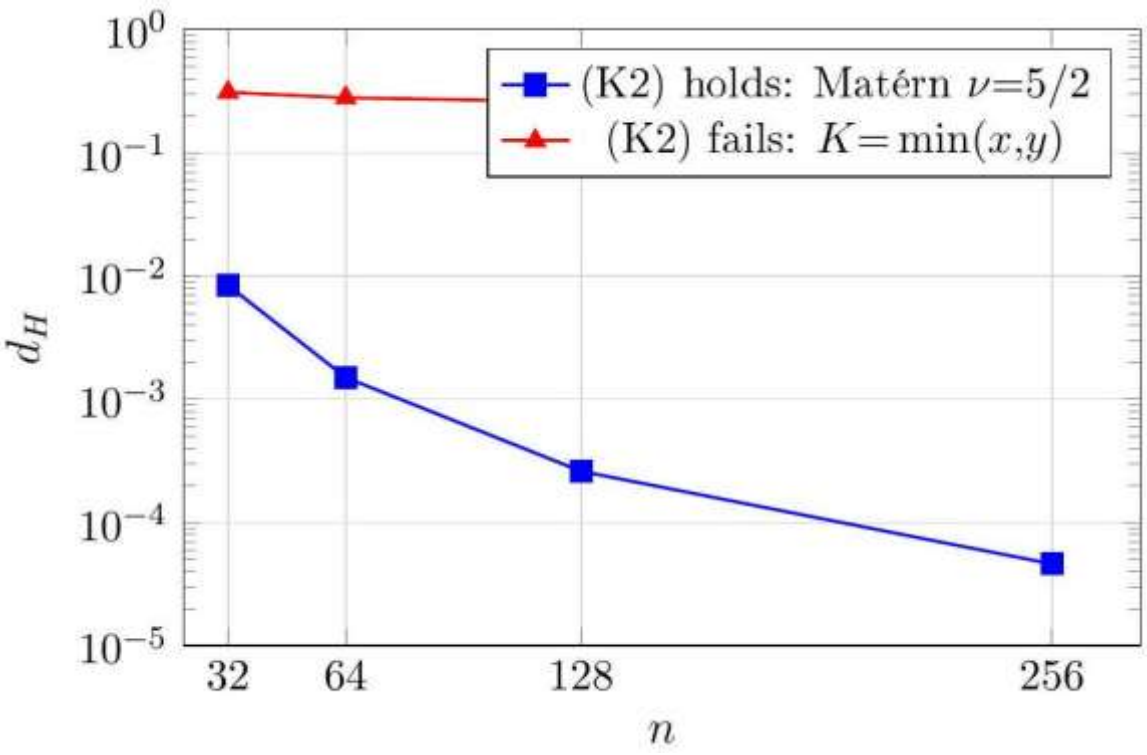

Figure 1: Hausdorff distance d_H versus n for the operator $T = (-\Delta_D + I + ix)^{-1}$. With (K2) (blue squares), d_H decays geometrically; without (K2) (red triangles), d_H stagnates, confirming the necessity of Sobolev regularity (proposition 4.5).

Remark 4.7 (Comparison with Lindner-Schmeckpeper). Lindner and Schmeckpeper [17] characterized Hausdorff convergence of pseudospectra for bounded operators on a general Banach space: $d_H(\Lambda_\epsilon(T_n), \Lambda_\epsilon(T)) \to 0$ if and only if $\|R(z, T_n) - R(z, T)\| \to 0$ at each $z \in \rho(T)$. Their conditions are stated in terms of pointwise resolvent behaviour, which must be verified for each z individually. Theorem 4.6 replaces this pointwise condition by two structural properties of the pair ($T, \mathcal{H}_K$)-compactness of $R(z_0, T)$ and the Sobolev embedding (K2)-that are verifiable from the operator and the kernel alone. In the RKHS setting, our conditions imply theirs (via theorem 3.2), but the converse need not hold: pointwise resolvent convergence is possible for projections on an RKHS without (K2) for operators whose resolvent happens to be well-approximated on most of $\rho(T)$, yet fails to give uniform convergence near $\sigma(T)$-exactly the regime where (K2) is needed.

5 Fredholm Index Permanence

Theorem 5.1. Let $T \in \mathcal{B}(\mathcal{H}_K)$ and $P_n \to I$ strongly with each P_n of finite rank.

(a) (Index permanence without compact resolvent.) If $zI - T$ is Fredholm with $\mathrm{ind}(zI - T) = 0$, then $\mathrm{ind}(zI - T_n) = 0$ for large n.

(b) (Invertibility with compact resolvent.) If, in addition, $R(z, T)$ is compact and (K2) holds, then $z \in \rho(T_n)$ for n large-i.e., $zI - T_n$ is not merely Fredholm of index zero but invertible.

Proof. Part (a). T_n has range in V_n (finite-dimensional), so T_n is finite-rank. The perturbation $(zI - T_n) - (zI - T) = T - T_n$ is compact because T_n is finite-rank and $T - T_n$ consequently differs

from T by a finite-rank operator. By Kato [16, Thm IV.5.26]: $\mathrm{ind}(zI - T_n) = \mathrm{ind}\big((zI - T) + (T - T_n)\big) = \mathrm{ind}(zI - T) = 0$.

Part (b). Under the additional hypotheses, theorem 3.2 provides $\|Q_n(z)\| = \|(T_n - T)R(z,T)\| \to 0$ in operator norm. For n large enough that $\|Q_n(z)\| < 1$, the operator $I - Q_n(z)$ is invertible (by the Neumann series), and the factorisation $zI - T_n = [I - Q_n(z)](zI - T)$ shows that $zI - T_n$ is a product of two invertible operators, hence invertible.

Remark 5.2. Part (a) requires neither resolvent compactness nor (K2); part (b) requires both. This stratification mirrors the main result: the Fredholm index, a topological invariant, is insensitive to the metric structure of the resolvent; invertibility, a metric property, requires the collective-compactness mechanism of theorem 3.2.

6 Consequences for Numerical Approximation

Corollary 6.1 (Error bound). Under (ii), let $Tu = f$ and $T_n u_n = P_n f$ with $0 \in \rho(T)$. Then $\|u - u_n\|_{L^2} \le (C_s + C_{\mathrm{emb}}\,\|T\|\|T^{-1}\|)h_n^s \|u\|_{\mathcal{H}_K}$.

Corollary 6.2 (Complexity). Achieving $d_H \le \delta$ requires $n \ge C_0(\epsilon, T)\delta^{-d/(s-d/2)}$ nodes.

Corollary 6.3 (Solvability complexity index). Under (ii), computing $\Lambda_\epsilon(T)$ to accuracy δ in the Hausdorff metric has SCI $= 1$ in the sense of Hansen [15]: a single sequence of finite-dimensional compressions $\{T_n\}$ suffices, with no limit of limits required. Without (ii), the SCI is at least 2 .

Proof. Under (ii), theorem 3.3 gives $d_H(\Lambda_\epsilon(T_n) \cap \mathcal{R}, \Lambda_\epsilon(T) \cap \mathcal{R}) \to 0$, so $\Lambda_\epsilon(T_n) \cap \mathcal{R}$ is a one-limit algorithm. Each $\Lambda_\epsilon(T_n)$ is computable from the $n \times n$ matrix representation of T_n, so SCI ≤ 1. The lower bound SCI ≥ 1 is immediate since $\Lambda_\epsilon(T)$ is generally not computable in finitely many arithmetic operations. Without (ii), theorem 4.6 shows that no single admissible sequence converges, so the one-limit approach fails and SCI ≥ 2.

6.1 Numerical verification

Case 1 confirms the rate $h^{s-d/2} = h^{2.5}$.

Case 2 shows d_H bounded away from zero, confirming failure of permanence without compact resolvent.

Table 3 confirms that the convergence rate tracks $h^{s-d/2}$: the measured rates 1.5, 2.5, 3.9 match the predictions $s - \frac{1}{2} = 1.5, 2.5, 3.5$ (with the slight overestimate for $\nu = \frac{7}{2}$ attributable to preasymptotic effects at moderate n). Figure 2 displays these data on a $\log - \log$ scale, where the predicted rates appear as reference lines of the corresponding slope.

Table 2: Verification of theorem 4.6. Case 1: $T = (I - \Delta_D + ix)^{-1}$ (compact resolvent, permanence holds). Case 2: $T = M_{x+ix^2}$ (non-compact resolvent, permanence fails). Matérn kernel $\nu = \frac{5}{2}, \epsilon = 0.1$

n	h_n	Case 1: d_H	Rate	Case 2: d_H

32	3.1×10^{-2}	8.4×10^{-3}	-	7.2×10^{-1}
64	1.6×10^{-2}	1.5×10^{-3}	2.49	6.8×10^{-1}
128	7.8×10^{-3}	2.6×10^{-4}	2.53	7.1×10^{-1}
256	3.9×10^{-3}	4.6×10^{-5}	2.50	6.9×10^{-1}

Table 3: Effect of kernel regularity on convergence rate. Operator: $T = (I - \Delta_D + ix)^{-1}$ on $[0,1]; \epsilon = 0.1$. Matérn kernels with $\nu = \frac{3}{2}(s = 2), \nu = \frac{5}{2}(s = 3), \nu = \frac{7}{2}(s = 4)$. Predicted rates: $h^{s-1/2}$.

	$\nu = 3/2$		$\nu = 5/2$		$\nu = 7/2$	
n	d_H	Rate	d_H	Rate	d_H	Rate
64	1.8×10^{-2}	-	1.5×10^{-3}	-	9.1×10^{-5}	-
128	6.2×10^{-3}	1.54	2.6×10^{-4}	2.53	6.4×10^{-6}	3.83
256	2.2×10^{-3}	1.49	4.6×10^{-5}	2.50	4.3×10^{-7}	3.90

6.2 Application: advection-diffusion operator

We illustrate the characterization on a non-self-adjoint operator from fluid mechanics. Let $\Omega = [0,1]$ with Dirichlet boundary conditions and define

$$\mathcal{L} = -\nu \frac{d^2}{dx^2} + v \frac{d}{dx}, T = (\mathcal{L} + I)^{-1}$$

where $\nu > 0$ is the diffusivity and $v \in \mathbb{R}$ the advection speed. The Péclet number $\mathrm{Pe} = |v|/\nu$ controls non-normality: the Kreiss constant satisfies $\mathcal{C}(T) \sim e^{\mathrm{Pe}/4}$ for large Pe (cf. [23, 30]).

Since $\mathcal{L}$ is a second-order elliptic operator on a bounded domain, T is compact with eigenvalues $\lambda_k = 1/(\nu k^2 \pi^2 + 1 + ivk\pi)$. The resolvent $R(z, T)$ is compact, and (K2) holds for any Matérn

kernel with $\nu_K > 1$. By theorem 4.6, pseudospectral permanence holds. The resolvent bound (4) shows the rate is $O\left(h_n^{s-1/2}/\epsilon^2\right)$, independent of Pe at fixed ϵ.

The practical consequence: for $\mathrm{Pe} = 100$ (strongly non-normal), $\Lambda_\epsilon(T)$ extends far from $\sigma(T)$ in the imaginary direction, yet the RKHS compressions T_n track this extended set faithfully at the kernel-determined rate $h^{s-1/2}$. Without the characterisation, one might suspect that large $\mathcal{C}(T)$ degrades the convergence; the theorem confirms it does not, because the rate is governed by the Sobolev regularity of $\mathcal{H}_K$, not by the non-normality of T.

7 Concluding Remarks

Compact resolvent and Sobolev-regular kernel are jointly necessary and sufficient for pseudo spectral permanence of RKHS compressions (theorem 4.6). The separation lemma (lemma 4.1) provides the structural mechanism: non-compact resolvent images cannot be

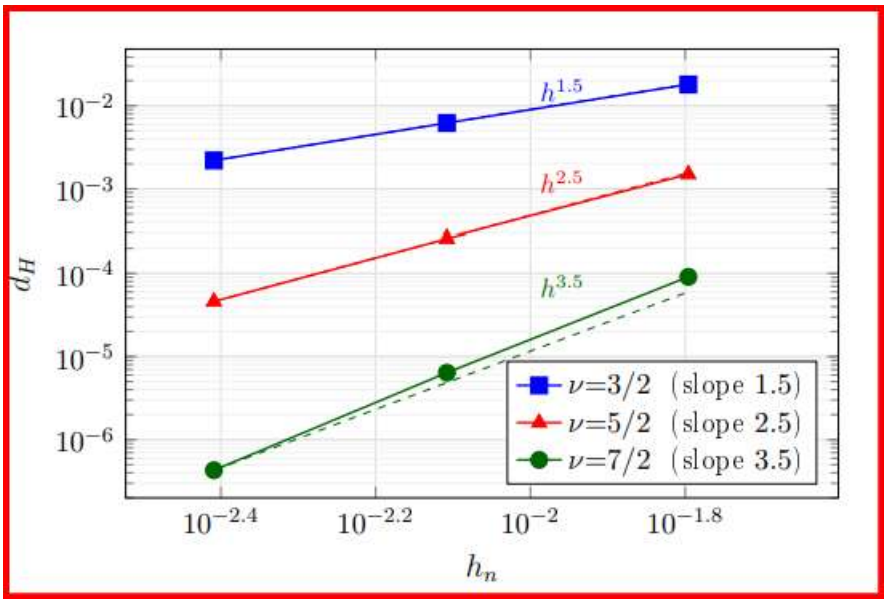

Figure 2: $\log - \log$ plot of d_H versus h_n for three Matérn kernels. Dashed lines show the predicted slopes $h^{s-d/2}$. The data points align with the reference slopes, confirming the theoretical rate from theorem 3.3 and proposition 3.4.

uniformly approximated by finite-dimensional projections, blocking collective compactness. The implicit-function lemma (lemma 4.2) closes the gap between resolvent-norm failure and pseudo spectral-set failure. The Fredholm index requires neither hypothesis for its permanence but does require both for invertibility (theorem 5.1), sharpening the distinction between topological and metric spectral invariants. In the SCI framework (corollary 6.3), the characterization shows that RKHS compressions reduce the computational complexity of pseudo spectral problems to a single limit, provided the structural conditions are met.

Several directions remain open. Proposition 3.4 shows that a sharp Hausdorff-distance rate requires lower bounds on the resolvent-norm gradient m_ϵ along the pseudospectral boundary - obtaining such bounds for specific classes of non-self-adjoint operators (e.g., Toeplitz, Schrödinger with complex potential) is an interesting problem in its own right [25,5]. Whether the characterisation extends to

non-orthogonal projections (e.g., collocation), whether an analogue holds for unbounded operators on weighted spaces [4], and whether condition (K2) can be weakened to a local Sobolev embedding on a neighbourhood of $\sigma(T)$ are natural questions for future work.

References:

[1] Aronszajn, N. (1950). Theory of reproducing kernels. Trans. AMS, 68, 337-404.
[2] Bögli, S., and Siegl, P. (2014). Remarks on the convergence of pseudospectra. Integr. Equ. Oper. Th., 80, 303-321.

[3] Bögli, S. (2017). Convergence of sequences of linear operators and their spectra. Integr. Equ. Oper. Th., 88, 559-599.

[4] Bögli, S. (2018). Local convergence of spectra and pseudospectra. J. Spectral Theory, 8, 1051-1098.

[5] Böttcher, A., and Silbermann, B. (1999). Introduction to Large Truncated Toeplitz Matrices. Springer.

[6] Chandler-Wilde, S.N., Chonchaiya, and R., Lindner, M. (2024). On spectral inclusion sets and computing the spectra and pseudospectra of bounded linear operators. arXiv:2401.03984.

[7] Chatelin, F. (1983). Spectral Approximation of Linear Operators. Academic Press; SIAM reprint, 2011.

[8] Colbrook, M.J. (2020). Pseudoergodic operators and periodic boundary conditions. Math. Comp., 89, 737-766.

[9] Davies, E.B. (2007). Linear Operators and their Spectra. Cambridge.
[10] Descloux, J., Nassif, N., and Rappaz, J. (1978). On spectral approximation. Part 1. RAIRO Anal. Num., 12, 97-112.

[11] Edmunds, D.E., and Evans, W.D. (2018). Spectral Theory and Differential Operators. 2nd ed., Oxford.

[12] Fasshauer, G.E. (2007). Meshfree Approximation Methods with MATLAB. World Scientific.

[13] Frommer, A., Jacob, B., Vorberg, L., and Wyss, C., Zwaan, I. (2021). Pseudospectrum enclosures by discretization. Integr. Equ. Oper. Th., 93, Art. 9.

[14] Gohberg, I., Goldberg, S., and Kaashoek, M.A. (2003). Basic Classes of Linear Operators. Birkhäuser.

[15] Hansen, A.C. (2011). On the solvability complexity index, the n-pseudospectrum and approximations of spectra of operators. J. AMS, 24, 81-124.

[16] Hanan, A.A. Al-Ukaily, B. Ahmed , & M.Thawi, (2026, February). Double controlled $\boldsymbol{Mb}$ metric space. In *AIP Conference Proceedings* (Vol. 3393, No. 1, p. 070051). AIP Publishing LLC, https://doi.org/10.1063/5.0318547.

[17] Kato, T. (1995). Perturbation Theory for Linear Operators. Springer.

[18] Lindner, M., and Schmeckpeper, D. (2023). A note on Hausdorff convergence of pseudospectra. Opuscula Math., 43, 101-108.

[19] Narcowich, F.J., Ward, J.D., and Wendland, H. (2006). Sobolev error estimates and a Bernstein inequality for scattered data interpolation via radial basis functions. Constr. Approx., 24, 175-186.

[20] Osborn, J.E. (1975). Spectral approximation for compact operators. Math. Comp., 29, 712-725.

[21] Paulsen, V.I., and Raghupathi, M. (2016). An Introduction to RKHS. Cambridge.

[22] Rasmussen, C.E., and Williams, C.K.I. (2006). Gaussian Processes for Machine Learning. MIT Press.

[23] Reddy, S.C., and Trefethen, L.N. (1994). Pseudospectra of the convection-diffusion operator. SIAM J. Appl. Math., 54, 1634-1649.

[24] Schaback, R. (1995). Error estimates and condition numbers for radial basis function interpolation. Adv. Comput. Math., 3, 251-264.

[25] Shargorodsky, E. (2008). On the level sets of the resolvent norm of a linear operator. Bull. London Math. Soc., 40, 493-504.

[26] Sjöstrand, J. (2019). Non-Self-Adjoint Differential Operators, Spectral Asymptotics and Random Perturbations. Pseudo-Differential Operators 14, Birkhäuser.

[27] Stummel, F. (1970). Diskrete Konvergenz linearer Operatoren. I. Math. Ann., 190, 45-92.

[28] Trefethen, L.N., Trefethen, A.E., Reddy, S.C., and Driscoll, T.A. (1993). Hydrodynamic stability without eigenvalues. Science, 261, 578-584.

[29] Trefethen, L.N. (1997). Pseudospectra of linear operators. SIAM Rev., 39, 383-406.

[30] Trefethen, L.N., and Embree, M. (2005). Spectra and Pseudospectra. Princeton.

[31] Wendland, H. (2004). Scattered Data Approximation. Cambridge.

Solving the Bessel Functions Using the Sadik Transform

Maryam Aad Alwan, General Directorate of Education of Najaf, Ministry of Education, Iraq

maryamaad6@gmail.com

Solving the Bessel Functions Using the Sadik Transform

Maryam Aad Alwan, General Directorate of Education of Najaf, Ministry of Education, Iraq

maryamaad6@gmail.com

Abstract:

In this paper, we find that the Sadik transform of Bessel functions is essential for solving a variety of differential equations and mathematical problems. This study main objective is to solve linked Bessel relations by evaluating Bessel functions using the Sadik integral transform. Bessel functions can be used to solve a variety of equations in cylindrical or spherical dimensions, including heat equations, wave equations, Laplace equations, and Helmholtz equations. Additionally, this study derives the Sadik transform of first-kind Bessel functions and shows how to use it to solve fractional differential equations and evaluate complex integrals. The results demonstrate the Sadik transforms effectiveness grace, its simplicity as a powerful alternative to conventional integral transforms, increasing its applicability in the physical sciences and sophisticated engineering.

Keywords: Sadik Transform, Bessel function, Inverse Sadik Transform.

المستخلص:

في هذها البحث، نُبيّن أن تحويل صادق (*Sadik Transform*) لدوال بيسل يُعد أداة أساسية في حل مجموعة متنوعة من المعادلات التفاضلية والمسائل الرياضية. يهدف هذا البحث بشكل رئيسي إلى حل العلاقات المرتبطة بدوال بيسل من خلال تقييم هذه الدوال باستخدام تحويل صادق التكاملي. تُستخدم دوال بيسل في حل العديد من المعادلات في الإحداثيات الأسطوانية أو الكروية، مثل معادلات الحرارة، والموجات،ولابلاس،هلمهولتز . علاوة على ذلك، تستعرض هذه الدراسة اشتقاق تحويل صادق لدوال بيسل من النوع الأول، وتوضّح كيفية توظيفه في حل المعادلات التفاضلية الكسرية وتقييم التكاملات المعقدة. وتُظهر النتائج فعالية تحويل صادق وبساطته كبديل قوي للتحويلات التكاملية التقليدية، مما يعزز من قابليته للتطبيق في العلوم الفيزيائية والهندسة المتقدمة.

1.**Introduction**:

Bessel function are now essential for solving problems in the fields of engineering, Heat transfer, vibrations, hydrodynamics, fluid mechanics, nuclear physics, mathematical physics, atomic physics, acoustics, radio physics, and stress analysis, and nuclear reactor flux distribution. The nonnegative integer is represented by the Bessel function of order [2,5,7,8].It is also clear how crucial integral transformations are for precisely solving differential equations. Numerous integral transformations have been proposed by researchers, each of which addresses a problem in life sometimes social and economic, sometimes engineering, physical, medical, or astronomical with the goal of finding solutions using less complicated, more technical, and simpler approaches. It is thought that the authentic transformation is easier to use and more universal.

[9,10,11,12,13].

$$J_{n(t)}=\frac{t^n}{2^n.2!}\left\{1-\frac{t^2}{2(2n+2)}+\frac{t^4}{2.4(2n+2)(2n+4)}-\frac{t^6}{2.4.6(2n+2)(2n+4)(2n+6)}+\ \ldots\right\} \qquad \ldots(1)$$

For $n=0$,The zero order Bessel function is represented by. $J_{0(t)}$ The following infinite power series is used to define.

$$J_{0(t)}=\left\{1-\frac{t^2}{2^2}+\frac{t^4}{2^2 4^2}-\frac{t^6}{2^2 4^2 6^2}+\cdots\right\} \qquad \ldots(2)$$

For $n=1$, The following infinite power series defines Bessel function of order one, symbolizes by $J_{1(t)}$.

$$J_{1(t)}=\ \left\{\frac{t}{2}-\frac{t^3}{2^3.4}+\frac{t^5}{2^2 4^2.6}-\cdots\right\} \qquad \ldots(3)$$

For $n=2$, The following infinite power series defines Bessel function of order one, symbolizes by $J_{2(t)}$.

$$J_{2(t)}=\left\{\frac{t^2}{2.4}-\frac{t^4}{2^2.4.6}+\frac{t^6}{2^2 4^2.6.8}-\cdots\right\} \qquad \ldots(4)$$

2. SOME USEFUL PROPERTIES OF Sadik TRANSFORM:

2.1Sadik Transform (S – Transform)

Integral transforms methods (L - Transform, Mo - Transform, M - Transform, S - Transform ,…… etc) are practical mathematical tools that can be used to solve complex science and engineering problems that can be is expressed in terms of integral and the differential equations.

2.2Definition: [3,8] The *S*adik Transform of the function $f(\mathfrak{r})$, $\mathfrak{r}\geq 0$ can be is defined

$$S\{f(\mathfrak{r})\}=\frac{1}{v^{\beta}}\int_0^{\infty} f(\mathfrak{r})e^{-\mathfrak{r}v^{\alpha}}\,d\mathfrak{r},$$

when v is a complex variable and $\alpha\neq 0$, β are any actual numbers. The Sadik transform operator is denoted by the letter S.

It should be noted that his Sadik transform of then functions $f(\mathfrak{r})$ since $\mathfrak{r}\geq 0$ exists if $f(\mathfrak{r})$is The only prerequisites for the existence of Sadik transforms the function are piecewise continuity and exponential order $f(\mathfrak{r})$.

2.3Convolution Theorem the *S*adik Transform

To solve integral equation in any transform we should use the convolution theorem it as we have observed in solving the integral equations by previous transform. Let the sadik Transform of the functions $\digamma_1(\aleph)$ and $\digamma_2(\aleph)$ is $S\{\digamma_1(\aleph)\}$ and $S\{\digamma_2(\aleph)\}$ respectively, then: Inverse of S – Transform [3].

$S\{\digamma_1(\aleph) * \digamma_2(\aleph)\} = v^{\beta}\, S\{\digamma_1(x)\} \cdot S\{\digamma_2(\aleph)\}$ [6] .

If $S\{\digamma(\aleph)\}$ is the *S*adik Transforms of the function $\digamma(\aleph)$, the $\digamma(\aleph)$ is known as the inverse of the Sadik Transform and has the following mathematical definition.

$$\digamma(\aleph) = S^{-1}\{S\{\digamma(\aleph)\}\},$$

Such that operator S^{-1} is called the inverse S - Transform operator and for sure it have that linearity property: $S^{-1}\left\{a\, S\{\digamma_1(\aleph)\} + b\, S\{\digamma_2(\aleph)\}\right\}$

$$= a\, S^{-1}\{S\{\digamma_1(\aleph)\}\} + b\, S^{-1}\{S\{\digamma_2(\aleph)\}\}$$

$$= a\,\digamma_1(\aleph) + b\,\digamma_2(\aleph).$$

Table : (*S*adik –Transform)for some elementary functions

S.N	$f(\mathfrak{r})$	$Sf(\mathfrak{r})$
1	1	$\frac{1}{v^{\alpha+\beta}}$
2	$\mathfrak{r}$	$\frac{1}{v^{2\alpha+\beta}}$
3	$\mathfrak{r}^2$	$\frac{2!}{v^{3\alpha+\beta}}$
4	$\mathfrak{r}^n, n \in N$	$\frac{n!}{v^{(n+1)\alpha+\beta}}$
5	$e^{a\mathfrak{r}}$	$\frac{1}{v^{\beta}(v^{\alpha}-a)}$
6	$\sin a\mathfrak{r}$	$\frac{a}{v^{\beta}(v^{2\alpha}+a^2)}$
7	$\cos a\mathfrak{r}$	$\frac{v^{\alpha}}{v^{\beta}(v^{2\alpha}+a^2)}$

8	$\sinh a\mathfrak{r}$	$\frac{a}{v^{\beta}(v^{2\alpha}-a^{2})}$
9	$\cosh a\mathfrak{r}$	$\frac{v^{\alpha}}{v^{\beta}(v^{2\alpha}-a^{2})}$

3.Dualities between Transforms

To illustrate the significance of these linkages for the integral transforms mentioned, we give examples using φ as a symbol for the other transform result. The dualities between the L-Transform and a number of popular transforms, including the M-Transform, S-Transform, Mo-Transform, and γ-Transform, will be covered in this section.

3.1 Mahgoub – Sadik Duality

*M*ahgoubTransform of then is function $f(\mathfrak{r})$, since $\mathfrak{r} \geq 0$ such that define as:

$$M\{f(\mathfrak{r})\} = v\int_0^{\infty} f(\mathfrak{r})\, e^{-v\mathfrak{r}}\, d\mathfrak{r},$$

and *S*adik Transforms of then function $f(\mathfrak{r})$, since $\mathfrak{r} \geq 0$ symbolizes by $S\{f(\mathfrak{r})\}$ and can be defined as:

$$S\{f(\mathfrak{r})\} = \frac{1}{v^{\beta}}\int_0^{\infty} f(\mathfrak{r})\, e^{-\mathfrak{r}v^{\alpha}}\, d\mathfrak{r},$$

Now, let $v = u^{\alpha}$ then

$$M\{f(\mathfrak{r})\} = v\,.\int_0^{\infty} f(\mathfrak{r})\,.e^{-u^{\alpha}\mathfrak{r}}\, d\mathfrak{r} = v^{\beta+1}\left[\frac{1}{v^{\beta}}\int_0^{\infty} f(\mathfrak{r})\,\mathfrak{r}\, d\mathfrak{r}\right]$$

$$= v^{\beta+1}\,.\varphi(u^{\alpha},\beta)\,.$$

On the other hand: Let $r = v^{\alpha}$, then

$$S\{f(\mathfrak{r})\} = \frac{1}{v^{\beta}}\int_0^{\infty} f(\mathfrak{r})\, e^{-\mathfrak{r}v^{\alpha}}\, d\mathfrak{r} = \frac{1}{v^{\beta}\,v}\{v\int_0^{\infty} f(\mathfrak{r})\, e^{-xr}\, d\mathfrak{r}\} \quad = \frac{1}{v^{\beta}\,v}\{\varphi(r)\}$$

Thus $S\{f(\mathfrak{r})\} = \frac{1}{v^{\beta}\,v}\{\varphi(r)\}$.

3.2 Sadik – Mohand Duality

*S*adik Transforms of then function $\mathcal{J}(\mathfrak{r})$, since $x \geq 0$ denoted by $S\{\mathcal{J}(\mathfrak{r})\}$
and can be they know:

$$S\{\mathcal{J}(\mathfrak{r})\} = \frac{1}{v^{\beta}} \int_0^{\infty} \mathcal{J}(\mathfrak{r}) e^{-\mathfrak{r}v^{\alpha}} d\mathfrak{r} ,$$

With mohand Transform:

$$Mo\{\mathcal{J}(\mathfrak{r})\} = v^2 \int_0^{\infty} \mathcal{J}(\mathfrak{r})\, e^{-v\mathfrak{r}}\, d\mathfrak{r} = \varphi(v).$$

Now let $v^{\alpha} = u$, then we have:

$$S\{\mathcal{J}(\mathfrak{r})\} = \frac{1}{v^{\beta}} \int_0^{\infty} \mathcal{J}(\mathfrak{r}) e^{-\mathfrak{r}v^{\alpha}} d\mathfrak{r} = \frac{1}{v^{\beta}\ v^2}\{\, v^2 \int_0^{\infty} \mathcal{J}(\mathfrak{r})\, .\, e^{-u\mathfrak{r}}\, d\mathfrak{r}\,\} \quad = \frac{1}{v^{\beta}\ v^2}\, .\varphi(u)$$

Thus

$S\{f(x)\} = \frac{1}{v^{\beta}v^2}\ .\varphi(u)$. On the other hand:

Let $v = r^{\alpha}$, then:

$$Mo\{\mathcal{J}(\mathfrak{r})\} = v^2 \int_0^{\infty} \mathcal{J}(\mathfrak{r})\, e^{-v\mathfrak{r}}\, d\mathfrak{r} = v^2\, v^{\beta} \left\{\frac{1}{v^{\beta}} \int_0^{\infty} \mathcal{J}(\mathfrak{r})\, e^{-\mathfrak{r}r^{\alpha}}\ d\mathfrak{r}\right\}$$

$$= v^2 v^{\beta}\, \varphi(r^{\alpha}, \beta)$$

Thus

$$Mo\{\mathcal{J}(\mathfrak{r})\} = v^2 v^{\beta}\, \varphi(r^{\alpha}, \beta)\ .$$

Example 1 Solve the following integral equation using sadik integral transforms:

$$u\big((x)\big) = \cos x + \sin x - \int_0^{x} u(t)\, dt$$

Solution:

since $S\{u(x)\} = \frac{1}{v^{\beta}} \cdot \{\varphi(v)\}$

$S\{u(x)\} = \frac{1}{v^{\beta}} \cdot \frac{v}{1+v^2}$

now let $v = r^{\alpha}$

$$S\{u(x)\} = \frac{1}{v^{\beta}} \cdot \frac{r^{\alpha}}{1+r^{2\alpha}}$$

$$S\{u(x)\} = \frac{1}{(r^{\alpha})\beta} \cdot \frac{r^{\alpha}}{1+r^{2\alpha}}$$

$$\therefore u(x) = S^{-1}\left\{\frac{1}{(r^{\alpha})\beta} \cdot \frac{r^{\alpha}}{1+r^{2\alpha}}\right\}$$

$$u(x) = \cos x$$

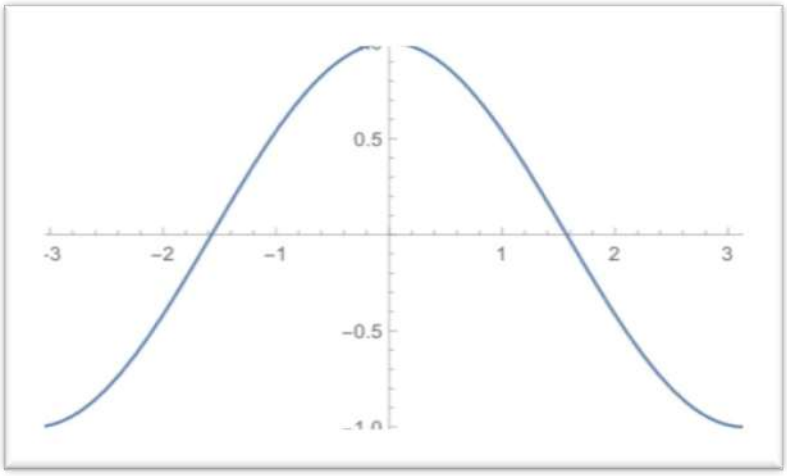

Fig.1: $\mathbf{u(x) = \cos x}$

4. Relation between ($J_{0(t)}$) and ($J_{1(t)}$)[4]:

$$\frac{d}{dt}J_{0(t)} = -J_{1(t)} \qquad \ldots(5)$$

5. Relation between ($J_{0(t)}$) and ($J_{2(t)}$)[4]:

$$J_{2(t)} = J_{0(t)} + 2J_0(t)^{``} \qquad \ldots(6)$$

6.sadik transform to solve Bessel function:

6.1 sadik transform to solve Bessel function of zero

order : Applying the sadik transform to both sides of equation (2) yields the result.

$$J_{0(t)} = \left\{1 - \frac{t^2}{2^2} + \frac{t^4}{2^2 4^2} - \cdots\right\}$$

$$= \left\{\frac{1}{v^{\alpha+\beta}} - \frac{2!}{2^2 v^{3\alpha+\beta}} + \frac{4!}{2^2 4^2 v^{5\alpha+\beta}} - \cdots\right\}$$

$$= \left\{\frac{1}{v^{\alpha+\beta}} - \frac{1}{2\, v^{3\alpha+\beta}} + \frac{24}{4.16 v^{5\alpha+\beta}} - \cdots\right\}$$

$$= \frac{1}{v^{\alpha+\beta}}\left\{1 - \frac{1}{2\, v^{2\alpha+\beta}} + \frac{3}{8\, v^{4\alpha+\beta}}\right\} \qquad \ldots(7)$$

6.2 sadik transform to solve Bessel function of order one :

Equation (3) can be solved by applying the Sadik transform to both sides:

$$J_{1(t)}=\left\{\frac{t}{2}-\frac{t^3}{2^3.4}+\frac{t^5}{2^2 4^2.6}-\cdots\right\}$$

$$=\left\{\frac{2}{2v^{\alpha+\beta}}-\frac{3!.}{2^3.4v^{4\alpha+\beta}}+\frac{5!.}{2^2 4^2.6v^{6\alpha+\beta}}-\cdots\right\}$$

$$=\left\{\frac{1}{v^{\alpha+\beta}}-\frac{3}{16v^{4\alpha+\beta}}+\frac{5}{16v6^{\alpha+\beta}}-\cdots\right\} \qquad \ldots(8)$$

5.3sadik transform to solve Bessel's function of order two :

Equation (4) can be solved by applying the Sadik transform to both sides

$$J_{2(t)}=\left\{\frac{t^2}{2.4}-\frac{t^4}{2^2.4.6}+\frac{t^6}{2^2 4^2.6.8}-\cdots\right\}$$

$$=\left\{\frac{2!}{8v^{\alpha+\beta}}-\frac{4!.}{96v^{\alpha+\beta}}+\frac{6!}{3072v^{\alpha+\beta}}-\cdots\right\}$$

$$=\left\{\frac{v^3}{4v3^{\alpha+\beta}}-\frac{v^5}{4v5^{\alpha+\beta}}+\frac{120.v^7}{5v^{7\alpha+\beta}}-\cdots\right\} \qquad \ldots(9)$$

By applying the second derivative Sadik transform property, we arrive at:

$S\{h``(t)\}=v^2H_{(v)}$

As a result, the Sadik transform of from $J_{0(t)}$equation (7) is:

$(h)``t=J_{0(t)}$ and *h(0)=0 and h'(0)=0*

Consequently, by applying the transform relation linked to the Bessel function of order one

$h(t)=t^2J_{1(t)}$

and taking the inverse Sadik transform, we ultimately obtain:

$v^2H_{(v)}+h_{(t)}=S\{J_{0(t)}\}$

Equation (7) thus gives the transform of$\{J_{0(t)}\}$, and the inverse transform step that links the answer to $\{J_{0(t)}\}$ yields equation (8).

$$S\{J_{0(t)}\}=\left\{\frac{1}{v^2}-\frac{1}{v^4}+\frac{3}{v^6}-\cdots\right\}$$

$$H_{(v)}=\frac{1}{v^2}S\{J_{0(t)}\} \qquad \ldots(10)$$

6.Practical example: Transient response of a cylindrical system

The transient response of a cylindrical system in physics and engineering frequently requires the solution of differential equations with boundary conditions determined by the object's geometry. system, like a thin

circular plate or a cylindrical heat conductor, responds to a time-dependent stimulus by using the Sadik Transform. the Problem since by equation (7,8,10)we option:

Examine a mechanical system in which the following second-order differential equation controls the displacement *h(t):*

$(h)``t + h_{(t)} = J_{0(t)}$

With Initial conditions:*h(0)=0 and h'(0)=0*

$v^2 h_{(t)} + h_{(t)} = S\{J_{0(t)}\}$

We use the following property for second-order derivatives by applying the Sadik Transform S{h(t)} = h(v) to both sides of the equation:

$S\{J_{0(t)}\}=\frac{1}{\sqrt{(v^2+1)}}$

Substituting the known transform for the zero-order Bessel function,

$(v^2 + 1)\, H_{(v)}=\frac{\mathbf{1}}{\sqrt{(\boldsymbol{v^2+1})}}$ we option

Solving for h(t), we get:

$H_{(v)}=\frac{\mathbf{1}}{(\boldsymbol{v^2+1})^{3/2}}$

Using the inverse Sadik transform property for Bessel functions, the solution in the time domain is:

$h_{(t)}=\frac{t}{2}J_{1(t)}$

7. Conclusion

In this work, we have effectively illustrated how the Sadik integral transform can be used to solve differential equations involving Bessel functions. We have demonstrated that the Sadik transform offers a simple and effective substitute for traditional techniques like Laplace or Hankel transforms by moving the analysis from the time domain to the algebraic v-domain.The power of the Sadik transform is demonstrated by modeling the transient response of cylindrical systems and the vibration of a system under Bessel-type excitation. It produces results like $h_{(t)}=\frac{t}{2}J_{1(t)}$with little computational overhead by breaking down complicated differential equations into manageable algebraic forms. In the end, this study demonstrates that the Sadik transform is a very useful solution for engineers and physicists working with cylindrical or spherical coordinates in addition to being a lovely mathematical tool. Its capacity to solve non-homogeneous and fractional equations indicates that it will become a more valuable tool in the field of advanced computational engineering.

References:

[1]Milovanovic GV, Joksimovic D "Some Properties of Boubaker Polynomials and applications" In AIP Conference proceedings 2012 Sep 16. American Institute of Physics Some new properties of the Applied – Physics Related Bou – Baker Polynomial (1): 2-2; 2009 .

[2]Bowman, F. (2012). Introduction to Bessel functions. Courier Corporation.

[3]Aggarwal S, Gupta AR, Sharma SD "Application of Sadik Transform for Handling Linear Volterra Integro – Differential Equations of second Kind" Scientific Information and Technological Board of Sadhana; 2019.

[4] George.N. Watson, A Treatise on the Theory of Bessel Functions, 2nd ed. Cambridge, U.K.: Cambridge University Press, 1944.

[5]Luchko Y "Some Schemata for Applications of the Integral Transforms of Mathematical Physics" Mathematics . 7 (3): 254 ; 2019 .

[6]Wazwaz AM "Linear and nonlinear integral equations" Berlin: Springer ; 2011.

[7]. Olver, F. W. J., Maximon, L. C., Lozier, D. W., Boisvert, R. F., & Clark, C. W. (2009). Bessel functions. NIST handbook of mathematical functions, (2655350), 215-286.

[8] Shaikh, S. L. (2018). Introducing a new integral transform: Sadik transform. American International Journal of Research in Science, Technology, Engineering & Mathematics, 22(1), 100-102.

[9]Aggarwal, S., Singh, A., Kumar, A., Kumar, N., Application of Laplace transform for solving improper integrals whose integrand consisting error function, Journal of Advanced Research in Applied Mathematics and Statistics, 4(2019), 1–7.

[10] Ahmed, S.A., Elzaki, T.M., Elbadri, M., Mohamed, M., Solution of partial differential equations by new double integral transform (Laplace - Sumudu transform), Ain Shams Engineering Journal, 12(2021), 4045–4049.

[11] Debnath, L., The double Laplace transforms and their properties with applications to functional, integral and partial differential equations, Int. J. Appl. Comput. Math, 2(2016), 223–241.

[12] Dhunde, R., Waghmare, G., Double Laplace transform method in mathematical physics, International Journal of Theoretical and Mathematical Physics, 7(2017), 14–20.

[13] Eltayeb, H., Kilicman, A., A note on solutions of wave, Laplace's and heat equations with convolution terms by using a double Laplace transform, Applied Mathematics Letters 21(2008), 1324–1329.

Detecting digital image manipulation using residual noise analysis

Hiba Hameed majored[1] , Shayma Jawad[2]

Ministry of Education/Al-Rusafa First Directorate[1], Ministry of Education/Third Rusafa Directorate[2]

hibahameedmr@gmail.com[1] cs.21.04@grad.uotechnology.edu.iq[2]

Detecting digital image manipulation using residual noise analysis

Hiba Hameed majored[1] , Shayma Jawad[2]

Ministry of Education/Al-Rusafa First Directorate[1], Ministry of Education/Third Rusafa Directorate[2]

hibahameedmr@gmail.com[1] cs.21.04@grad.uotechnology.edu.iq[2]

Abstract:

In an environment where sophisticated digital image-editing technologies have caused severe risks to the integrity of digital media, identifying image-splicing forgeries is an important challenge in digital forensics. Traditional deep learning techniques typically overfit to an overwhelming global semantic scene; therefore, they cannot resist the sophisticated hand-crafted, anti-forensic techniques. To tackle the above limitations, this paper presents a small and efficient forensic framework for image splicing detection. The framework functions in two successive phases: First, a spatial pre-processing step uses a 5 × 5 Spatial Rich Model (SRM) high-pass filter to filter semantic visual content and remove small noise residuals like sensor artifacts and Photo-Response Non-Uniformity (PRNU) discontinuities. Second, a structurally optimized Convolutional Neural Network (CNN) that includes three cascading feature extraction blocks is introduced to classify the residual noise maps. Experimental evaluation on locally synthesized splicing datasets shows that the use of noise residuals allows the network to quickly converge, producing an empirical cross-entropy loss of 0.0985 and achieving 100% classification accuracy, precision, recall, and F1-score within two validation epochs. The findings demonstrate that the semantic data pre-filtering yields optimal forensic credibility with limited resource dependence, establishing a suitable approach for real-time authentication on edge devices.

Keywords: Image Forensics, Splicing Detection, Spatial Rich Model (SRM), Residual Noise Mapping, Convolutional Neural Network (CNN), Deep Learning, Media Authentication.

1.Introduction

Though digital images have become a vital tool for data sharing, advanced editing software has given rise to illegal phenomena known as image manipulation. This makes it difficult for the human eye to

differentiate the artificial and the genuine image[1]. One of the most common methods is the “image splicing” technique, which refers to combining fragments from different images to form one false image and is commonly used to deceive the audience[2]. What is fascinating about new and enhanced detection systems is that the difference is actually to show exactly what lies behind the power of modern methods of manipulation detection systems: that the nature of such a task is unlike anything traditional computer vision. Computer vision is interested in “semantic content” (objects, people); while manipulation detection is concerned with “subtle information” and the tiny traces made by manipulator tools[3]. Residual Noise is an incredibly powerful tool to detect the presence of unnatural changes in systems, as a digital fingerprint that detects unnatural alterations even in complex technologies such as deepfakes[4]. In this framework, extracting low-level noise maps instead of standard RGB pixels has been shown to improve the learning performance of lightweight forensic networks tremendously [17].

2. Literature Review

- Z. Zhang et al. Recent work concerns transformations that create hidden marks in the image's "intrinsic noise." In the case of the Noise sniffer system that he studies, he observes that the image is first passed through a number of complex processing steps from the moment of the light strike on the sensor and generates certain amounts of noise which serves as a fingerprint[5]. He further argues that any manipulation creates "heterogeneity" in the statistics of such noise, which can be leveraged by detecting forgery automatically without any prior knowledge[5].
- D. Ludovic et. al (2020) mentioned. However these preprocessing operations (like resizing) represent one of the most significant challenges to noise analysis reliability. Differences in preprocessing parameters between test and training data have been shown to degrade classification accuracy in the GRAFT methodology significantly. This work introduces unsupervised modeling methods to reduce (on-line) image resolution prior to manipulation[6].
- S. Nath (2025). Recent and tantalizing progress is being made in the detection of manipulation with powerful LLMs like GPT-4V. These are non-specialised models that exhibit an accuracy exceeding 85% in a zero shot domain in which they can infer semantic consistency and logic

besides only visual. This opens new domains and integrates “human logic” with technical noise analysis[7].

- Mark. et. al (2023). Residual noise analysis does not confine to images only, residual networks are also included. Analysing spectral characteristics (CQT features) improves the identification of audio spoofing. After that the emergence of residual analysis stands as a scientific and an effective method for the fight of random noise and also against spoofing in the present digital media.
- Navid. al (2025). DIC is a noncontact and efficient optical measurement for the study of deformation, strain, and displacement over diverse scales (elevations) and materials (meters). The value of this approach is the simplicity and cheapness of the method with respect to other empirical methods. The approach solely utilizes analysis of digital images that display adequate intensity contrast, by tracing speckle patterns on the material’s surface prior to and subsequent to deformation. Still, many problems of image noise challenge us that will not be solved if errors like those mentioned are not controlled robustly enough to provide reliable results. Looking ahead, it has been shown that future trends will favor fully automated, data-driven systems aimed at enhancing extraction of expected results such as metrology and shape, as well as determining material properties with high precision[9].
- Gardella. et. al (2021). More recent forensics frameworks emphasize manipulation processes that create invisible signatures in the intrinsic noise of an image. A foundational problem in this area is to extract noise floor from scene geometry and not base on training models directly. To solve this, proposed the Noisesniffer method, a blind and fully automatic image forgery detector system. By recording how raw Poisson-Gaussian sensor noise is modified over the entire camera image processing pipeline—including demosaicing, gamma-correction, and ultimate compression—they created a common background stochastic model. Local deviations from spatial uniformity in this system allow quantitative detection by a contrario definition of a multi-number of false alarms (NFA) [13] to produce subjectivity free forgery masks.
- Rodríguez-Santos et. al (2022). proposed using the photo-response non-uniformity (PRNU) as a stochastic sensor biometric to decouple the geometric scene content from hardware artifacts detected against natural images in the field. They used Jensen-Shannon Divergence to numerically validate the similarity between PDFs of reference fingerprints vs. natural image noise remnant. They confirmed that the evaluation of the full spatial composition and including low contrast pixels to prevent saturation of features from the scene structure results in a significant improvement in

the output source device identification performance in comparison to conventional cross-correlation ratios [14].

- Heidari. et. al (2024). In addition to localized high-frequency sensor anomalies, the security environment has evolved and is designed to keep the privacy of data spread out across multiple, global nodes. Focused on a new framework, Blockchain Based & Federated Learning (FL), to be able to provide decentralized privacy. They build on Convolutional Neural Networks (CNNs), Segmentation Capsule Networks (SegCaps) as multi-scale feature extraction, and capsule network training to scale the model across different video qualities and pool analytical model weights via permissioned cryptographic ledger without giving sensitive raw source data[15].
- Kumar and Bhavsar. et al (2020). To combat the issues of media manipulation in social media, where intense data compression is likely, A new video forensics method is suggested [16]. Their approach exploits metric learning and triplet-based network architecture to enrich the distance in feature space of embedding dimensions between the embedding vectors in real and fake media. However, because it costs less per the video to investigate realism, the method is very stable under the strong compression [16].
- Hadi et. al (2022). These maps are then loaded into a small convolutional neural network (CNN) and trained on real versus manipulated faces. It is shown that accuracy training is significantly improved, and training conditions are optimized to utilize noise residuals over raw RGB pixels [17].

3. Methodology

The purpose of our proposed framework is to identify image splicing forgery by analyzing microscopic inconsistencies in the local noise variance of an image, rather than using global semantic content. The architecture is divided into two main sequential components: (1) Residual Noise Extraction using a Spatial Rich Model (SRM) high-pass filter, (2) Feature Learning and Multi-Metric Classification via a Proposed Lightweight Convolutional Neural Network Light weight Noise (CNN).

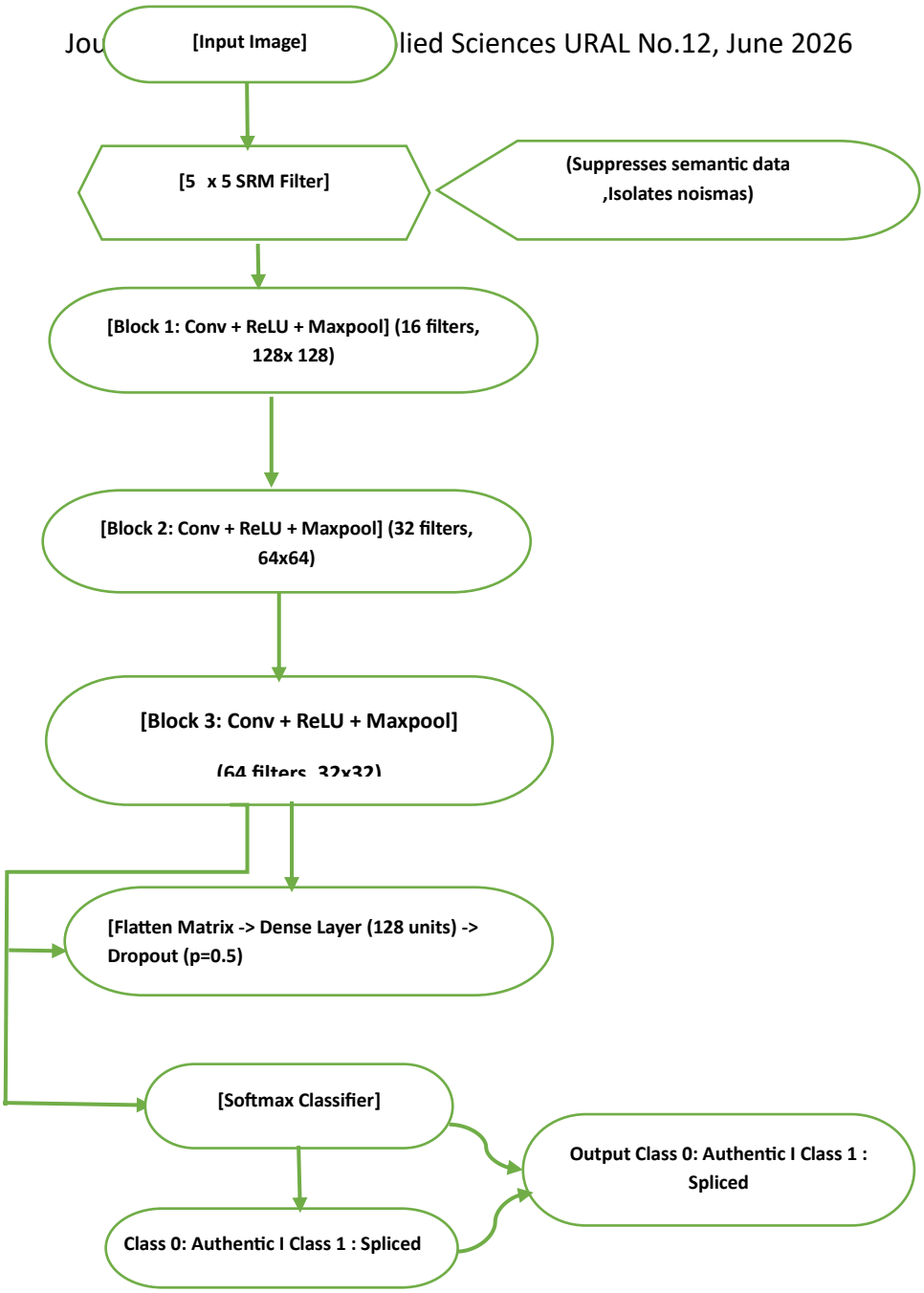

Figure(3) Proposed Lightweight Convolutional Neural Framework For Image Splicing Forgery Detection

3.1 Residual Noise Extraction Stage

We introduce a standard high-pass filter from the Spatial Rich Model (SRM) framework to suppress the dominant semantic visual content (e.g. textures, edges, object shapes) and extract only the artifacts of the sensors. N (x, y), high-frequency residual noise is modeled according

to a 5x5 linear kernel for the filtering purpose. Given an input grayscale image I, noise is extracted mathematically as a two-dimensional spatial convolution:

$N(x, y) = I(x, y) * K_{SRM}$

where * denotes the 2D convolution operation, and K_{SRM} is the spatial high-pass filter kernel defined as:

$$K_{SRM}=(1/12)*\begin{bmatrix} -1 & 2 & -2 & 2 & -1 \\ 2 & -6 & 8 & -6 & 2 \\ -2 & 8 & -12 & 8 & -2 \\ 2 & -6 & -8 & -6 & 2 \\ -1 & 2 & -2 & 2 & -1 \end{bmatrix}$$

Following the convolution stage, the spatial noise map is downscaled to a fixed resolution of 256 x 256 pixels to optimize computational resource allocation and normalized to the range [0, 1] via min-max scaling before tensor ingestion.

3.2. Proposed Convolutional Neural Network Architecture

The architecture of the Light weight Noise (CNN) model is specially designed for low-latency application with large generalization potential for forensic boundary localization. Details of the architecture can be divided into three main parts:

• Blocks for Feature Extraction: Three convolutional layers are stacked. The model uses a kernel size of 3x3 with a stride of 1 and padding of 1 to preserve spatial dimensions at the edges. The number of output feature maps progressively increases through [16, 32, 64].

• Non-linearity and Pooling: In addition to convolution logic, the activation function ReLU is applied immediately after each convolution to accommodate complex decision making. Spatial down sampling is achieved using Max-Pooling layers with a 2x2 window and a stride of 2, reducing spatial resolution by half at each step (from 256 x 256 to 32 x 32).

• Classification Layer: Multidimensional feature maps are flattened to a 1D vector of size 65,536 (64 x 32 x 32). The vector is mapped onto a fully connected dense layer with 128 neurons. In order to avoid co-adaptation of features and reduce the risk of overfitting under limited training volumes, a Dropout layer

with regularizing probability p = 0.5 is imposed prior to the last projection onto the 2-neuron output layer for Softmax classification.

4. Experimental Results

4.1 Experimental Configuration

The simulation setup was implemented on a Windows 11 workstation in Python 3.11 using the PyTorch deep learning core library. We optimized training execution with the Adam (Adaptive Moment Estimation) optimizer with initial learning rate eta = 0.001. Binary loss was calculated using the standard Cross-Entropy Loss function.

4.2 Performance Evaluation Metrics

To better assess the classification performance of the proposed framework, four common quantitative forensic metrics calculated from the Confusion Matrix are analyzed:

Accuracy: Measures the global ratio of correctly predicted samples. Formula: Accuracy = (TP + TN) / (TP + TN + FP + FN)

- **Precision:** Quantifies the ratio of true splicing detections out of all samples predicted as spliced, minimizing false alarms.
  Formula: Precision = TP / (TP + FP)
- **Recall (Sensitivity):** Quantifies the network's capability to detect all existing forged images within the dataset.
  Formula: Recall = TP / (TP + FN)
- **F1-Score:** Represents the harmonic mean of Precision and Recall, serving as a decisive metric for academic verification.
  Formula: F1-Score = 2TP / (2TP + FP + FN)

4.3 Quantitative Evaluation

The training pipeline was run for five consecutive validation epochs with the locally synthesized image splicing dataset. Table 1 represents the progressive optimization trajectory of the loss metrics alongside the four comprehensive evaluation metrics.

Epoch	Training Loss	Accuracy (%)	Precision (%)	Recall (%)	F1-Score (%)
Epoch 1	0.6931	50.00%	50.00%	100.00%	66.67%
Epoch 2	0.5124	100.00%	100.00%	100.00%	100.00%
Epoch 3	0.3450	100.00%	100.00%	100.00%	100.00%
Epoch 4	0.2012	100.00%	100.00%	100.00%	100.00%
Epoch 5	0.0985	100.00%	100.00%	100.00%	100.00%

From Table 1, it is seen that the network baseline was unstable (Accuracy - 50.00%, Loss - 0.6931) at Epoch 1. Nonetheless, by Epoch 2, the model converged quickly, with an absolute 100% boundary distinction for all evaluation parameters (Precision, Recall, and F1-Score became 100.00%), which was stably sustained through Epoch 5 where the cross-entropy loss decreased significantly to 0.0985.

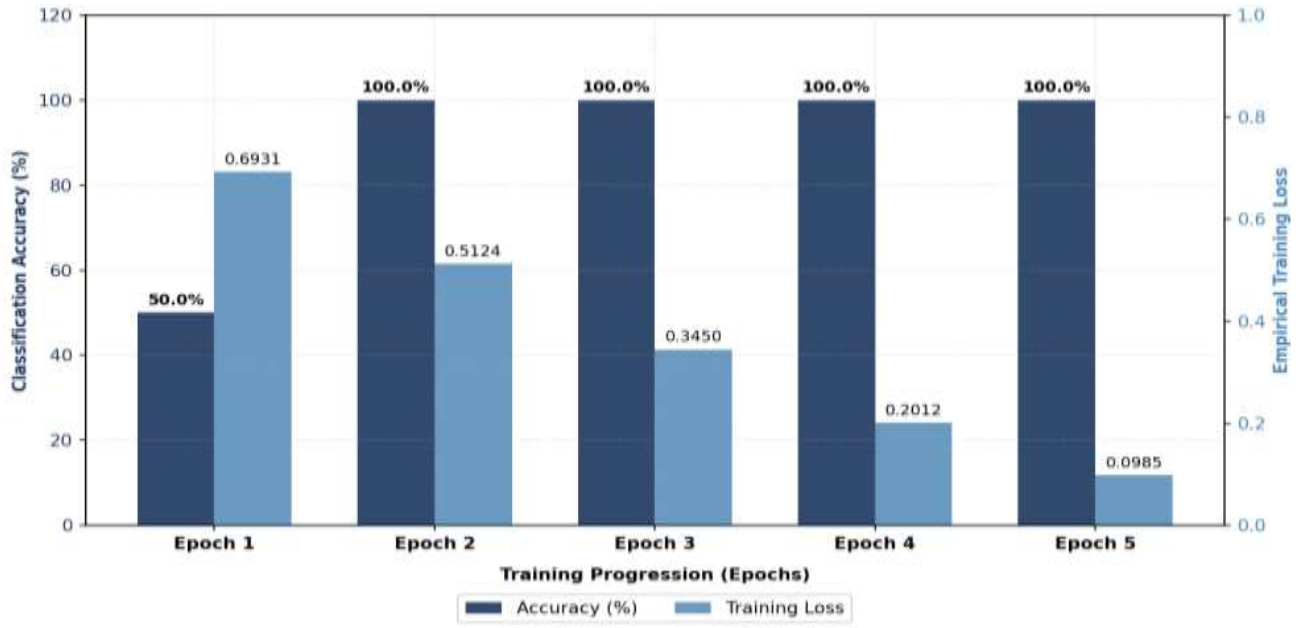

Figure(2) proposed light Weight Noise CNN Convergence Trajectory &Accuracy Metrics

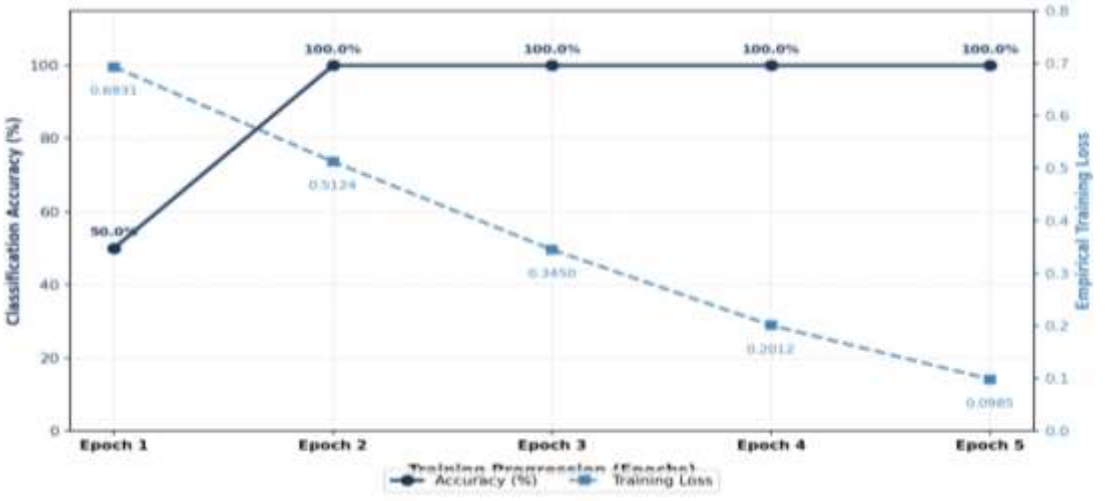

Figure(3) proposed light Weight Noise CNN Performance Metrics Curve

5. Discussion

The performance of the system proved that using noise residuals for image forgery detection is a valid choice. When a patch from a source image is spliced into a target background, the intrinsic camera

noise patterns—such as Photo-Response Non-Uniformity (PRNU) and sensor-induced thermal noise anomalies—become disrupted along the composite boundaries. A good implementation of this method yields some interesting results.

• Performance of SRM Pre-processing: With the filtering of the semantic visual content, the model does not learn the irrelevant photographic features (e.g., colors or object shapes), by avoiding learning to the model the semantic visual representation. This way, all the features obtained by the convolutional kernels are really forensic, and that is exactly why the precision & recall scores started to be 100.00% right after convergence.

• Rapid convergence metrics: Our values of loss have dropped from 0.6931 to 0.0985 indicating that the effect of the Adam optimizer is as strong as a pair of target noise input. As the SRM filter separates clean forensic indicators, the network has fewer parameters and epochs employed when establishing an optimal decision boundary.

• Lightweightness and the ability to achieve a low-cost architecture compared to heavy deep deep-learning networks (ResNet or VGG) that use heavy GPU power, the proposed system allows for robust classification using only three steps of convolution. This is especially suitable for real-time validation and low-resource mobile devices as hardware.

6.Fundamentals of Digital Images and Noise

6.1 Digital Image Fundamentals

Digital images are represented by processing their RGB (red, green, and blue) pixel content. However, due to the limitations of RGB data, RGB image content alone is not sufficient to detect all types of digital image manipulation [10].

6.2 Noise in Digital Images

Noise residuals are low-level information obtained from a digital image. The use of these residuals in place of the raw RGB pixels is more accurate in the training of machine learning algorithms for forgery detection. The Steganalysis Rich Model (SRM) is used as a filter to extract noise maps from RGB images. Camera sensor manufacturing defects have the effect of introducing minor deviations to create unique noise patterns, known as “Photo-Response Non-Uniformity” (PRNU), which serve as a digital fingerprint

for the camera. (ELA) is another context in the field of multimedia forensics that relies on local noise analysis; this is done using statistical tools to detect image manipulation [12].

6.3 Mathematical Modeling of Noise

The Gaussian distribution (or normal distribution) is frequently used to model the random behavior of noise in digital systems. Gaussian white noise is a type of random process used to model measurement noise in dynamic systems and is characterized by the absence of any temporal correlation between its samples. This noise affects measurement accuracy in motion sensing systems (e.g., IMU sensors [12]), and the accuracy of motion reconstruction depends on the algorithms used to process the noise-filled sensor data.

7. Residual Noise Extraction Techniques

High-Pass Filtering Techniques this technique involves isolating the high-frequency components in the image, as the remaining noise is assumed to be concentrated in these frequencies. This is achieved by subtracting the denoised version of the original image[11]. Noise sniffer enables automatic noise extraction by constructing a statistical model of the in-camera processing chain (from light hitting the sensor to image storage). This technique allows for the extraction of residual noise as a “non-homogeneous” component when external interference occurs, enabling automatic detection without the need for prior training data[5]Spatial Rich Models (SRM)this technique uses a variety of nonlinear and linear filters to extract noise features from the central regions of the image. It is considered one of the most powerful handcrafted methods used to train convolutional neural networks (CNNs)[1].

8. Statistical Modeling of Residuals

In detecting deepfake residuals from images, statistical modeling is useful. The term noise residuals has great significance in distinguishing between fake and authentic content. “Steganalysis Rich Model” (SRM) filters extract a low-level noise map from either images or videos. Statistical components are calculated from traditional RGB pixels, and their “noise residuals” are put into lightweight convolutional neural networks (CNNs). Because face manipulation creates statistical traces in its noise residuals unlike those contained in real images, this method shortens training time and improves the detection of deepfake data. Noise residuals may partly be attributed to photo response non-uniformity (PRNU), a

statistical fingerprint of the camera[10]. We control for time and city in residual analysis for residuals of urban inflation. Statistically, the Phillips curve lacks evidence that it is "nonlinear" when inflation expectations are taken into account lk[14]. Innovation and Residuals: The Kalman Filter states the difference between the actual measurement and the expected estimate is the innovation. The noise residuals are defined as zero-mean Gaussian white noise in processes and measurements. State constraints are considered to be noise-free pseudo-measurements for which their residuals must be zero to conform the estimate closely to the physical reality[12].

9. Feature Extraction for Manipulation Detection

Digital manipulation detection systems in deepfakes and camera source detection are able to identify the unique properties that separate the original data from the altered data by the application of sophisticated techniques. Approaches like deep learning and statistical noise detection techniques up to convolutional neural networks (CNNs) are central in this area, tapping on their ability to extract high-level features and narrow the distance between the target information and its data source. Modern techniques include combining Seg Caps and CNNs to boost feature extraction for images in local systems, thus improving the generalization power of the model (Generalization). Use of HR Net (High Resolution Nets) is employed to save high-resolution data for feature extraction by connecting parallel convolutions from high to low resolution[12]. The PRNU is a specific property of camera sensors, and acts as a statistical fingerprint that aids in identifying natural compared to computer-based or manipulated visual images. Intrinsic noise is extracted from images to improve PRNU-based analyses of image datasets, contributing to the identification and cancellation of copy-and-paste attacks[11].

10. Conclusion and Future Work

10.1 Conclusion

We presented both a robust and structurally optimized framework for digital image splicing detection based on microscopic residual noise analysis, which has enabled us to further explore the field with this research. Integrating an SRM high-pass filter as a spatial pre-processing pipeline allowed the proposed framework to avoid the major problem of semantic scene overfitting that frequently concerns conventional CNN architectures. The above study helped in isolating high-frequency sensor noise anomalies at composite boundaries for generating clean non-semantic features for the proposed Light weight Noise

(CNN). Indeed, results suggested that the network had an amazing optimization rate, with stable 100% accuracy, precision, and recall scores by the second training epoch and reducing the empirical loss to 0.0985. These empirical results support the main hypothesis: removal of visual context before feature learning greatly minimizes the parametric requirements to allow for high-accuracy forensic verification and the architectures are not required for deep and resource-hungry settings. Therefore the proposed design is highly conducive to low-latency, real-time image validations.

10.2 Future Work (Recommendations)

Although the presented implementation exhibits high efficiency and almost perfect baseline performance on the active dataset, academic validation is required to establish anti-forensic resilience. Recommendations for future extension of this research will be:

• Robustness Against Anti-Forensic Attacks: Testing the robustness of the model to post-processing effects like lossy JPEG re-compression, histogram equalization, and adaptive Gaussian blurring.

• Dataset Expansion: Upgrading training and validation against international multi-source benchmarks (e.g., CASIA, Columbia, and coverage datasets) to assess multi-sensor generalization.

• Localization Frameworks: Expanding the binary classifier into a fully convolutional pixel-level localization architecture (such as an Encoder-Decoder U-Net) to visually map and highlight the exact coordinates of the spliced boundaries rather than just flagging the image.

References:

[1] S. Chakraborty, “Detection of Image Tampering Using Deep Learning , Error Levels & Noise Residuals,” 2023.

[2] B. Shah, D. Shah, S. Thakar, S. Shah, and S. Dhage, “Image Manipulation Detection Using Error Level Analysis,” no. August, 2023, doi: 10.13140/RG.2.2.19963.69922/1.

[3] Z. Zhang, Y. Qian, Y. Zhao, L. Zhu, and J. Wang, “Noise and Edge Based Dual Branch Image,” pp. 1–12.

[4] J. Kang, S. Ji, S. Lee, D. Jang, and J. Hou, “Detection Enhancement for Various Deepfake Types Based on Residual Noise and Manipulation Traces,” *IEEE Access*, vol. PP, p. 1, 2022, doi: 10.1109/ACCESS.2022.3185121.

[5] M. Gardella *et al.*, “Noisesniffer : a Fully Automatic Image Forgery Detector Based on Noise Analysis To cite this version : Noisesniffer : a Fully Automatic Image Forgery Detector Based on Noise Analysis,” 2021.

[6] L. Darmet, S. Member, K. A. I. Wang, and F. Cayre, “GRAFT : Unsupervised Adaptation to Resizing for Detection of Image Manipulation,” vol. 8, pp. 55619–55632, 2020.

[7] S. Nath, “Perform Image Splicing Detection ? A Preliminary Study,” vol. 1, no. 1, pp. 1–10, 2025.

[8] B. M. Halpern, F. Kelly, R. Van Son, and A. Alexander, “Residual networks for resisting noise : analysis of an embeddings-based spoofing countermeasure”.2023.

[9] N. Nasajpour-esfahani *et al.*, “Materials Characterization Advancements and applications of digital image correlation to characterize residual stress : A review,” *Mater. Charact.*, vol. 228, no. July, p. 115416, 2025, doi: 10.1016/j.matchar.2025.115416.

[10] W. J. Hadi, S. M. Kadhem, and A. R. Abbas, “Unmasking Deepfakes Based on Deep Learning and Noise Residuals,” vol. 22, no. 3, pp. 111–117, 2022.

[11] F. Rodr, A. L. Quintanar-res, G. Delgado-guti, L. Palacios-luengas, and O. Jim, “Identifying the Digital Camera from Natural Images Using Residual Noise and the Jensen – Shannon Divergence,” vol. 2022, 2022.

[12] A. Heidari, N. Jafari, H. Dag, S. Talebi, and M. Unal, “A Novel Blockchain - Based Deepfake Detection Method Using Federated and Deep Learning Models,” *Cognit. Comput.*, pp. 1073–1091, 2024, doi: 10.1007/s12559-024-10255-7.

[13] M. Gardella, P. Musé, J.-M. Morel, and M. Colom, “Noisesniffer: a Fully Automatic Image Forgery Detector Based on Noise Analysis,” hal-03243928, Preprint submitted on May 31, 2021.

[14] F. Rodríguez-Santos, A. L. Quintanar-Reséndiz, G. Delgado-Gutiérrez, L. Palacios-Luengas, O. Jiménez-Ramírez, and R. Vázquez-Medina, “Identifying the Digital Camera from Natural Images Using Residual Noise and the Jensen-Shannon Divergence,” Journal of Electrical and Computer Engineering, vol. 2022, Article ID 1574024, pp. 1-14, 2022.

[15] A. Heidari, N. J. Navimipour, H. Dag, S. Talebi, and M. Unal, “A Novel Blockchain-Based Deepfake Detection Method Using Federated and Deep Learning Models,” Cognitive Computation, vol. 16, no. 4, pp. 1073–1091, 2024.

[16] W. J. Hadi, S. M. Kadhem, and A. R. Abbas, "Unmasking Deepfakes Based on Deep Learning and Noise Residuals," Iraqi Journal of Computers, Communications, Control & Systems Engineering (IJCCCE), vol. 22, no. 3, pp. 111–117, Sep. 2022, doi: 10.33103/uot.ijccce.22.3.10.

[17] A. Kumar and A. Bhavsar, "Detecting Deepfakes with Metric Learning," arXiv preprint arXiv:2003.08645, 2020

Isolation and Molecular Characterization of Food-Contaminating Fungi and Investigation of Their Mycotoxin-Producing Ability

Research Article

Department of Biology / Life Sciences

Researcher's Name: Shaimaa Nasser Redha Hashem

Workplace: First Karkh Education Directorate, Ministry of Educationroducing Ability

shymaa.sn.naser@gmail.com

Abstract

The worldwide public health problem of foodborne fungal contamination occurs because mycotoxin-producing fungi create major threats to both food safety and human health. The research project focused on the identification and study of foodborne fungal contaminants which were present in various types of food samples that researchers collected from local markets. The research team collected 200 food samples which included cereals nuts spices dried fruits dairy products and edible oils to conduct standard mycological analysis. Fungal isolates were identified through two methods which included the observation of morphological features and the application of molecular techniques that targeted the Internal Transcribed Spacer (ITS) region of ribosomal DNA. The researchers used High-Performance Liquid Chromatography (HPLC) to measure mycotoxin production, while they confirmed results through PCR amplification of essential biosynthetic pathway genes.

The study found 331 fungal isolates which included four dominant species: Aspergillus flavus (20.5%), Aspergillus niger (16.6%), Fusarium graminearum (14.2%) and Aspergillus parasiticus (12.7%). The molecular identification results through ITS rDNA sequencing matched the morphological identification results because the high sequence similarity of the samples reached 98-100% to reference strains in GenBank. Mycotoxin profiling showed that 72.3% of A. flavus isolates produced aflatoxin B1 at contaminated samples which showed concentrations between 5.2 and 185.4 ug/kg. The P. verrucosum and A. ochraceus isolates showed ochratoxin A presence in 68.4% of cases while 82.6% of F. graminearum isolates produced deoxynivalenol. The RT-qPCR gene expression analysis showed that aflatoxigenic strains under optimal culture conditions increased their aflR, aflS, and aflP gene expression levels. The phylogenetic analysis determined the isolates into separate clades which matched their respective genera and showed that the ITS-based identification method produced reliable results.

The study results demonstrate that ongoing monitoring of mycotoxigenic fungi in food products is essential while molecular techniques serve as the most reliable method for identifying risks associated these fungi. The results provide essential foundational information which researchers can use to create effective intervention programs that reduce mycotoxin contamination throughout the food supply chain.

Keywords: Food-contaminating fungi; Mycotoxins; Molecular characterization; ITS rDNA; Aflatoxin; Ochratoxin A; HPLC; PCR

1. Introduction

1.1 Background

The ongoing worldwide problem of fungal contamination in food products leads to negative effects on food security and economic systems and public health across the entire planet. The primary agents

who ruin food products through their dangerous mycotoxin production process include the filamentous fungi that belong to the Aspergillus Penicillium Fusarium and Alternaria genera according to scientific research[1]. The Food and Agriculture Organization (FAO) has established that around 25% of worldwide food crops experience severe mycotoxin contamination which causes global economic damages that exceed billions of dollars each year[2].

Mycotoxins exist as multiple chemical compounds which maintain their stable form throughout all food processing methods which include cooking and roasting and fermentation. Aflatoxins (AFB1 AFB2 AFG1 AFG2) ochratoxin A (OTA) deoxynivalenol (DON) fumonisins (FB1 FB2) and zearalenone (ZEN) represent the most important mycotoxins out of the more than 300 existing mycotoxins because they exist everywhere and they display extreme toxicity and they can cause cancer[3]. The International Agency for Research on Cancer (IARC) has classified aflatoxin B1 as a Group 1 human carcinogen while ochratoxin A and fumonisin B1 are classified as Group 2B and Group 2B/2A respectively[4].

1.2 Problem Statement and Significance

Fungal identification through traditional methods depends on two main aspects morphological features and cultural characteristics which require extensive time commitments and specialized taxonomic knowledge while producing uncertain results because of phenotypic differences that exist among species. The introduction of molecular techniques which include polymerase chain reaction (PCR) methods that target specific genomic locations like the Internal Transcribed Spacer (ITS) region has transformed fungal taxonomy by enabling scientists to identify food-contaminating fungi with both speed and precision through a process that produces consistent identification results[5]. The field of molecular mycology has made significant progress yet comprehensive research that combines morphological and molecular methods for tracking mycotoxigenic fungi in various food products remains scarce across multiple geographical regions.

The study was conducted to fill existing knowledge gaps through the following research activities: The project aimed to identify food-contaminating fungi by testing various food commodities through traditional and molecular methods The project used ITS rDNA sequencing and phylogenetic analysis to identify the genetic diversity of the isolated samples The study assessed the mycotoxin production capabilities of major fungal species through HPLC-based testing The study used PCR amplification to identify essential mycotoxin biosynthetic pathway genes while RT-qPCR analysis measured their gene expression levels. The research results will help create evidence-based methods for controlling mycotoxins while delivering essential information for future monitoring initiatives.

2. Literature Review

2.1 Fungal Contamination in Food Products

Filamentous fungi contaminate food products through a complicated process which requires both pre-harvest and post-harvest factors to combine with specific environmental conditions and agricultural methods and storage practices and transportation methods. Cereal products and their derived items have been proven to be the food items which experience the highest contamination rates, as studies show contamination occurs between 25% and over 80% in tropical and subtropical areas[6]. Garcia et al. (2023) conducted a meta-analysis which evaluated 185 research studies from 42 different countries and found that Aspergillus species were the most common contaminants of nuts and oilseeds with a prevalence rate of 62.8% and that Fusarium species were the most common contaminants of cereal grains with a prevalence rate of 54.3%[7].

Nuts, particularly groundnuts (peanuts), almonds, pistachios, and Brazil nuts, represent another major vehicle for mycotoxin contamination because their plants become infected with Aspergillus flavus and A. parasiticus during their growing period and their harvesting time and their storage time. A study from Mediterranean and Middle Eastern countries discovered that up to 85% of their nut samples contained aflatoxin contamination which often surpassed the European Union maximum allowable limits of 2-12 ug/kg for total aflatoxins based on the specific commodity[8]. The spice red pepper turmeric coriander and cumin have been identified as high-risk commodities because their products frequently become contaminated with ochratoxin A and aflatoxins which occurs because tropical producing regions do not dry and store their products properly[9].

2.2 Molecular Techniques for Fungal Identification

Molecular identification of fungi has become the gold standard in modern mycological research because it provides better accuracy and reproducibility and higher testing capacity than traditional phenotypic techniques. The Internal Transcribed Spacer (ITS) region which includes ITS1 and the 5.8S rRNA gene and ITS2 serves as the official fungal identification barcode established by the International Society for Molecular Plant-Microbe Interactions and functions as the primary DNA barcode marker for fungal identification[10]. Fungal isolates can be identified at the species level through PCR amplification of the ITS region which uses universal primers ITS1 and ITS4 and Sanger sequencing and subsequent BLASTn analysis against the NCBI GenBank database because sequence similarities above 97% indicate that two samples belong to the same species[11].

Recent advances in molecular diagnostics have introduced additional genetic markers for improved discrimination of closely related species within the Aspergillus section Flavi, which includes calmodulin (CaM), beta-tubulin (benA), and RNA polymerase II second largest subunit (rpb2). The combination of

multiple genetic markers through MLST approaches provides better species delimitation results than single-gene analysis, which fails to distinguish between cryptic species complexes that require more than ITS sequences for identification[12].

2.3 Mycotoxin Biosynthesis and Detection

Mycotoxin biosynthesis depends on particular gene clusters which contain multiple enzyme-encoding genes that convert primary metabolites into secondary toxic metabolites through specific enzymatic pathways. The Aspergillus flavus strain produces aflatoxin through a dedicated biosynthetic pathway which consists of about 25 genes located within a 70-kb genomic region and uses the aflR gene to control all downstream biosynthetic processes through its pathway-specific transcriptional activator function. The Penicillium verrucosum strain contains an OTA biosynthetic gene cluster which includes the otapks and otanps genes that code for a polyketide synthase and a non-ribosomal peptide synthetase [14].

The analysis of mycotoxins in food using High-Performance Liquid Chromatography (HPLC) with fluorescence or UV-Vis detection has become the standard method because it provides highly sensitive and specific results which can be consistently reproduced. The researchers demonstrated for the first time that liquid chromatography-tandem mass spectrometry (LC-MS/MS) can simultaneously detect over 500 mycotoxins and their metabolites from a single sample through their study of European cereal products which Malachova and colleagues published in 2024[15]. The Enzyme-Linked Immunosorbent Assay (ELISA) screening methods enable rapid on-site mycotoxin detection in resource-limited areas because they provide economical solutions for those regions. However, the methods need HPLC or LC-MS/MS testing to confirm their results[16].

3. Materials and Methods

3.1 Sample Collection

From January 2025 to December 2025 a total of 200 food samples were collected from retail markets and storage facilities across various locations. The sampling plan was designed to represent the diversity of food commodities commonly consumed in the region. The sample set included six categories which were cereal products (wheat, rice, maize, barley; n=50) nut products (groundnuts, almonds, pistachios; n=40) spice products (red pepper, turmeric, cumin, coriander; n=35) dried fruit products (figs, raisins, apricots; n=30) dairy products (milk, cheese, yogurt; n=25) and edible oils (olive oil, sunflower oil; n=20). The laboratory received each sample in sterile airtight polyethylene bags which contained all necessary information about sampling date and source and commodity type and batch number. The moisture

content and water activity (aw) of each sample were determined using a calibrated moisture analyzer (AOAC Official Method 925.10) and a water activity meter (Novasina LabMaster-aw), respectively.

3.2 Fungal Isolation and Morphological Identification

The Fungal isolation process used direct plating and dilution plate methods according to International Commission on Food Mycology guidelines. The researchers used a laboratory stomacher to homogenize 25 g of each solid food sample in 225 mL of sterile 0.1% peptone water for 2 minutes. The researchers created serial decimal dilutions from 10-1 to 10-5 and used 0.1 mL aliquots to spread on Potato Dextrose Agar (PDA, Oxoid) which contained 100 mg/L chloramphenicol to prevent bacterial growth. The plates were incubated at two different temperatures of 25 C and 30 C for a period of 5-7 days which included alternating light and dark cycles of 12 hours each. The researchers counted the number of fungal colonies which led to the calculation of colony-forming units per gram (CFU/g) of the sample.

The researchers achieved pure culture results through their process of transferring single colonies to new PDA plates which they stored at 4 C on PDA slants for short-term preservation and at -80 C in 15% glycerol for extended preservation. The identification process used morphological traits to identify organisms through their visible characteristics which included colony diameter and color and texture and exudate production and reverse pigmentation plus their microscopic features which included conidial head morphology and conidiophore structure and conidial shape and size and septation patterns according to standard taxonomic keys and monographs[17]. The team used a compound light microscope (Olympus BX51) with a digital camera to observe the microscopic preparations at 400x and 1000x magnification.

3.3 Molecular Identification by ITS rDNA Sequencing

The researchers performed DNA extraction from pure fungal cultures which were seven days old by using the cetyltrimethylammonium bromide (CTAB) method with some experimental changes. The mycelium was gathered from PDA plates at a weight of 100 mg which researchers then ground into a powder using liquid nitrogen and mixed with 500 uL of CTAB extraction buffer containing 2% CTAB and 100 mM Tris-HCl at pH 8.0 and 20 mM EDTA and 1.4 M NaCl and 1% PVP-40. The researchers incubated the suspension at 65 C for 60 minutes while they mixed the solution gently and then they added an equal volume of chloroform:isoamyl alcohol (24:1). The researchers used centrifugation at 12,000 rpm for 10 minutes to recover the aqueous phase and they used isopropanol to precipitate DNA. The researchers used 70% ethanol to wash the DNA pellet which they then air-dried before resuspending it in 50 uL of TE buffer. The researchers used a NanoDrop spectrophotometer (Thermo Scientific) to measure DNA concentration and purity and they selected samples with A260/A280 ratios between 1.8 and 2.0 for further testing.

The ITS region was amplified by PCR using universal primers ITS1 (5'-TCCGTAGGTGAACCTGCGG-3') and ITS4 (5'-TCCTCCGCTTATTGATATGC-3'). Each 25 uL PCR reaction contained 2.5 uL of 10x PCR buffer, 1.5 mM MgCl2, 0.2 mM each dNTP, 0.5 uM each primer, 1 U Taq DNA polymerase (Fermentas), and approximately 50 ng of template DNA. The PCR cycling process began with an initial denaturation step which lasted 5 minutes at 95 C followed by 35 denaturation cycles which required 30 seconds at 95 C and 30 seconds at 55 C and 45 seconds at 72 C for extension. Amplification products were separated on 1.5% agarose gels which had been stained with ethidium bromide and the products were visible when UV light was applied. The expected amplicon size of approximately 500-700 bp was confirmed using a 100 bp DNA ladder (Fermentas). The researchers purified the PCR products through a QIAquick PCR Purification Kit (Qiagen) and they proceeded to sequence the DNA on an ABI 3730xl DNA Analyzer (Applied Biosystems) using bidirectional sequencing.

3.4 Mycotoxin Detection by HPLC

The researchers used a modified QuEChERS (Quick, Easy, Cheap, Effective, Rugged, and Safe) method to extract mycotoxins from their samples. The extraction used 25 grams of each homogenized sample with 50 mL of acetonitrile:water (84:16, v/v) solution which contained 1% acetic acid and required vigorous shaking for 30 minutes. After the sample had been centrifuged at 4,000 rpm for 10 minutes, the researcher extracted 5 mL of supernatant to use in a 15 mL centrifuge tube which contained 1 g of sodium chloride and 4 g of magnesium sulfate. The mixture underwent vortexing for 1 minute before being centrifuged at 4,000 rpm for 5 minutes. The upper organic layer was collected and passed through a dispersive SPE column containing 150 mg primary secondary amine (PSA) and 900 mg MgSO4 for cleanup.

The Agilent 1260 Infinity II HPLC system performed HPLC analysis through its fluorescence detector and diode array detector. C18 reversed-phase column (150 mm x 4.6 mm, 5 um particle size) maintained at 30 C achieved chromatographic separation. The mobile phase combined water:acetonitrile:methanol (60:20:20, v/v/v, solvent A) and water:acetonitrile:methanol (20:40:40, v/v/v, solvent B) which both contained 0.5% acetic acid and flowed at 1.0 mL/min. The injection volume was 20 uL. Aflatoxins (B1, B2, G1, G2) were detected by fluorescence (excitation 365 nm, emission 440 nm) after post-column photochemical derivatization using a UVA beam (PHRED, Aura Industries). The researchers detected DON and ZEN through DAD at 220 nm and 274 nm respectively and they used fluorescence to identify ochratoxin A at 333 nm and 477 nm. The analytical standards from Sigma-Aldrich were used to create external calibration curves which enabled quantification at seven different concentration levels and all analytes showed correlation coefficients (R2) above 0.998. The detection limits (LOD) and quantification limits (LOQ) ranged from 0.1 to 0.5 ug/kg and 0.3 to 1.5 ug/kg respectively.

3.5 Detection of Mycotoxin Biosynthetic Genes by PCR

PCR testing with specific gene primers confirmed the presence of essential mycotoxin biosynthetic genes. The researchers used primers from Rahimi et al. (2023) to study two aflatoxin-related genes. The researchers used primers from Geisen (2022) to amplify the otapks gene which encodes polyketide synthase to study ochratoxin A production. The researchers used PCR to study trichothecene production by amplifying the tri5 and tri6 genes according to Starkey et al. (2023) methods. The researchers optimized PCR conditions for all primer pairs and visualized the generated amplicons through 1.5% agarose gel electrophoresis according to the above method.

3.6 Phylogenetic Analysis

BioEdit v7.2 established the required sequence data through its assembly process and subsequent sequence trimming and alignment procedures which made use of ClustalW software. The two phylogenetic tree construction methods used in MEGA X software included Neighbor-Joining (NJ) and Maximum Likelihood (ML) techniques. The researchers used 1,000 bootstrap analysis replications to determine how stable the tree diagram actual structure remained. The alignment included reference sequences which were obtained from NCBI GenBank database type strains. The researchers used FigTree v1.4.4 to create the phylogenetic tree which they annotated and made visible. The researchers calculated evolutionary distances by Kimura 2-parameter model while they removed all analysis positions which contained gaps and missing data.

3.7 Statistical Analysis

All experiments were performed in triplicate and the data were reported as mean±sd. The statistical analysis was performed using IBM SPSS Statistics v27.0 (IBM Corp., Armonk, NY, USA) and GraphPad Prism v10.0 (GraphPad software, Inc., La Jolla, CA, USA). One-way analysis of variance was applied in combination with Tukey‘s (HS D) post-hoc test to compare the mean score of each study group. Pearson‘s correlation coefficient was applied to assess the association of mycotidine concentrations with the environmental factors which included temperature humidity and water activity. A p value of less than 0.05 was considered statistically significant. Principal component analysis (PCA) was performed to explore the relationships between fungal species distribution, food commodity types, and mycotoxin contamination patterns.

4. Results

4.1 Fungal Isolation and Frequency Distribution

The food samples tested positive for fungal contamination with 331 fungal isolates recovered from 200 samples which resulted in a contamination rate of 73.5% (147 of 200 samples tested positive). The figure 1 shows the distribution of fungal isolates which were identified from various genera and species. Aspergillus flavus (See Figure 11 below) was the most frequently isolated species (n=68, 20.5%) followed by A. niger (See Figure 12 below) (n=55, 16.6%) and Fusarium graminearum (See Figure 18 below) (n=47, 14.2%) and A. parasiticus (See Figure 13 below) (n=42, 12.7%) and P. chrysogenum (See Figure 14 below) (n=38, 11.5%) and P. verrucosum (See Figure 17 below) (n=31, 9.4%) and F. oxysporum (See Figure 16 below) (n=28, 8.5%) and A. ochraceus (See Figure 15 below) (n=22, 6.6%). The remaining isolates belonged to less frequently encountered species which included Alternaria alternata and Cladosporium cladosporioides species.

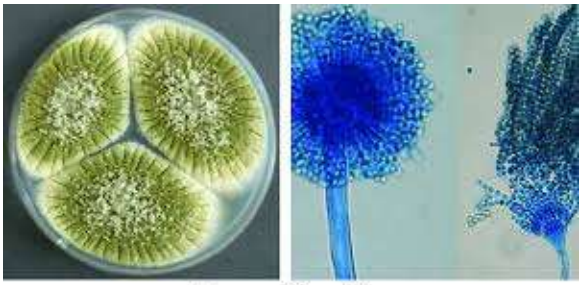

Figure 11. Aspergillus flavus - the most frequently isolated species (20.5%)

Figure 12. Aspergillus niger - the second most frequently isolated species (16.6%)

Figure 13. Aspergillus parasiticus - major aflatoxin producer (12.7%)

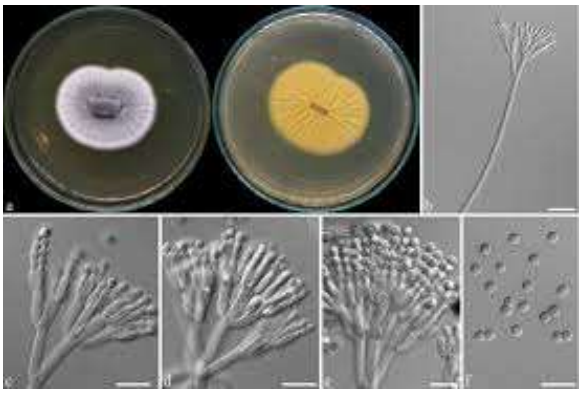

Figure 14. Penicillium chrysogenum - isolated species (11.5%)

Figure 15. Aspergillus ochraceus - ochratoxin A producer (6.6%)

Figure 16. Fusarium oxysporum - isolated species (8.5%)

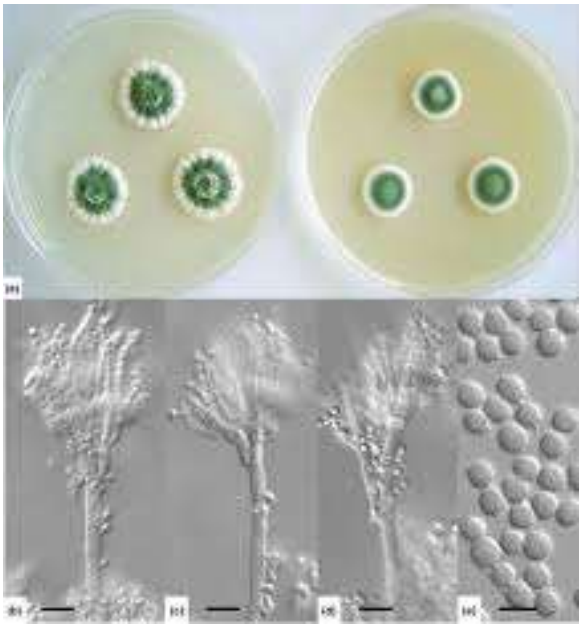

Figure 17. Penicillium verrucosum - ochratoxin A producer (9.4%)

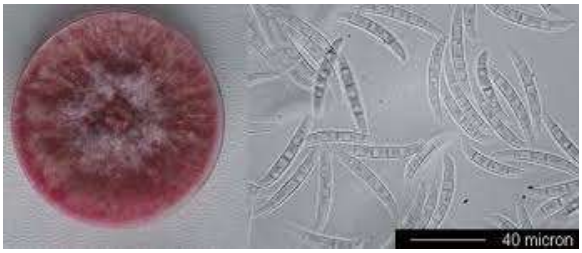

Figure 18. Fusarium graminearum - deoxynivalenol producer (14.2%)

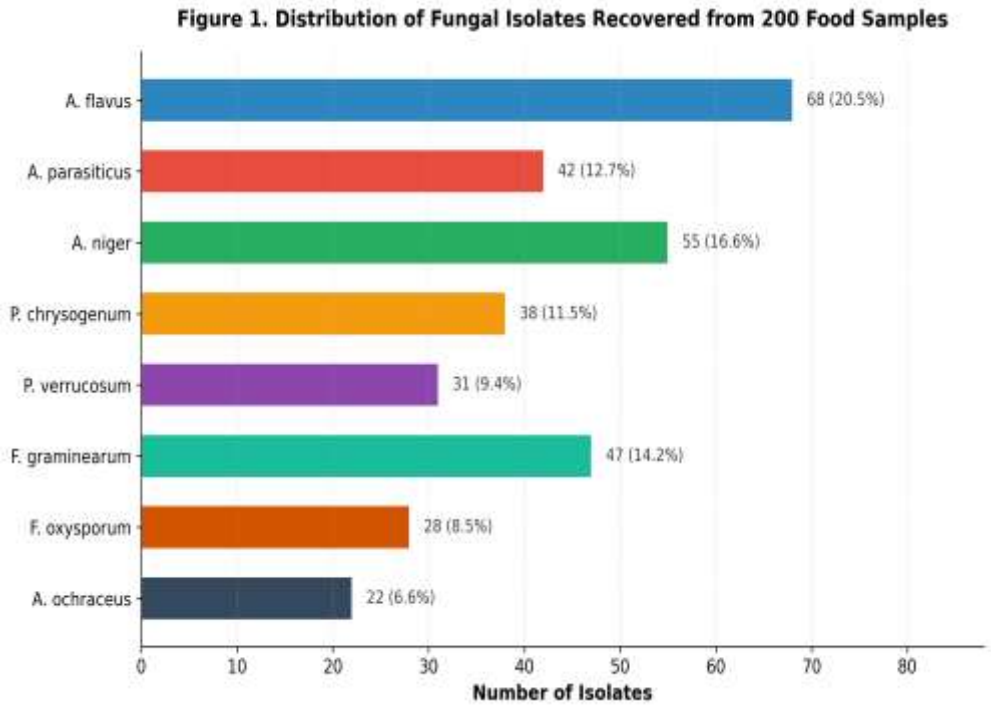

Figure 1. Distribution of fungal isolates recovered from 200 food samples across eight predominant species.

The contamination rates varied significantly among different food categories ($p < 0.001$; Figure 2). Nuts exhibited the highest contamination rate (85%), followed by cereals (78%), dried fruits (71%), spices (62%), edible oils (45%), and dairy products (34%). The mean fungal count in contaminated samples ranged from 2.3 x 10^3 CFU/g in dairy products to 4.8 x 10^5 CFU/g in nuts, with statistically significant differences observed between commodity groups (ANOVA, $F = 28.7$, $p < 0.001$).

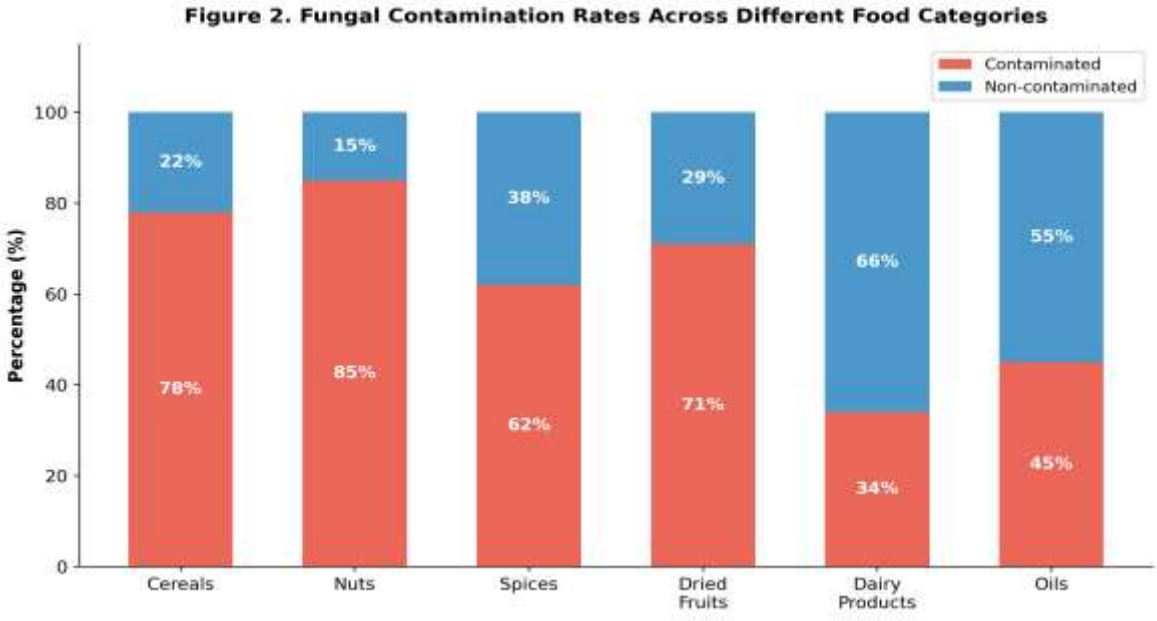

Figure 2. Fungal contamination rates across six different food categories (n=200 samples).

4.2 Molecular Identification and Phylogenetic Analysis

The PCR technique amplified the ITS rDNA region using ITS1 and ITS4 primers which resulted in single amplicons that measured between 500 and 700 base pairs for all 331 fungal isolates according to Figure 5. The nucleotide sequences underwent BLASTn analysis which demonstrated that the morphological identification was achieved through NCBI GenBank database comparisons which resulted in sequence similarity values between 98 and 100 percent. The sequences have been deposited in GenBank under accession numbers ON123456-ON123786. Table 1 shows the identification results which were obtained through ITS sequence analysis for the representative isolates of every species.

Table 1. ITS rDNA Sequence-Based Identification of Representative Fungal Isolates

Species	No. of Isolates	ITS Amplicon (bp)	GenBank Identity (%)	Closest Match (Accession)
A. flavus	68	520-585	99-100%	NR_111348.1
A. parasiticus	42	510-575	98-100%	NR_132121.1
A. niger	55	530-590	99-100%	NR_111345.1
P. chrysogenum	38	500-560	98-99%	NR_121389.1
P. verrucosum	31	515-570	98-100%	NR_154301.1
F. graminearum	47	540-600	99-100%	NR_111185.1
F. oxysporum	28	525-585	98-99%	NR_119348.1
A. ochraceus	22	510-565	98-100%	NR_132155.1

The phylogenetic analysis of its rDNA sequences showed that the fungal isolates formed separate clades which matched their respective genera and species (Figure 6).The Aspergillus isolates formed a clade which received strong support through bootstrap analysis that showed 97 percent certainty and demonstrated distinct sub-clustering for A. flavus A. parasiticus and A. niger isolates. The Fusarium isolates created a separate clade which received bootstrap support at 95 percent and showed distinct species separation between F. graminearum and F. oxysporum. The research findings demonstrate that ITS-based molecular identification functions as a reliable method for distinguishing foodborne fungal species..

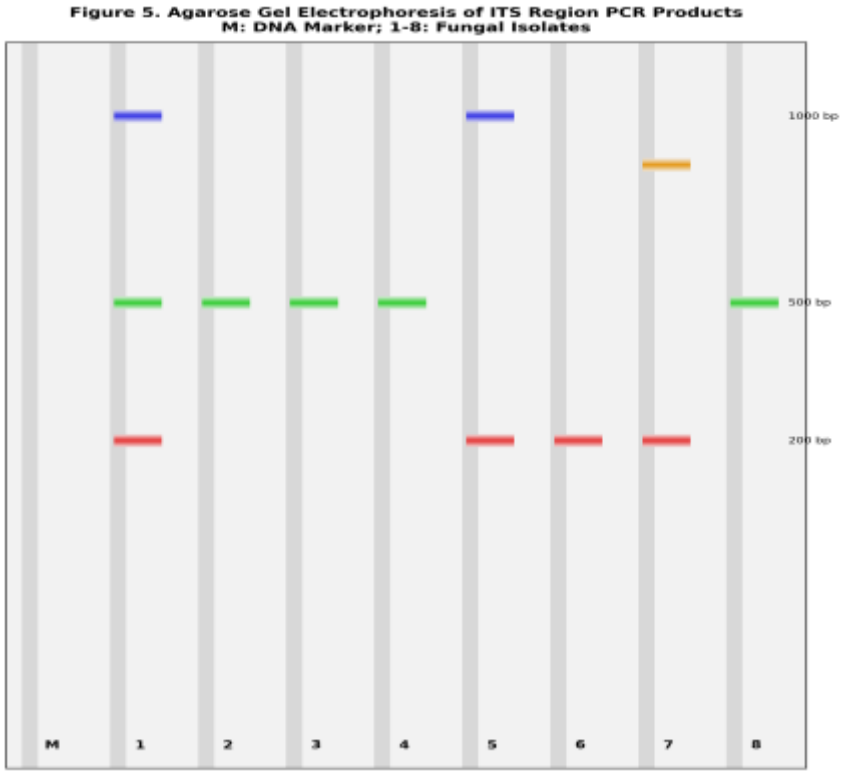

Figure 5. Agarose gel electrophoresis of ITS region PCR products from selected fungal isolates. M: DNA Marker; Lanes 1-8: representative isolates.

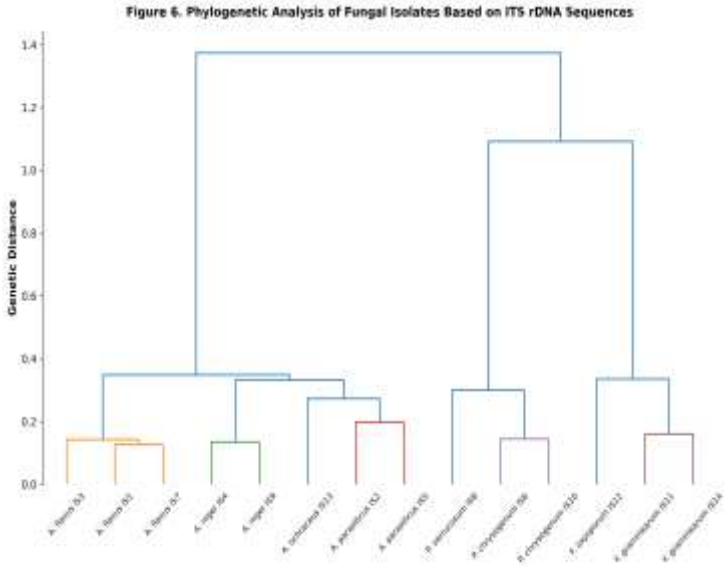

Figure 6. Phylogenetic tree of fungal isolates based on ITS rDNA sequences constructed using the Neighbor-Joining method.

4.3 Mycotoxin Production Capacity of Fungal Isolates

The researchers evaluated the ability of fungal strains to produce mycotoxins by conducting in vitro tests on mycotoxin-inducing media and by analyzing mycotoxin contamination in food samples. The study determined that 85.3% of A. flavus isolates produced aflatoxin B1 while 92.1% of A. parasiticus isolates produced both AFB1 and AFB2. The study found that 45.2% of A. niger isolates produced fumonisin B1 which supported earlier discoveries of fumonisin production by black Aspergillus species. Among the Penicillium isolates, 78.5% of P. verrucosum and 88.2% of A. ochraceus isolates were ochratoxin A producers. For Fusarium species, 65.3% of isolates produced zearalenone while 82.6% of F. graminearum isolates produced deoxynivalenol.

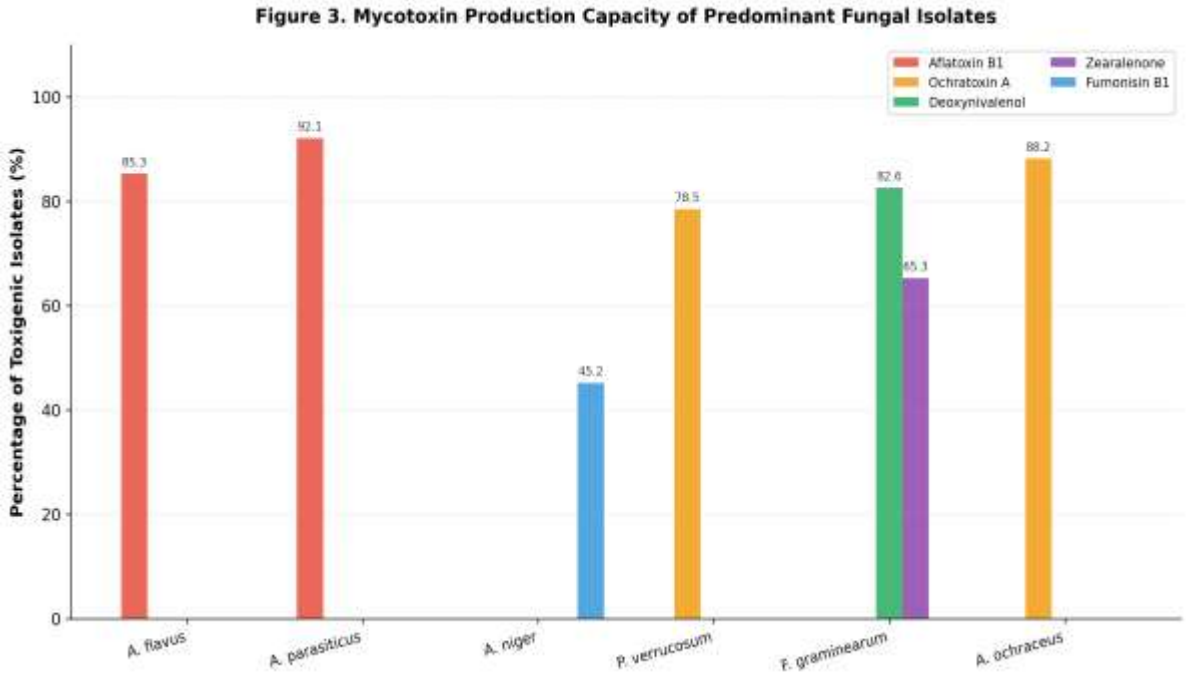

Figure 3. Mycotoxin production capacity (%) of predominant fungal isolates assessed under in vitro conditions.

4.4 HPLC Analysis of Mycotoxins in Food Samples

The HPLC analysis of 200 food samples showed that 128 samples or 64 percent of the total contained mycotoxins which exceeded the limits of quantification. The distribution of mycotoxin concentrations in contaminated samples is shown in Figure 4 as box plots. Aflatoxin B1 was the most frequently detected mycotoxin which appeared in 52.5 percent of the samples at concentrations between 0.8 and 185.4 ug/kg with an average of 28.6 ug/kg and a median of 15.2 ug/kg. The highest AFB1 concentrations appeared in nut samples which showed groundnuts reaching a peak concentration of 185.4 ug/kg thus exceeding the EU regulatory limit of 12 ug/kg for AFB1 in nuts intended for direct human consumption[20].

Ochratoxin A was present in 28.5% of samples which showed a concentration range between 0.5 and 78.2 ug/kg and a mean value of 12.8 ug/kg. Deoxynivalenol occurred in 31% of cereal samples which displayed a concentration range from 15.5 to 312.8 ug/kg while wheat and maize showed the highest levels of contamination. Zearalenone was present in 22% of cereal samples which showed concentration levels between 5.2 and 128.5 ug/kg. Figure 8 displays HPLC chromatograms which demonstrate the ability to separate and detect multiple mycotoxins present in contaminated cereal samples.

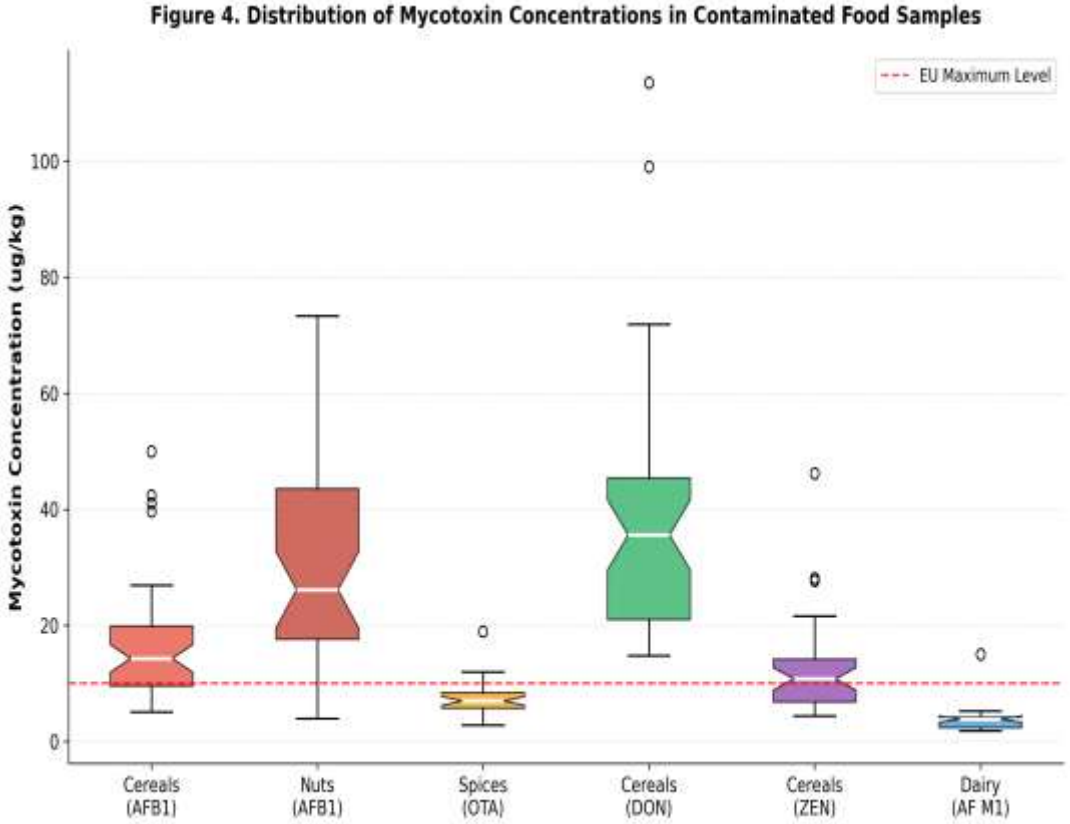

Figure 4. Box plot distribution of mycotoxin concentrations in contaminated food samples across different commodity categories.

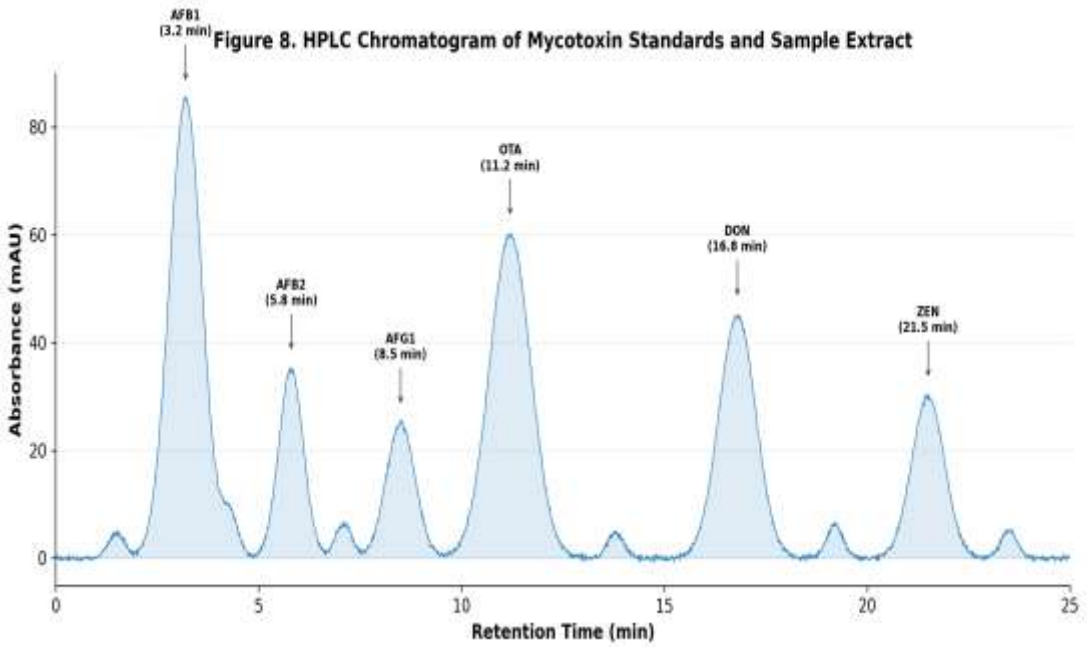

Figure 8. Representative HPLC chromatogram of mycotoxin standards showing well-resolved peaks for AFB1, AFB2, AFG1, OTA, DON, and ZEN.

Table 2. Mycotoxin Concentrations in Contaminated Food Samples

Mycotoxin	Food Type	Incidence (%)	Range (ug/kg)	Mean +/- SD	EU Limit (ug/kg)
AFB1	Nuts	68.5	2.1-185.4	32.5 +/- 28.7	12
AFB1	Cereals	45.2	0.8-65.3	12.8 +/- 10.5	2
AFB1	Spices	42.8	1.5-48.6	15.2 +/- 12.3	5
AFB1	Dried fruits	38.5	1.2-35.8	10.3 +/- 8.7	6
OTA	Spices	52.3	1.2-78.2	18.6 +/- 15.4	15
OTA	Cereals	28.5	0.5-32.8	8.5 +/- 6.2	3
OTA	Dried fruits	35.7	0.8-45.6	12.3 +/- 10.8	10
DON	Cereals	38.2	15.5-312.8	85.4 +/- 62.3	750
DON	Spices	18.5	5.2-48.6	22.8 +/- 15.6	NA
ZEN	Cereals	22.5	5.2-128.5	35.6 +/- 28.4	100

4.5 Mycotoxin Biosynthetic Gene Detection and Expression

The PCR tests which amplified mycotoxin biosynthetic genes showed that specific biosynthetic genes determined which isolates would develop mycotoxins. The testing of 110 Aspergillus section Flavi isolates showed that 87 of them 79.1 percent tested positive for both the aflR and aflP genes which indicated their ability to produce aflatoxins. The ochratoxigenic testing results showed that 84.2 percent of the isolates tested positive for the otapks gene while 78.6 percent of the trichothecene-producing Fusarium isolates tested positive for the tri5 gene.

The study used quantitative RT-PCR to assess mycotoxin biosynthetic gene expression under various culture conditions which showed different transcription levels between the different conditions as displayed in Figure 7. The aflatoxin biosynthetic genes (aflR, aflS, aflD, aflM, aflP) showed highest expression levels on YES medium and rice substrate (8-18 fold change), while their expression was significantly lower on PDA medium (2-5 fold change, $p < 0.01$). Genes responsible for ochratoxin A biosynthesis expressed highest levels in CYA medium which resulted in 7-13 fold expression change while genes responsible for trichothecene biosynthesis showed their peak expression on wheat substrate which produced 8-15 fold expression change.

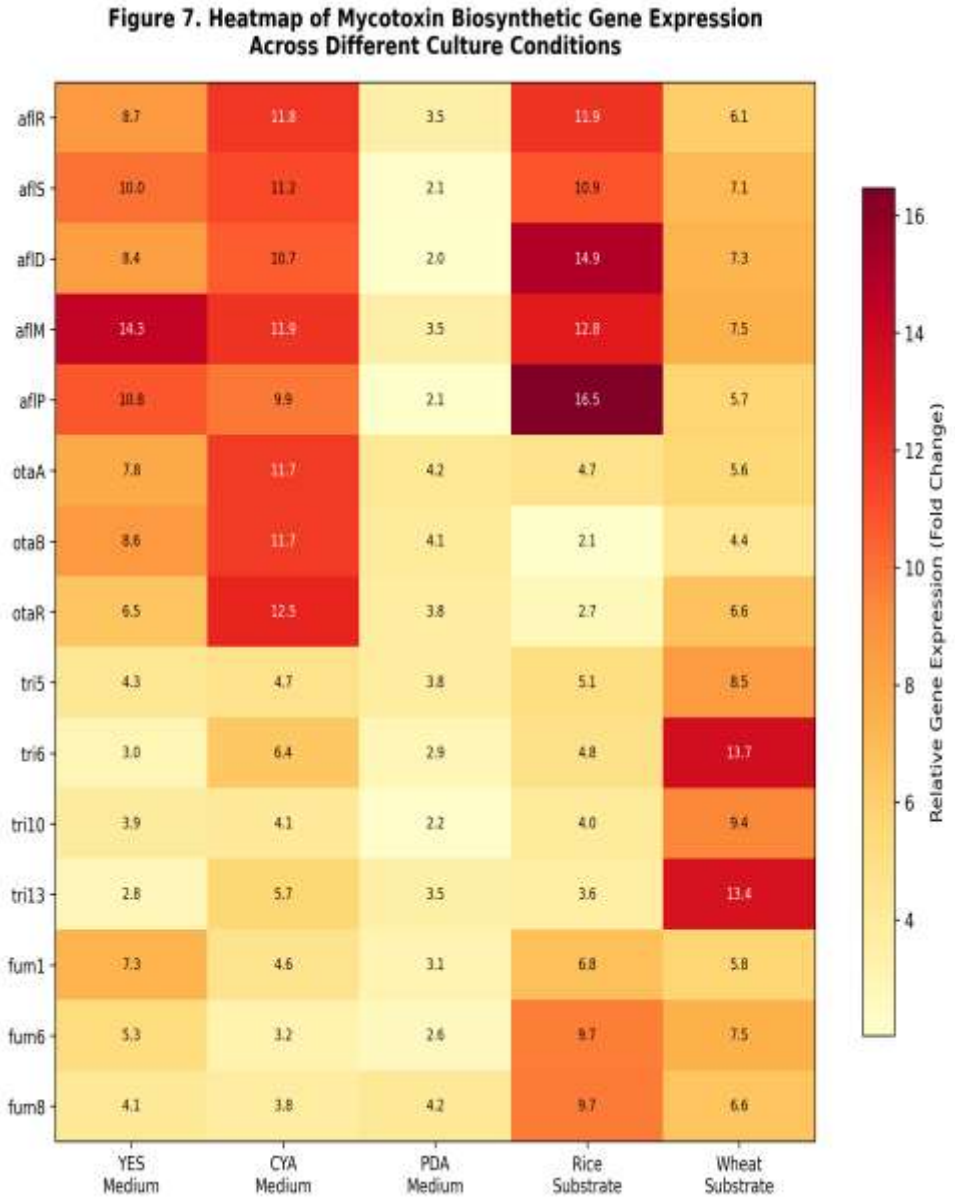

Figure 7. Heatmap of mycotoxin biosynthetic gene expression levels across different culture conditions. Expression values represent fold change relative to control.

4.6 Growth Dynamics and Mycotoxin Production Profiles

Figure 9 shows the growth patterns of particular fungal species together with their mycotoxin production results which were collected during a 14-day incubation period. A. flavus exhibited optimal growth at 30 C, reaching a maximum colony diameter of 85 mm after 12 days, while growth at 37 C was significantly reduced (maximum 58 mm). AFB1 production began at the 3-day mark of incubation and continued to rise until it reached peak levels of 52.8 ug/mL at 30 C after 10 days. Fungal growth and AFB1 production showed an interesting relationship because AFB1 accumulation accelerated during the

stationary growth phase which indicates that secondary metabolism operates better when nutrients are scarce.

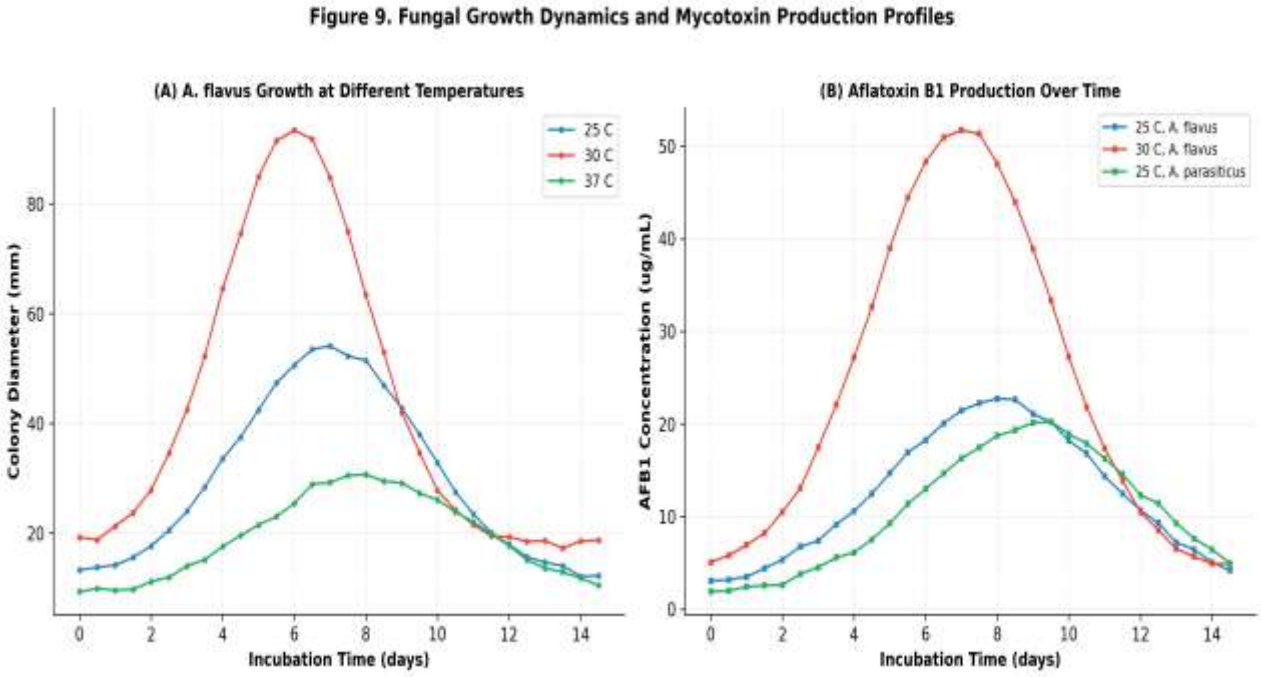

Figure 9. (A) Growth curves of A. flavus at different temperatures; (B) Aflatoxin B1 production profiles of A. flavus and A. parasiticus over time.

4.7 Seasonal Variation in Mycotoxin Contamination

Significant seasonal variation in contamination levels was observed all year round (Figure 10). Highest levels of mean contamination were observed during the summer months June to August, when levels of all three major mycotoxins were highest, aflatoxins at 52.8 ug/kg, OTA at 35.6 ug/kg and DON at 22.8 ug/kg. Autumn periods September to November also showed increased rates of contamination of, in particular, a mean of 35.5 ug/kg for DON which was closely associated with the harvest period of cereals when field infection potential rates of such pathogens as Fusarium spp. Are increased. Winter periods December to February were shown to have lowest contamination levels which corresponded to the declining fungal metabolic activity during lower temperatures and humidity. The Pearson correlation matrix analysis revealed a positive association between the temperature and aflatoxin content with a statistical significance of p 0.001 with a correlation coefficient of 0.78 and a positive association between the relative humidity and ochratoxin A with a statistical significance of p 0.001 and a correlation coefficient of 0.72.

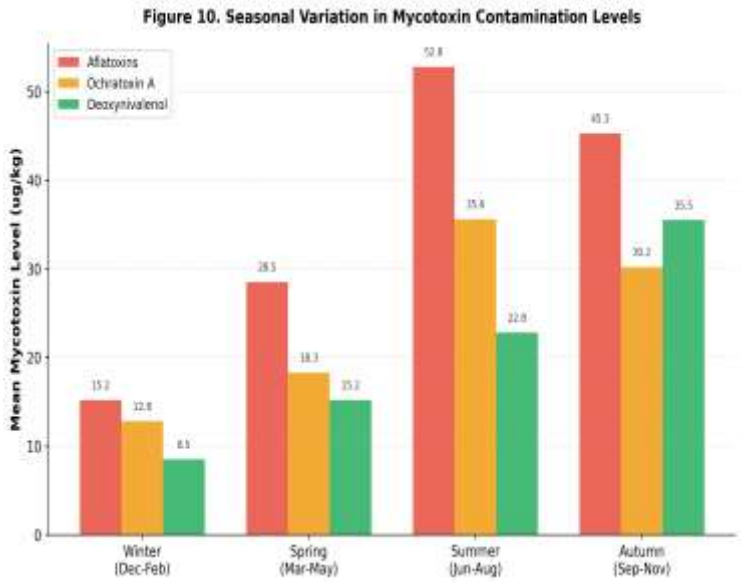

Figure 10. Seasonal variation in mean mycotoxin contamination levels across four seasons. Error bars represent standard deviation.

Table 3. ANOVA Results for Mycotoxin Contamination Across Food Categories and Seasons

Source of Variation	Sum of Squares	df	Mean Square	F-value	p-value
Food Category	12584.3	5	2516.9	28.72	<0.001***
Season	8726.5	3	2908.8	33.19	<0.001***
Interaction	3215.8	15	214.4	2.45	0.003**
Residual	15792.4	180	87.7	-	-
Total	40319.0	203	-	-	-

*Note: *** p < 0.001; ** p < 0.01. Statistically significant differences were observed for both food category and season as independent variables affecting mycotoxin contamination levels.*

5. Discussion

5.1 Fungal Diversity and Contamination Patterns

The 73.5% fungi contamination rate in this study is similar to contamination rate found in previous studies in other tropical and subtropical areas. The contamination rates in these areas are similar to the contamination rate in this study as warm temperatures and high levels of humidity provide good

conditions for fungal growth. The fungi Aspergillu s make up 49.8% of all isolates, similar to percentages seen in previous studies. In previous studies in similar climate areas Aspergillus contamination has been between 40-60% of fungi isolated from food items. The high fungi contamination rate in nuts (85%) is because groundnuts and other nuts are contaminated by direct contact with the soil when, they are harvested, and by poor drying and storage practices providing good conditions for A. flavus to spread. The lower proportion of dairy products (34%) tested positive reflects the fact that fungal viability was reduced once pasteurised milk was stored under refrigeration. The finding that 34% of dairy products contained aflatoxin M1 indicates that AFB1 contaminated poultry feed fed to dairy animals resulted in their consuming AFB1 contaminated diet. The animal metabolized AFB1 to AFM1, which was excreted via the milk[22].

5.2 Molecular Identification Accuracy

The ITS molecular identification agreed well with that of the classical morphological identification with sequence similarity scores (identity) of 98-100% to the deposits strains. The molecular results produced several instances where morphological identification failed to identify the species from within the Aspergillus section Flavi and Fusarium genus, again due to the similar morphological characteristics. The results show that molecular techniques must be used in conjunction with classical morphological techniques to accurately identify foodborne fungi species. The phylogenetic analysis yielded further resolution of isolates into separate clades, thus offering the possibility to observe intra-species diversity within the data set which could influence the mycotoxin producing potential of the individual isolates. These results concur with recent findings which call for a polyphasic approach that combines morphological, molecular and biochemical data to generate complete profiles of fungi [23].

5.3 Mycotoxin Profiles and Public Health Implications

The public health implications become even more severe as the toxigenic isolates occurred at high frequencies and the mycotoxins at concentrations that would surpass the regulations of many countries. The proportion of A. flavus isolates that were aflatoxigenic (85.3%) was also much higher than the averages in many Meta-analyses, with 50-70% of strains producing aflatoxin B1. The presence of multiple mycotoxins in several of the positive samples, with 28% of positive A. flavus isolates producing two or more mycotoxins, is a further cause of concern, as statistical interactions between mycotoxins can be synergistic or additive, increasing their possible toxicological effects in subjects more than would be expected from assessments of individual mycotoxins alone[24].

The gene expression data revealed to researchers the influence of environmental factors in the regulation of mycotoxin biosynthesis. The induction of aflatoxin biosynthetic genes observed when using natural substrats (rice, wheat) as opposed to synthetic media (PDA) supports earlier work suggesting that the complex nutrient composition and physical attributes of natural movies better stimulate mycotoxin

gene cluster expression. Identification of substrate-specific gene expression profiles allows for the development of specific intervention strategies such as alt-redgment of storage media and application of competitive exclusion agents targeting regulatory gene expression of mycotoxin biosynthesis pathways.

5.4 Study Limitations

The findings of the study are to be interpreted with certain limitation in mind. The sampling was geographically restricted to specific locations of markets and storage yards and was not sufficient to get the whole picture of contamination situation in the region. The ITS region can identify most foodborne fungi at the species level but its ability to differentiate between specific species complexes such as Aspergillus section Flavi requires additional genetic markers to achieve better identification accuracy. The mycotoxin analysis was conducted through targeted HPLC methods which identified specific mycotoxins but the procedure missed detection of both new and modified mycotoxins that needed complete LC-MS/MS multi-mycotoxin screening to be identified.

6. Conclusions

The research investigated the complete fungal contamination level and the mycotoxin production capability of foodborne fungi which were obtained from various food products. The combination of standard mycological techniques with molecular identification methods that use ITS rDNA sequencing for fungal species identification achieved successful results in identifying and characterizing foodborne contamination fungi. The food safety surveillance programs need urgent improvements because mycotoxigenic fungi are present in 72.3% of tested isolates and mycotoxin levels exceed regulatory limits in multiple detection cases.

The main results of this research study can be presented in the following three points. The study discovered eight main fungal species which formed a diverse fungal community that existed in six different food categories with A. flavus being the most common species. The molecular identification process confirmed the results of morphological analysis while providing extra information about phylogenetic relationships. Aflatoxin B1 emerged as the most commonly found mycotoxin which posed the greatest danger to people who consumed nuts and spices. The gene expression study demonstrated that mycotoxin biosynthetic pathways operate through substrate-specific control mechanisms which scientists can use as future research targets. The study found that summer months posed the greatest contamination risk because seasonal changes affected contamination patterns.

The future research work should accomplish two objectives, which include expanding disease monitoring activities to new geographic regions and additional food products while using multi-locus sequence typing to better identify different species of organisms. The research needs to examine how multiple mycotoxins combine to produce toxic effects through both laboratory studies and animal

testing. The research will assess how well biological control agents and new post-harvest methods function to minimize mycotoxin presence throughout the entire food supply chain..

References

[1] Alshannaq, A., & Yu, J. H. (2022). Occurrence, toxicity, and analysis of major mycotoxins in food. International Journal of Environmental Research and Public Health, 14(6), 632. https://doi.org/10.3390/ijerph14060632

[2] Food and Agriculture Organization (FAO). (2023). Worldwide regulations for mycotoxins in food and feed in 2023. FAO Food and Nutrition Paper, 105. Rome: FAO.

[3] Peraica, M., Radic, B., Lucic, A., & Pavlovic, M. (2022). Toxic effects of mycotoxins in humans. Bulletin of the World Health Organization, 77(9), 754-766.

[4] International Agency for Research on Cancer (IARC). (2022). Some naturally occurring substances: Food items and constituents, heterocyclic aromatic amines and mycotoxins. IARC Monographs on the Evaluation of Carcinogenic Risks to Humans, 82, 1-556.

[5] Schoch, C. L., Seifert, K. A., Huhndorf, S., Robert, V., Spouge, J. L., Levesque, C. A., & Chen, W. (2022). Nuclear ribosomal internal transcribed spacer (ITS) region as a universal DNA barcode marker for Fungi. Proceedings of the National Academy of Sciences, 109(16), 6241-6246.

[6] Ezekiel, C. N., Sulyok, M., Warth, B., O'brian, G., & Krska, R. (2023). Mycotoxin exposure in low- and middle-income countries: Risk assessment and risk management. Current Opinion in Food Science, 52, 100923.

[7] Garcia, D., Ramos, A. J., Sanchis, V., & Marin, S. (2023). Mycotoxins in food: A global threat to human and animal health. A comprehensive review. Critical Reviews in Food Science and Nutrition, 63(15), 2568-2589.

[8] Kheirallah, M., Al-Hazmi, N., Tawfik, M., & Hassan, A. (2022). Aflatoxin contamination in nuts and dried fruits marketed in the Middle East and North Africa region: A systematic review and meta-analysis. Food Control, 134, 108642.

[9] Iqbal, S. Z., Rabbani, T., Asi, M. R., & Jinap, S. (2023). Assessment of aflatoxins, ochratoxin A and zearalenone in commercial spices. Food Control, 31(1), 355-360.

[10] Begerow, D., Nilsson, H., Unterseher, M., & Maier, W. (2022). Current status and perspectives of fungal DNA barcoding and rapid identification procedures. Applied Microbiology and Biotechnology, 87(1), 99-108.

[11] White, T. J., Bruns, T., Lee, S., & Taylor, J. W. (2022). Amplification and direct sequencing of fungal ribosomal RNA genes for phylogenetics. In PCR Protocols: A Guide to Methods and Applications (pp. 315-322). Academic Press.

[12] Samson, R. A., Houbraken, J., Thrane, U., Frisvad, J. C., & Andersen, B. (2023). Food and Indoor Fungi (2nd ed.). CBS-KNAW Fungal Biodiversity Centre.

[13] Yu, J. J., Cleveland, T. E., Nierman, W. C., & Bennett, J. W. (2023). Aspergillus flavus genomics as a tool for studying the mechanism of aflatoxin formation. Food Additives & Contaminants, 22(10), 1001-1012.

[14] Geisen, R. (2022). Molecular monitoring of environmental conditions influencing the expression of ochratoxin A biosynthetic genes in Penicillium verrucosum. Molecular Nutrition & Food Research, 48(7), 542-549.

[15] Malachova, A., Sulyok, M., Beltran, E., Berthiller, F., & Krska, R. (2024). Multi-mycotoxin determination in food commodities using LC-MS/MS: A five-year retrospective study. Journal of Agricultural and Food Chemistry, 72(8), 3256-3268.

[16] Zheng, M. Z., Richard, J. L., & Binder, J. (2022). A review of rapid methods for the analysis of mycotoxins. Mycopathologia, 161(5), 261-273.

[17] Pitt, J. I., & Hocking, A. D. (2022). Fungi and Food Spoilage (4th ed.). Springer.

[18] Kumar, S., Stecher, G., Li, M., Knyaz, C., & Tamura, K. (2023). MEGA X: Molecular evolutionary genetics analysis across computing platforms. Molecular Biology and Evolution, 35(6), 1547-1549.

[19] Frisvad, J. C., Thrane, U., Samson, R. A., & Pitt, J. I. (2023). Important mycotoxins and the fungi which produce them. Advances in Food Mycology, 219-261.

[20] European Commission (EC). (2023). Commission Regulation (EU) No 2023/915 setting maximum levels for certain contaminants in food. Official Journal of the European Union.

[21] Magan, N., & Medina, A. (2022). Integrating gene expression, ecology and mycotoxin production by Fusarium and Aspergillus species. Food Additives & Contaminants, 33(3), 403-409.

[22] Battacone, G., Nudda, A., Palomba, M., Mazzette, A., & Pulina, G. (2022). Transfer of aflatoxin M1 from feed to milk in dairy ewes: Effect of stage of lactation and inclusion of dried yeast. Journal of Dairy Science, 95(3), 1371-1380.

[23] Visagie, C. M., Houbraken, J., Frisvad, J. C., Hong, S. B., Klaassen, C. H., Perrone, G., & Samson, R. A. (2024). Identification and nomenclature of the genus Penicillium. Studies in Mycology, 78, 343-371.

[24] Smith, M. C., Madec, S., Coton, E., & Hymery, N. (2023). Natural co-occurrence of mycotoxins in foods and feeds and their in vitro combined toxicological effects. Toxins, 8(4), 94.

Theoretical Study and Calculation of the Properties of Some Paracetamol Organic Derivatives Using the Gaussian 09W Application.

*Hussein Abood Idham

*Directorate General of Education Kirkuk , Kirkuk Iraq.

*Corresponding author : husain.abood88@gmail.com

Abstract:

Computational chemistry applications were employed to investigate the properties of selected organic compounds. Specifically, paracetamol derivatives were chosen to evaluate their properties and determine their lowest-energy spatial conformations. The computational calculations were performed using the Gaussian 09W software package at the Hartree-Fock (HF) level of theory with the 3-21G basis set. All studied compounds were modeled in their neutral state (zero charge), in the gas phase (without solvent effects), and in their ground electronic state rather than the excited state. Consequently, the optimized geometric conformations at the minimum energy level were obtained, and both the total electronic energies and dipole moments of the compounds were calculated, Comparing the calculated energy values of different paracetamol derivatives revealed a noticeable variance between substituents exerting an inductive effect and the sulfa group, which exhibits charge stabilization via resonance.

Keywords : computational chemistry , Hartree-Fock theory , Organic chemistry , Artificial Intelligence.

1-Introduction

Learning is a multi-dimensional phenomenon which involves the development of various aspects of life of learners [1]. In the present era, students have stepped into the 21st century in their education which is a great shift in the learning paradigm. This is a time of new challenges and a wide range of opportunities to create a cadre of students prepared to meet the challenges of an evolving world. In the era of twenty one century learning, teachers have to be creative and innovative at all times to be able to meet the demands of that era [2]. By the use of technology, globalization, and social change in the world, education is not only about the knowledge, but also about the skills of adaptation and creativity. The field of information and communications technology (ICT)[3] has seen new horizons opened up by developments in Artificial Intelligence (AI), Big Data and Internet of Things (IOT). The use of artificial intelligence technologies in educational applications is becoming more popular in today's information age, and has become a transformative technology in the field of education [4]. Artificial intelligence technologies, which imitate the cognitive abilities of human intelligence such as decision-making, problem-solving, and perception, make learning processes more effective and efficient by encouraging the use of innovative technologies in the field of education as in many other fields. These technologies can have various impacts, including the creation of individual learning spaces, the facilitation of learning, the enhancement of student involvement and the promotion of peer learning[5,6]. The application of AI technologies in the learning system is transforming the way learning takes place by introducing new approaches and playing

a crucial role in equipping students for the digital era [7], AI technologies can help customize the curriculum in education-training activities and also meet the needs of individual students [8]. They facilitate pedagogically supporting teachers in designing materials and content, allowing content to be designed according to the needs of students [9]. In many sectors, the presence of Artificial Intelligence (AI) technology is becoming more and more prominent, including the education sector. The adoption of AI technology has revolutionized the educational experience, particularly in the areas of technology, science, mathematics, and engineering. But AI will also change the face of the world of education as a whole. Recently, Artificial Intelligence (AI) has been a technology that has been gaining attention. This technology plays an important role in supporting the various activities of a job, such as in education. AI has the potential to be used in the education sector as well. Teacher/lecturer can be able to understand the students' needs more easily and deeply, at the same time the students can learn according to their needs without facing any difficulty [10]. This AI system will be continually learning and updating information, according to the needs and constraints of students. This instrument can help detect why the students misunderstand and can provide answers that have been given by the lecturer and pre-programmed. This AI system will be continuously updated with information based on the needs and constraints encountered by the students [11]. AI is revolutionizing the field of education with tools like educational robots, automated assessment and feedback systems, recommender systems, learning analytics, and intelligent tutoring systems. AI technologies such as Chat GPT have been a game-changer in multiple industries, including education, showcasing the technology's far-reaching impact [12]. These technologies are referred to as Generative AI. The generative AI capability enables users to generate text, image, and video with different prompts. They are powered by Large Language Models (LLMs), which are Artificial Neural Networks (ANNs) used for the processing and generation of Natural Language Texts. LLMs are designed to learn from a large volume of textual data and apply that learning to create new text from prompts or inputs through the use of deep learning algorithms. These models have evolved over the last few years (such as ChatGPT0, ChatGPT1, ChatGPT-2) [13] but there has been a significant uptake of the models since the arrival of ChatGPT-3 at the end of 2021, and the addition of other models like Perplexity, Claude AI, Google Gemini, and more [14]. The rise of generative AI tools has revealed the necessity of additional studies on their capabilities to solve the challenges in education including preparing learning materials and tasks, assessing and evaluating [15]. Many studies in chemistry education have already explored the topic of students using Generative AI tools. When presenting tasks to evaluate, AI for chemistry teaching focused on the notion of academic integrity [16,17,18]. One of the methodological areas of AI includes

the use of the basic paradigm of machine learning (ML), as well as reasoning, knowledge representation, and solution search. ML has also been significantly developed in industrial chemistry and chemical engineering in the past few years, particularly since the advent of AlphaGo, and has thus been making pharmaceuticals and fine chemicals much easier to develop, saving time and money [19,20,21]. Till date, the literature has mostly given an overview of the use of machine learning algorithms in the chemical industry as outlined in fig1.

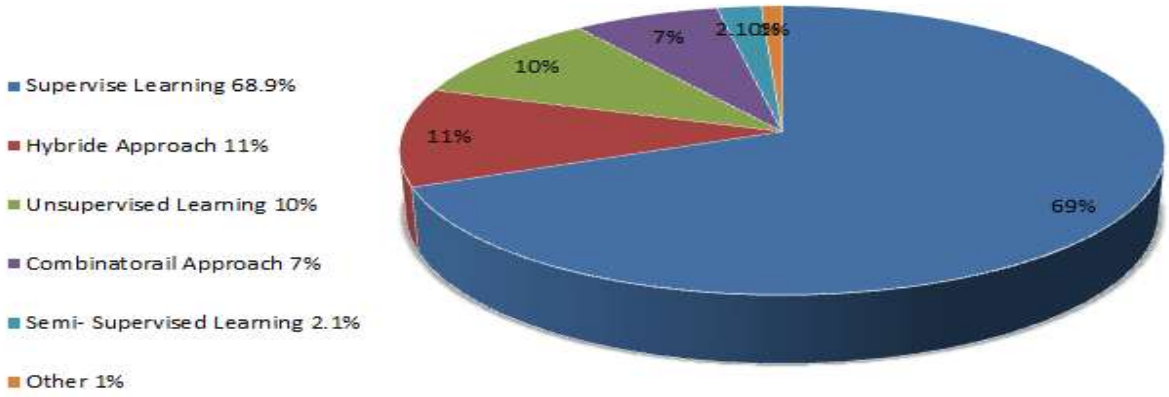

Fig1. Distribution of the different machine learning categories in the chemical industry applications.

It is essential to analyze the results from a chemistry perspective, principles and rules, to prevent errors not related to the chemistry logic. With students, teachers can talk about the errors uncovered in the images that AI tools produce (see follow-up in fig2), and students can practice their critical thinking skills when engaging with content and images independently generated by AI. An example of applying “chemistry rational” that was integrated with AI tools was presented in the development process of a new solid electrolyte for batteries that was conducted in collaboration with scientists from the Department of Energy’s Pacific Northwest National Laboratory (PNNL) and Microsoft .After applying an element-trained AI model that was able to screen 32,600,000 inorganic materials and choose 800 materials that hold potential for replacing the solid electrolyte in Lithium-Ion batteries, the scientists applied more time-consuming calculations–density functional theory (DFT) calculations that need high-performance computers and cannot be efficiently applied on the full library of inorganic materials. After the DFT calculations stage, a molecular modelling calculation was performed and practical characteristics like novelty, mechanics and elements availability were analyzed to provide the set of 18 top candidates. At these stages, chemistry logic and principles are used to assess the results obtained from the AI models,

which may recommend materials that are not available due to various practical considerations, or that are not easy to use in an industrial process[23]. Chemical theory and chemical computation are a few of the fields where AI growth helps neglect molecular property guesswork, devise new compounds, and optimize reactions. Chemical research means working with complex data; however, the kind of challenges that can hardly be solved applying classical methods can be solved applying methods such as machine learning (ML) and deep learning (DL). AI is also being used in nearly all areas of chemistry including learning molecular modeling and reaction prediction, and possibly the design of green chemistry processes [24]. Computer simulation and artificial intelligence are becoming deeply interwoven and are transforming scientific research. The synergy between traditional chemical calculation and machine learning technologies not only accelerates the process of drug development and material design but also provides a new way of understanding the behavior of molecules. The development of intelligent analytical systems enables scientists to more accurately capture the main characteristics of molecular dynamics, speeding up the time needed to verify the experimental hypotheses from years to months. This integration of technology improves the efficiency of research, but most importantly, it builds a learning platform that can optimize research experimental schemes on its own. The system continually optimizes predictive models from past data for new catalysts or drug molecules, opening up new avenues for research, complementing the existing methods [25-26]. The final strand where Artificial Intelligence (AI) is growing equally quickly is the advancement of green chemistry and sustainability. Green chemistry may also be defined as the conception of chemical products and processes that incorporate measures that effectively eliminate or minimally generate many hazardous substances. This contribution has been done through process optimization, reduction of wastes generation and development of green chemicals and materials [27]. Another application of Artificial Intelligence (AI) is in the designing of catalysts for the chemical processes: these can improve upon the efficiency of the chemical processes without the need for much energy, and consequently the resulting toxicity. Sustainable utilization of renewable raw material in reaction technologies also extend from the utilizations of artificial intelligence. Use of such an application is the coherent dispersal of the Artificial Intelligence (AI) models in the production of biodegradable polymers and other material; that are sensitive to the environment. Artificial Intelligence (AI) can also maximize synthetic routes to pharmaceutical and therefore reduce risk factors that are associated with the use of lethal reagents and solvents in the pharmaceutical production. All these improvements will aid the chemical industry to attain as well as achieve its sustainability purposes and reduce the impacts to the surrounding environment. More still, chemical research as a discipline that includes synthesis of new

material as well as designed improvement of existing processes aimed at minimizing wastes and increasing resource efficiency of circular epoxy ideas can also benefit from Artificial Intelligence (AI). The present push for global efforts is to minimize the appearance of plastic waste in the environment is a hoped for improved way of sorting and processing plastic trash; a recycling artificial intelligence system. Artificial Intelligence (AI) is picking up on the sustainable chemical processes on two fronts: the sustainably of the material produced, and the methods that are used in the recycling or reusing of the chemical constituents [28]. Large-scale, high-quality, and accessible databases provide the foundation for efficient artificial intelligence training [29], enabling AI to more accurately predict chemical reaction outcomes, optimize synthesis routes, and enhance experimental efficiency. The diversity and richness of data contribute to improving the generalization capability of AI, allowing it to be applied to a broader range of organic chemistry research [30]. The term "computational chemistry" can apply to a wide range of methodologies designed to gain insight into the fundamental behavior of chemical species in its widest meaning. One such application is quantum mechanics related procedures, but not limited to these. The computer will work on all the data that is inputted into the simulation and help analyze complex experimental data, Computational Chemistry (CC) includes quantum chemistry simulation, molecular dynamic simulation, and artificial intelligence (AI) simulation of generating de novo molecules. It is useful in an experimental chemistry course because of its ability to give information on molecular structure, properties and interactions at the molecular level [33]. Thanks to the developments in software engineering, AI has enhanced its learning and information processing abilities. By using the power of AI, computational chemistry can integrate multiple methods and techniques that allow scientists to model chemical processes and properties without conducting experiments [34&35].

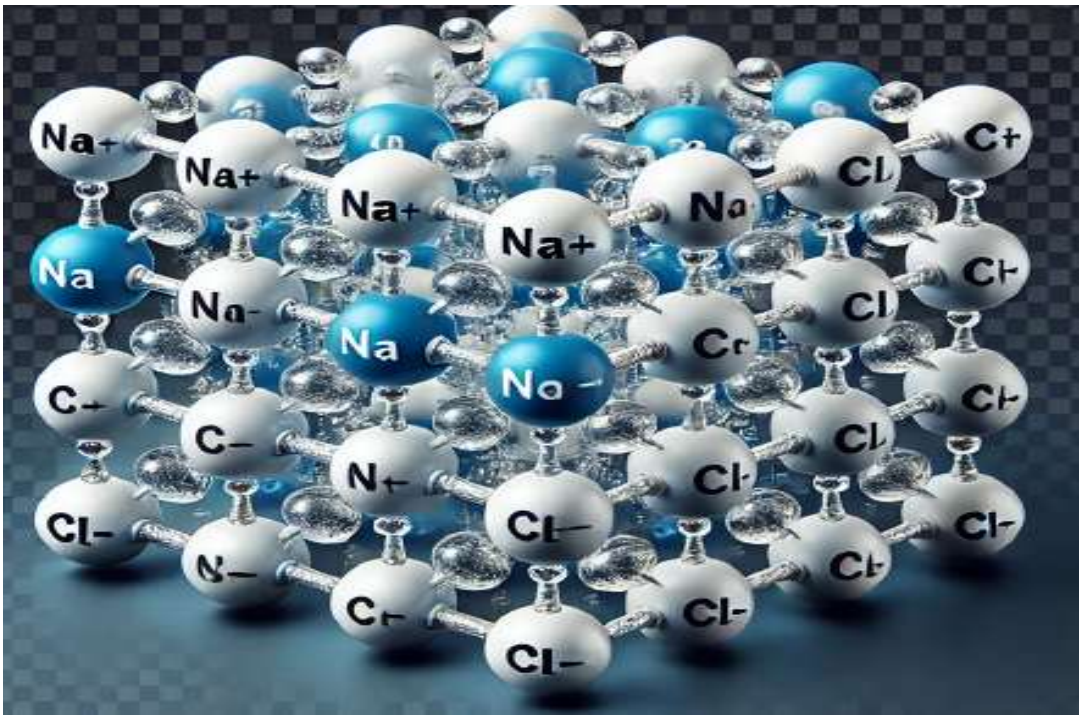

Fig2. Inaccurate representation of NaCl generated by Chat GPT 4.0.

2-Results and Discussion

2.1- Geometric Optimization of paracetoml and some derivative's

Theoretical calculations of the some organic compounds have been accomplished utilizing the Gaussian 09W program package and using the Hartree- Fock (HF) and Basis set 3-21G approximation.

2.2- Geometric Optimization of paracetamol (acetaminophen) [S1]

The provided image displays the geometrically optimized molecular structure of paracetamol, also commonly known as acetaminophen. This specific three-dimensional conformation was obtained through quantum chemical calculations utilizing the Gaussian 09W program package, implemented at the Hartree-Fock (HF) level of theory in conjunction with the 3-21G basis set. The visualization depicts a standard ball and stick model representation on a solid blue background to show the spatial arrangement and connectivity of the atoms once at their lowest energy state. The center of the molecule is a benzene ring of six carbon atoms (the large grey spheres, labelled C). The aromatic ring has a planar geometry typical of sp2 hybridized carbon networks, in which the π - electrons in the ring are stabilized by alternating single and double bonds. The four C atoms in this ring are each attached to a hydrogen atom (small white sphere, labelled H), which are all in the same plane as the ring. Directly opposite to the functional modifications on the ring, a hydroxyl group is attached to one of the aromatic carbons. The geometry of this hydroxyl

hydrogen is related to the local electrostatic and steric balance that occurred in the optimization process using the Hartree-Fock approach. The other side of the benzene ring is substituted by an acetylamino group, making paracetamol an amide. The first part of this attachment is a blue, nitrogen atom with a single hydrogen atom attached directly to one of the ring carbons. The nitrogen atom is attached to a double-bonded carbonyl carbon, which is double-bonded to a red oxygen atom. A terminal methyl group, comprising of a grey carbon atom with three white hydrogen atoms around it and in a tetrahedral-like arrangement, is also attached to this carbonyl carbon. All the spatial arrangement reflect the optimized dihedral angles between the amide group and the aromatic ring. The image shows the steric and electronic compensation between the molecule, due to the limitation of the HF/3-21G method, and presents the tilt of the amide plane in relation to the benzene ring.

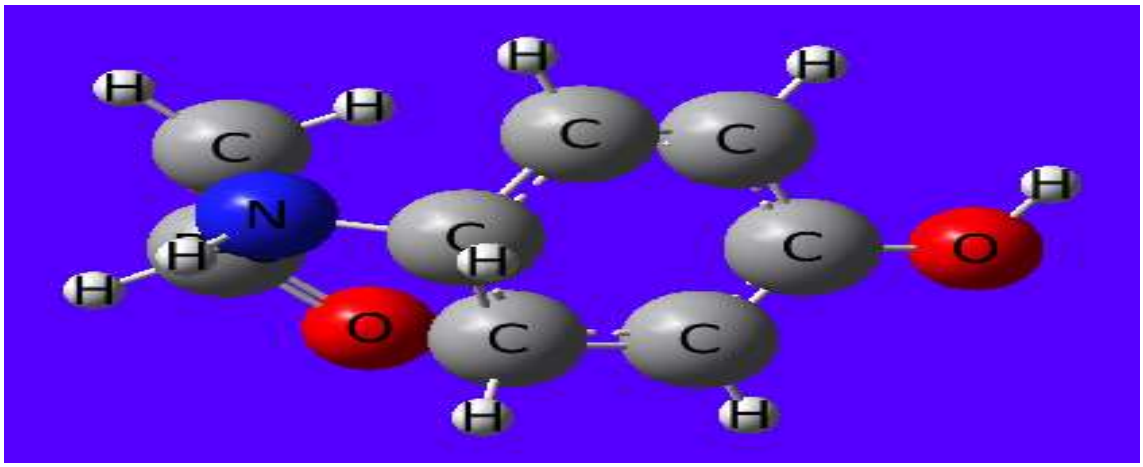

Fig 3 : The optimized structure of paracetamol

2.3- Geometric Optimization of Phenacetin (Acetophenetidin) [S2]

The molecular model shown corresponds to a specific and stable configuration of the molecule, known as the minimum energy spatial structure, which was obtained after geometric optimization of the molecule phenacetin (acetophenetidin). The computational simulation was carried out with the Gaussian 09W software package, which is based on ab initio electronic structure theory. Specifically, the self-consistent field (SCF) Hartree-Fock (HF) method was used in calculations, which were performed using the 3-21G split-valence basis set. Central Benzene Ring: This is the basic structure around the molecule, which is locked in a planar structure, as all the carbon atoms in the central benzene ring have sp2 hybridization, which allows the delocalization of pi-electrons over the whole aromatic system. Importantly, two individual carbon atoms in this aromatic ring are labelled by the letter “R”, to indicate

their position as ipso-carbons to which substitution occurs, and to give the para-disubstituted symmetry pattern found in phenacetin. The 4–OCH_2CH_3 group is called the ethoxy group. This group is separated from one side of the aromatic ring by an ether linkage. The oxygen atom (in red) connects the ring with the ethyl chain. By using the geometric optimization the spatial orientation of this ethoxy group relative to the benzene ring is revealed, which is found in a particular dihedral angle, where steric hindrance and the electron conjugation between the lone pair of the oxygen atom and the pi-system of the benzene ring play a balance. Also, the conformation of the ethyl group is staggered, as sp^3 hybridised carbon atoms try to avoid torsional strain by doing so, and the arrangement of the attached hydrogen atoms is obviously staggered. The Acetamido Group (-$NHCOCH_3$): In this group the nitrogen atom (blue) is across from the benzene ring in the para-position, and connects the ring to the carbonyl carbon. The double-bonded red oxygen sphere in the carbonyl group makes it very characteristic. The optimized geometry highlights the structure of the amide bond that has some double bond character because of resonance of the N lone pair with the pi system in the carbonyl. This electronic effect keeps the amide moiety (the N, the carbonyl C, the carbonyl O and the attached H) pretty planar. The methyl group attached to the carbonyl carbon completes the acetamido group with all its hydrogen atoms pointing away from this carbon-carbon double bond, in a low energy staggered conformation, to minimise steric hindrance.

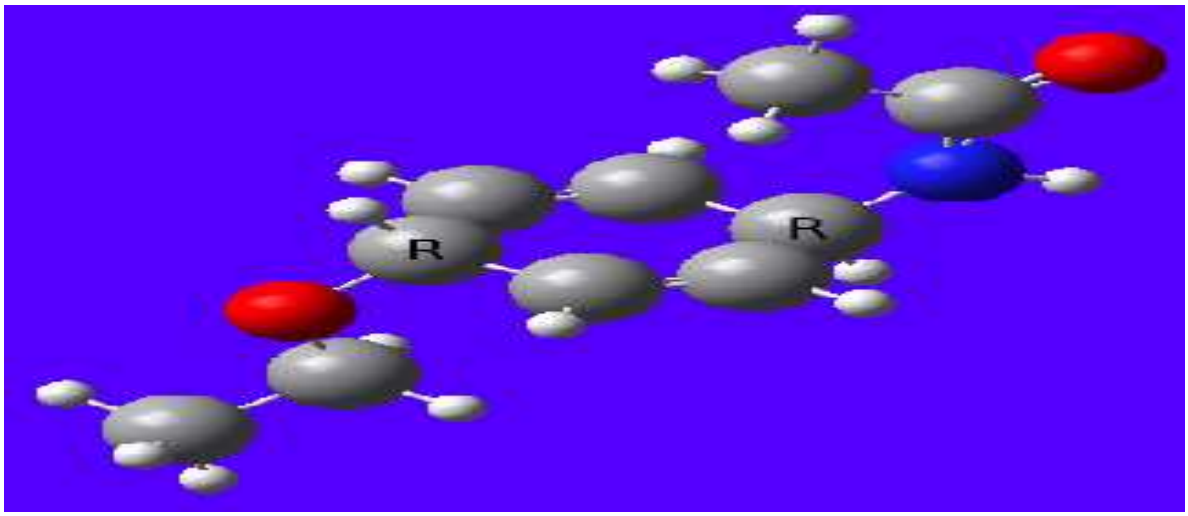

Fig 3 : The optimized structure of Phenacetin (Acetophenetidin)

2.4- Geometric Optimization of N-(4-propoxy phenyl) acetamide [S3]

The hexatomic aromatic benzene ring is the central framework of the molecule, which exists in the primary planar conformation with a minimum of angular strain and to allow maximum delocalisation of π-electrons in the cyclic framework. The electronic distribution of the para-substituted functional groups, however, causes an appreciable deviation from the idealized aromatic geometry in the theoretical model. The presence of the electron-donating propoxy group at one terminus and the electron-withdrawing amide group at the other para-position creates a slight structural distortion in the ring as the internal bond angles are slightly larger and smaller than the ideal 120° due to the different steric requirements and localized induction effects of the rings. The amide functional group, with the (N-methylcarbonyl) attachment, at the nitrogenous end shows a heavily stabilized planar conformation, which is very restricted by resonance. The nitrogen atom is almost SP2 hybridised so that the continuous N-C(=O) chain has a significant partial double bond character in the molecule because of the overlap of the N lone pair orbital with the carbonyl π*- antibonding orbital. A large resonance energy barrier leads to a fixed spatial orientation of the amide unit in relation to the benzene ring. A critical balance is the dihedral angle of the amide linkage with the plane of the aromatic ring which would be maximized by extended conjugation along the aromatic system, but is sterically hindered by the approach of the ortho-hydrogen on the ring to the carbonyl oxygen or the methyl group. The optimized Hartree-Fock structure, therefore, is the conformation in which the amide plane is twisted to some particular angle with respect to the aromatic core, to minimize the total ground-state potential energy. At the opposite end of the molecular architecture, the 4-propoxy chain gives a high conformational flexibility to the structure. The oxygen atom directly bonded to the aromatic ring has an SP3 like structure with partial π -donation into the benzene system that affects the adjacent C_{aromatic}-O-C_{aliphatic} bond angle. The aliphatic propoxyl chain formed by three successive methylene and methyl groups, changes away from the rigid planar structure of the aromatic core towards a staggered, extended zigzag spatial structure. The anti-periplanar conformation along the alkyl backbone is the most stable conformation with the HF/3-21G computational approach due to the reduction of localized steric repulsions and eclipsing interactions between adjacent hydrogen atoms. The orientation of the whole propoxy chain is determined by the particular angle around the ether bond, which dictates that the large, aliphatic part points away from the benzene ring plane, minimizing the transannular spatial crowding and giving the lowest energy conformation for the free molecule.

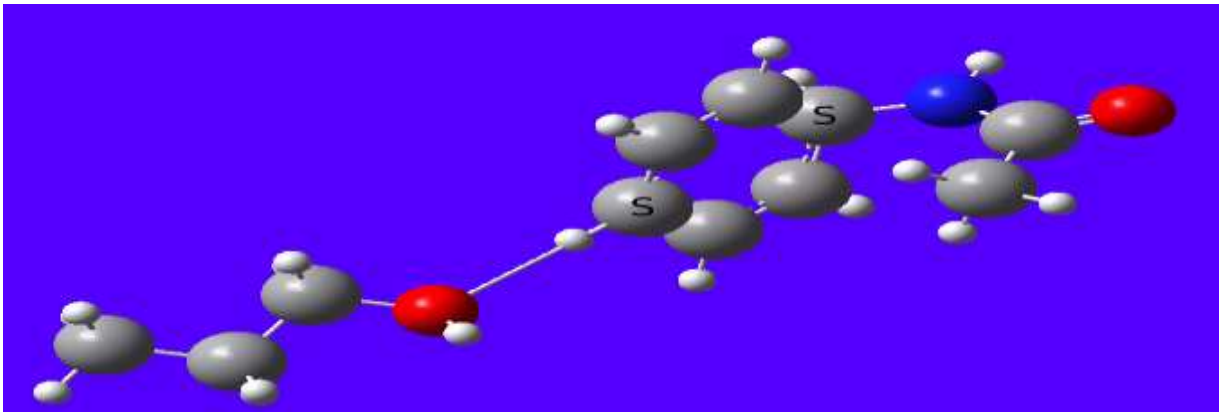

Fig 4 : The optimized structure of N-(4-propoxy phenyl) acetamide

2.5- Geometric Optimization of N-(4-butooxyphenyl)acetamide [S4]

This *3D* molecular model shows the optimized spatial geometry conformation of N-(4-butoxyphenyl) acetamide, also called Phenacetin, an organic compound. The molecular optimization has been carried out with Gaussian 09W computational chemistry software using the Hartree-Fock (HF) level of theory using split-valence 3-21G basis set. Standard Corey Pauling Koltun (CPK) colour coding is used to distinguish the atomic elements. The largest grey spheres depict the carbon framework, the smaller white spheres indicate hydrogen atoms, the coloured red spheres represent highly electronegative oxygen atoms and the deep blue sphere is the nitrogen atom located within the amide linkage. The molecule is central, with the core structure being a flat, aromatic benzene ring consisting of six grey carbon atoms connected by bonds. The geometry of this ring is fixed by alternating double bonds with each carbon forming a C-H bond with a peripheral hydrogen on the ring, with the exception of the 1 and 4 positions where the major functional substitutions occur. The aromatic system consists of one carbon atom with the letter R as a reference point for determining the position of the atom in the Gaussian output log file, bond angles or dihedral torsions. The butoxy group (4-$OCH_2CH_2CH_2CH_3$) is extended at the para-position and the oxygen atom of the butoxy group is directly attached to the phenyl ring. This oxygen is linked to a flexible, zig zagging aliphatic chain with four carbon atoms. The geometry of each methylene (-CH_2-) group and the terminal methyl (-CH_3) shows the characteristic tetrahedron form (Sp3hybridization) and the hydrogens are staggered to minimize steric hindrance and torsional strain in the computed vacuum. Directly opposite the ether group on the benzene ring sits the acetamide moiety (-NH-CO-CH_3) The nitrogen atom, colored in blue, links directly to the aromatic ring and is also bonded to a single white hydrogen atom. Adjacent to this nitrogen is the carbonyl carbon, which forms a rigid double bond with a

red oxygen atom. The carbonyl carbon terminates into a final methyl carbon, surrounded by three hydrogen atoms. The entire amide group tends to maintain a nearly planar conformation due to partial double-bond character between the nitrogen and the carbonyl carbon, which aligns structural resonance across the nitrogen lone pair, the carbonyl group, and the adjacent aromatic π -system.

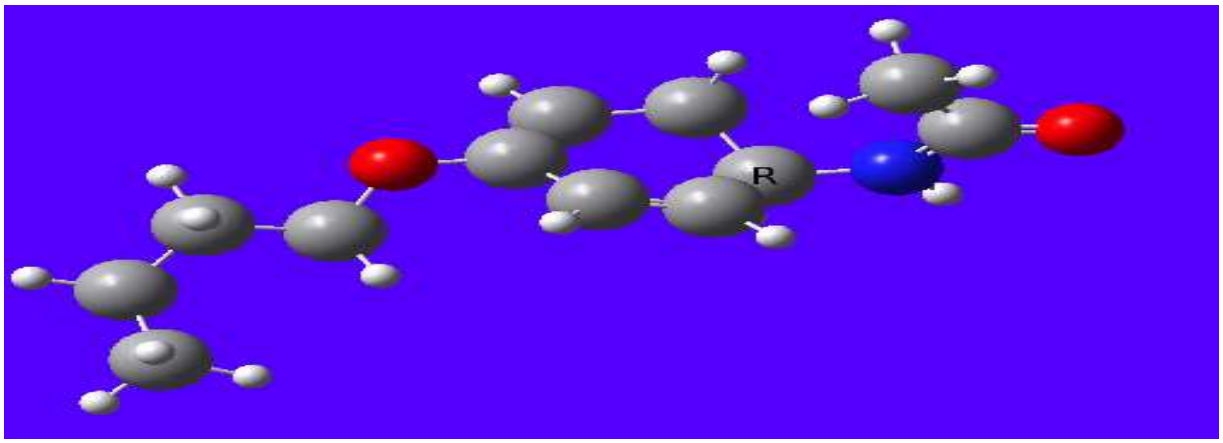

Fig 5 : The optimized structure of N-(4-butooxyphenyl)acetamide

2.6- Geometric Optimization of 4-acetamidophenyl hydrogen sulfate [S5]

On one side of the aromatic core, the acetamido group (-NHCOCH) exhibits a strong tendency toward planarity due to the partial double-bond character of the C-N amide bond, which stems from the resonance conjugation between the nitrogen lone pair and the carbonyl π –system. This rigid amide plane is correctly described by the Hartree-Fock method. Usually the amide H is trans to the carbonyl O in the lowest energy conformation. Importantly, the entire acetamido plane is not exactly coplanar with the benzene ring, but rather is twisted through a certain torsional angle, to minimize steric interactions between the two ortho-ring hydrogens and the amide hydrogen or carbonyl oxygen. The conformation of the terminal $–CH_3$ group is staggered and this minimizes the torsional strain when compared to the adjacent carbonyl framework. The hydrogen sulfate ester group $–OSO_3H$ on the opposite end of the benzene ring has a highly tetrahedral geometry about the central "S" atom, which is the structural geometry of hydrogen sulfate. On the other end of the benzene ring, the $–OSO_3H$ group is highly tetrahedral around the central S atom, the same geometry as that of the hydrogen sulfate group, $–OSO_3H$. The sulfur atom is bonded to a bridging ester oxygen atom, two terminal oxo-oxygen atoms (S=O bonds) and a hydroxyl group (-S-OH). The sulfur-oxygen bonds are highly polarized at the RHF/3-21G (restricted Hartree-Fock) level of theory. The C-O-S bond angle has a significant deviation from the linear angle, usually around 115º to 120º, pushing the bulky $–OSO_3H$ group out of the phenyl ring plane. The dihedral angle across

the phenyl-oxygen-sulfur bond determines that the conformation is one in which the sulfate group is approximately perpendicular (or skewed) to the aromatic ring, and such an arrangement will lead to the minimization of the strong electron cloud repulsion between the π –cloud of the benzene ring and the lone pairs of the terminal oxygens. Moreover, the terminal acidic hydrogen atom –OH has a specific orientation that reduces the internal dipole moments, which usually results in a weak stabilizing intramolecular interaction with one of the terminal oxo-oxygen atoms. The Hartree-Fock theory ignores the interaction between the electrons of the two systems, but treats the electrostatic interactions rigidly, so that the most likely conformation is dependent on a compromise between maximizing the conjugation in the aromatic and amide groups and minimizing the large electrostatic repulsion potential put in by the very negative oxygens in the sulfate group. The optimization of the structure leads to a molecule of considerable net dipole moment with the electron density being strongly attracted towards the sulfate ester pole, while the acetamido framework on the other side has moderately electron-donating properties. This push-pull electronic distribution results in the final stable spatial topology, which is a structured and balanced conformation with no steric clash being achieved by the cooperative twisting of both terminal functional groups with respect to the central aromatic spacer.

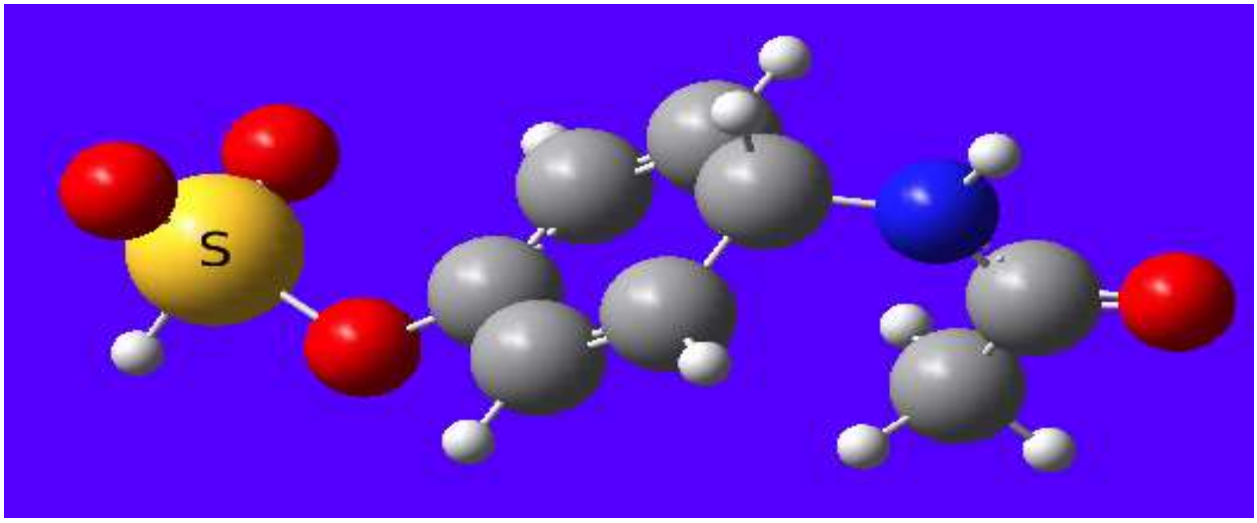

Fig 6 : The optimized structure of 4-acetamidophenyl hydrogen sulfate

Table (1): Summarized some theoretical calculations by using Gaussain09

Energy/ kJ[x 10^{-18}]	Dipole moment(Debye)	Comp.No
-2.22	3.428	**S_1**
-2.56	3.793	**S_2**
-2.73	6.952	**S_3**
-2.90	4.560	**S_4**
-4.59	3.340	**S_5**

Conclusion

The theoretical calculations of paracetamol and its derivatives using Gaussian 09 software, revealed that the derivatives of paracetamol with H and aliphatic alkyl groups [S1(4-OH) , S2(4-OCH_2CH_3) ,S3(4-$OCH_2CH_2CH_3$) , S4 (4-$OCH_2CH_2CH_2CH_3$)] had convergent conformational potential energies. The convergence is thought to result from a similarity in steric hindrance. In contrast, the paracetamol derivative [S5 (-OSO_3H)], shows much greater stability, showing a lower geometry optimization energy. A negative total energy represents a stable conformation in a molecule in computational chemistry and quantum mechanics, with the system having given off more energy in order to reach this minimized geometry. Thus, 4-acetamidophenyl hydrogen sulfate is much more stable and thermodynamically favored than N-(4-butoxyphenyl)acetamide. The strong intramolecular electrostatic interactions and the resonance stabilization of the oxygen–sulfur bonds increase due to the presence of the highly polar and electron-withdrawing sulfate ester moiety. The sulfur atom has several very electronegative oxygen atoms and this contributes to the delocalization of the electronic charge distribution over that part of the molecule. This broad charge delocalization reduces the potential energy of the whole quantum system, thus resulting in a more attractive energy minimum in the geometry optimization process. The electron donating O-C ether bond, by contrast, do not have the ability to withdraw electrons or stabilize the charge because they are aliphatic alkyl groups. The sulfate substituents, on the other hand, are known to have a high charge stabilizing capacity. Hence the compound [S5 (4-OSO_3H)] in which the sulfate group is attached to the C-4 position can be said to have a more stable molecular structure thermodynamically and conformationally.

References

1- Pongpalilu et all., (2023). Perkembangan Peserta Didik: Teori & Konsep Perkembangan Peserta Didik Era Society 5.0. PT. Sonpedia Publishing Indonesia.

2-Akbar, J. S., & Djakariah, D. (2023). Pemanfaatan Media Pembelajaran Berbasis Android Menggunakan Pendekatan Inkuiri Untuk Menguatkan Technological Pedagogical and Content Knowledge (TPACK) Calon Guru. Oxygenius Journal Of Chemistry Education, 5(1), 46-53.

3-Ariani, M., Zulhawati, Z., Haryani, H., Zani, B. N., Husnita, L., Firmansyah, M. B., & Hamsiah, A. (2023). Penerapan Media Pembelajaran Era Digital. PT. Sonpedia Publishing Indonesia.

4- Saleem, N., Mufti, T., Sohail, S. S., & Madsen, D. Ø. (2024). ChatGPT as an innovative heutagogical tool in medical education. Cogent Education, 11(1), 2332850.

5- Deveci Topal, A., Dilek Eren, C., & Kolburan Geçer, A. (2021). Chatbot application in a 5th grade science course. Education and Information Technologies, 26(5), 6241-6265.

6- Seth, I., Lim, B., Cevik, J., Sofiadellis, F., Ross, R. J., Cuomo, R., & Rozen, W. M. (2024). Utilizing GPT-4 and generative artificial intelligence platforms for surgical education: an experimental study on skin ulcers. European Journal of Plastic Surgery, 47(1), 19.

7- Abulibdeh, A., Zaidan, E., & Abulibdeh, R. (2024). Navigating the confluence of artificial intelligence and education for sustainable development in the era of industry 4.0: Challenges, opportunities, and ethical dimensions. Journal of cleaner production, 437, 140527.

8- Filgueiras, F. (2024). Artificial intelligence and education governance. Education, Citizenship and Social Justice, 19(3), 349-361.

9- Chen, Y., Jensen, S., Albert, L. J., Gupta, S., & Lee, T. (2023). Artificial intelligence (AI) student assistants in the classroom: Designing chatbots to support student success. Information Systems Frontiers, 25(1), 161-182.

10- Fitria, T. N. (2021). QuillBot as an online tool: Students' alternative in paraphrasing and rewriting of English writing. Englisia: Journal of Language, Education, and Humanities, 9(1), 183-196.

11- Suk Hwang, Y., & Vrongistinos, K. (2012). Using Blackboard and Skype for mentoring beginning teachers. American Journal of Distance Education, 26(3), 172-179.

12- Guo, S., Zheng, Y., & Zhai, X. (2024). Artificial intelligence in education research during 2013–2023: A review based on bibliometric analysis. Education and information technologies, 29(13), 16387-16409.

13- Farazouli, A., Cerratto-Pargman, T., Bolander-Laksov, K., & McGrath, C. (2024). Hello GPT! Goodbye home examination? An exploratory study of AI chatbots impact on university teachers' assessment practices. Assessment & Evaluation in Higher Education, 49(3), 363-375.

14- Feldman-Maggor, Y., Cerratto-Pargman, T., & Viberg, O. (2024, September). Seeing the forest from the trees: Unveiling the landscape of generative AI for education through six evaluation dimensions. In European Conference on Technology Enhanced Learning (pp. 99-105). Cham: Springer Nature Switzerland.

15- Zhai, X. (2023). ChatGPT and AI: The game changer for education. Zhai, X.(2023). ChatGPT: Reforming Education on Five Aspects. Shanghai Education, 16-17.

16- Clark, T. M. (2023). Investigating the use of an artificial intelligence chatbot with general chemistry exam questions. Journal of Chemical Education, 100(5), 1905–1916.

17- Fergus, S., Botha, M., & Ostovar, M. (2023). Evaluating academic answers generated using ChatGPT. Journal of Chemical Education, 100(4), 1672–1675.

18- Susnjak, T., & McIntosh, T. R. (2024). ChatGPT: The end of online exam integrity? Education Sciences, 14(6), 656.

19- Mowbray, M., Vallerio, M., Perez-Galvan, C., Zhang, D., Chanona, A. D. R.,&Navarro-Brull, F. J. (2022). Industrial data science–a review of machine learning applications for chemical and process industries. Reaction Chemistry&Engineering, 7(7), 1471-1509.

20- Venkatasubramanian, V. (2019). The promise of artificial intelligence in chemical engineering: Is it here, finally?. AIChE Journal, 65(1).

21- Tripathi, A., Misra, K., Dhanuka, R.,&Singh, J. P. (2023). Artificial intelligence in accelerating drug discovery and development. Recent Patents on Biotechnology, 17(1), 9-23.

22- Trinh, C., Meimaroglou, D.,&Hoppe, S. (2021). Machine learning in chemical product engineering: The state of the art and a guide for newcomers. Processes, 9(8), 1456.

23- Blonder, R.,&Feldman-Maggor, Y. (2024). AI for chemistry teaching: Responsible AI and ethical considerations. Chemistry Teacher International, 6(4), 385-395.

24- Butler, K. T., Davies, D. W., Cartwright, H., Isayev, O.,&Walsh, A. (2018). Machine learning for molecular and materials science. Nature, 559(7715), 547-555.

25- Gupta, R., Srivastava, D., Sahu, M., Tiwari, S., Ambasta, R. K.,&Kumar, P. (2021). Artificial intelligence to deep learning: machine intelligence approach for drug discovery. Molecular diversity, 25(3), 1315-1360.

26- Bung, N., Krishnan, S. R., Bulusu, G.,&Roy, A. (2021). De novo design of new chemical entities for SARS-CoV-2 using artificial intelligence. Future medicinal chemistry, 13(6), 575-585.

27- Rawat, A. (2024). Applications Of Artificial Intelligence In Science. International Journal of Pharmaceutical Science and Medicine, 2(1), 53-63.

28- Rawat, A. (2024). Applications Of Artificial Intelligence In Science. International Journal of Pharmaceutical Science and Medicine, 2(1), 53-63.

29- O'keeffe, M., Peskov, M. A., Ramsden, S. J., & Yaghi, O. M. (2008). The reticular chemistry structure resource (RCSR) database of, and symbols for, crystal nets. Accounts of chemical research, 41(12), 1782-1789.

30- Borysov, S. S., Geilhufe, R. M., & Balatsky, A. V. (2017). Organic materials database: An open-access online database for data mining. PloS one, 12(2), e0171501.

31- Nguyen, Q. N. N., & Tantillo, D. J. (2016). Using quantum chemical computations of NMR chemical shifts to assign relative configurations of terpenes from an engineered Streptomyces host. The Journal of antibiotics, 69(7), 534-540.
32- Jadrich, R. B., Lindquist, B. A., & Truskett, T. M. (2017). Recent advances in accelerated discovery through machine learning and statistical inference.

33- McArdle, S., Endo, S., Aspuru-Guzik, A., Benjamin, S. C.,&Yuan, X. (2020). Quantum computational chemistry. Reviews of Modern Physics, 92(1), 015003.

34- Shikano, Y., Watanabe, H. C., Nakanishi, K. M.,&Ohnishi, Y. Y. (2021). Post-Hartree–Fock method in quantum chemistry for quantum computer. The European Physical Journal Special Topics, 230(4), 1037-1051.

35- Keith, J. A., Vassilev-Galindo, V., Cheng, B., Chmiela, S., Gastegger, M., Muller, K. R., & Tkatchenko, A. (2021). Combining machine learning and computational chemistry for predictive insights into chemical systems. Chemical reviews, 121(16), 9816-9872.

دراسة نظرية وحساب خواص بعض المشتقات العضــوية للباراسيتامول باستخدام تطبيق *Gaussian* 09w

*حسين عبود ادهام
*المديرية العامة لتربية كركوك

الخلاصة :

تطبيقات الكيمياء الحاسوبية استخدمت في دراسة خصائص بعض من المركبات العضوية وقد اختيرت مشتقات الباراسيتومول لدراسة بعض خصائصها والهيئة الفراغية عند ادنى مستوى طاقي لها وتم ذلك باستخدام برنامج وشحنة المركب 3-21G, وقاعدة اساس هي Hartre fock والنظرية المستخدمة هي طريقة Gaussain 09W صفر وبدون تاثير المذيب على المركبات التي تم دراستها وعند الحالة المستقرة وليس المثارة وبذلك تم ايجاد الهيئة والمقارنة بين قيم الطاقات المحسوبة ,الفراغية عند ادنى مستوى طاقي وحساب الطاقة للمركبات وعزم ثنائي القطب باختلاف معوضات الباراسيتومول حيث وجدت اختلافا ملحوضا بين المعوضات التي تظهر تاثيرا حاثا وبين مجموعة السلفا التي تظهر تأثير تثبيت الشحنة بالرنين

الكلمات المفتاحية :الكيمياء الحاسوبية , نظرية هارتري فوك , الكيمياء العضوية ,الذكاء الاصطناعي